Dissertation zur Erlangung des Doktorgrades

der Fakultät für Chemie und Pharmazie

der Ludwig-Maximilians-Universität München

Synergy of Single-Crystal X-Ray Diffraction and Atomic Scale Electron Microscopy – Structure Elucidation of Novel Nitridophosphates and Nitrides

Monika Martina **Pointner**

aus

Erding, Deutschland

2024

Erklärung

Diese Dissertation wurde im Sinne von § 7 der Promotionsordnung vom 28. November 2011 von Herrn Prof. Dr. Wolfgang Schnick betreut.

Eidesstattliche Versicherung

Diese Dissertation wurde eigenständig und ohne unerlaubte Hilfe erarbeitet.

München, den 09.04.2024

_____

Monika Martina Pointner

Dissertation eingereicht am	10.04.2024
1. Gutachter	Prof. Dr. Wolfgang Schnick
2. Gutachter	Prof. Dr. Oliver Oeckler
Mündliche Prüfung am	22.05.2024

All sorts of things can happen when you are open

to new ideas and playing around with things.

Stephanie Kwolek (1923–2014), Chemikerin

Sie müssen ihr Talent entdecken und benutzen.

Sie müssen herausfinden, wo ihre Stärke liegt.

Haben Sie den Mut, mit ihrem Kopf zu denken.

Das wird ihr Selbstvertrauen und ihre Kräfte verdoppeln.

Marie Curie zu ihren Schülern und Mitarbeitern,
zitiert in: „Das strahlende Metall", von Wilhelm Strube, S. 167

Für meine Familie.

Danksagung

Mein Dank gilt vor allem Prof. Dr. Wolfgang Schnick für die Möglichkeit meine Dissertation in seiner Arbeitsgruppe anzufertigen. Ich danke Ihnen herzlich für das angenehme Arbeitsklima, alle verfügbaren Ressourcen und die große Flexibilität in der Gestaltung meiner eigenen Forschung.

Bei Prof. Dr. Oliver Oeckler bedanke ich mich für die Übernahme des Koreferats. Vielen herzlichen Dank für die bis heute andauernde Betreuung, die schon während meiner Bachelorarbeit begonnen hat. Die zahlreichen informativen Gespräche, der fachliche Beistand vor allem in Fragen der Kristallographie und die Erfahrungen am DESY und ESRF haben maßgeblich zu dieser Arbeit beigetragen.

Mein Dank geht an Prof. Dr. Johrendt, Prof. Dr. Müller-Caspary, PD Dr. Hoch, sowie Prof. Dr. Ivanović-Burmazović für die Teilnahme an der Prüfungskommission meiner mündlichen Prüfung.

Dr. Markus Döblinger und Dr. Steffen Schmidt danke ich für die Zeit, die sie sich genommen haben, um mich in die Handhabung der Elektronenmikroskope einzuarbeiten. Über die Jahre haben sie immer ein offenes Ohr für meine Fragen gehabt – auch dafür meinen herzlichsten Dank. Bei Dr. Benjamin März, Tizian Lorenzen und allen anderen aus dem AK Müller-Caspary wollte ich mich für die entspannte Zusammenarbeit an den Elektronenmikroskopen bedanken.

Allen Kollaborationspartnern danke ich für die produktive Atmosphäre. Danke an alle, die mir Proben für atomar aufgelöste Elektronenmikroskopie bereitgestellt haben. Es freut mich stets aufs Neue, wenn ich bei der Aufklärung interessanter Strukturen helfen konnte. Mein Dank geht auch an Olga Lorenz für die Hilfe bei administrativen Dingen, Wolfgang Wünschheim für die IT-Betreuung und Dr. Dieter Rau für die Wahrung der Arbeitssicherheit, die Betreuung der Röntgendiffraktometer und die stehst engagierte Übernahme von Heizmessungen. Peter Mayer und Christian Minke danke ich für die Messungen von Einkristallen, sowie die Betreuung von NMR und Rasterelektronenmikroskop.

Herzlicher Dank geht an die Arbeitskollegen aus dem zweiten Stockwerk für die entspannte und freundschaftliche Atmosphäre. Dank an meine ehemaligen und derzeitigen Laborkollegen Dr. Eugenia Elzer, Dr. Lucien Eisenburger, Dr. Simon Kloß, Dr. Dieter Rau, Dr. Sophia Wandelt und

Hannah Waldmann im Labor D2.100. Besonders möchte ich Dr. Lucien Eisenburger danken. Als Mentor und Freund habe ich viel von ihm gelernt, was mir den Einstieg in das wissenschaftliche Arbeiten erleichtert hat.

Danke an meine beiden Praktikanten Jonas Albrecht und Markus Linhart. Eure herausragende Arbeit hat das Betreuen zu einer Leichtigkeit werden lassen und es hat mir ausordentlich viel Spaß gemacht, mein Wissen mit euch zu teilen.

Mein aufrichtiger Dank geht an Alex Feige, Lennart Staab, Dr. Daniel Günther, Dr. Christopher Benndorf, Markus Jakob und dem Rest des AK Oeckler, die mich immer herzlichst auf Tagungen, und Messzeiten aufgenommen haben. Diese Erfahrungen möchte ich wirklich nicht missen.

Danke an den Arbeitskreis Hoch, die mich von Beginn an herzlichst aufgenommen haben und besonders Irina Zaytseva. Ich glaube, ich kann es gar nicht in Worte fassen, aber danke, dass wir von Anfang an geklickt und zusammen scheinbar Unmögliches geschafft haben.

Ganz herzlichen Dank an der Stelle an Dr. Sophia Wandelt, Reinhard Pritzl und Ferdinand Kiss, die die Arbeit Korrektur gelesen haben und mir mit kräftig Rat zur Seite standen.

Danke an meine Freunde Anna Preiwisch und Mihai Manolescu, Margarita Shnipova, Johanna und Florian Schmalhofer und Fabian Knechtel, deren Beistand und das gemeinsame Unileben eine Bereicherung waren. Ohne euch wäre ich nicht so weit gekommen.

Meine Eltern Maria und Franz Pointner danke ich für die Unterstützung. Ohne eure aufopferungsvolle Liebe würde ich nicht hier stehen. Meiner Schwester Tanja Pointner gilt mein tiefster Respekt und Dank für die Zusammenarbeit auf unserem Hof. Ohne dich wäre ich nicht der Mensch, der ich heute bin und ich könnte auch nicht mein Leben so führen, wie ich es tue und meine Träume und Wünsche erfüllen. Danke an meinen Verlobten und baldigen Mann Ferdinand Lajos Kiss. Für jedes Hoch und Tief und für die Unterstützung bei all meinen Ideen.

Monika Pointner

Table of Contents

1. Introduction 15

1.1. General Aspects 17

1.2. Phosphorus Nitrides and Nitridophosphate Structures 17

1.2.1. Structure Overview 17

1.2.2. Structural Patterns in Nitridophosphates 18

1.2.3. Multicationic Nitridophosphates 22

1.3. High-Pressure High-Temperature Syntheses of Nitrides and Nitridophosphates 24

1.4. Analytical Methods 26

1.4.1. Single-Crystal X-Ray Diffraction 26

1.4.2. Synchrotron X-Ray Diffraction 27

1.4.3. Transmission Electron Microscopy 29

1.4.3.1. General Aspects of Transmission Electron Microscopy 29

1.4.3.2. Conventional Transmission Electron Microscopy 29

1.4.3.3. Scanning Transmission Electron Microscopy 31

1.5. Combining X-Ray Diffraction and Electron Microscopy Analysis 35

1.6. Scope of this Thesis 36

1.7. References 37

2. Tetra-Face-Capped Octahedra in a Tetrahedra Network – Structure Determination and Scanning Transmission Electron Microscopy of $SrAl_5P_4N_{10}O_2F_3$ 43

2.1. Abstract 44

2.2. Introduction 45

2.3. Experimental Section 47

2.3.1. Preparation of Starting Materials 47

2.3.2. Multianvil Synthesis 47

2.3.3. Powder X-Ray Diffraction 47

2.3.4. Energy-Dispersive X-Ray Spectroscopy 48

2.3.5. Scanning Transmission Electron Microscopy 48

2.3.6. Single-Crystal X-Ray Diffraction 48

2.3.7. IR Spectroscopy 49

2.3.8. Luminescence Measurements 49

2.4. Results and Discussion 50

2.4.1. Synthesis 50

2.4.2. Crystal Structure Determination 51

2.4.3. Structure Description 54
2.4.4. Luminescence 57
2.5. Conclusion 59
2.6. References 60

3. Tetrahedra Networks with Additional Cations – Isolated AlN_6 Octahedra in the Imido-nitridophosphates $AE_2AlP_8N_{15}(NH)$ (*AE* = Ca, Sr, Ba) 63

3.1. Abstract 64
3.2. Introduction 65
3.3. Experimental Part 67
3.3.1. Preparation of Starting Materials 67
3.3.2. Multianvil Synthesis 67
3.3.3. Powder X-Ray Diffraction 68
3.3.4. Energy-Dispersive X-Ray Spectroscopy 68
3.3.5. Scanning Transmission Electron Microscopy 68
3.3.6. Single-Crystal X-Ray Diffraction 69
3.3.7. Bond Valence Sum Calculations 69
3.3.8. Madelung Part of Lattice Energy 70
3.3.9. Solid-State Magic Angle Spinning NMR Spectroscopty 70
3.3.10. IR Spectroscopy 70
3.3.11. Luminescence Measurements 70
3.4. Results and Discussion 71
3.4.1. Synthesis 71
3.4.2. Crystal Structure Determination 72
3.4.3. Structure Description 74
3.4.4. Solid-State NMR 79
3.4.5. Luminescence Measurements 80
3.5. Conclusion 83
3.6. References 84

4. $Cr_{5.7}Si_{2.3}P_8N_{24}$ – A Chromium(+IV) Nitridosilicate Phosphate with Amphibole-Type Structure 87

4.1. Abstract 88
4.2. Introduction 89
4.3. Experimental Part 91
4.3.1. Preparation of Starting Materials 91
4.3.2. Multianvil Synthesis 91

4.3.3. (High-Temperature) Powder X-Ray Diffraction 92
4.3.4. Single-Crystal X-Ray Diffraction 92
4.3.5. Bond Valence Sum Calcultions and Partial Values of the Madelung Part of Lattice Energy 92
4.3.6. Electron Microscopy and Energy-Dispersive X-Ray Spectroscopy 93
4.3.7. Vibrating Sample Magnetometer 93
4.3.8. Electron Paramagnetic Resonance 94
4.3.9. IR Spectroscopy 94
4.3.10. UV-Vis-NIR Spectroscopy 94
4.4. Results and Discussion 95
4.4.1. Synthesis 95
4.4.2. Crystal Structure Determination 95
4.4.3. Structure Description 96
4.4.4. Magnetic Measurements 99
4.4.5. Optical Measurements 100
4.5. Conclusion 101
4.6. References 102

5. $P_{1-x}Ta_{8+x}N_{13}$ (x = 0.1–0.15): A Phosphorus Tantalum Nitride With High Specific Resistivity Featuring Mixed-Valent Tantalum and P/Ta Disorder 107

5.1. Abstract 108
5.2. Introduction 109
5.3. Experimental Part 110
5.3.1. Preparation of Starting Materials 110
5.3.2. Multianvil Synthesis 110
5.3.3. (High-Temperature) Powder X-Ray Diffraction and Rietvled Refinement 111
5.3.4. Single-Crystal X-Ray Diffraction 111
5.3.5. Energy-Dispersive X-Ray Spectroscopy 112
5.3.6. (Scanning) Transmission Electron Microscopy 112
5.3.7. Physical Property Measurement System 112
5.3.7.1. Temperature-Dependent Resistivity Measurements 112
5.3.7.2. Vibrating Sample Magnetometer 113
5.3.8. Electron Paramagnetic Resonance 113
5.3.9. Density Functional Theory Calculations 113
5.3.10. Electron Localization Function and Bader Analysis 114
5.3.11. UV-Vis-NIR Spectroscopy 115
5.4. Results and Discussion 116
5.4.1. Synthesis 116

5.4.2. Crystal Structure Determination ... 117
5.4.3. Structure Description ... 118
5.4.4. Magnetic Measurements ... 120
5.4.5. Bader Charge Population Analysis ... 120
5.4.6. Density Functional Theory and Electron Localization Function Calculations ... 121
5.5. Conclusion ... 123
5.6. References ... 124
6. Conclusion and Outlook ... 129
6.1. Prospects on the Synthesis of Nitrides and Nitridophosphates ... 130
6.2. Prospects on Analytical Methods ... 131
6.3. Prospects on the Structural Composition of Nitrides and Nitridophosphates ... 132
7. Summary ... 137
8. Appendix ... 143
A. Supporting Information for Chapter 2 ... 144
A.1. Synthesis ... 144
A.2. Rietveld Refinement ... 145
A.3. FTIR Spectrum ... 145
A.4. Crystallographic Data ... 146
A.5. Transmission Electron Microscopy ... 147
A.6. Structure Description ... 149
A.7. Luminescence Spectrum ... 151
B. Supporting Information for Chapter 3 ... 152
B.1. Synthesis ... 152
B.2. Crystallographic Data ... 152
B.3. Transmission Electron Microscopy ... 155
B.4. Rietveld Refinements ... 156
B.5. High-Temperature PXRD ... 157
B.6. Partial MAPLE Values ... 158
B.7. Bond Valence Sum Calculations ... 159
B.8. Charge Distribution Calculatioins ... 161
B.9. EDX Measurements ... 162
B.10. FTIR Spectrum ... 163
B.11. Structure Description ... 163
B.12. Interatomic Distances ... 165
B.13. Scanning Transmission Electron Microscopy ... 168
B.14. Luminescence ... 171

C. Supporting Information for Chapter 4 172
C.1. Synthesis 172
C.2. Structure Determination 172
C.3. Rietveld Refinement 176
C.4. High-Temperature PXRD 177
C.5. Elemental Analysis 177
C.6. FTIR Spectrum 178
C.7. Coordination Environments 178
C.8. Polyhedra Volumina 179
C.9. BVS Calculations and Partial MAPLE values 180
C.10. Scanning Transmisison Electron Microscopy 181
C.11. References to Known Nitridochromates and Chromium Nitrides 182
C.12. Magnetization Isotherm 183
C.13. Electron Paramagnetic Resonance 184
C.14. UV-Vis Spectrum 185

D. Supporting Information for Chapter 5 186
D.1. Synthesis 186
D.2. Structure Elucidation 186
D.3. Rietveld Refinement 192
D.4. High-temperature PXRD 192
D.5. Elemental Analysis 193
D.6. Comparison with Ta_3N_5 193
D.7. Coordination Environment 194
D.8. Scanning Transmission Electron Microscopy 194
D.9. UV-Vis Spectrum 197
D.10. Magnetic Measurements 197
D.11. Electron Paramagnetic Resonance Measruements 198
D.12. Bader Charge Population Analysis 199
D.13. Density Functional Theory Calculations 201

9. Miscellaneous 205

A. List of Publications Within this Thesis 206

B. List of Publications Beyond this Thesis 207

C. Contributions to Conferences and Seminars 210

D. Deposited Crystallographic Data 212

E. Curriculum Vitae 213

Chapter 1

Introduction

1.1. General Aspects

The chemical composition and atomic structure dictates the physical and chemical properties, and a thorough structural analysis allows us a profound understanding of solid-state structures. Progress in the methods used for structural analysis, for example for X-ray diffraction or electron microscopy, enables an improving resolution of the provided information. The faster and easier determination of structural parameters combined with increasing accuracy is a step forward to understand structures, explain properties, derive structure-property relationships and aid the development of new compounds for applications. Synthesis, detailed elucidation and potential applications do not necessarily have to be related events, as GaN shows. Its initial synthesis traces back to 1932, the wurtzite structure-type was reported in 1938,[1] and the first crystal structure refinement data could be obtained by 1977.[2] With an ideal band gap of 3.4 eV,[3] GaN was the final puzzle piece for creating light-emitting diodes (LED) of all primary colors.[4-6] Structural similarities paved the way for the identification of numerous other semiconductors with wurtzite and zinc blende structure types.[7-10]

This thesis presents the synthesis and characterization of novel solid-state nitrides and nitridophosphates. The main objective is the comprehensive structural analysis by a combination of information provided by X-ray diffraction and electron microscopy, in cases where individual methods for structure determination are limited.

1.2. Phosphorus Nitrides and Nitridophosphate Structures

1.2.1. Structure Overview

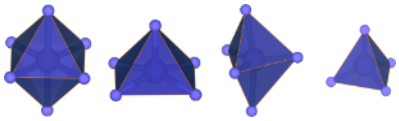

Nitrides are solid-state compounds that contain nitrogen with a formally assigned oxidation state of –III and phosphorus nitrides include phosphorus with an assigned oxidation state of +V. Phosphorus is coordinated by four to six nitrogen atoms and resulting coordination polyhedra can be described as tetrahedra, trigonal bipyramids, square pyramids and octahedra. Structures are referred to as nitridophosphates if they contain an anionic network formed by PN_4 tetrahedra together with additional metal cations, for example, alkali metals, and alkaline earth metals. Common structural motifs are discrete tetrahedra, vertex-sharing chains, layers and networks and provide an ample structural variety. This is associated with the isolobal relation between P-N and Si-O bonds, which preserves a close analogy to silicate structures.[11]

Imidonitridophosphates contain additional imide $(NH)^{2-}$ groups[12-17] and oxonitridophosphates include oxygen in addition to nitrogen.[18-22] Both cases lead to a modified charge of the network due to $(NH)^{2-}$ and O^{2-} anions next to N^{3-}. In addition to P-centered tetrahedra, the network can also consist of polyhedra whose central atoms have a similar radius to phosphorus (P^{+V}: 17 pm, CN = 4).[23] Known representatives include SiN_4 tetrahedra (Si^{+IV}: 26 pm, CN = 4),[23-25] as well as BN_3 units and BN_4 tetrahedra (B^{+III}: 11 pm, CN = 4).[23, 26-28]

In addition to networks that exclusively consist of vertex-sharing PN_4 tetrahedra, edge-sharing tetrahedra,[16, 27, 29-31] as well as higher coordination numbers of phosphorus (CN = 5–6)[28, 31-35] can be found. Latter have so far only been discovered under high-pressure in binary and ternary phosphorus nitrides. The structure of δ-P_3N_5 exhibits vertex-, edge-, and face-sharing PN_6 octahedra.[31] In the high-pressure polymorphs β-BP_3N_6 and spinel-type γ-BeP_2N_4 edge-sharing PN_6 octahedra are present and the structure of PN_2 is exclusively consisting of vertex-sharing PN_6 octahedra (Figure 1.1 left side).[28, 31, 35] The phosphorus nitride γ-P_3N_5 contains square PN_5 pyramids next to PN_4 tetrahedra.[34] Edge-sharing trigonal bipyramids can be found in the high-pressure polymorph of the phosphorus nitride imide HP_4N_7, as well as in the nitridophosphate AlP_6N_{11}.[32-33] However, the majority of structures rich in nitrogen and phosphorus exhibit an anionic network of vertex-sharing PN_4 tetrahedra together with additional metal cations and are classified as nitridophosphates (Figure 1.1 right side).

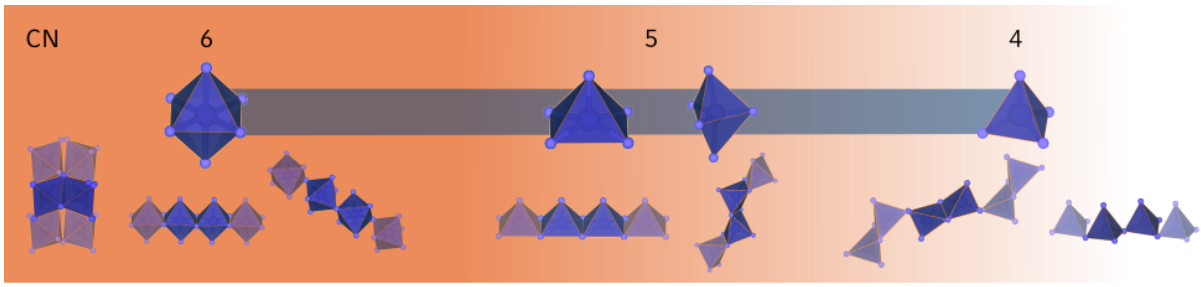

Figure 1.1. Structure motifs found in phosphorus nitrides and nitridophosphates; displayed is the highest degree of interconnection found in each structure; CN = 6: face-(δ-P_3N_5)[31], edge-(β-BP_3N_6, γ-BeP_2N_4)[28, 35] and vertex-(PN_2)[31] sharing PN_6 octahedra; CN = 5: edge-sharing square pyramids (γ-P_3N_5)[34] and trigonal bipyramids (AlP_6N_{11}, HP_4N_7);[32-33] CN = 4: edge-sharing tetrahedra (α-/α'-P_3N_5, HP_4N_7, P_4ON_6, α-BP_3N_6);[16, 27, 29-31] nitridophosphate structures are illustrated in Figure 1.2.

1.2.2. Structural Patterns in Nitridophosphates

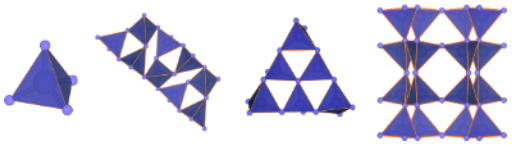

The discovery and categorization of structural patterns are the first steps to reveal crystallographic similarities and to classify new structures. Here the use of coordination polyhedra to display the chemical bonding situation serves as valuable tool for identifying similarities and trends. By comparing compounds rich in additional metal cations with compositions rich in phosphorus and nitrogen, a structural transition in ternary and multinary nitridophosphates can be systematically characterized. Therefore, structures can be classified based on their cation ratio CR = N(*M*)/N(NFC), that gives the ratio of the metal cation (*M*) to the network forming cation (NFC), for example phosphorus (P).[21] The coordination polyhedra of cations, along with their degree of interconnection are analyzed. The degree of interconnection is a generalized term derived from the degree of condensation κ = $N(T)/N(L)$ that characterizes the atomic ratio between tetrahedral centers (T) and ligands (L). It quantifies, whether the coordination polyhedra are isolated form each other, or share common vertices, edges and/or faces. This gives an insight how densely packed a structure is.

In ternary or multinary nitridophosphates where metal cations outweigh phosphorus, a dominating cationic matrix may emerge, with PN_4 tetrahedra either non-condensed or interconnected to a limited extent. In return, structures rich in phosphorus and nitrogen often feature a dense anionic network built up by vertex-sharing PN_4 tetrahedra, with metal cations spread out in the structure. The resulting coordination polyhedra around metal cations are often only partially interconnected or isolated from each other. The subsequent examples and corresponding Figure 1.2 provide an overview of ternary structures, highlighting structural patterns and resulting trends.

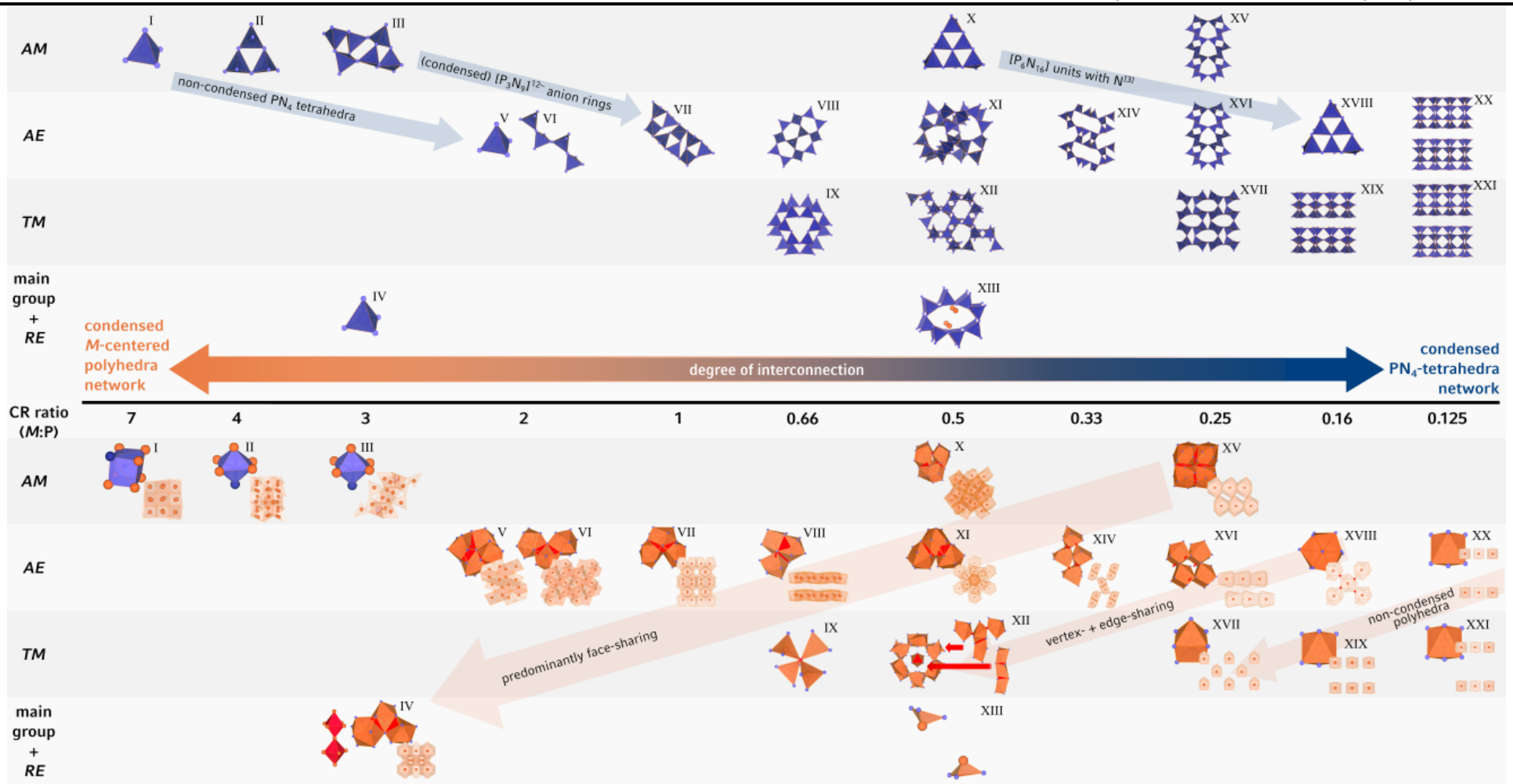

Figure 1.2. Overview of (oxo)nitridophosphate structures sorted by CR (7 to 0.125) and by metal cation (*AM* = alkali metal, *AE* = alkaline earth metal, *TM* = transition metal, *RE* = rare earth metal); structures are numbered by roman numerals with the respective sum formula given in the text; *M*-centered polyhedra (orange), PN_4 network (blue); *M* (orange), P (dark blue), N/O (bright blue), OHo_6 octahedra (red), $N(Li,P)_{6/8}$ polyhedra (bright blue); red highlights mark common faces, edges, and vertices of *M*-centered polyhedra for better visibilty; for reasons of clarity, no distinction was made between O and N

If the cation ratio CR is high, structures can be described by the dominating cationic metal substructure. Many lithium nitridophosphates exhibit a framework of Li^+ ions housing non-condensed PN_4 tetrahedra or small units of vertex-sharing tetrahedra, such as $[P_3N_9]^{12-}$ rings and cyclic $[P_6N_{16}]^{18-}$ anions. The cations could even be described as ligands for the nitride anions. For instance, the structure of Li_7PN_4 showcases N(Li_7P)-cubes (I)[36], while $Li_{12}P_3N_9$ (II)[37] and $Li_{18}P_6N_{16}$ (III)[38] contain N(LiP)$_6$ octahedra, among other polyhedra. Roman numerals mark the respective structure in Figure 1.2.

The structure of the nitridophosphate oxide $Ho_3(PN_4)O$ (CR = 3, IV)[39] can also be characterized by cation ligands and exhibits OHo_6 octahedra. Considering Ho-centered polyhedra, they form a dense structure by sharing common faces. $Ho_3(PN_4)O$ and the oxonitridophosphates M_2PO_3N (*M* = Ca, Sr, V, CR = 2)[40] contain non-condensed PN_4 tetrahedra.

As the proportion of the tetrahedra substructure in the overall structure increases, the PN_4 tetrahedra start to share vertices and the metal substructure becomes more spread out. *M* atoms are further away from each other and resulting coordination polyhedra start to share edges next to common faces. Ca_2PN_3 (VI, CR = 2)[41] contains single chains of vertex-sharing tetrahedra, located in a dense network of face-sharing *M*-centered polyhedra. $Sr_3P_3N_7$ (CR = 1, VII)[42] and $M_2P_3N_7$ (*M* = La-Nd, Sm-Eu, Ho, Yb, CR = 0.66, VIII),[43] exhibit *M*-centered polyhedra connected by common faces and edges. In $Sr_3P_3N_7$, vertex-sharing PN_4 tetrahedra form infinite *dreier* (as defined by Liebau[11]) double chains, and the layered structure of $M_2P_3N_7$ alternates layers of *M* ions with layers of vertex-sharing tetrahedra. In $Zn_8P_{12}N_{24}O_2$ (CR = 0.66, IX)[44], small units of $[Zn_4N_{13}]$ are located in the cage-like network of the sodalite structure.

The increasing degree of condensation of the PN_4 network leads to anionic tetrahedra networks that can be well described by rings of vertex-sharing tetrahedra. Structures with a CR of 0.5 demonstrate a wide variety of differently sized rings. BaP_2N_4 and $BaSr_2P_6N_{12}$ (XI)[45] have the same compact network with *dreier* and *siebener* rings. Here, the metal ions form a dense network with *M*-centered polyhedra sharing common faces and vertices. MP_2N_4 (*M* = Sr, Mn, Cd, XII)[46-47] and GeP_2N_4 (XIII)[48] exhibit *sechser* rings and *achter* rings, respectively, condensed to large channels that are occupied by the *M* ions. In MP_2N_4 (XII), the metal substructure becomes less interconnected and coordination polyhedra share vertices, edges and faces. The structure of SrP_3N_5NH (CR of 0.33, XIV)[49] features large *zehner* rings condensed into channels providing

space for the *M* ions. The *M*-centered polyhedra share common vertices and edges within the channels.

Structures of the $M_3P_6N_{11}$ (*M* = Na, K, Rb, Cs, CR = 0.5, X)[50-52] phases do not yet form networks with tetrahedra rings condensed into large channels, but triangular $[P_6N_{16}]$ units connected by vertices. The metal substructure is dense and coordination polyhedra around the large alkali metal cations are still highly interconnected by sharing faces. Only from a CR of 0.25 onwards, structures with alkali metals begin to exhibit a PN_4 network channel structure. MP_4N_7 (*M* = K, Rb, Cs, XV)[53] and $MSiP_3N_7$ (*M* = Sr, Ba, XVI)[25] are built up by the same network of *sechser* rings that are condensed to channels, and are occupied by the *M* ions. In the case of the larger alkaline metal ions, coordination polyhedra are still connected by common faces, whereas coordination polyhedra around alkaline earth metal cations form layers and share common edges. With the same CR, the structures of the two polymorphs of TiP_4N_8 (CR = 0.25, XVII)[54] contain non-condensed TiN_6 octahedra.

$BaP_6N_{10}NH$ (CR = 0.16, XVIII)[55] shows a high degree of condensation of the PN_4 network with the same triangular $[P_6N_{16}]$ units found in $M_3P_6N_{11}$ (X). This is the first case in which alkaline earth metal ions are so thinly populated in a structure that *M*-centered coordination polyhedra solely share common vertices. It becomes clear that with a decreasing CR the metal substructure becomes less dense. AlP_6N_{11} (CR = 0.16, XIX)[32] forms layers, in which the highly-condensed network not only contains PN_4 tetrahedra, but also edge-sharing trigonal PN_5 bipyramids. Discrete AlN_6 octahedra are located in between the layers. $SrP_6N_{10}(NH)_2$ (CR = 0.16)[14] and the MP_8N_{14} (*M* = Ca, Sr, Ba, Fe, Co, Ni, CR = 0.125, XX + XXI)[56-57] phases exhibit a similar layered structure to AlP_6N_{11} containing only PN_4 tetrahedra. MP_8N_{14} structures form currently the endpoint of this list with the largest proportion of the PN_4 substructure to the overall structure and the lowest CR of 0.125.

Two trends can be summarized. The first one addresses the impact of the metal ion (*M*) to phosphorus (P) ratio (CR = N(*M*)/N(P)) on the resulting structure. At a high CR, compounds are rich in metal cations, and structures exhibit a dense *M* substructure that can be characterized by the coordination polyhedra of the metal cations extensively sharing faces. At a low CR, compounds are rich in phosphorus and nitrogen, and structures are dominated by highly condensed PN_4 tetrahedra networks. Figure 1.2 shows, that as the *M* content declines, the level of *M* substructure

condensation decreases. Conversely, the condensation of the PN_4 network increases with a rising P and N content. The second trend deals with the impact of the nature of the metal ion on the structural transition. Structures containing main group 1 and 2 elements exhibit a higher degree of interconnection among coordination polyhedra around metal cations. This results in denser metal cation substructures at the same CR ratio compared to structures with smaller transition metal ions (diagonal arrow Figure 1.2). For example, at a CR of 0.25, MP_4N_7 structures (*M* = K, Rb, Cs, XV) feature *M*-centered polyhedra sharing common faces, while TiP_4N_8 (XVII) already comprises non-condensed TiN_7-polyhedra.

1.2.3. Multicationic Nitridophosphates

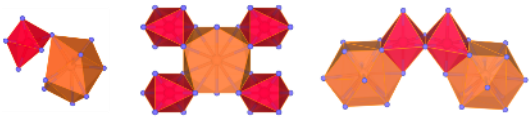

So far, only ternary (oxo/imido)nitridophosphates have been considered. Multicationic nitridophosphates are a group of nitridophosphates with a network hosting at least two different metal cations. The cations typically have different charges and ionic radii resulting in an occupation of different sites and no occupational disorder. Consequently, multicationic phases can form structures unattainable by ternary nitridophosphates and the ample structural diversity of nitridophosphates can be further expanded. Continuing with the nomenclature of the cation ratio CR = N(*M*)/N(P), now the additional metal as well as the alkaline earth ions contribute as counter cations to N(*M*).

A group of compounds, that has been the subject of ongoing research since the 1990s, are the oxonitridophosphates $Na_3MP_3O_9N$ (*M* = Al, V, Ti),[50, 58-61] Non-condensed propeller-like $[P_3N_{10}]$ units share common corners with AlO_6 octahedra in a dense matrix of Na^+ ions. Large different-sized ring-types form channels in $LiNdP_4N_8$ and $Ce_4Li_3P_{18}N_{34}O$ (CR = 0.5 and 0.39) and layers in $LiPr_2P_4N_7O_3$ (CR = 0.75). *M* ions are located in the channels or in between the layers, respectively.[62-64]

The few known representatives of multicationic alkaline earth nitridophosphates, namely $MSi_3P_4N_{10}(NH)_2$ (*M* = Mg, Ca, Sr), α-/β-$MgSrP_3N_5O_2$ and $CaMg_2P_6N_{10}O_3$ exhibit different interconnections of the *M*-centered polyhedra (Figure 1.3).[19-21, 65]

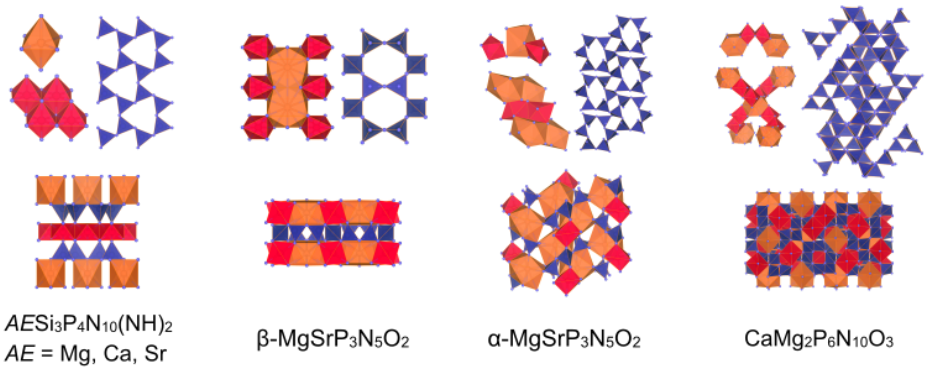

CR	1	0.66	0.66	0.5
M:*AE*	0.33:1	1:1	1:1	2:1

Figure 1.3. Structures of known multinary alkaline earth nitridophosphates. Alkaline earth-centered polyhedra (orange), $(Si/Mg)(O,N)_6$ octahedra (red) and PN_4 tetrahedra (blue), for reasons of clarity, no distinction was made between O and N; *M*:*AE* ratio gives the ratio of the metal cation (Si, Mg) next to the alkaline earth ions (Mg, Ca, Sr).

In this thesis, several new structures ranging from phosphorus nitrides to nitridophosphates are presented. A new phosphorus tantalum nitride with PN_6 octahedra (CR = 8) and a chromium silicon nitridophosphate (CR = 1) are thoroughly characterized. Furthermore, aluminium is introduced as an additional cation into multicationic alkaline earth nitridophosphate systems. Two new aluminium alkaline earth nitridophosphate structures are thoroughly characterized and their luminescence properties are investigated.

1.3. High-Pressure High-Temperature Syntheses of Nitrides and Nitridophosphates

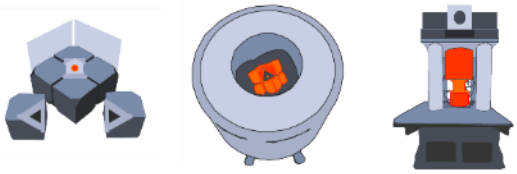

Exploratory synthesis is the foundation in solid-state chemistry and materials synthesis can be challenging in unfamiliar areas. Synthesis limitations such as differing reactivities of precursors, the exclusion of unwanted reactants and equipment parameters that restrict reaction conditions, including pressure and temperature ranges complicate the discovery of new functional materials. This is the case within nitrides and nitridophosphates. The formation of nitridic compounds is usually unfavored in the presence of oxygen due to the preferred formation of oxides. Oxygen is a diradical with a nominal double bond (498 kJ/mol) that can easily be activated by moderate heat.[66] With its high electron affinity (–1.46 eV), elemental oxygen can rapidly get reduced to –II, acting as a strong oxidizer.[67] Nitrogen features a triple bond (941 kJ/mol) that is almost twice as stable as the oxygen double bond.[66] With a positive electron affinity (+0.07 eV) it does not form stable isolated anions.[68] The exclusion of oxygen is therefore a key criterion for a successful synthesis of pure nitrides. Further synthetic challenges for nitridophosphates are created by the decomposition of P_3N_5 at temperatures above 850 °C, the chemical inertness of easily available starting materials such as refractory nitrides, and the high thermal energy needed for the cleavage and reformation of chemical bonds in numerous solid-state compounds. Applying external pressure serves as a solution to employ starting materials with different reactivities and further prevents the decomposition of P_3N_5. In addition, the use of stable azides of alkali and alkaline earth elements provides readily activatable precursors and promotes the formation of N_2. Employing transition metal nitrides for the synthesis of ternary transition metal nitrides or nitridophosphates was proved to be challenging as many demonstrate a refractory and unreactive character. A higher oxidation state of transition metal makes it increasingly difficult to avoid the reduction of the phosphorus cation under the formation of the favored stable metal phosphides. Applying high external pressures and temperatures realized by a multianvil press is an established way to address these challenges and allow a straightforward synthesis of nitridic compounds.[62, 69] Further, high partial pressures of HCl or employing small amounts of NH_4F facilitates crystal growth.[15, 25] Using mineralizing agents like NH_4F can help to overcome differing reactivities of starting materials by reversibly cleave the bonds in refractory nitrides.[25, 70] Within this thesis, NH_4F-mediated high-pressure high-temperature conditions are used to facilitate chemical reactions.

A large volume press used supplies a maximum pressure of about 25 GPa, and a maximum temperature of about 1600 °C.[71] A modified Walker-type module enabling a Kawai-type compression setup, as illustrated in Figure 1.4, was used.[72-75] The Kawai-type multianvil technique uses an octahedron-within-cubes payload for the generation of a quasi-hydrostatic pressure.[72] The uniaxial pressure of a hydralic press is distributed to six steel anvils, creating a cubic compression space.[73] Tungsten carbide cubes with truncated edges compress an octahedron, which contains the sample and an electronic resistance heating system. Latter uses graphite furnaces and provides an inert and heatable reaction chamber. The octahedron is commonly made out of Cr_2O_3-doped MgO. Further information on the assembly can be found in literature.[69] Starting materials can be handled by preparing the assembly inside a glovebox under inert-gas atmosphere. The assemblies are characterized by the octahedron edge length (OEL) and the truncated edge length (TEL). Typically used assemblies are 25/17, 18/11, 14/8, 10/5, and 8/3 (OEL/TEL in millimeter). The pressure range depends on the octahedron size and smaller octahedra allow higher pressures to be generated.

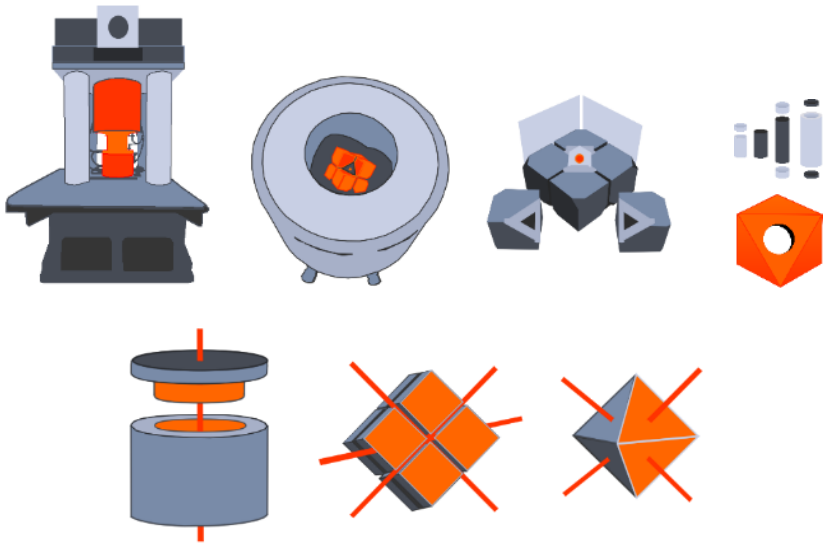

Figure 1.4. Illustration of the 1000 t large volume press (top left) used for high-pressure high-temperature syntheses. Modified Walker module (middle left) with the Kawai-type octahedron-within-cubes assembly (middle right) that enables a quasi-hydrostatic pressure by an equal pressure distribution along several spatial axes (bottom). Assembly (top right) consists of an h-BN cubicle with lid, two graphite furnaces with MgO spacers inside a ZrO_2 sleeve contacted by two Mo plates, placed inside a 5% Cr_2O_3 doped MgO octahedra; inspired by a similar representation.[76]

1.4. Analytical Methods

The prediction of solid-state structures is still a complex and challenging matter. After a successful synthesis of nitrides and nitridophosphates, a thorough structure elucidation has to be carried out, and a combination of different analytical methods enables a full characterization. X-ray diffraction is the gold standard when it comes to structure analysis in solid-state chemistry, but where powder and single-crystal X-ray diffraction may come up short, electron microscopy can often provide suitable help by providing data on a different length scale.

1.4.1. Single-Crystal X-Ray Diffraction

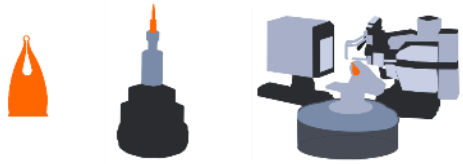

Single-crystal X-ray (SCXRD) diffraction is the most common, and powerful technique for the elucidation of crystal structures providing a fast and high -quality collection of single-crystal data. The technique can be briefly summarized as the scattering of a collimated, monochromatic beam of X-rays by a single crystal, and the detection of the diffracted beams. Figure 1.5 shows a schematic illustration of the widelyf used four-circle diffractometers with a rotating anode as X-ray source and an area detector. Processing information about the position and intensity of the diffracted X-ray beams yields information about the atomic arrangement within the crystalline material. The resulting knowledge includes the positions of the atoms, and the corresponding bond distances and angles.

The beam interacts with electrons resulting in an easy detection of heavy elements with a high electron density. The atomic form factors *f* of elements are the Fourier transforms of the spatial electron density distribution of atoms. Heavy atoms, e.g. of the 5th to 7th row pose a challenge in accurately determining the positions of relatively light elements like nitrogen, as well as in distinguishing between elements with very similar *f*, such as nitrogen/oxygen or aluminum/phosphorus. X-rays are not very sensitive to light atoms and the determination of the crystallographic positions of hydrogen, is only possible with relatively large errors, if at all. The atomic form factor *f* decays with increasing diffraction angle θ, but *f* of heavy atoms decreases faster at high angles than *f* of light atoms, which makes high-angle data essential for the accurate determination of light atoms. If one or more of these conditions are encountered, other analytical methods should be consulted for a reliable structure analysis.

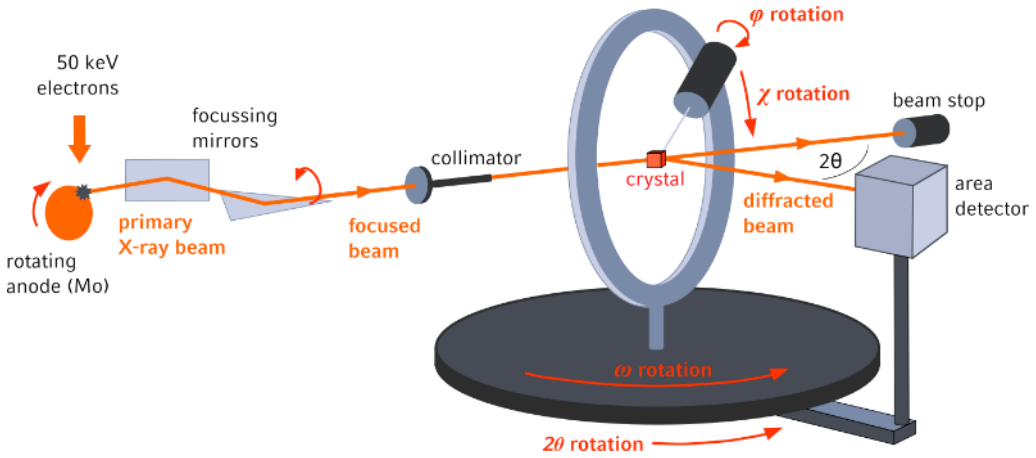

Figure 1.5. Schematic illustration of the beam and measurement geometry of a four-circle diffractometer with rotating anode and area detector to obtain single-crystal X-ray diffraction data.

1.4.2. Synchrotron X-Ray Diffraction

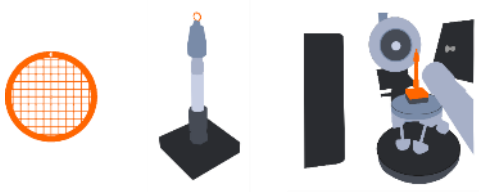

For crystalline samples with crystals too small for conventional SCXRD, it is possible to record single-crystal data using synchrotron radiation. The high brilliance of the beam allows high-quality data to be recorded, especially at high angles, which in turn enables precise structural analysis where this is not technically possible with laboratory X-ray radiation. Therefore, charge carriers are accelerated in a linear accelerator and fed into a storage ring via an upstream booster ring. Synchrotron radiation is generated by the deflection of these charge carriers through magnetic fields. The emittance is a broad spectrum of wavelengths (from the infrared to the γ-range; 10^{-5}–10^{-15} m) and hard X-rays can be focused and utilized for structural analysis.[77] The intensity, stability, reliability and efficiency of the synchrotron beam can be further enhanced by upgrades.[78-80] Pre-focusing the beam in the first optic hutch allows a high flux, which decreases scanning times and offers high spatial resolution (Figure 1.6). Focusing of the beam in vertical and horizontal direction to give a point-like spot can be achieved by in-line optics of refractive lenses and slits. A detector upgrade provides high sensitivity and high quantum efficiency. This setup has been installed at beamline ID11 at the ESRF. It enables for high energy (30–70 keV) X-ray diffraction experiments with nano-focus (150–500 nm) beam sizes. A sophisticated setup including a hexapod mounted on a piezo stage on top of a single rotation axis and a high-precision y-translation stage enables a high mechanical accuracy and spatial stability.

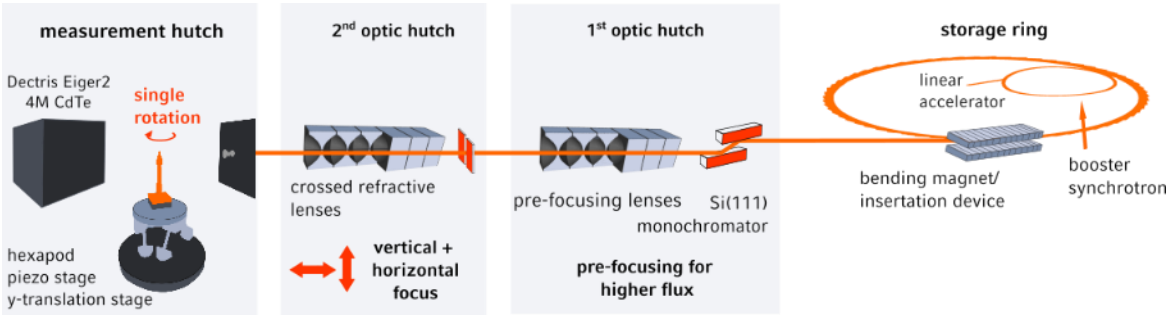

Figure 1.6. Strongly simplified illustration of the measuring setup and beamline geometry at the beamline ID11 at the ESRF (Grenoble, France).

Individual crystals can be identified and pre-characterized by transmission electron microscopy. TEM grids with an X-ray transparent carbon film serve as an ideal medium and bright field images and selected area electron diffraction patterns are used to identify suitable crystals and record their positions (Figure 1.7). With a high magnification telescope and a fluorescence detector, crystals smaller than 1 μm^3 can be precisely centered and total diffraction scans can be obtained. This is particularly beneficial because large volume presses often generate conditions that can lead to microcrystalline or heterogeneous samples. The pre-characterization of samples also gives ideal utilization of limited measuring time and can be considered an established method.[55-56, 65, 81-82]

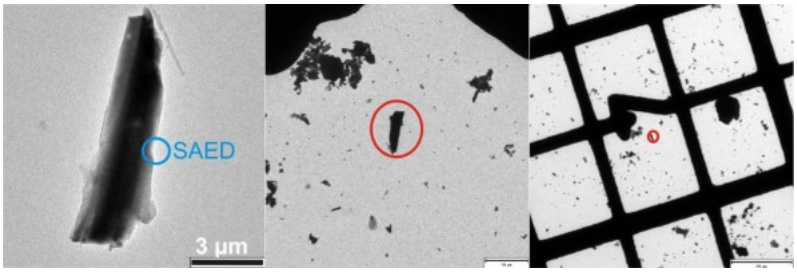

Figure 1.7. Position of the crystallite of $BaP_6N_{10}NH$ used for single-crystal X-ray data collection with microfocused synchrotron bream.[55]

1.4.3. Transmission Electron Microscopy

1.4.3.1. General Aspects of Transmission Electron Microscopy

The short wavelength of electrons compared to X-ray (λ(e, 300 kV) ≈ 0.02 Å; λ(Mo-Kα) = 0.71073 Å) allows for a large section of the reciprocal space to be imaged simultaneously and almost undistorted. Therefore, in transmission electron microscopy (TEM), unique structural features, e.g. dopant atoms or stacking disorder can be observed on a local scale in the specimen.[83-84] TEM combines imaging methods, diffraction techniques and spectroscopy at atomic resolution.[85-86] The range of methods focusing on different signals allows to gather a spectrum of different crystallographic data. Conventional TEM (CTEM) and scanning TEM (STEM) include bright-field (BF) and dark-field (DF) imaging,[87] high resolution microscopy (HR-TEM),[88] and various different electron diffraction (ED) techniques.[89-92] Different detectors can record images with *Z*-contrast (high-angle annular dark field, HAADF detector, in STEM)[93] or a complete reconstruction of the 3D internal and external structure of a specimen from a tilt-series of 2D projection images.[94-97] This can be combined with energy dispersive X-ray (EDX) or electron energy loss spectroscopy (EELS). The main setup of a TEM consists of an electron source, an illumination system including the condenser lens system, the specimen with the objective lens system, an imaging system that combines diffraction, intermediate and projector lenses and the detectors.[98] In the case of an aberration-corrected STEM, the illuminating system includes a probe corrector.[99-101]

In this thesis, electron microscopes were operated in CTEM mode to acquire BF images and selected area electron diffraction (SAED) patterns, and in STEM mode to record *Z*-contrast images in combination with EDX mapping. Other methods are not elaborated upon in this context. Ground samples were applied with an ethanol suspension on TEM grids with a lacey carbon film. The grids were mounted in a double-tilt holder (tilt ranges ±30°). Analysis was carried out with a FEI Tecnai G20 transmission electron microscope operated at an acceleration voltage of 200 kV and equipped with a thermal emitter, as well as a Titan Themis 300 transmission electron microscope (300 kV) equipped with a Schottky type high-brightness electron gun, and a spherical aberration corrector. The STEM setup was operated with an inner semi convergence angle of 33 mrad for a camera length of 245 mm.

1.4.3.2. Conventional Transmission Electron Microscopy

In CTEM mode, the sample is illuminated with a plane wave and a magnified image, generated by lenses located in the imaging system, is recorded (Figure 1.8). TEM samples require electron transparency, as well as vacuum and beam stability. Lens imperfections such as spherical and chromatic aberration are unavoidable properties of rotationally symmetric magnetic fields. These lens aberrations, astigmatism, and the partial coherence of the system lower the attainable point resolution significantly. A conventional TEM operating at 200 kV yields a typical point resolution of about 1.96 Å.

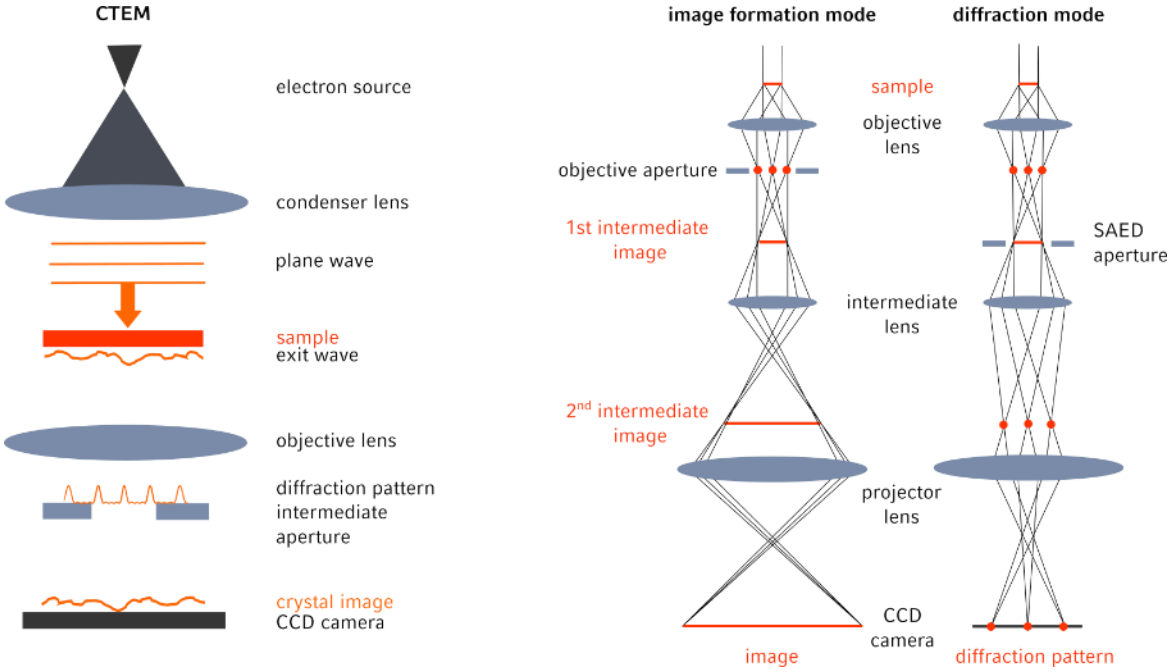

Figure 1.8. Left: Illustration of illuminating system and data acquisition in CTEM mode. Right: Lenses allow the change between imaging and diffraction mode and either the objective aperture (image) or the SAED (diffraction) aperture is selected for image acquiring.

Bright-field images can be used to obtain an overview of crystal sizes and topology. Prominent contrasts in BF images are the amplitude and phase contrast. They visualize the amount of scattering and the contrast depends on the atomic number *Z*, the sample thickness and density, as well as the aperture size, which influences the exclusion of high-angle scattered beams. Electron diffraction allows for atomic structure determination quite similar to X-ray diffraction. Structure solution by ED has grown rapidly over the past decade, mostly due to the introduction of 3D methods and systematization of the acquisition and analysis of diffraction data.[83, 102] Further, ED

can help to identify different phases, stacking sequences, crystal domains, and superstructure reflexes (Figure 1.9).[103-106]

In this thesis, BF imaging is used to gather an overview of crystal quality in the respective samples and to select crystals for further analysis steps. ED is used to confirm the unit cell metric obtained by X-ray data. For this purpose, tilt series with SAED patterns of different zone axes of a crystalline sample are recorded and compared with simulations of the respective space group.

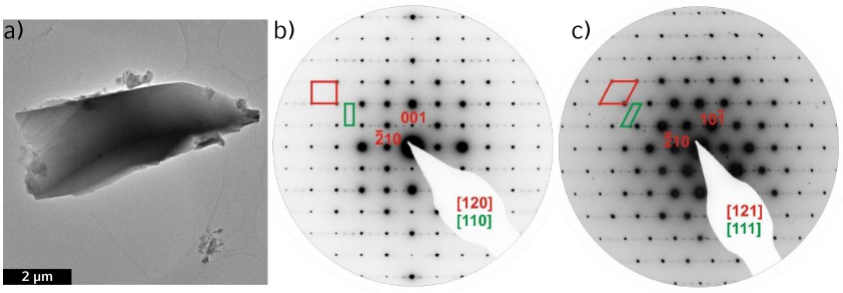

Figure 1.9. a) Bright-field image of patterns of $Ce_{4-0.5x}Li_3P_{18}N_{35-1.5x}O_{1.5x}$ ($x \approx 0.72$) and SAED patterns along [120]; **(b)** and [121] **(c)** zone axis containing superstructure reflections; The average structure model is highlighted in red and the supercell model in green.[64]

1.4.3.3. Scanning Transmission Electron Microscopy

Scanning transmission electron microscopy techniques are nowadays routinely used to image materials and modern aberration-corrected STEMs can achieve a sub-50 pm resolution.[107-108] With a highly coherent electron source that accelerates electrons to energies ranging from 100 to 300 kV, samples with a thickness of up to 100 nm can be penetrated without significant beam dispersion. Optimal samples should to be thin enough that the electron probe will not spread significantly in the crystal, but thick enough that bulk-like, and not surface, atoms dominate the signal. A series of electron lenses and corrective optics upstream of the sample focuses the electron beam to an energy spread of 0.3–1 eV, which can be narrowed to below 100 meV by a monochromator. Corrective optics focus the beam to a spot size of between 0.05 to around 0.3 nm and scan coils control the scanning movement of the electron probe across the sample.[109] An annular dark-field (ADF) detector below the sample collects elastically scattered electrons that undergo large angle deflections (Figure 1.10).

Signals registered by an annular dark field detector can be regarded largely incoherent and multiple scattering is neglected. If the incoherent imaging approximation applies, a nearly direct image interpretation is possible.[110-112] To a first approximation, when the beam is placed on an atom column, strong Rutherford-like scattering deflects the transmitted electrons to form bright features in an ADF image, with less scattering between the columns. The scattering is determined by the scattering at the atomic nucleus with an atomic number *Z* reduced by the X-ray scattering amplitude f^X. A straightforward interpretation of the intensity in STEM-HAADF images is possible under conditions where f^X becomes negligible. This applies for high spatial frequencies that describe electron density in orbitals close to the nucleus. Therefore, the high-angle electron-scattering cross-section scales roughly as the atomic number $Z^{1.7}$, tenting towards the Rutherford scattering limit of Z^2 and the imaging mode is therefore oftentimes referred to as *Z*-contrast imaging with a strong compositional sensitvity.[110, 113-116]

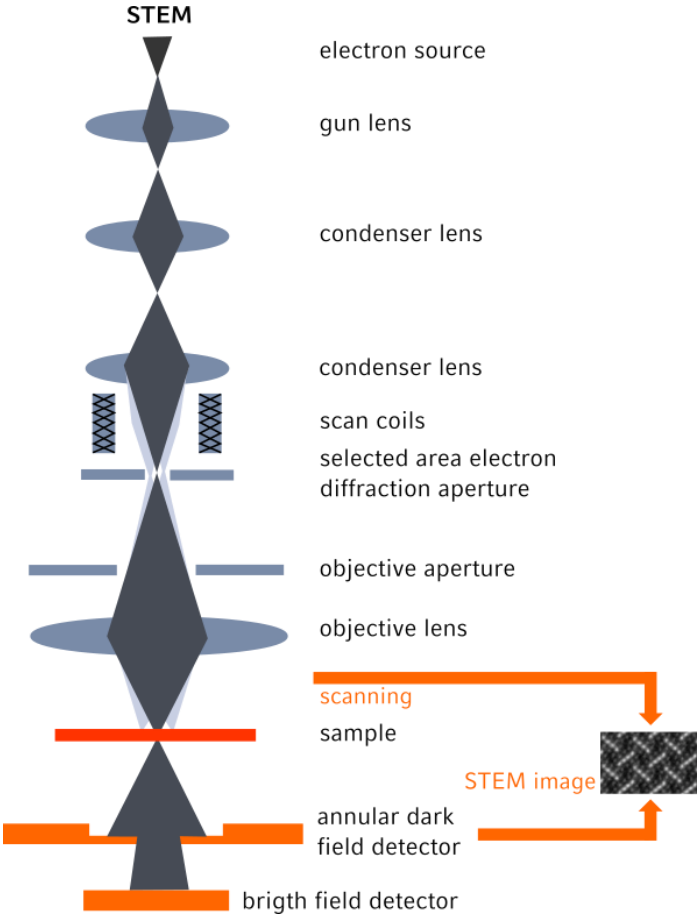

Figure 1.10. Schematic illustration of illuminating system and data aquisition in STEM mode. Scan coils control the position of the scanning probe. The final STEM image is generated by combining the scanning probe position with the recorded signal on the HAADF detector.

A low-angle ADF signal allows for strain mapping and the identification of light dopant atoms and vacancies.[117-119] At higher angles, the Z-contrast from nuclear scattering dominates the signal, with bright features that result from high-*Z* atoms, or higher densities of atoms.[109, 118, 120] Ordered and disordered structure models, as well as individual dopant atoms and slight displacements of high-*Z* atoms, can be distinguished and identified.[54, 64, 84, 121]

The setup also enables that inelastic scattering is collected simultaneously with the elastic ADF signal and the energy losses of the electrons reflect characteristic excitations. The method is based on excitation of core electrons of the atoms by accelerated electrons. Electrons of higher energy in upper shells close this gap and release the energy difference as X-ray radiation, characteristic for the specific element (Figure 1.11). This enables element-specific and electronic identification from single atom columns. Compounds with both phosphor and silicon generate a complication because an assignment of element types to crystallographic positions based on X-ray is not always easily possible due to their similar X-ray scattering form factors. Combined with heavy atoms, this results in X-ray scattering and ADF signals that only show a small relative difference in the respecting intensity. STEM-EDX mapping with atomic resolution provides a spatial resolution that makes it possible to determine whether order or occupational disorder of P and Si is present. The overlay of STEM-EDX maps with an HAADF image of the mica-analog phases MSi$_3$P$_4$N$_{10}$(NH)$_2$ (*M* = Mg, Ca, Sr) shows the ordering of Si and P and led to the conclusion that the compounds consist of PN$_4$ tetrahedra and SiN$_4$(NH)$_2$ octahedra.[65] For the case of the nitridosilicatephosphate BaSiP$_3$N$_7$, STEM-EDX mapping validated the structure model with a partial order of Si and P (Figure 1.11).[25]

In this thesis, STEM-HAADF images and atomic resolution EDX-mapping are employed to address various structural ambiguities. Consequently, disorder in Ta/P- and Cr/Si-containing phases, as well as order in Si/P- and Al/P-containing phases, could be identified.

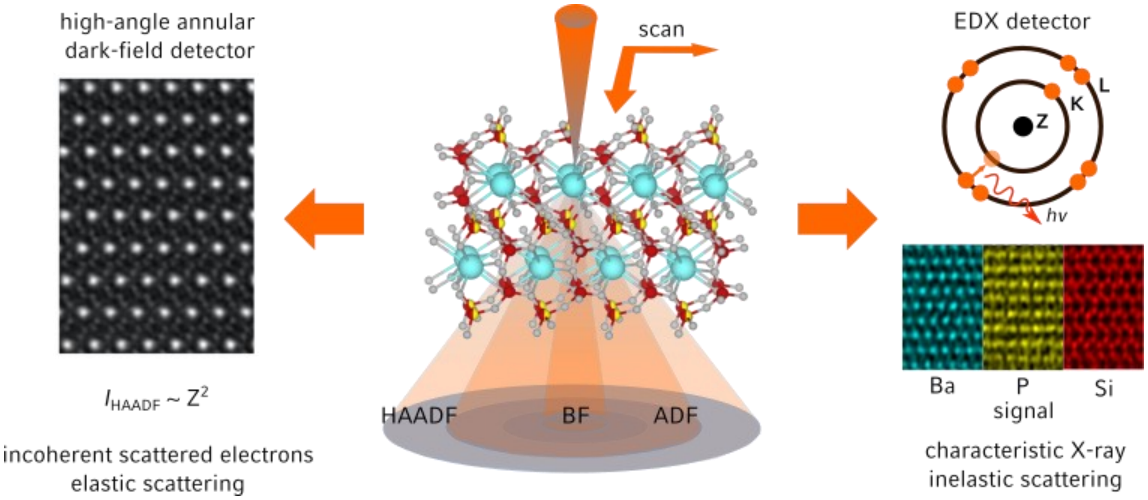

Figure 1.11. STEM analysis of $BaSiP_3N_7$ with simultaneous recording of scattering and spectroscopy data along the zone axis [001]. Left: STEM-HAADF signal of incoherent scattered electrons with intensity contrast proportional to Z^2. Middle: Visualization of the STEM probe scanning over the crystal sample and signal being recorded depending on the scattering angle; bright-field (BF), annular dark-field (ADF) and high-angle annular dark-field (HAADF). Right: Characteristic X-ray radiation getting detected on an EDX detector for every scan point resulting in an element specific 2D atomic resolution EDX maps.[25]

1.5. Combining X-Ray Diffraction and Electron Microscopy Analysis

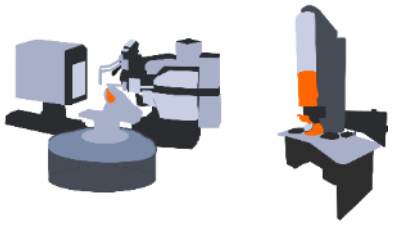

The different energy and charge of electrons and X-rays provides a different interaction with the sample. For X-rays, the structure factor results from the Fourier transform of the spatial electron density distribution and therefore represents an electron density map, whereas for electrons, the structure factor is the Fourier transform of the electrostatic potential, as accelerated electrons interact with both the nucleus and the electron shell of the atoms. The short wavelength of electrons enables imaging of a section of the reciprocal space almost undistorted and structures can be observed on a very local scale in the specimen.

The acquisition of single-crystal X-ray datasets is an established and sophisticated method, which allows to easily generate high-quality data. Where this method falls short, electron microscopy is oftentimes suited to bridge remaining ambiguities. With electron diffraction and EDX spectroscopy, electron microscopy can target and identify single crystals in heterogeneous mixtures and build a key step for synthesis optimization. When the acquisition of single-crystal X-ray data faces the challenge of limited crystal size, electron microscopy is a reasonable first step toward X-ray diffraction data, if a pre-characterization of microcrystalline sample for nano-focused synchrotron radiation measurements is needed. Vague X-ray data can be clarified by STEM-HAADF images in combination with atomic resolution chemical mapping. This method can offer information on a different length scale and is one of the most directly interpretable visualization methods.

1.6. Scope of this Thesis

The aim of this thesis is to utilize the joint application of X-ray diffraction and STEM-HAADF analysis toward a routine approach in the structure analysis of nitridic solid-state compounds.

NH_4F-mediated high-pressure high-temperature synthesis is utilized to overcome the challenges posed by phosphorus nitride chemistry. The synthetic approach focused on elemental combinations where the analytical approach of X-ray and electron diffraction can be particularly useful, as elements with similar atomic X-ray form factors cannot be easily distinguished by X-ray radiation. The combinations Al/P, P/Si, and O/N were selected and obtained compounds were comprehensively characterized. X-ray diffraction methods include the evaluation of laboratory data, as well as the recording and evaluation of synchrotron data from the ESRF and DESY research facilities. STEM-HAADF imaging with atomic resolution elemental mapping was employed to confirm and finalize data obtained by single-crystal X-ray diffraction. Properties like luminescence upon doping with Eu^{2+}, semiconducting behavior with an industrially applicable band gap and metallic behavior, as well as potential applications are analyzed and discussed.

The structures within this thesis were classified into the group of known nitridophosphates and phosphorus nitrides. Two new compounds expand the group of transition metal nitridophosphates and phosphorus nitrides and four aluminum nitridophosphate-based structures extend the group of multinary alkaline earth nitridophosphates. Thereby, the compounds show a diverse cation ratio from 0.375:1 up to 8:1 and span a wide structural range with implementing known silicate structure types as well as exhibiting novel structure motifs.

1.7. References

[1] R. Juza, H. Hahn, *Z. Anorg. Allg. Chem,* **1938,** *239*, 282–287.

[2] H. Schulz, K. H. Thiemann, *Solid State Commun.* **1977,** *23*, 815–819.

[3] H. P. Maruska, J. Tietjen, *Appl. Phys. Lett.* **1969,** *15*, 327–329.

[4] H. Amano, M. Kito, K. Hiramatsu, I. Akasaki, *Jpn. J. Appl. Phys.* **1989,** *28*, L2112.

[5] S. Nakamura, N. Iwasa, M. S. M. Senoh, T. M. T. Mukai, *Jpn. J. Appl. Phys.* **1992,** *31*, 1258–1266.

[6] S. Nakamura, T. Mukai, M. Senoh, *Appl. Phys. Lett.* **1994,** *64*, 1687–1689.

[7] M. Cardona, *J. Phys. Chem. Solids* **1963,** *24*, 1543–1555.

[8] M. L. Cohen, J. R. Chelikowsky, M. L. Cohen, J. R. Chelikowsky, *Wurtzite structure semiconductors*, **1989**, pp. 140–160.

[9] A. De, C. E. Pryor, *Phys. Rev. B* **2010,** *81*, 155210.

[10] Y.-N. Xu, W. Ching, *Phys. ReV. B* **1993,** *48*, 4335–4351.

[11] F. Liebau, *Structural chemistry of silicates: structure, bonding, and classification*, Springer-Verlag, Berlin Heidelberg, **2012**, pp. 59–62. The terms *"dreier"/"sechser"/"siebener"* and *"achter*" rings have been defined by Liebau and are derived from the German words "drei" (engl. three), "sechs" (engl. six), "sieben" (engl. seven) and "acht" (engl. eight), describing rings consisting of the respective amount of tetrahedra.

[12] A. Marchuk, F. J. Pucher, F. W. Karau, W. Schnick, *Angew. Chem. Int. Ed.* **2014,** *53,* 2469–2472.

[13] L. Neudert, F. Heinke, T. Bräuniger, F. J. Pucher, G. B. Vaughan, O. Oeckler, W. Schnick, *Chem. Commun.* **2017,** *53*, 2709–2712.

[14] S. Wendl, W. Schnick, *Chem. Eur. J.* **2018,** *24*, 15889–15896.

[15] S. Vogel, A. T. Buda, W. Schnick, *Angew. Chem. Int. Ed.* **2019**, *131*, 3436–3439.

[16] S. Horstmann, E. Irran, W. Schnick, *Angew. Chem. Int. Ed.* **1997,** *36*, 1992–1994.

[17] D. Baumann, W. Schnick, *Inorg. Chem.* **2014,** *53*, 7977–7982.

[18] S. J. Sedlmaier, M. Döblinger, O. Oeckler, J. Weber, J. Schmedt auf der Günne, W. Schnick, *J. Am. Chem. Soc.* **2011,** *133*, 12069–12078.

[19] F. J. Pucher, W. Schnick, *Z. Anorg. Allg. Chem.* **2014,** *640*, 2708–2713.

[20] A. Marchuk, L. Neudert, O. Oeckler, W. Schnick, *Eur. J. Inorg. Chem.* **2014,** *2014*, 3427–3434.

[21] R. M. Pritzl, N. Prinz, P. Strobel, P. J. Schmidt, D. Johrendt, W. Schnick, *Chem. Eur. J.* **2023**, e202301218.

[22] S. Wendl, M. Mallmann, P. Strobel, P. J. Schmidt, W. Schnick, *Eur. J. Inorg. Chem.* **2020,** *2020*, 841−846.

[23] R. D. Shannon, *Acta Crystallogr. Sect. A* **1976,** *32*, 751–767.

[24] H. P. Baldus, W. Schnick, J. Luecke, U. Wannagat, G. Bogedain, *Chem. Mater.* **1993,** *5*, 845–850.

[25] L. Eisenburger, O. Oeckler, W. Schnick, *Chem. Eur. J.* **2021,** *27*, 4461–4465.

[26] E. M. Bertschler, T. Bräuniger, C. Dietrich, J. Janek, W. Schnick, *Angew. Chem.* **2017,** *56*, 4884–4887.

[27] S. Vogel, A. T. Buda, W. Schnick, *Angew. Chem. Ind. Ed.* **2018**, *57*, 13202–13205.

[28] S. Vogel, M. Bykov, E. Bykova, S. Wendl, S. D. Kloß, A. Pakhomova, S. Chariton, E. Koemets, N. Dubrovinskaia, L. Dubrovinsky, *Angew. Chem. Int. Ed*. **2019**, *58*, 9060–9063.

[29] S. Horstmann, E. Irran, W. Schnick, *Angew. Chem. Int. Ed. Engl.* **1997**, *36*, 1873–1875.

[30] J. Ronis, B. Bondars, A. Vitola, T. Millers, J. Schneider, F. Frey, *J. Solid State Chem.* **1995,** *115*, 265–269.

[31] D. Laniel, F. Trybel, A. Néri, Y. Yin, A. Aslandukov, T. Fedotenko, S. Khandarkhaeva, F. Tasnádi, S. Chariton, C. Giacobbe, *Chem. Eur. J.* **2022,** *28*, e202201998.

[32] S. J. Ambach, M. Pointner, S. Falkai, C. Paulmann, O. Oeckler, W. Schnick, *Angew. Chem. Int. Ed.* **2023**, e202303580.

[33] D. Baumann, W. Schnick, *Angew. Chem. Int. Ed.* **2014**, *53*, 14490–14493.

[34] K. Landskron, H. Huppertz, J. Senker, W. Schnick, *Angew. Chem. Int. Ed.* **2001**, *40*, 2643–2645.

[35] S. Vogel, M. Bykov, E. Bykova, S. Wendl, S. D. Kloß, A. Pakhomova, N. Dubrovinskaia, L. Dubrovinsky, W. Schnick, *Angew. Chem.* **2020**, *59*, 2752–2756.

[36] W. Schnick, J. Luecke, *J. Solid State Chem.* **1990,** *87*, 101–106.

[37] E. M. Bertschler, R. Niklaus, W. Schnick, *Chem. Eur. J.* **2017,** *23*, 9592–9599.

[38] E. M. Bertschler, C. Dietrich, J. Janek, W. Schnick, *Chem. Eur. J.* **2017,** *23*, 2185–2191.

[39] S. D. Kloß, N. Weidmann, W. Schnick, *Eur. J. Inorg. Chem.* **2017,** *2017*, 1930–1937.

[40] A. Marchuk, P. Schultz, C. Hoch, O. Oeckler, W. Schnick, *Inorg. Chem.* **2016,** *55*, 974−982.

[41] V. Schultz-Coulon, W. Schnick, *Z. Anorg. Allg. Chem.* **1997,** *623*, 69–74.

[42] M. Mallmann, S. Wendl, P. Strobel, P. J. Schmidt, W. Schnick, *Chem. Eur. J.* **2020,** *26*, 6257–6263.

[43] S. D. Kloß, N. Weidmann, R. Niklaus, W. Schnick, *Inorg. Chem.* **2016,** *55*, 9400–9409.

[44] F. Karau, O. Oeckler, F. Schäfers, R. Niewa, W. Schnick, *Z. Anorg. Allg. Chem,* **2007,** *633*, 1333–1338.

[45] F. Karau, W. Schnick, *Z. Anorg. Allg. Chem.* **2006,** *632*, 231–237.

[46] F. W. Karau, L. Seyfarth, O. Oeckler, J. Senker, K. Landskron, W. Schnick, *Chem. Eur. J.* **2007,** *13*, 6841–6852.

[47] F. J. Pucher, F. W. Karau, J. Schmedt auf der Günne, W. Schnick, *Eur. J. Inorg. Chem.* **2016,** *2016*, 1497–1502.

[48] S. J. Ambach, C. Somers, T. de Boer, L. Eisenburger, A. Moewes, W. Schnick, *Angew. Chem. Int. Ed.* **2023**, e202215393.

[49] S. Vogel, W. Schnick, *Chem. Eur. J.* **2018,** *24*, 14275–14281.

[50] J. Ronis, B. Bondars, A. Vitola, T. Millers, *Latv. PSR Zinat. Akad. Vestis Kim. Ser.* **1990**, *90*, 299–301.

[51] H. Jacobs, R. Nymwegen, *Z. Anorg. Allg. Chem,* **1997,** *623*, 429–433.

[52] K. Landskron, W. Schnick, *J. Solid State Chem.* **2001,** *156*, 390–393.

[53] K. Landskron, E. Irran, W. Schnick, *Chem. Eur. J.* **1999,** *5*, 2548–2553.

[54] L. Eisenburger, V. Weippert, C. Paulmann, D. Johrendt, O. Oeckler, W. Schnick, *Angew. Chem. Int. Ed*. **2022**, *61*, e202202014.

[55] S. Wendl, L. Eisenburger, M. Zipkat, D. Günther, J. P. Wright, P. J. Schmidt, O. Oeckler, W. Schnick, *Chem. Eur. J.* **2020,** *26*, 5010–5016.

[56] S. Wendl, L. Eisenburger, P. Strobel, D. Günther, J. P. Wright, P. J. Schmidt, O. Oeckler, W. Schnick, *Chem. Eur. J.* **2020,** *26*, 7292–7298.

[57] S. D. Kloß, O. Janka, T. Block, R. Pöttgen, R. Glaum, W. Schnick, *Angew. Chem. Int. Ed.* **2019**, 58, 4685–4689.

[58] R. Conanec, P. L'Haridon, W. Feldmann, R. Marchand, Y. Laurent, *Eur. J. Inorg. Chem.* **1994,** *31*, 13–24.

[59] M. Kim, S.-J. Kim, *Acta Cryst. Sect. E* **2013,** *69*, i34.

[60] I. V. Zatovsky, T. V. Vorobjova, K. V. Domasevitch, I. V. Ogorodnyk, N. S. Slobodyanik, *Acta Cryst. Sect. E* **2006,** *62*, i32–i34.

[61] L. M. Gandia, R. Malm, R. Marchand, R. Conanec, Y. Laurent, M. Montes, *Appl. Catal., A* **1994,** *114*, L1–L7.

[62] S. D. Kloß, W. Schnick, *Angew. Chem. Int. Ed.* **2015**, *54*, 11250–11253.

[63] S. D. Kloß, W. Schnick, *Inorg. Chem.* **2018,** *57*, 4189–4195.

[64] S. D. Kloß, L. Neudert, M. Döblinger, M. Nentwig, O. Oeckler, W. Schnick, *J. Am. Chem. Soc.* **2017,** *139*, 12724–12735.

[65] L. Eisenburger, P. Strobel, P. J. Schmidt, T. Bräuniger, J. Wright, E. L. Bright, C. Giacobbe, O. Oeckler, W. Schnick, *Angew. Chem. Int. Ed.* **2022**, *61*, e202114902.

[66] E. Riedel, C. Janiak, *Anorganische Chemie*, De Gruyter, Berlin, New York, 8th Ed., **2011**.

[67] C. Blondel, *Phys. Scr.* **1995,** *1995*, 31–42.

[68] J. Mazeau, F. Gresteau, R. Hall, A. Huetz, *J. Phys. B: At. Mol. Phys.* **1978,** *11*, L557.

[69] H. Huppertz, *Z. Kristallogr.* **2004,** *219*, 330–338.

[70] L. Eisenburger, V. Weippert, O. Oeckler, W. Schnick, *Chem. Eur. J.* **2021,** *27*, 14184–14188.

[71] H. Huppertz, habilitation thesis, Ludwig-Maximilians-Universität (DE), **2003**.

[72] N. Kawai, S. Endo, *Rev. Sci. Instrum.* **1970**, *41*, 1178 – 1181.

[73] D. Walker, *Am. Mineral.* **1991,** *76*, 1092–1100.

[74] D. Rubie, *Phase Transitions* **1999,** *68*, 431–451.

[75] D. Walker, M. Carpenter, C. Hitch, *Am. Mineral.* **1990,** *75*, 1020–1028.

[76] S. Vogel. Phosphorus nitrides at extreme conditions. LMU, Munich, **2019**.

[77] J. Wright, C. Giacobbe, M. Majkut, *Curr. Opin. Solid State Mater. Sci.* **2020,** *24*, 100818.

[78] P. Raimondi, *Synchrotron Radiat. News* **2016,** *29*, 8–15.

[79] C. G. Schroer, I. Agapov, W. Brefeld, R. Brinkmann, Y.-C. Chae, H.-C. Chao, M. Eriksson, J. Keil, X. Nuel Gavaldà, R. Röhlsberger, *J. Synchrotron Radiat.* **2018,** *25*, 1277–1290.

[80] P. Raimondi, C. Benabderrahmane, P. Berkvens, J. C. Biasci, P. Borowiec, J.-F. Bouteille, T. Brochard, N. B. Brookes, N. Carmignani, L. R. Carver, J.-M. Chaize, J. Chavanne, S. Checchia, Y. Chushkin, F. Cianciosi, M. Di Michiel, R. Dimper, A. D'Elia, D. Einfeld, F. Ewald, L. Farvacque, L. Goirand, L. Hardy, J. Jacob, L. Jolly, M. Krisch, G. Le Bec, I. Leconte, S. M. Liuzzo, C. Maccarrone, T. Marchial, D. Martin, M. Mezouar, C. Nevo, T. Perron, E. Plouviez, H. Reichert, P. Renaud, J.-L. Revol, B. Roche, K.-B. Scheidt, V. Serriere, F. Sette, J. Susini, L. Torino, R. Versteegen, S. White, F. Zontone, *Commun. Phys.* **2023,** *6*, 82.

[81] F. Fahrnbauer, T. Rosenthal, T. Schmutzler, G. Wagner, G. B. Vaughan, J. P. Wright, O. Oeckler, *Angew. Chem. Int. Ed.* **2015,** *54*, 10020–10023.

[82] M. Nentwig, S. D. Kloß, L. Neudert, L. Eisenburger, W. Schnick, O. Oeckler, *Chem. Eur. J.* **2019,** *25*, 14382–14387.

[83] C. L. Ciobanu, A. Kontonikas-Charos, A. Slattery, N. J. Cook, K. Ehrig, B. P. Wade, *Minerals* **2017**, *7*, 227.

[84] P. Voyles, J. Grazul, D. A. Muller, *Ultramicroscopy* **2003**, *96*, 251–273.

[85] C. B. Carter, D. B. Williams, *Transmission electron microscopy: Diffraction, imaging, and spectrometry*, Springer, **2016**.

[86] M. O'Keefe, C. Hetherington, Y. Wang, E. Nelson, J. Turner, C. Kisielowski, J.-O. Malm, R. Mueller, J. Ringnalda, M. Pan, *Ultramicroscopy* **2001,** *89*, 215–241.

[87] S. Findlay, N. Shibata, H. Sawada, E. Okunishi, Y. Kondo, Y. Ikuhara, *Ultramicroscopy* **2010,** *110*, 903–923.

[88] K. Lambert, B. D. Geyter, I. Moreels, Z. Hens, *Chem. Mater.* **2009,** *21*, 778–780.

[89] P. A. Midgley, M. Weyland, *Ultramicroscopy* **2003,** *96*, 413–431.

[90] M. Gemmi, A. E. Lanza, *Acta Cryst. Sect. B* **2019,** *75*, 495–504.

[91] B. Lippens, J. De Boer, *Acta Cryst.* **1964,** *17*, 1312–1321.

[92] M. Tanaka, *Acta Cryst. Sect. A* **1994,** *50*, 261–286.

[93] P. Donnadieu, Y. Shao, F. De Geuser, G. Botton, S. Lazar, M. Cheynet, M. De Boissieu, A. Deschamps, *Acta Mater.* **2011,** *59*, 462–472.

[94] M. Humphry, B. Kraus, A. Hurst, A. Maiden, J. Rodenburg, *Nat. Commun.* **2012,** *3*, 730.

[95] P. A. Midgley, R. E. Dunin-Borkowski, *Nat. Mater.* **2009,** *8*, 271–280.

[96] M. Scott, C.-C. Chen, M. Mecklenburg, C. Zhu, R. Xu, P. Ercius, U. Dahmen, B. Regan, J. Miao, *Nature* **2012,** *483*, 444–447.

[97] M. Weyland, P. A. Midgley, *Mater. Today* **2004,** *7*, 32–40.

[98] B. K. Vainshtein, *Fundamentals of crystals: Symmetry, and methods of structural crystallography*, Springer Science & Business Media, **2013**, Vol. 1, pp. 220–360.

[99] M. Haider, S. Uhlemann, E. Schwan, H. Rose, B. Kabius, K. Urban, *Nature* **1998,** *392*, 768–769.

[100] S. Uhlemann, M. Haider, *Ultramicroscopy* **1998,** *72*, 109–119.

[101] M. Haider, H. Rose, S. Uhlemann, E. Schwan, B. Kabius, K. Urban, *Ultramicroscopy* **1998,** *75*, 53–60.

[102] T. E. Weirich, X. Zou, R. Ramlau, A. Simon, G. L. Cascarano, C. Giacovazzo, S. Hovmöller, *Acta Cryst. Sect. A* **2000,** *56*, 29–35.

[103] T. Kogure, J. Elzea-Kogel, C. T. Johnston, D. L. Bish, *Clays Clay Miner.* **2010,** *58*, 62–71.

[104] M. Otoničar, S. D. Škapin, B. Jančar, R. Ubic, D. Suvorov, *J. Am. Ceram. Soc.* **2010,** *93*, 4168–4173.

[105] K.-D. Schierbaum, *Surf. Sci.* **1998,** *399*, 29–38.

[106] N. Cordes, M. Nentwig, L. Eisenburger, O. Oeckler, W. Schnick, *Eur. J. Inorg. Chem.* **2019,** *2019*, 2304–2311.

[107] C. Kisielowski, B. Freitag, M. Bischoff, H. Van Lin, S. Lazar, G. Knippels, P. Tiemeijer, M. van der Stam, S. von Harrach, M. Stekelenburg, *Microsc. Microanal.* **2008,** *14*, 469–477.

[108] S. J. Pennycook, *Ultramicroscopy* **2017,** *180*, 22–33.

[109] D. A. Muller, *Nat. Mater.* **2009,** *8*, 263–270.

[110] E. J. Kirkland, R. F. Loane, J. Silcox, *Ultramicroscopy* **1987**, *23*, 77–96.

[111] J. M. Cowley, *Ultramicroscopy* **1976**, *2*, 3–13.

[112] S. E. Hillyard, R. F. Loane, J.Silcox, *Ultramicroscopy* **1993**, *49*, 14–25.

[113] J. Wall, J. Langmore, M. Isaacson, A. Crewe, *Proc. Natl Acad. Sci.* **1974**, *71*, 1–5.

[114] A. Howie, *J. Microsc.* **1979**, *17*, 11–23.

[115] S. J. Pennycook, D. E. Jesson, *Ultramicroscopy* **1991,** *37*, 14–38.

[116] S. J. Pennycook, B. Rafferty, P. D. Nellist, *Microsc. Microanal.* **2000,** *6*, 343–352.

[117] D. A. Muller, N. Nakagawa, A. Ohtomo, J. L. Grazul, H. Y. Hwang, *Nature* **2004**, *430*, 657–661.

[118] S. E. Hillyard, J. Silcox, *Ultramicroscopy* **1995**, *58*, 6–17.

[119] D. D. Perovic, C. J. Rossow, A. Howie, *Ultramicroscopy* **1993**, *52*, 353–359.

[120] H. L. Xin, V. Intaraprasonk, D. A. Muller, *Appl. Phys. Lett*. **2008**, *92*, 013125.

[121] J. Häusler, L. Eisenburger, O. Oeckler, W. Schnick, *Eur. J. Inorg. Chem.* **2018,** *2018*, 759–764.

Chapter 2

Tetra-Face-Capped Octahedra in a Tetrahedra Network – Structure Determination and Scanning Transmission Electron Microscopy of $SrAl_5P_4N_{10}O_2F_3$

Monika M. Pointner, Oliver Oeckler, and Wolfgang Schnick

published in: *Chem. Eur. J.* **2023**, *29*, e202301960, DOI: 10.1002/chem.202301960.

2.1. Abstract

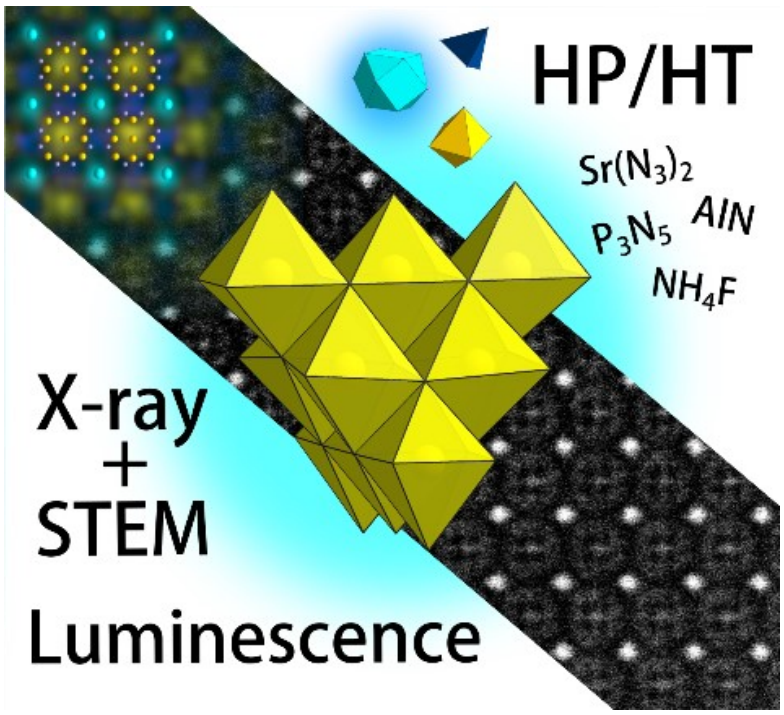

Tetrahedra-based nitridophosphates show a rich structural chemistry, which can be further extended by incorporating cations in higher coordinated positions, e.g., in octahedral voids or by substituting the nitrogen atoms in the network with other anions. Following this approach, $SrAl_5P_4N_{10}O_2F_3$ was synthesized at high-temperature and high-pressure conditions using a multianvil press (1400 °C, 5 GPa) starting from $Sr(N_3)_2$, c-PON, P_3N_5, AlN, and NH_4F. $SrAl_5P_4N_{10}O_2F_3$ crystallizes in space group $I\bar{4}m2$ with a = 11.1685(2) and c = 7.84850(10) Å. Atomic-resolution EDX mapping with scanning transmission electron microscopy (STEM) indicates atom assignments, which are further corroborated by bond valence sum (BVS) calculations. Ten Al^{3+}-centered octahedra form a highly condensed tetra-face-capped octahedra-based unit that is a novel structure motif in network compounds. A network of vertex-sharing PN_4 tetrahedra and chains of face-sharing Sr^{2+}-centered cuboctahedra complement the structure. Eu^{2+}-doped $SrAl_5P_4N_{10}O_2F_3$ shows blue emission (λ_{em} = 469 nm, fwhm = 98 nm; 4504 cm^{-1}) when irradiated with UV light.

2.2. Introduction

Nitridophosphates feature a large diversity of crystal structures due to the isolobal relation between P–N and Si–O bonds, which preserves a close analogy to silicate-related structural motifs like discrete tetrahedra, layers and networks.[1] Compared to silicate bonds, the elemental combination of phosphorus and nitrogen offers a more covalent bonding situation due to a smaller electronegativity difference, and thus, a more significant structural rigidity. Trivalent nitrogen substituting divalent oxygen enables motifs scarcely seen in silicates like edge-sharing tetrahedra and triply coordinated anions as well as trigonal bipyramids (PN_5), which is scarcely realized with oxygen.[2-5]

These structural modifications can result in high thermal and chemical stability and favorable mechanical, electronic, and optical properties. $MH_4P_6N_{12}$ (*M* = Mg, Ca), $M^{I}_3M^{III}(PO_3)_3N$ and $M^{I}_2M^{II}_2(PO_3)_3N$ (M^{I} = Li, Na; M^{III} = Al, V; M^{II} = Mg) show ion conduction, and the latter are further studied as a potential cathode material for batteries.[6-10] Eu^{2+}-doped (oxo)nitrido-phosphates like $AESiP_3N_7$ (*AE* = Sr, Ba), Ba_2PO_3N and β-$MgSrP_3N_5O_2$ are investigated as phosphor materials with intriguing luminescence properties.[11-13]

Variability in regard to structures and properties can be further increased by diversifying cations embedded in the nitridic network. Due to its capability to occupy both tetrahedra and octahedra, aluminum takes a unique role in the choice of cations concerning structural diversity. For example, in the efficient and thermally stable narrow-band emitter $Al_9O_3N_7{:}Eu^{2+}$ face- and edge-sharing $Al(O,N)_4$ tetrahedra are observed.[14] In SiAlONs, which are explored for their remarkable thermal, mechanical and chemical stability and which are employed for high-temperature engineering applications, aluminum shares tetrahedral sites with silicon and thus is part of the network.[15] Discrete $Al(O,N)_6$ octahedra are found in $Na_3Al(PO_3)_3N$, $AlP_6O_{3x}(NH)_{3-3x}N_9$ ($x \approx 0.33$), and AlP_6N_{11}.[7, 16-17] Materials in the system Al/P/O/N represent catalysts with high surface areas and tuneable acid-base properties that feature excellent conversion rates and selectivity.[18-19] A more condensed structure can be found in the oxonitride Nd_2AlO_3N with vertex-sharing Al-centered octahedra.[20] Still, the pool of compounds with both a nitridophosphate network and sixfold coordinated aluminum, especially with condensed octahedra, is minimal and holds great potential for further exploration.

One area for improvement has been the availability of advanced synthesis methods. At ambient pressure, P_3N_5 decomposes above 850 °C with the formation of N_2. Therefore, high-pressure high-temperature (HP/HT) synthesis has been proposed as a viable pathway to stabilize P_3N_5 and nitridophosphates. Using stable azides and nitrides promotes the formation of N_2 and averts the decomposition of P_3N_5. This established method could be further improved by using NH_4F as a mineralizer to overcome differing reactivities of starting materials and results in new mixed nitridic networks.[11, 21] Pushing for the limits of this technique and an extension of common networks and host lattices, we work with easily accessible materials and promising elemental combinations.

Here, we report on the discovery and structural characterization of $SrAl_5P_4N_{10}O_2F_3$ containing a structural motif of ten Al^{3+}-cations in a tetra-face-capped octahedra-based topology that has not been found so far in any network compound.

2.3. Experimental Section

2.3.1. Preparation of Starting Materials

P_3N_5 was prepared by heating P_4S_{10} (Sigma-Aldrich, 99.99%) in a constant ammonia flow.[22] After drying (at 1273 K) a fused silica tube and silica boat under dynamic vacuum (<10^{-3} bar), P_4S_{10} was loaded into the boat in a constant flow of argon. The setup was purged with dry ammonia (Air Liquide, 5.0) for 4 h, and the reaction was carried out at 1123 K for 4 h. The furnace was cooled to room temperature (heating and cooling ramp of 5 K/min), and the product was washed with diluted HCl and H_2O. The product was obtained as an orange powder. PXRD and CHNS analyses confirmed its purity (in wt%: C 0%, H 0%, N 42.69%, S 0%; expected C 0%, H 0%, N 42.98%, S 0%). PON was synthesized according to the literature, and PXRD confirmed the phase purity.[23]

2.3.2. Multianvil Synthesis

$SrAl_5P_4N_{10}O_2F_3$ was synthesized under high-pressure high-temperature conditions (T = 1400 °C, p = 5 GPa) using a 1000 t hydraulic press (Voggenreiter, Mainleus, Germany) with a modified Walker module. Details on the preparation and handling of the 1000 t Walker-type multianvil press are described in the literature.[24-27] Stoichiometric amounts of the starting materials $Sr(N_3)_2$, AlN, PON, P_3N_5 and 3 wt% NH_4F (Table A.1) were thoroughly mixed in an agate mortar in an Ar-filled glovebox (Unilab, MBraun, Garching, O_2 < 1 ppm, H_2O < 0.1 ppm), transferred into a crucible of h-BN (HeBoSint® S100, Henze, Kempten, Germany) and sealed with a h-BN lid. After sample insertion, the setup was compressed to 5 GPa and heated to 1400 °C within 60 min. The temperature was kept constant for 300 min before cooling to room temperature and slowly decompressing.

2.3.3. Powder X-Ray Diffraction

A powder diffractometer Stadi P (Stoe & Cie GmbH, Darmstadt, Germany) with Cu-Kα_1 radiation (λ = 1.54056 Å; Ge(111) single-crystal monochromator) with parafocusing Debye-Scherrer geometry and MYTHEN 1K Si strip detector (Dectris Ltd., Baden, Switzerland) was used. Powder diffractograms of finely ground samples in glass capillaries (Ø 0.3 mm, wall thickness 0.01 mm, Hilgenberg GmbH, Malsfeld, Germany) were recorded at an angular range of 2θ = 3–93°. TOPAS

Academic 6.1 was used for Rietveld refinements, employing a fundamental parameters approach and a Chebyshev polynomial for background modelling.[28-29]

2.3.4. Energy-Dispersive X-Ray Spectroscopy

Isolated crystals of the sample were placed on a conducting carbon foil and coated with carbon. A FEI Gelios NanoLab G3 Dual Beam UC (Fei, Hillsboro, OR, USA) with an attached X-Max 80 SDD detector (Oxford Instruments, Abingdon, UK) obtained EDX spectra.

2.3.5. Scanning Transmission Electron Microscopy

The sample was ground thoroughly in absolute ethanol and distributed on a lacey carbon film covered Cu grid (S-166-2, Plano GmbH, Lünen, Germany) and mounted in a double-tilt holder (±30°). STEM was carried out with a Titan Themis 300 (FEI, USA) transmission electron microscope equipped with an X-FEG source, a post-column filter (Enfinium ER-799), a Cs DCOR probe corrector, a US1000XP/FT camera system (Gatan, Germany), a 4k × 4k FEI Ceta CMOS camera (FEI, USA) and a windowless 4-quadrant Super-X EDX detector. The system was operated at an acceleration voltage of 300 kV. Data processing was performed with the following software: Digital Micrograph (Fourier filtering of STEM images), ProcessDiffraction7 (calculations of SAED patterns), JEMS (SAED simulations) and Velox (STEM images, EDX maps).[30-33]

2.3.6. Single-Crystal X-Ray Diffraction

A Bruker D8 Venture TXS diffractometer (rotating anode, Mo-Kα radiation, λ = 0.71073 Å, multilayer monochromator) was used to obtain single-crystal X-ray diffraction data. For indexing, integration and semiempirical absorption correction, the program package APEX3 was used.[34-35] Structure solution was performed with direct methods (SHELXS), whereas the structure refinement was conducted using the full-matrix least-squares methods (SHELXL-2018).[36] For visualization, Diamond3 was used.[37] VaList was used to perform BVS calculations.[38-39] Deposition Number CSD 2261405 contains the supplementary crystallographic data for this paper. These data are provided free of charge by the joint Cambridge Crystallographic Data Centre and Fachinformationszentrum Karlsruhe (http://www.ccdc.cam.ac.uk/structures).

2.3.7. FTIR Spectroscopy

An FTIR spectrum was recorded on a Spectrum BX II spectrometer (PerkinElmer Waltham, MA, USA) with a DuraSampler ATR unit in the range of 650–4400 cm^{-1}.

2.3.8. Luminescence Measurements

Luminescence measurements of single crystals of $SrAl_5P_4N_{10}O_2F_3:Eu^{2+}$ were carried out on small particles in air. The spectrum was obtained on a HORIBA Fluoromax4 spectrofluorimeter system with an Olympus BX51 microscope. Emission spectra of the single crystals ranged from 400 to 800 nm (step size of 2 nm) and were collected at room temperature after excitation with blue light (λ_{exc} = 390 nm).

2.4. Results and Discussion

2.4.1. Synthesis

$SrAl_5P_4N_{10}O_2F_3$ was obtained by a mineralizer-assisted high-pressure high-temperature approach at 5 GPa and 1400 °C in a multianvil press. The synthesis started from stoichiometric amounts of $Sr(N_3)_2$, cristobalite-type phosphorus oxide nitride (c-PON), P_3N_5, AlN and NH_4F as fluorine source as well as mineralizing agent (Table A.1) and follows the reaction equation (1).

$$Sr(N_3)_2 + 2\ \text{c-PON} + \frac{2}{3}\,P_3N_5 + 5\ AlN + 6\ NH_4F \rightarrow SrAl_5P_4N_{10}O_2F_3 + HF + N_2 \qquad (1)$$

EuF_3 was used as a doping agent to obtain Eu^{2+} luminescence. The reductive conditions upon formation of N_2 lead to the reduction of Eu^{3+}. $SrAl_5P_4N_{10}O_2F_3$ is a crystalline solid with a light-gray body color and is stable towards air and moisture. Scanning electron microscopy (SEM) images show rod-shaped crystals with a length of up to 80 µm and a width of around 30 µm (Figure A.1 left). Rietveld refinement based on the PXRD data indicates no crystalline side phases (Figure 2.1, Table A.2). Figure A.2 displays a FTIR spectrum of $SrAl_5P_4N_{10}O_2F_3$ with P–N framework vibrations between 600–1500 cm^{-1}. The weak signal around 3250 cm^{-1} corresponds to O–H vibrations, most likely due to a small extent of surface hydrolysis or a minor substitution of O^{2-} by NH^{2-}.

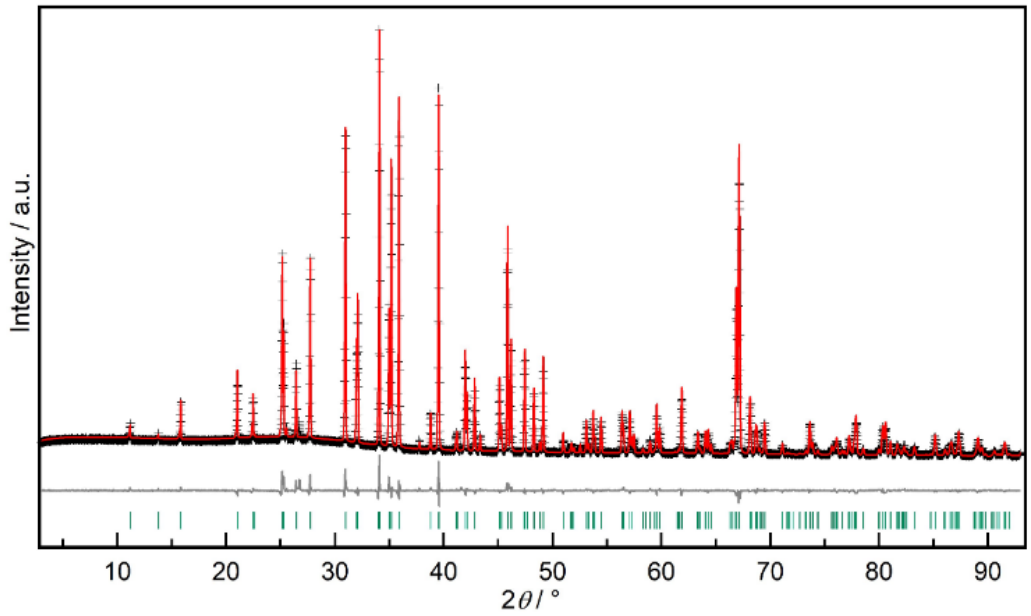

Figure 2.1. Rietveld refinement of $SrAl_5P_4N_{10}O_2F_3$ based on PXRD data of the bulk sample at ambient temperature with Cu-Kα_1 radiation (λ = 1.5406 Å): observed (black data points), calculated pattern (red line) and difference curve (gray line), Bragg reflection markers for $SrAl_5P_4N_{10}O_2F_3$ (green), R_{wp} = 0.061. No evidence for a crystalline side phase was found.

2.4.2. Crystal Structure Determination

The crystal structure of $SrAl_5P_4N_{10}O_2F_3$ was solved and refined based on single-crystal X-ray diffraction data in the tetragonal space group $I\bar{4}m2$ (no. 119, a = 11.17931(5), c = 7.85305(5) *Å, Z = 2*). Crystallographic data are summarized in Table 2.1. Wyckoff positions, atomic coordinates, and displacement parameters are given in Tables A.3 and A.4.

The metrics was verified by a tilt series of selected area electron diffraction (SAED) patterns and simulations based on the structure model (Figure A.3). The sum formula was confirmed by TEM-EDX results taking into account BVS calculations. TEM-EDX spectroscopy data were obtained from several crystallites (example shown in Figure A.1 right, results in Table A.5) and agree with the expected values, particularly with respect to the atomic ratio Al:P of 1.25:1.

Table 2.1. Crystallographic data of the single-crystal structure refinement of $SrAl_5P_4N_{10}O_2F_3$. Standard deviations are given in parentheses.

formula	$SrAl_5P_4N_{10}O_2F_3$
molar mass / g·mol^{-1}	1151.00
crystal system	tetragonal
space group	$I\bar{4}m2$ (no. 119)
lattice parameters / Å	a = 11.1685(2) c = 7.84850(10)
cell volume / Å^3	978.99(4)
formula units / unit cell	2
density / g·cm^{-3}	3.905
μ / mm^{-1}	6.701
temperature / K	299(4)
absorption correction	semiempirical
radiation	Mo-Kα (λ = 0.71073 Å)
F(000)	1104
θ range / °	3.6–36.3
total no. of reflections	15183
independent reflections [I≥2σ(I) / all]	1261 / 1280
R_σ, R_{int}	0.0241, 0.0347
refined parameters	75
restraints	0
GooF	1.073
R values [I≥2σ(I)]	R1 = 0.0197, wR2 = 0.0438
R values (all data)	R1 = 0.0203, wR2 = 0.0441
$\Delta\rho_{max}$, $\Delta\rho_{min}$ / e·Å^{-3}	1.373, –1.110

The structure contains five fully occupied cation sites and eight anion sites. The possible disorder of Al and P atoms on the octahedral and tetrahedral positions was ruled out by scanning transmission electron microscopy (STEM), including high-angle annular dark-field (HAADF) *Z*-contrast imaging and EDX mapping with atomic resolution. The corresponding intensities of the *Z*-contrast image and the spatial separation of STEM-EDX signals identify the Sr positions and confirm the allocation of Al and P on separate Wyckoff positions. The combination of the STEM-HAADF image and the corresponding STEM-EDX maps of the three cation columns Sr, Al and P along [001] are shown in Figure 2.2 (enlarged version Figure A.4) and support the model of Al exclusively occupying octahedral sites, whereas P only occupies the single tetrahedral site. The obtained EDX spectrum is shown in Figure A.5.

BVS values of all cations, all nitrogen atoms and the fluorine positions F2 and F3 agree well with the expected charges (Table 2.2), F1 and O1 show more significant deviations of 18% and 50%, respectively, which may imply a certain extent of O/F mixed occupation. BVS values of all nitrogen positions suggest full occupation, and the displacement parameters do not indicate partial occupancies. Minor mixed occupations in all anionic sites cannot be excluded, but data from SCXRD and BVS support the presented ordered model.

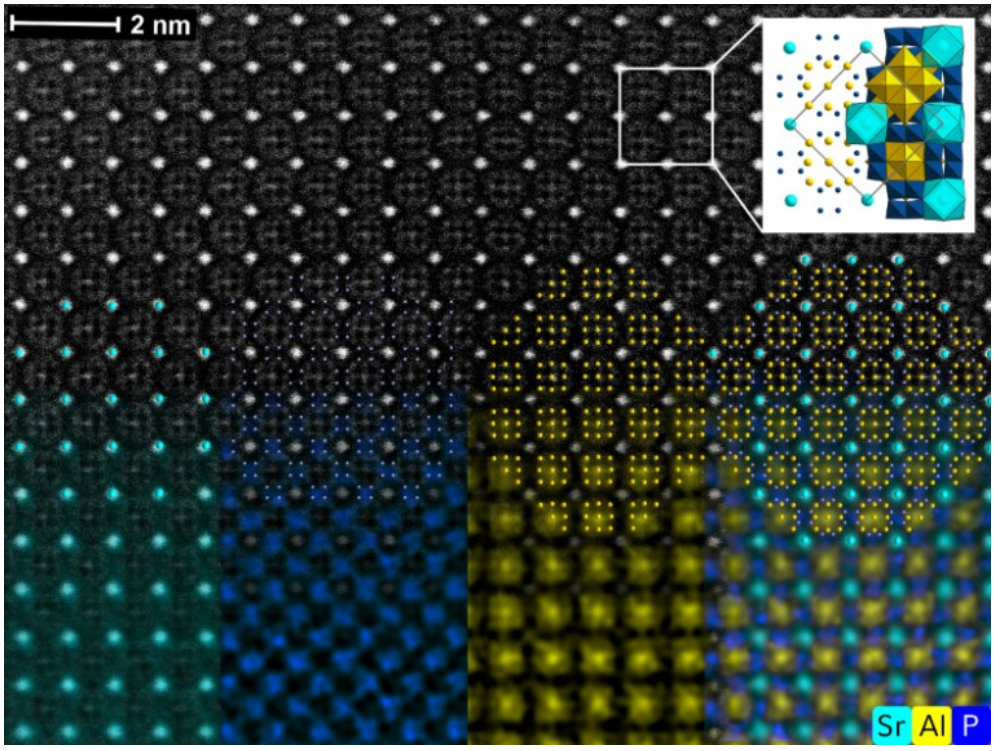

Figure 2.2. STEM-EDX mapping of $SrAl_5P_4N_{10}O_2F_3$ along [001]. STEM-HAADF image (top) with structure overlay (middle, Sr cyan, P blue, Al yellow). The corresponding EDX maps are shown at the bottom: Sr cyan, P blue, Al yellow, and the resulting combined map. The inset shows the unit cell.

Table 2.2. Calculated bond valence sums and expected charges for the atom sites in the crystal structure of $SrAl_5P_4N_{10}O_2F_3$.

atom site	*bond valence sums*	$charge_{exp.}$
Sr1	2.16	+2
P1	4.82	+5
Al1	3.20	+3
Al2	2.92	+3
Al3	2.88	+3
O1	1.47	−2
F1	1.18	−1
F2	0.92	−1
F3	0.91	−1
N1	3.13	−3
N2	2.97	−3
N3	3.01	−3
N4	2.98	−3

2.4.3. Structure Description

The structure can be described as a distorted joint *fcc* packing of all anions and Sr atoms with partly filled octahedral and tetrahedral voids. Vertex-sharing PN_4 tetrahedra build a three-dimensional network in which Sr-centered face-sharing cuboctahedra form chains along [001]. Ten edge-sharing Al-centered octahedra build a substructure with a tetra-face-capped octahedra-based topology. An isoelectronic arrangement of the metal cations has only been observed in molecular compounds with mixed-valent $Mn^{II/III}$ ions so far.[40] Mn^{3+} ions in the cation $[Mn_{10}O_4(N_3)_4(hmp)_{12}]^{2+}$ (hmp = 2-(hydroxyl-methyl)pyridine) build an octahedron of which the non-adjacent faces are capped by four external Mn^{2+} atoms. All anions related to the complex are coordinated tetrahedrally through metal cations. In $SrAl_5P_4N_{10}O_2F_3$ the same tetra-face-capped octahedra-based topology is formed by cations and all cationic positions are occupied by Al^{3+}. Anionic positions differ slightly from the literature. Two anionic positions are coordinated tetrahedrally and one position occupies an octahedral coordination. This is the first case of a network compound in which such a structure motif occurs. For better visualization, the unit cell in Figure 2.3 shows only one Al_{10} unit (yellow), one chain of Sr-centered cuboctahedra (cyan) and the PN_4 tetrahedra network (dark blue). Figure 2.4 illustrates all coordination polyhedra.

Vertex-sharing PN_4 tetrahedra form corrugated ten- and eight-membered rings (Figure A.6). P–N distances and N–P–N angles vary between 1.6141(18)–1.6708(15) Å and 105.33(12)–122.44(8)°, respectively, which is in good agreement with known nitridophosphates.[41-43]

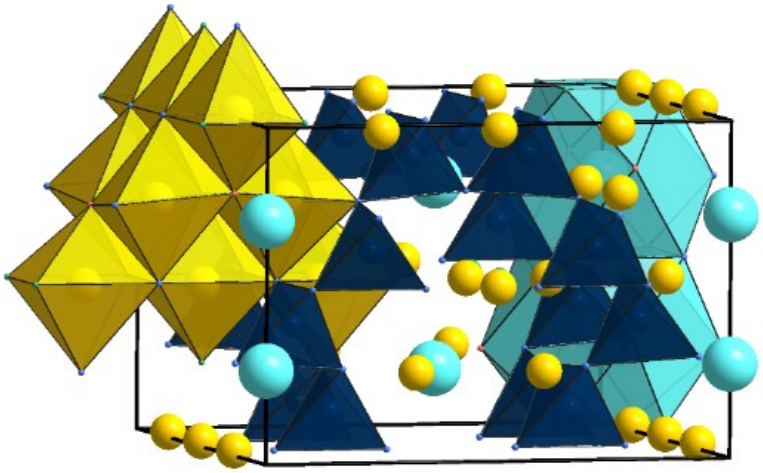

Figure 2.3. Illustration of a $SrAl_5P_4N_{10}O_2F_3$ unit cell with $Sr(N_6O_2F_4)$ cuboctahedra (cyan), one $(Al(N,O,F)_6)_{10}$ unit (yellow) and PN_4 tetrahedra (dark blue).

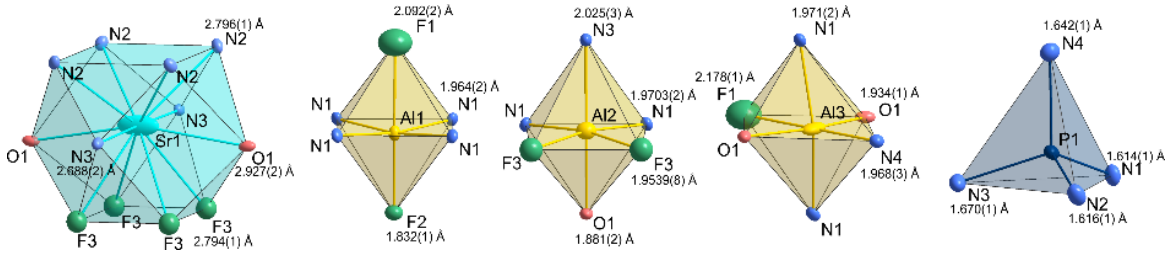

Figure 2.4. Coordination polyhedra around Sr1, Al1, Al2, Al3 and P1. Displacement ellipsoids are shown for 90% probability.

The strontium atoms occupy a single crystallographic site, which is coordinated by N, O and F atoms, leading to a $Sr(N_6O_2F_4)$ cuboctahedra. The Sr atom position is somehow modulated along [100], resulting in shorter (3.4799(10) Å) and longer (4.3686(10) Å) $d_{Sr–Sr}$ that deviate by ≈ 11% from an average value of 3.9242 Å. This leads to more acute Sr–N–Sr angles of 76.94(5)° between the shorter Sr–Sr distances compared to the more obtuse Sr–F–Sr angles of 102.82(5)° associated with the larger Sr–Sr distances (Figure A.7). Even with this alternation of the Sr–Sr chain, interatomic distances within the cuboctahedra reveal only a small overall distortion of the single cuboctahedron. The topology of the cations in the Al_{10} unit has been described as a tetra-face-

capped octahedron.[40] In literature, anions are surrounded by four metal cations, forming tetrahedra. Here, the central anion F1 is surrounded by six Al^{3+} ions (Al1 + Al3), forming an octahedron. All twelve edges are bridged by eight nitrogen atoms and four oxygen atoms (Figure 2.5). All bridging anions are linked to external Al^{3+} ions (Al2). The units are connected to each other through vertices. Al2- and Al1-centered octahedra share common F3 and F1 atoms, respectively (Figure 2.6 a). Al_{10} units alternate with the Sr-centered cuboctahedra chains along the directions *a* and *b* (Figure 2.6 b).

The three crystallographically independent Al^{3+} ions differ in their coordinating anions leading to AlN_4F_2, AlN_3OF_2 and AlN_3O_2F octahedra. They are slightly distorted and tilted against each other, with the Al^{3+} atoms slightly displaced from the centers. The distances of the aluminum atoms to their neighboring anions vary between 1.8319(14)–2.1778(10) Å and increase from Al–O (1.916 Å) to Al–N (1.973 Å), as expected. However, Al–F bond lengths do not follow the trend with the shortest and longest average distance found for Al–F bonds. Some Al–F bonds are unexpectedly long, e.g., Al1–F1/Al3–F1 with 2.0924(14)/ 2.1778(10) Å. An overview of interatomic distances and angles is provided in Table A.6 and A.7.

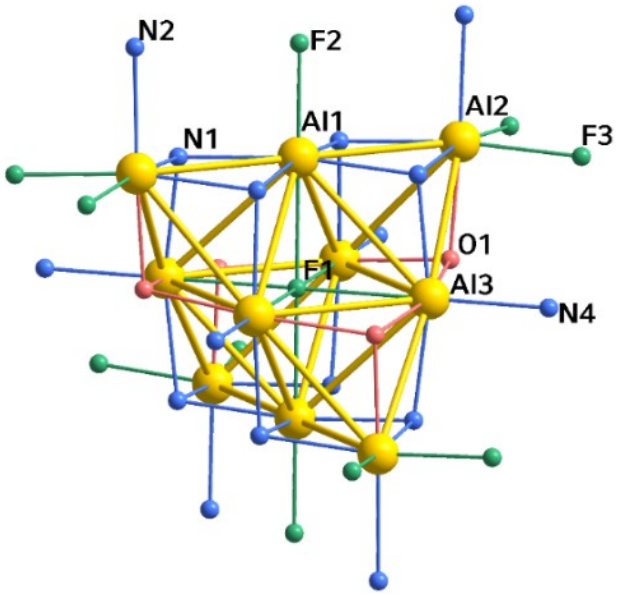

Figure 2.5. Partially labeled representation of an Al_{10} unit with Al^{3+} yellow, O light red, N light blue, F light green and bonds from Al^{3+} ions to Al^{3+}/anions in respective colors. Ten Al^{3+} cations build a tetra-capped octahedron, marked with yellow lines between Al^{3+} ions. The central octahedron is occupied by F1.

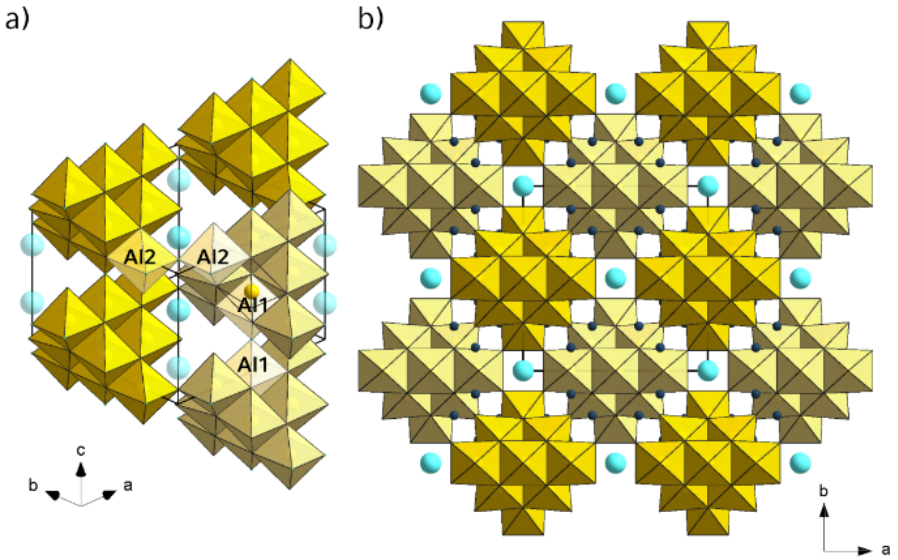

Figure 2.6. Illustration of the Al_{10} substructure. Light and dark yellow for better distinction; a) Octahedra sharing vertices are partially highlighted: Common F3 anions connect Al2 octahedra in the [001] plane, common F1 atoms connect Al1 octahedra along the *c* axis b) Alternating Al_{10} units and Sr columns in [001]. Sr cyan, $(Al(N,O,F)_6)_{10}$ units (yellow, light yellow), P (dark blue).

2.4.4. Luminescence

To investigate luminescence properties, Eu^{2+}-doped samples have been synthesized by adding ≈ 1 mol% of EuF_3, referring to the Sr content to the starting mixtures. EuF_3 was chosen as a europium source to support the formation of HF additionally. The photoluminescence properties were investigated on single particles (Figure A.8). The blue luminescence of $SrAl_5P_4N_{10}O_2F_3$ most likely originates from Eu^{2+} located on a cuboctahedrally coordinated Sr^{2+} site, owing to similar ionic radii of Eu^{2+} and Sr^{2+}. In addition, the highly condensed PN_4 network with additional $Al(N,O,F)_6$ octahedra leaves no other suitable position for a possible luminescence center with respect to the ion sizes. The Eu^{2+}-doped material features a strong blue emission with a single broad emission maximum peaking at λ_{em} = 469 nm upon excitation with λ_{exc} = 390 nm. The full width at half maximum is 98 nm (4504 cm^{-1}). Emission from Eu^{2+} on a highly symmetric site often results in a narrow emission band, as observed in AEP_8N_{14} (*AE* = Ca, Sr) or $AEBe_{20}N_{14}:Eu^{2+}$ (*AE* = Sr, Ba).[43-44] $SrAl_5P_4N_{10}O_2F_3$ provides a symmetric, only slightly distorted cuboctahedral coordination around the alkaline-earth atom. The relatively broad emission band probably results from the displacement of the Sr atom out of the center of the cuboctahedron. Furthermore, the three different anions N, O and F surrounding Eu^{2+} generate an inhomogeneous ligand field, which further broadens the emission

band. Nitrides tend to have a red-shifted emission compared to oxonitrides because *AE*–N bonds are more covalent than *AE*–O/–F bonds. In the case of $SrAl_5P_4N_{10}O_2F_3:Eu^{2+}$, the position of the emission maximum is thus rather comparable to oxides and oxonitrides like $SrLi_2Be_4O_6:Eu^{2+}$ or $Sr_{0.25}Ba_{0.75}Si_2O_2N_2:Eu^{2+}$ (CN = 8, λ_{em} = 456 and 472 nm,) than to nitrides such as $Sr[LiAl_3N_4]:Eu^{2+}$ (λ_{em} = 650 nm).[45-47]

2.5. Conclusion

An NH_4F-mediated HP/HT synthesis obtained $SrAl_5P_4N_{10}O_2F_3$. Its successful synthesis with a mineralizer-assisted approach demonstrates the feasibility to employ different potentially inert starting materials to form mixed nitride networks.[11] The crystal structure was determined by single-crystal X-ray diffraction and is consistent with element ratios from EDX. STEM-EDX mapping with atomic resolution and high-angle annular dark-field *Z*-contrast images confirm the cation site assignment. The crystal structure can be described as a network of vertex-sharing PN_4 tetrahedra, chains of face-sharing Sr-centered cuboctahedra and a substructure of condensed Al_{10} units formed by ten edge-sharing $Al(N,O,F)_6$ octahedra, yet unseen in network structures.

$SrAl_5P_4N_{10}O_2F_3$ is suitable as a host lattice for rare-earth activator ions and shows blue emission upon doping with Eu^{2+}. This highlights the potential for the development of new host compounds for phosphors with mixed alkaline-earth and aluminum cations. In theory, a large number of charge-balanced compounds with diverse structural motifs can be accessed. A possible site-selectivity of doping due to differences in ionic radii of Al^{3+} and AE^{2+} and charges (e.g., Ce^{3+} on Al^{3+} sites versus Eu^{2+} on AE^{2+} sites) makes the research on aluminum-containing nitrides and nitridophosphates a promising field worth investigating.

Supporting

Deposition number 2261405 contains the supplementary crystallographic data for this paper. These data are provided free of charge by the joint Cambridge Crystallographic Data Centre and Fachinformationszentrum Karlsruhe Access Structures service.

Acknowledgements

Financial support by the Deutsche Forschungsgemeinschaft DFG (projects SCHN 377/18-1 and OE 513/6-1) is gratefully acknowledged. The authors thank Dr. Peter Mayer and Christian Minke for single-crystal data collection and SEM measurements, respectively (all at LMU Munich) and Dr. Philipp Strobel (Lumileds Phosphor Center Aachen) for luminescence measurements.

2.6. References

[1] S. D. Kloß, W. Schnick, *Angew. Chem.* **2019**, *131*, 8015–8027; *Angew. Chem. Int. Ed.* **2019**, *58*, 7933–7944.

[2] D. Baumann, W. Schnick, *Angew. Chem.* **2014**, *126*, 14718–14721; *Angew. Chem. Int. Ed.* **2014**, *53*, 14490–14493.

[3] S. Horstmann, E. Irran, W. Schnick, *Z. Anorg. Allg. Chem.* **1998**, *624*, 221–227.

[4] W. Schnick, *Angew. Chem.* **1993**, *105*, 846–858; *Angew. Chem. Int. Ed. Engl.* **1993**, *32*, 806–818.

[5] D. Baumann, W. Schnick, *Inorg. Chem.* **2014**, *53*, 7977–7982.

[6] A. Marchuk, V. R. Celinski, J. Schmedt auf der Günne, W. Schnick, *Chem. Eur. J.* **2015**, *21*, 5836–5842.

[7] K. Higashi, M. Ochi, Y. Nambu, T. Yamamoto, T. Murakami, N. Yamashina, C. Tassel, Y. Matsumoto, H. Takatsu, C. M. Brown, H. Kageyama, *Inorg. Chem.* **2021**, *60*, 11957–11963.

[8] M. R. Cosby, G. S. Mattei, Y. Wang, Z. Li, N. Bechtold, K. W. Chapman, P. G. Khalifah, *J. Phys. Chem. Sect. C* **2020**, *124*, 6522–6527.

[9] J. Liu, X. Yu, E. Hu, K.-W. Nam, X.-Q. Yang, P. G. Khalifah, *Chem. Mater.* **2013**, *25*, 3929–3931.

[10] M. Reynaud, A. Wizner, N. A. Katcho, L. C. Loaiza, M. Galceran, J. Carrasco, T. Rojo, M. Armand, M. Casas-Cabanas, *Electrochem. Commun.* **2017**, *84*, 14–18.

[11] . Eisenburger, O. Oeckler, W. Schnick, *Chem. Eur. J.* **2021**, *27*, 4461–4465.

[12] S. Wendl, M. Mallmann, P. Strobel, P. J. Schmidt, W. Schnick, *Eur. J. Inorg. Chem.* **2020**, *2020*, 841−846.

[13] R. M. Pritzl, N. Prinz, P. Strobel, P. J. Schmidt, W. Schnick, *Chem. Eur. J.* 2023, e202301218.

[14] J. Ding, Y. Wei, W. Liu, Y. Li, Q. Wu, J. Zhou, *Chem. Eng. J.* **2021**, *403*, 126382.

[15] K. H. Jack, *J. Mater. Sci.* **1976**, *11*, 1135–1158.

[16] L. Neudert, F. Heinke, T. Bräuniger, F. J. Pucher, G. B. Vaughan, O. Oeckler, W. Schnick, *Chem. Commun.* **2017**, *53*, 2709–2712.

[17] S. J. Ambach, M. Pointner, S. Falkai, C. Paulmann, O. Oeckler, W. Schnick, *Angew. Chem.* **2023**, e202303580; *Angew. Chem. Int. Ed.* **2023**, e202303580.

[18] P. Grange, P. Bastians, R. Conanec, R. Marchand, Y. Laurent, L. Gandia, M. Montes, J. Fernandez, J. A. Odriozola, A new strong basic high surface area catalyst: the nitrided aluminophosphate: AlPON and Ni-AlPON. In *Studies in Surface Science and Catalysis*, Elsevier, **1995**,vol. 91, pp 381–389.

[19] E. Guéguen, S. Delsarte, V. Peltier, R. Conanec, R. Marchand, Y. Laurent, P. Grange, *J. Eur. Ceram. Soc.* **1997**, *17*, 2007–2010.

[20] R. Marchand, *Rev. Chim. Minér.* **1982**, *19*, 684–689.

[21] L. Eisenburger, V. Weippert, O. Oeckler, W. Schnick, *Chem. Eur. J.* **2021**, *27*, 14184–14188.

[22] A. Stock, H. Grüneberg, *Ber. Dtsch. Chem. Ges.* **1907**, *40*, 2573–2578.

[23] S. Vogel, D. Baumann, R. Niklaus, E. Bykova, M. Bykov, N. Dubrovinskaia, L. Dubrovinsky, W. Schnick, *Angew. Chem.* **2018**, *130*, 6801–6805; *Angew. Chem. Int. Ed.* **2018**, *57*, 6691–6695.

[24] D. Rubie, *Ph. Transit.* **1999**, *68*, 431–451.

[25] H. Huppertz, *Z. Kristallogr. - Cryst. Mater.* **2004**, *219*, 330–338.

[26] D. Walker, *Am. Mineral.* **1991**, *76*, 1092–1100.

[27] D. Walker, M. Carpenter, C. Hitch, *Am. Mineral.* **1990**, *75*, 1020–1028.

[28] A. Coelho, TOPAS Academic Vers. 6.1, Brisbane (Australia), **2007**.

[29] H. M. Rietveld, *J. Appl. Crystallogr.* **1969**, *2*, 65–71.

[30] I. Gatan, DigitalMicrograph, Pleasanton, California, **1999**.

[31] J. L. Lábár, *Ultramicroscopy* **2005**, *103*, 237–249.

[32] J. P. A. Stadelmann, jems, Saas-Fee, **2008**.

[33] Thermo Fisher Scientific, Velox, Version 3, Waltham, Massachusetts, **2021**.

[34] Bruker-AXS, APEX3, Version 2016.5-0, Karlsruhe (Germany), **2001**.

[35] G. M. Sheldrick, SADABS v.2: Multi-Scan Absorption Correction, Brucker AXS Inc, Kennewick, Washington, **2012**.

[36] G. M. Sheldrick, *Acta Crystallogr. Sect. C* **2015**, *71*, 3–8.

[37] K. Brandenburg, Diamond, Bonn (Germany), **1997–2014**.

[38] A. S. Wills, VaList, University College London, London, **1998–2010**.

[39] N. E. Brese, M. O'Keeffe, *Acta Crystallogr. Sect. B* **1991**, *47*, 192–197.

[40] T. C. Stamatatos, K. A. Abboud, W. Wernsdorfer, G. Christou, *Angew. Chem.* **2006**, *118*, 4240–4243; *Angew. Chem. Int. Ed.* **2006**, *45*, 4134–4137.

[41] F. J. Pucher, A. Marchuk, P. J. Schmidt, D. Wiechert, W. Schnick, *Chem. Eur. J.* **2015**, *21*, 6443–6448.

[42] A. Marchuk, S. Wendl, N. Imamovic, F. Tambornino, D. Wiechert, P. J. Schmidt, W. Schnick, *Chem. Mater.* **2015**, *27*, 6432–6441.

[43] S. Wendl, L. Eisenburger, P. Strobel, D. Günther, J. P. Wright, P. J. Schmidt, O. Oeckler, W. Schnick, *Chem. Eur. J.* **2020**, *26*, 7292–7298.

[44] E. Elzer, R. Niklaus, P. J. Strobel, V. Weiler, P. J. Schmidt, W. Schnick, *Chem. Mater.* **2019**, *31*, 3174–3182.

[45] P. Strobel, C. Maak, V. Weiler, P. J. Schmidt, W. Schnick, *Angew. Chem.* **2018**, *57*, 8875–8879; *Angew. Chem. Int. Ed.* **2018**, *57*, 8739–8743.

[46] M. Seibald, T. Rosenthal, O. Oeckler, F. Fahrnbauer, A. Tücks, P. J. Schmidt, W. Schnick, *Chem. Eur. J.* **2012**, *18*, 13446–13452.

[47] P. Pust, V. Weiler, C. Hecht, A. Tücks, A. S. Wochnik, A.-K. Henß, D. Wiechert, C. Scheu, P. J. Schmidt, W. Schnick, *Nat. Mater.* **2014**, *13*, 891–896.

Chapter 3

Tetrahedra Networks with Additional Cations – Isolated AlN_6 Octahedra in the Imidonitridophosphates $AE_2AlP_8N_{15}(NH)$ (*AE* = Ca, Sr, Ba)

Monika M. Pointner, Reinhard M. Pritzl, Jonas M. Albrecht, Leopold Blahusch, Jonathan P. Wright, Eleanor Lawrence Bright, Carlotta Giacobbe, Oliver Oeckler, and Wolfgang Schnick

published in: *Chem. Eur. J.* **2024***,* e202400766, DOI: 10.1002/chem.202400766.

3.1. Abstract

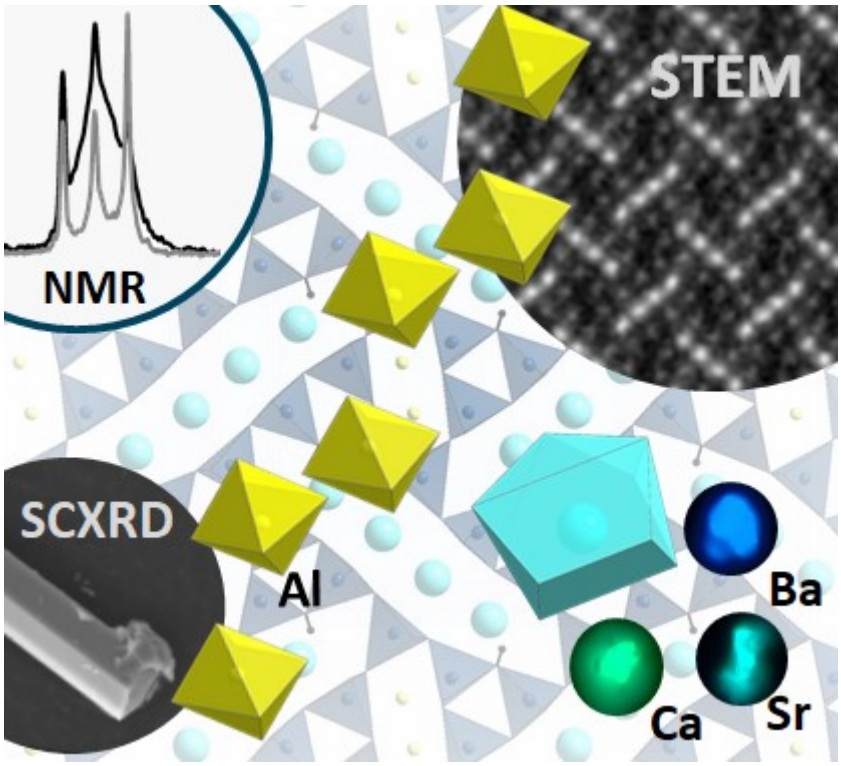

A series of isostructural imidonitridophosphates $AE_2AlP_8N_{15}(NH)$ (*AE* = Ca, Sr, Ba) was synthesized at high-pressure/high-temperature conditions (1400 °C and 5–9 GPa) from alkaline-earth metal nitrides or azides Ca_3N_2/$Sr(N_3)_2$/$Ba(N_3)_2$ and the binary nitrides AlN and P_3N_5. NH_4F served as a hydrogen source and mineralizing agent. The crystal structures were determined by single-crystal X-ray diffraction and feature a three-dimensional network of vertex-sharing PN_4 tetrahedra forming diverse-sized rings that are occupied by aluminum and alkaline-earth ions. These structures represent another example of nitridophosphate-based networks that simultaneously incorporate AlN_6 octahedra and alkaline-earth-centered polyhedra, with aluminum not participating in the tetrahedra network. They differ from previously reported ones by incorporating non-condensed octahedra instead of strongly condensed octahedra units and contribute to the diversity of multicationic nitridophosphate network structures. The results are supported by atomic resolution EDX mapping, solid-state NMR and FTIR measurements. Eu^{2+}-doped samples show strong luminescence with narrow emissions in the range of green to blue under UV excitation, marking another instance of Eu^{2+}-luminescence within imidonitridophosphates.

3.2. Introduction

The demand for environmentally friendly, energy-efficient, and cost-effective luminescent materials rises steadily.[1] Alkaline-earth-(*AE*)-containing nitridophosphates can offer many key characteristics crucial for phosphor-converted LED applications. One reason why they are so well suited is their diverse structural chemistry with tetrahedra-based networks and an easily changeable local environment of the alkaline-earth ions. They span the entire visible spectral range with only a handful of known compounds, and understanding the influence of structural parameters on materials properties not only allows the explanation of current characteristics but also helps to predict structure-property relationships.

Nitridophosphate networks can be characterized by their degree of condensation κ, which is defined by the atomic ratio of tetrahedra centers (P) to vertices (N) and range from non-condensed PN_4 tetrahedra (κ_{min} = ¼) to highly condensed networks with vertex- and edge-sharing tetrahedra (κ_{max} = 3/5 in P_3N_5).[2-3] Compounds with a degree of condensation $\kappa < 0.5$ exhibit structural motifs often comprising non-condensed units like non-condensed rings built up from vertex-sharing tetrahedra.[4-5] Single and double chains can differ in stretching factors and periodicity.[6-7] Structures with $0.3 \leq \kappa \leq 0.5$ can form column-type and condensed layer phosphate structures, and $\kappa > 0.5$ often results in layered structures and condensed three-dimensional networks, including a wide range of different-sized rings and channels.[8-12]

Upon doping with Eu^{2+}, three-dimensional network compounds can provide favorable properties like a small Stokes shift, low thermal quenching and high quantum efficiencies.[13] The local environment of the alkaline-earth ion and the activator ion, the symmetry, and the number of crystallographic sites may affect the number of emission maxima as well as their shape and position. High symmetry and a small number of sites are expected to result in favorable properties like a low number of emission maxima with a narrow-band emission. Different ligand atoms change the electron density between the activator ion and the ligand. Opting for oxonitridophosphates with a more red-shifted emission or incorporating halides can offer the flexibility to tune for specific emission regions.[14]

The cation ratio *CR* (ratio of counter cations to network cations) and the resulting changes in structure and physical properties are relatively disregarded aspects.[15] Cations that do not belong to the tetrahedra network but occupy positions that are unfavorable for activator ions are one

particular research focus. These additional cations may feature their own substructures, modifying the nitridophosphate-based network. Until now, only a few such cases have been studied. The structures range from non-condensed and edge-sharing Mg-centered octahedra in $MgSrP_3N_5O_2$ and $CaMg_2P_6N_{10}O_3$ to a highly condensed vertex- and edge-sharing substructure of Al-centered octahedra as found in $SrAl_5P_4N_{10}O_2F_3{:}Eu^{2+}$, the first representative of multicationic nitridophosphate-based structure containing an alkaline-earth element and aluminum.[15-17]

In this context, we present the synthesis and structural characterization of the isostructural multicationic imidonitrido-phosphates $AE_2AlP_8N_{15}(NH)$ (*AE* = Ca, Sr, Ba), which contain a PN_4 tetrahedra network that gives room to AlN_6 octahedra and *AE*-centered polyhedra.

3.3. Experimental Part

3.3.1. Preparation of Starting Materials

Alkaline-earth element azides $AE(N_3)_2$ (*AE* = Sr, Ba) were prepared by reaction of the respective alkaline-earth element carbonates ($SrCO_3$: Sigma Aldrich, 99.995%; $BaCO_3$: Grüssing, 99.8%) with in situ generated aqueous HN_3.[18] A solution of HN_3 is formed by passing an aqueous solution of NaN_3 (Acros Organics, 99%, extra pure) through a cation exchanger (Amberlyst 15). Formed HN_3 dropped into a suspension of the carbonate in water until the eluate showed a neutral pH value. Carbonate residues were filtered off, and the solvent was removed with a rotary evaporator (50 mbar, 40 °C). The products were obtained as colorless powders, recrystallized from acetone, and dried under vacuum. PXRD and FTIR spectroscopy confirmed the purity. Partially crystalline P_3N_5 was prepared following the synthesis of Stock et al..[19] A fused silica tube and silica boat were dried at 1273 K under dynamic vacuum (<10^{-3} bar), and P_4S_{10} (Sigma-Aldrich, 99.99%) was loaded in a constant flow of argon. The setup was flooded with dry ammonia (Air Liquide, 5.0) for 4 h. The reaction was carried out at 1123 K for 4 h before the furnace was cooled to room temperature with heating and cooling ramps of 5 K/min. The product was washed with diluted HCl and H_2O and yielded as an orange powder. PXRD and CHNS analysis confirmed its purity (C 0%, H 0%, N 42.69%, S 0%; expected C 0%, H 0%, N 42.98%, S 0%). Ca_3N_2 (Sigma Aldrich, 99.5%), AlN (abcr, grade B) and EuF_3 (Sigma Aldrich, 99.99%) were used as purchased.

3.3.2. Multianvil Synthesis

Eu-doped and undoped $AE_2AlP_8N_{15}(NH)$ (*AE* = Ca, Sr, Ba) were synthesized under high-pressure high-temperature conditions with T = 1400 °C, p = 5 GPa for Sr, Ba, and T = 1400 °C, p = 9 GPa for Ca using a 1000 t hydraulic press (Voggenreiter, Mainleus, Germany) with a modified Walker module. Details on the preparation and handling of the 1000 t Walker-type multianvil press are described in the literature.[20-23] The starting materials Ca_3N_2/$Sr(N_3)_2$/$Ba(N_3)_2$, AlN, P_3N_5, NH_4F, and if needed, EuF_3 as a doping agent (Table B.1) were thoroughly ground in an agate mortar in an Ar-filled glovebox (Unilab, MBraun, Garching, O_2<1 ppm, H_2O<0.1 ppm), transferred into a crucible of h-BN (HeBoSint® S100, Henze, Kempten, Germany) and sealed with a h-BN lid. For Sr- and Ba-containing samples: After sample insertion, the setup was compressed to 5 GPa and heated to 1400 °C within 60 minutes. The temperature was held constant for 300 minutes before cooling to

room temperature and slow decompression within 60 minutes. For Ca-containing samples: The setup was compressed to 9 GPa and heated to 1400 °C within 30 minutes. The temperature was held constant for 150 minutes before cooling and decompression within 30 minutes.

3.3.3. Powder X-Ray Diffraction

A powder diffractometer Stadi P (Stoe & Cie GmbH, Germany) with either a Cu- or Ag-Kα_1 radiation (λ = 1.54056 Å and 0.5595378 Å; Ge(111) single-crystal monochromator) with modified (parafocusing) Debye-Scherrer geometry and a MYTHEN 1K Si strip detector (Dectris Ltd., Baden, Switzerland) was used. Samples were finely ground and transferred into glass capillaries (Ø 0.3 mm, wall thickness 0.01 mm, Hilgenberg GmbH, Malsfeld, Germany). Powder diffraction patterns of $Ba_2AlP_8N_{15}(NH)$ were recorded with Ag-Kα_1 radiation at an angular range of 2θ = 3–37° and a step width of 0.015°. Powder diffraction patterns of $Ca_2AlP_8N_{15}(NH)$ and $Sr_2AlP_8N_{15}(NH)$ were recorded with Cu-Kα_1 radiation at an angular range of 2θ = 3–92° with a step width of 0.015°. TOPAS Academic 6.1 was used for Rietveld refinements, employing a fundamental parameter approach and a Chebyshev polynomial for background modeling.[24-25]

Temperature-dependent powder X-ray diffraction was carried out on a STOE StadiP diffractometer equipped with a high-temperature graphite furnace, an image plate position sensitive detector, Ag-Kα_1 radiation (λ = 0.5595378 Å) and a Ge(111) monochromator. Powder diffraction patterns were collected up to 900 °C with 50 °C increments.

3.3.4. Energy-Dispersive X-Ray Spectroscopy

Isolated crystals of the compounds were placed on a conducting carbon foil and coated with carbon. Secondary electron images were obtained with a FEI Helios NanoLab G3 DualBeam UC (FEI, USA).

3.3.5. Scanning Transmission Electron Microscopy

Samples were ground thoroughly in absolute ethanol and distributed on Cu grids covered with lacey carbon film (S-166-2, Plano GmbH, Germany). The grids were mounted in an analytical double-tilt holder (tilt ranges ±30°) and analysis was carried out with a Titan Themis 300 (FEI, USA) transmission electron microscope equipped with a Schottky type high-brightness electron gun (X-

FEG), a post-column filter (Enfinium ER-799, Gatan, USA), a spherical aberration (Cs) corrector (DCOR, CEOS, Germany), a camera system (US 1000XP, Gatan, Germany), a 4k × 4k FEI Ceta CMOS camera (FEI, USA) and a windowless 4-quadrant Super-X energy-dispersive X-ray spectroscopy detector. The system was operated at an acceleration voltage of 300 kV. Data processing and Fourier filtering were performed using Digital Micrograph (Fourier filtering), ProcessDiffraction7 (calculations of SAED patterns), jEMS (SAED simulations) and Velox (STEM images, EDX maps).[26-29]

3.3.6. Single-Crystal X-Ray Diffraction

A Bruker D8 Venture TXS diffractometer (rotating anode, Mo-Kα radiation, λ = 0.71073 Å, multilayer monochromator) was used to obtain single-crystal X-ray diffraction data of $Ba_2AlP_8N_{15}(NH):Eu^{2+}$ and $Ca_2AlP_8N_{15}(NH):Eu^{2+}$. For indexing, integration and semiempirical absorption correction, the program package APEX3 was used.[30]

Single-crystal diffraction data with synchrotron radiation were collected for $Sr_2AlP_8N_{15}(NH)$ at beamline ID11 (ESRF, France) at ambient conditions. Crystallites on TEM finder grids (S-160, Plano GmbH, Germany) were optically centered in the synchrotron beam (λ = 0.28820 Å) with a high-magnification telescope. Centering was optimized by fluorescence and diffraction scans utilizing a hexapod setup (Symétrie Hexapods Nanopos and PI-MARS P561 piezo stage). Data were collected using a Dectris Eiger2 X 4M CdTe detector. Indexing and integration were performed with the CrysAlis^{Pro} software package.[31] Semi-empirical absorption correction was done with SADABS.[32]

The structure solution was performed using direct methods (SHELXS) and refined against F^2 using full-matrix least-squares methods (SHELXL-2018).[33] Crystal structures were visualized using Diamond3.[34]

3.3.7. Bond Valence Sum Calculations

VaList was used to perform BVS calculations.[35-36] Vesta was used to perform CHARDI calculations.[37]

3.3.8. Madelung Part of Lattice Energy

The program MAPLE (Madelung part of lattice energy) was used to verify the assignment of nitrogen and oxygen to crystallographic layers.[38-39]

3.3.9. Solid-State Magic Angle Spinning NMR Spectroscopty

An Advance III 500 (Bruker, Karlsruhe) equipped with an 11.7 T magnet operating at 500.25 MHz ^1H frequency, and a commercial double resonance MAS probe was used to record solid-state MAS NMR spectra. The sample was ground and packed into a ZrO_2 rotor with an outer diameter of 2.5 mm. At 20 kHz spinning frequency, ^1H, ^{31}P and $^1H \rightarrow {}^{31}P$ spectra were recorded. The ^{27}Al spectrum was recorded at 10 kHz spinning frequency.

3.3.10. FTIR Spectroscopy

The Fourier transform technique on a Spectrum BX II spectrometer (PerkinElmer Waltham, MA, USA) with a DuraSampler ATR unit was used to obtain FTIR spectra. Data of the title compounds were obtained in the range of 650–4400 cm^{-1}.

3.3.11. Luminescence Measurements

Luminescence measurements of Eu^{2+}-doped $AE_2AlP_8N_{15}(NH)$ samples with *AE* = Ca, Sr, Ba were carried out on small particles in air. The spectra were obtained on a HORIBA Fluoromax4 spectrofluorimeter system, attached via optical fibers to an Olympus BX51 microscope. $Ca_2AlP_8N_{15}(NH):Eu^{2+}$ was measured with λ_{exc} = 420 and 450 nm, $Sr_2AlP_8N_{15}(NH):Eu^{2+}$ and $Ba_2AlP_8N_{15}(NH):Eu^{2+}$ with λ_{exc} = 400 nm. Emission spectra were recorded at room temperature with a step size of 2 nm and ranged from 400 to 800 nm.

3.4. Results and Discussion

3.4.1. Synthesis

Eu^{2+}-doped and undoped representatives of the imidonitridophosphates $AE_2AlP_8N_{15}(NH)$ (*AE* = Ca, Sr, Ba) were obtained by applying high-pressure high-temperature conditions (*T* = 1400 °C, *p* = 5 GPa for Sr and Ba, 9 GPa for Ca). The syntheses are assumed to follow the reaction equations (1) and (2). $AE(N_3)_2$ (*AE* = Sr, Ba) or Ca_3N_2, α-P_3N_5, AlN and NH_4F were used as starting materials (Table B.1). EuF_3 was used as an europium source, and NH_4F functions as a hydrogen source as well as a mineralizing agent. Further details of the multianvil setup are given in the Experimental Section.

$$6\ AE(N_3)_2 + 8\ P_3N_5 + 3\ AlN + NH_4F \rightarrow 3\ AE_2AlP_8N_{15}(NH) + 16\ N_2 + HF \quad (1)$$

$$2\ Ca_3N_2 + 8\ P_3N_5 + 3\ AlN + NH_4F \rightarrow 3\ Ca_2AlP_8N_{15}(NH) + HF \quad (2)$$

The title compounds are yielded as crystalline solids with a light-gray body color. They are stable towards air and moisture, and samples doped with Eu^{2+} show photoluminescence in the range of green to blue upon irradiation with UV light. Crystallites exhibit a rod-shaped morphology with lengths of up to 100 µm and widths of around 50 µm for $Ca_2AlP_8N_{15}(NH)$ and $Ba_2AlP_8N_{15}(NH)$ (Figure 3.1). Synthesis for $Sr_2AlP_8N_{15}(NH)$ yielded microcrystalline material.

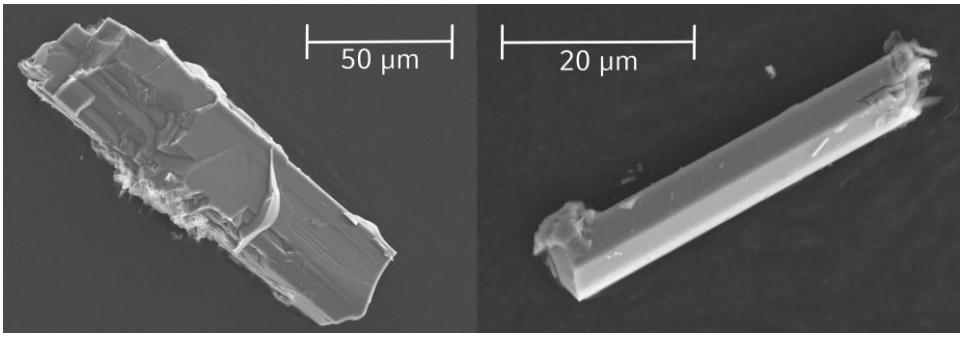

Figure 3.1. Secondary electron image of $Ca_2AlP_8N_{15}(NH):Eu^{2+}$ (left) and $Ba_2AlP_8N_{15}(NH):Eu^{2+}$ (right).

3.4.2. Crystal Structure Determination

The crystal structures of $AE_2AlP_8N_{15}(NH)$ (*AE* = Ca, Sr, Ba) were solved and refined from single-crystal X-ray diffraction (SCXRD) data in the orthorhombic space group *Pnma* (no. 62). Table 3.1 summarizes the details of the structure determinations. Wyckoff positions, atomic coordinates and displacement parameters are given in the Supporting Information (Tables B.2–B.7). A tilt series of selected area electron diffraction (SAED) patterns matches simulations and confirms unit cell metrics (Figure B.1). Pre-characterization of crystallites by transmission electron microscopy (TEM) made it possible to obtain single-crystal data of $Sr_2AlP_8N_{15}(NH)$ (Figure B.2). Crystals of around 2–3 µm in size were identified on TEM grids by energy dispersive X-ray (EDX) spectroscopy and SAED patterns, and SCXRD data were collected with micro-focused synchrotron radiation at the beamline ID11 of the ESRF (Grenoble, France).

Table 3.1. Crystallographic data of $AE_2AlP_8N_{15}(NH):Eu^{2+}$ (*AE* = Ca, Ba) and $Sr_2AlP_8N_{15}(NH)$.

formula	$Ca_{1.89}Eu_{0.11}AlP_8N_{15}(NH)$	$Sr_2AlP_8N_{15}(NH)$	$Ba_{1.89}Eu_{0.11}AlP_8N_{15}(NH)$
molar mass / g·mol^{-1}	592.85	675.13	776.21
crystal system		orthorhombic	
space group		*Pnma* (no. 62)	
lattice parameters / Å	*a* = 13.1482(4) *b* = 8.0446(3) *c* = 11.4981(4)	*a* = 13.261(3) *b* = 8.0610(16) *c* = 11.636(2)	*a* = 13.5546(2) *b* = 8.16370(10) *c* = 11.8541(2)
cell volume / Å^3	1216.18(7)	1243.9(4)	1311.72(3)
formula units / unit cell		4	
density / g·cm^{-3}	3.238	3.605	3.930
temperature / K	297(2)	293(2)	297(2)
absorption correction		semiempirical	
radiation	Mo-Kα (*λ* = 0.71073 Å)	synchrotron (*λ* = 0.2882 Å)	Mo-Kα (*λ* = 0.71073 Å)
µ / mm^{-1}	2.636	0.874	7.248
F(000)	1163.7	1288	1435.2
d_{min} / Å	0.6500	0.7000	0.6000
total no. of reflections	37804	18636	78015
independent reflections [I≥2σ(I) / all]	*2347 / 2429*	*1813 / 2001*	*3082 / 3345*
R_σ, R_{int}	0.0125, 0.0284	0.0342, 0.0623	0.0163, 0.0469
refined parameters	141	137	139
restraints		1	
GooF	1.343	1.079	1.117
R values [I≥2σ(I)]	*R*1 = 0.0263, *wR*2 = 0.0619	*R*1 = 0.0242, *wR*2 = 0.0584	*R*1 = 0.0151, *wR*2 = 0.0343
R values (all data)	*R*1 = 0.0273, *wR*2 = 0.0622	*R*1 = 0.0273, *wR*2 = 0.0596	*R*1 = 0.0177, *wR*2 = 0.0348
$\Delta\rho_{max}$, $\Delta\rho_{min}$ / e·Å^{-3}	0.683, −0.563	0.965, −0.734	1.147, −1.002

Rietveld refinements on powder X-ray diffraction (PXRD) data were used to analyze the phase compositions. No crystalline side phases are present for samples of $AE_2AlP_8N_{15}(NH)$ (*AE* = Sr, Ba), and $Ca_2AlP_8N_{15}(NH)$ is the main phase next to CaP_8N_{14} (Figures 3.2 and B.3–B.4). High-temperature PXRD on $Ba_2AlP_8N_{15}(NH)$ demonstrates stability up to at least 900 °C in air and shows only very little change in lattice parameters or cell volume (Figure B.5).

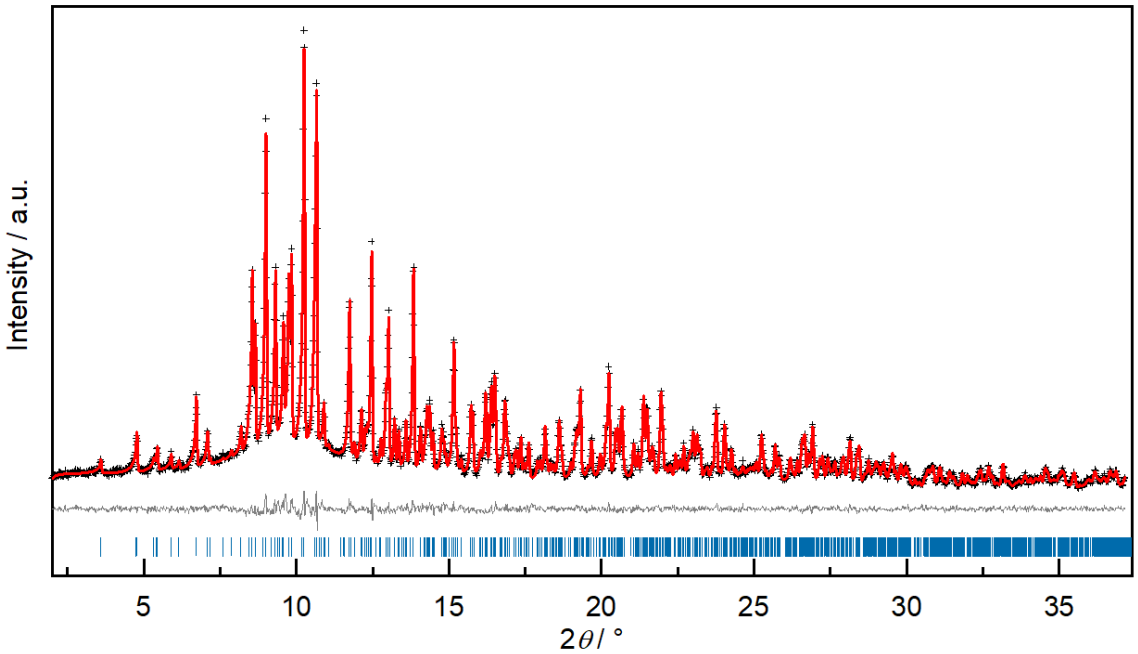

Figure 3.2. Rietveld refinement for $Ba_2AlP_8N_{15}(NH):Eu^{2+}$; observed (black data points) and calculated (red line) PXRD patterns, positions of Bragg reflections of $Ba_2AlP_8N_{15}(NH):Eu^{2+}$ (vertical blue bars), and difference profile (gray line); R_p = 0.035, R_{wp} = 0.048, R_{exp} = 0.016, R_{Bragg} = 0.019.

Lattice energy (MAPLE), bond valence sums (BVS) and charge distribution (CHARDI) calculations support the structure model (Tables B.8–B.11). They show the lowest “charge” for the N1 and N7 sites, indicating either hydrogen in their vicinity or a positional disorder of nitrogen and oxygen. The elemental compositions were analyzed by EDX spectroscopy (Table B.12), and crystals exemplarily used for electron microscopy analysis are shown in Figure B.6. Some EDX measurements show a significant oxygen peak, few cases even exceeding expected values of a possible N/O disorder, which could indicate a marked sensitivity to moisture. Slight compositional variations cannot be ruled out, and a phase width according to $AE_2AlP_8N_{15}(NH)_xO_{1-x}$ (x = 0–1) could be considered. However, magic angle spinning (MAS) NMR data show a clear signal in the ^1H and in the cross-polarized $^1H \rightarrow ^{31}P$ spectra, which are discussed in detail in the NMR section. FTIR data

of Sr and Ba compounds show weak but present absorption bands in the region of N–H stretching vibrations (Figure B.7), suggesting imide groups.[40] The position of H for all structures was determined from difference Fourier maps. The N1–H1 bond length was restrained at 0.90 Å, and the thermal displacement parameter of H1 was refined together with N1.

3.4.3. Structure Description

The structures consist of a three-dimensional network of vertex-sharing PN_4 tetrahedra incorporating channels occupied by Al^{3+} and AE^{2+} (*AE* = Ca, Sr, Ba) ions (Figure 3.3). The channels are created by six- and twelve-membered rings interconnected along *b*. The topology of the anionic network is described by the point symbol $\{3.4.5.6^2.7\}2\{3.6^5\}\{6^6\}$ as calculated using TOPOS.[41] The mineral paracelsian $BaAl_2Si_2O_8$ (Figure B.8) shows a similar structure with smaller four- and eight-membered rings, but this exact topology has not been found for tetrahedra networks so far.[42]

The anionic network is built up by four crystallographically distinct vertex-sharing PN_4 tetrahedra. Interatomic P–N distances and N–P–N angles vary between 1.592(2)–1.6627(16) Å and 98.99(11)–118.99(6)°, which is in good agreement with known nitrido-phosphates.[15-17] Bond lengths and bonding angles of the network do not change significantly when the polyhedra of the AEN_x-polyhedra (x = 8–10) increase in size from Ca to Ba. Figure 3.4 depicts all coordination polyhedra. An overview of interatomic distances and angles is provided in Tables B.12–B.15. The tetrahedra network contains rings condensed to channels running along *b*. These channels can be separated into void channels formed by rings of three vertex-sharing tetrahedra, channels formed by rings of six vertex-sharing tetrahedra occupied by Al^{3+} and channels formed by rings of twelve vertex-sharing tetrahedra occupied by AE^{2+}. These rings are interconnected along *b* by up- and downward pointing tetrahedra. Figure B.9 illustrates the different ring types and shows the additional rings along the columns. In the case of the six-membered rings, these are additional six-membered rings, and in the case of twelve-membered rings, additional four- and six-membered rings.

Alkaline-earth atoms occupy channels formed by condensed twelve-membered rings. Eight to ten nitrogen atoms coordinate two distinct crystallographic positions. The *AE*-centered polyhedra share vertices and edges. Interatomic *AE*–N distances are in agreement with the literature and slightly increase from 2.4933(16)–3.1545(17) Å for Ca, over 2.5894(19)–3.3476(19) Å for Sr to 2.7240(11)–3.3354(12) Å for Ba.[7, 10, 13] The *AE*1 site is coordinated by nine nitrogen atoms, and

the resulting polyhedron can be described as a monocapped distorted tetragonal prism. In the case of Ba and Sr, the *AE*2 site is coordinated by ten nitrogen atoms, and the resulting polyhedron can described as a distorted pentagonal prism. For the Ca2 site, partial BVS values indicate that only eight nitrogen atoms, instead of ten, contribute to strong bonds (Table B.9), resulting in 8-fold coordination and a dicapped distorted pentagonal prism. This coincides with, e.g., $BaCa_2P_6N_{12}$, in which Ca is 9-fold coordinated, and Ba is 12-fold coordinated.[43]

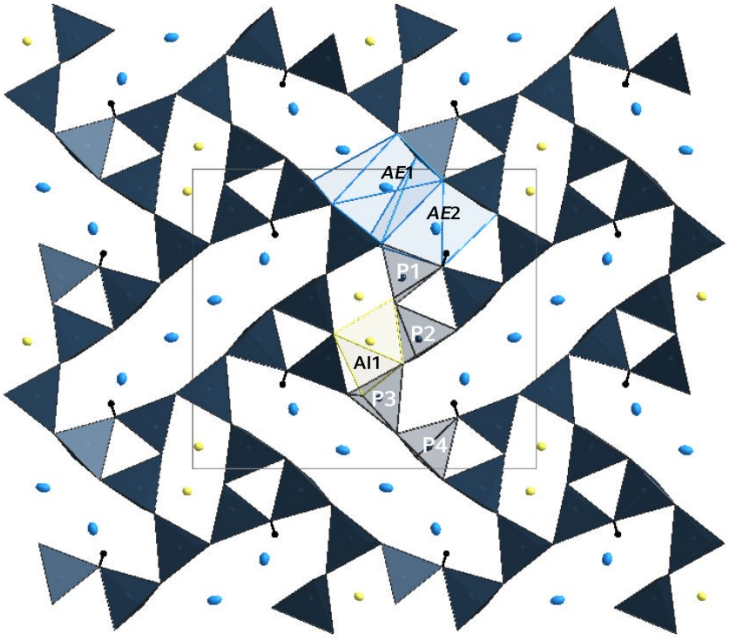

Figure 3.3. Projection of the crystal structure of $Ba_2AlP_8N_{15}(NH)$ along [010]. Ba bright blue, Al yellow and PN_4/$PN_3(NH)$ tetrahedra dark blue with H black. Cationic sites are partially labeled. Gray lines highlight the unit cell. The atoms are displayed with anisotropic displacement ellipsoids at 90% probability.

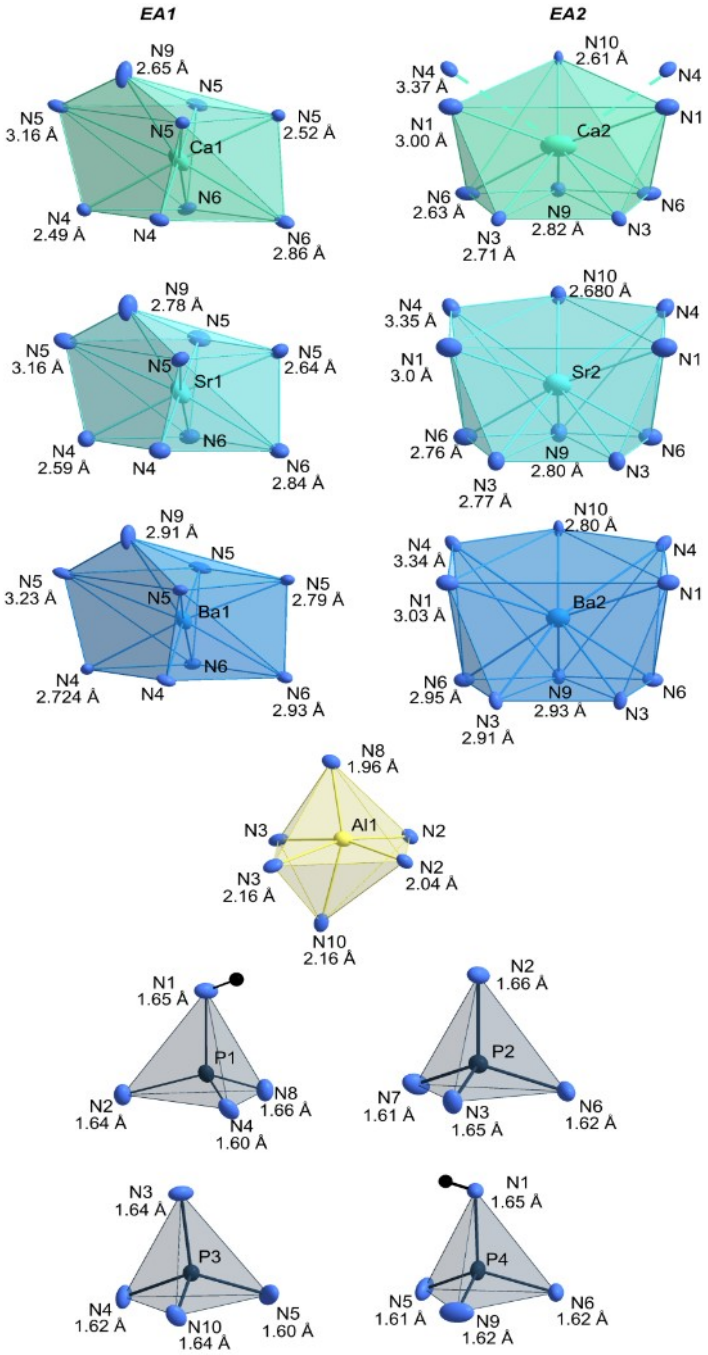

Figure 3.4. Coordination polyhedra around *AE*1, *AE*2 (*AE* = Ca, Sr, Ba), Al1 and P1–P4. Atoms are displayed with anisotropic displacement ellipsoids at 90% probability; coordination spheres of *AE*1 (CN = 9) and *AE*2 (CN = 8 for Ca and 10 for Sr, Ba). Polyhedra and interatomic distances for Al1 and P1–P4 are given for $Ba_2AlP_8N_{15}(NH)$. All interatomic distances with standard deviations are given in the Tables B.10–B.12.

Aluminum atoms occupy the smaller channels formed by six-membered rings. The resulting AlN_6 octahedra are not connected to each other but share edges and vertices with PN_4 tetrahedra (Figure B.10). Al^{3+} ions are slightly displaced from the center of the octahedra, which results in Al–N8 being the shortest and Al–N10 the longest bond lengths. Interatomic Al–N distances range between 1.948(2)–2.151(2) Å (Ca), 1.936(3)–2.136(3) Å (Sr) and 1.9565(17)–2.1658(17) Å (Ba). As the size of the alkaline-earth polyhedra increases, the octahedra slightly increase in volume due to the expansion of the network.

The structure model has been validated by scanning transmission electron microscopy high-angle annular dark-field (STEM-HAADF) images with a *Z*-contrast according to Z^2.[44] The established structure agrees well with STEM-HAADF images obtained along the zone axes [010] and [101] (Figure 3.5 upper parts). The projection along [010] shows distinct intensities for the alkaline-earth ions, and the positions of all phosphorus ions are resolved. Aluminum is not visible due to its low atomic fraction, the large *Z*-contrast between Ba (Z = 56) and Al (Z = 13), and the low number of atoms within the Al columns. However, STEM-EDX maps along the same projection reveal aluminum in the anticipated positions (Figure 3.5 lower parts). Regions rich in respective elements are clearly separated from others in both directions, and a possible disorder of Al and P atoms on either octahedral or tetrahedral positions can be ruled out. Enlarged versions and raw EDX spectra are given in the Figures B.12–B.15.

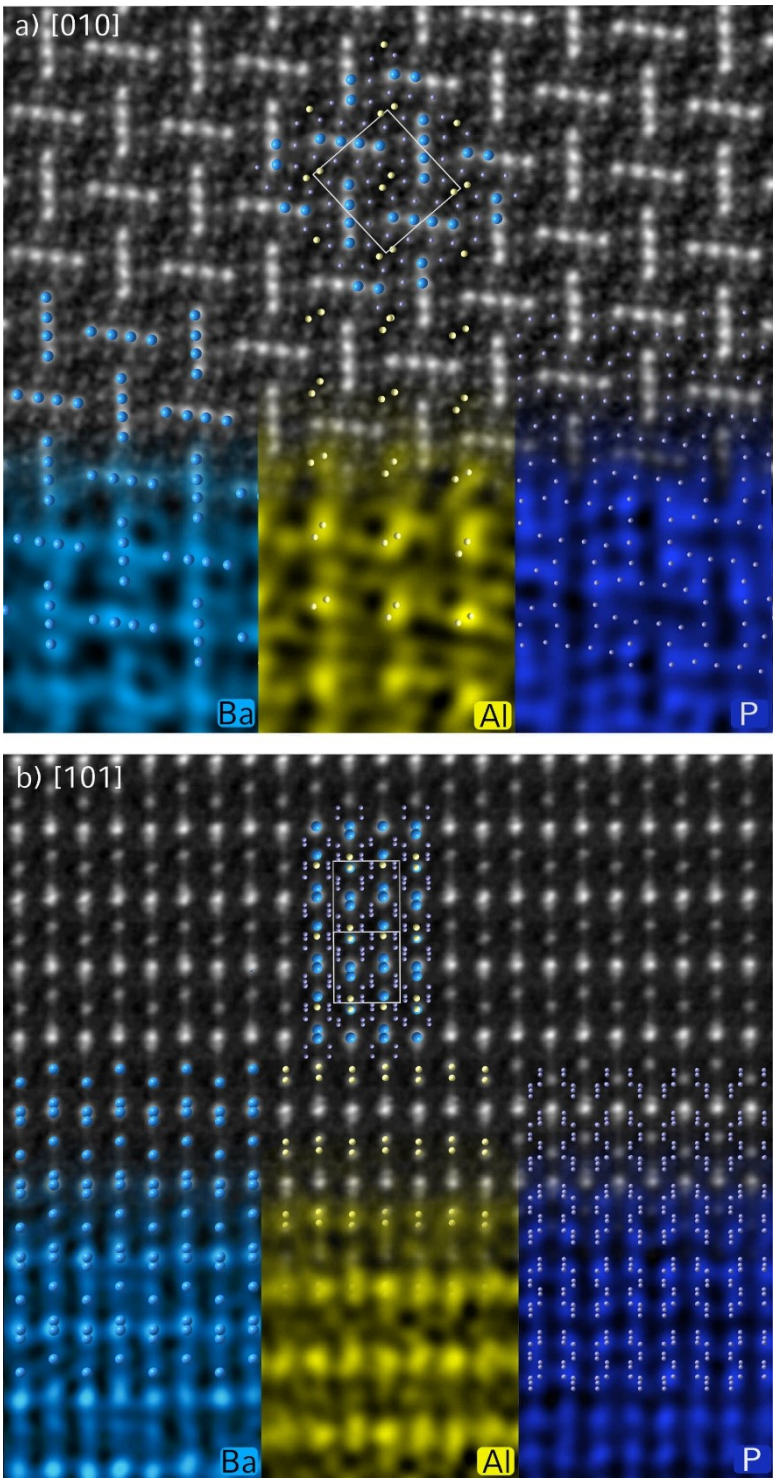

Figure 3.5. STEM-EDX maps of $Ba_2AlP_8N_{15}(NH)$ along **a)** [010] and **b)** [010]; STEM-HAADF image (top) with structure overlay (middle, Ba bright blue, Al yellow, P pale blue) and corresponding EDX maps (bottom); the unit cell is shown in the insert in light gray. Enlarged versions are shown in the Supporting Information.

3.4.4. Solid-State NMR

^{27}Al, ^{1}H, ^{31}P and cross-polarized $^{1}H \rightarrow {}^{31}P$ MAS NMR spectra of $Ba_2AlP_8N_{15}(NH)$ and ^{1}H MAS NMR spectra of $Sr_2AlP_8N_{15}(NH)$ were measured (Figure 3.6). The resonance line of the central transition in the ^{27}Al (spin $I = {}^{5}/_{2}$) NMR spectrum shows one Al signal centered around δ = 5.4 ppm (Figure 3.6 a). A narrow signal indicates a highly symmetrical position with low quadrupolar interaction, and the shift is in the range of octahedrally N-coordinated Al reported in the literature.[11, 45] Each of the solid-state ^{1}H NMR spectra (Figure 3.6 b) features a peak attributable to the imide group (δ = 6.5 ppm), agreeing with literature values.[46] The additional signal at δ = 7.5 ppm could be attributed to NH_4^+, presumably from an unknown secondary phase.[46] It could not be unambiguously clarified whether the signal at δ = 1.2 ppm in both measurements originates from the target compound or an unknown secondary phase. The ^{31}P spectrum shows three signals at δ = 9.88, –3.42 and –17.11 ppm with an estimated integral ratio of 1:1:2 (Figure 3.6 c). This is in the typical range for tetrahedrally N-coordinated P, as observed in, e.g., AlP_6N_{11} and $AlP_6O_{3x}(NH)_{3-x}N_9$.[11, 47] The intensity distribution is consistent with four crystallographically independent P sites when two P sites have a similar chemical environment. This leads to a signal overlap at –17.11 ppm with a roughly doubled intensity. To confirm the proximity of H to the P atoms, magnetization was transferred from ^{1}H to ^{31}P. The presence of three signals in cross-polarized experiments with δ = 9.9, –3.5, –17.3 ppm indicates the vicinity of H to at least three P atom sites. They align with the phosphorus signals present in the ^{31}P measurement. This supports the assumption of an imido group in the structure and the localization of H bound to N1, as this position enables spatial proximity to all P sites.

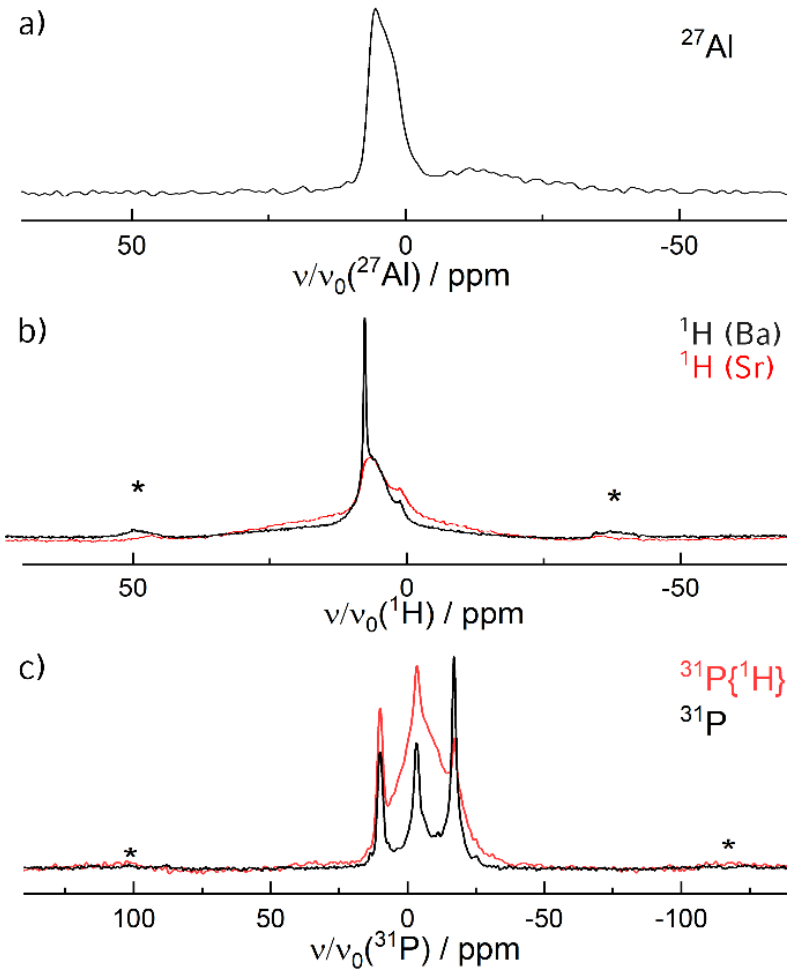

Figure 3.6. Solid-state MAS NMR spectra of $Ba_2AlP_8N_{15}$(NH); **a)** One signal in the ^{27}Al spectrum (10 kHz); **b)** ^{1}H spectra (both 20 kHz) of $Ba_2AlP_8N_{15}$(NH) (black) and $Sr_2AlP_8N_{15}$(NH) (red), two signals appear in both measurements and one high-intensity signal only appears in the $Ba_2AlP_8N_{15}$(NH) spectrum; latter may originate in a NH_4^+ containing side phase; **c)** Three signals in the ^{31}P spectrum (black) with an estimated integral ratio 1:1:2 and three overlapping signals in the ^{1}H→^{31}P spectrum (both 20 kHz), showing a coupling of H to at least three P sites; sidebands are marked with asterisks.

3.4.5. Luminescence Measurements

Eu^{2+}-doped samples of $AE_2AlP_8N_{15}$(NH) (*AE* = Ca, Sr, Ba) (~5 mol% Eu^{2+} with respect to the *AE* content) can be excited by near-UV to blue light, showing strong luminescence with narrow emissions in the visible spectral region (Figure 3.7, unsmoothed spectra Figure B.16). The emission curve of $Ca_2AlP_8N_{15}$(NH):Eu^{2+} was extrapolated using Savitzky-Golay-Filter to enable a comparison of the emission spectra. Excitation at 400 nm (*AE* = Ba, Sr) and 450 nm (*AE* = Ca) results in blue to green luminescence and one emission band for all compounds ($Ca_2AlP_8N_{15}$(NH):Eu^{2+} λ_{max} =

512 nm, *fwhm* = 54 nm / 2018 cm^{-1}; $Sr_2AlP_8N_{15}(NH):Eu^{2+}$: λ_{max} = 496 nm, *fwhm* = 46 nm / 1859 cm^{-1}; $Ba_2AlP_8N_{15}(NH):Eu^{2+}$: λ_{max} = 474 nm, *fwhm* = 38 nm / 1666 cm^{-1}). Based on the ionic radius of Eu^{2+}, only the *AE* sites are considered because the octahedrally coordinated Al^{3+} site and the tetrahedrally coordinated P^{5+} sites are not suitable for Eu^{2+} due to their much smaller size (ionic radii P^{5+} 17 pm, Al^{3+} 53.5 pm, Ca^{2+}: 112–123 pm, Sr^{2+}: 131–136 pm, Ba^{2+}: 147–152 pm, Eu^{2+}: 125–135 pm).[48] In general, the luminescence of Eu^{2+}-doped compounds strongly depends on the immediate environment of the activator site. The luminescence series of the three compounds shows a strong dependence on AE^{2+}–N distances. An excitation of $Ca_2AlP_8N_{15}(NH):Eu^{2+}$ at 420 nm shows a smaller second band with a maximum at 455 nm (Figure B.17). Due to the high chemical similarity of the two Ca sites (polyhedral volume Ca1 ≈ 35.4 $Å^3$, Ca2 ≈ 31.7 $Å^3$), we assume both sites were doped. Comparing the distances between the nearest ligands of the two Ca sites, the N atoms coordinate closer to Ca1 than to Ca2 ($d_{Ca1–N4}$: 2.493(2) Å, $d_{Ca2–N10}$: 2.608(2) Å) and the average Ca–N distances are shorter for Ca1 ($d_{Ø}$Ca1–N: 2.744 Å, $d_{Ø}$Ca2–N: 2.762 Å). Shorter distances result in an increase in the nephelauxetic effect, and the red-shifted band with a maximum at λ_{max} = 516 nm is likely caused by doping of the Ca1 site, whereas the second band with a maximum at around 455 nm should result from doping of the Ca2 site. The observation of the second band can help to explain the observed luminescence of the other two compounds. The observed emission bands of $AE_2AlP_8N_{15}(NH):Eu^{2+}$ (*AE* = Sr, Ba) could originate from doping of the *AE*1 site, as well, whereas possible further emission bands lie within the UV range and cannot be detected with the measurement setup used. This is consistent with the narrow band emission of $Ba_2AlP_8N_{15}(NH):Eu^{2+}$, compared to similar Ba compounds, which contain only one Ba site as well, such as $BaP_8N_{14}:Eu^{2+}$, $BaP_6N_{11}NH:Eu^{2+}$ (λ_{em} = 417/460 nm, *fwhm* = 2075/2423 cm^{-1}).[10, 49] Due to the very similar ionic radii of Sr^{2+} and Eu^{2+} (Sr^{2+}: 131–136 pm, Eu^{2+}: 125–135 pm), it is possible that the emission maximum nevertheless originates from doping of both sites, but our results agree with findings in the literature, which describe that Eu^{2+} preferentially occupies sites <40 $Å^3$ (Sr1 ≈ 37.8 $Å^3$, Sr2 ≈ 43.2 $Å^3$).[50] Theoretical spectroscopy studies could be made to verify these results further.[51]

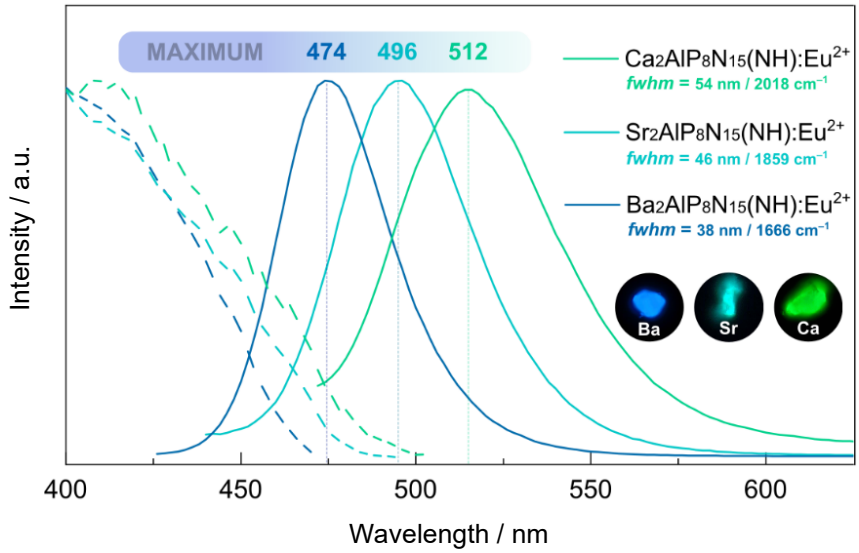

Figure 3.7. Single particle luminescence spectra of $AE_2AlP_8N_{15}(NH):Eu^{2+}$ (AE = Ca, Sr, Ba). Normalized excitation spectra (left) (Ca λ_{exc} = 450 nm, Sr/Ba λ_{exc} = 400 nm) and emission spectra (middle) for Ca (green), Sr (cyan), Ba (blue); insert: photograph of luminescent particles (λ_{exc}= 420 nm).

3.5. Conclusion

The isostructural compounds $AE_2AlP_8N_{15}(NH)$ with *AE* = Ca, Sr, Ba were obtained by NH_4F-mediated HP/HT syntheses. Their crystal structures were determined by single-crystal X-ray diffraction. Electron microscopy, EDX mapping with atomic resolution, and solid-state NMR studies agree with the structure model. The non-condensed Al-centered octahedra represent a structural motif that differs strongly from other nitridophosphate-based compounds, e.g., $SrAl_5P_4N_{10}O_2F_3$, which forms a highly condensed substructure of edge-sharing Al-centered octahedra. The compounds show emission from blue to green upon doping with Eu^{2+} and belong to the small group of imidonitridophosphates exhibiting luminescent properties. We expect that research on further modifying the nitridophosphate network with additional cations not participating in the tetrahedra network, e.g., Mg^{2+} ions, opens up the possibility to access a number of stable compounds with diverse structural motifs featuring interesting luminescent properties. Plus, a possible site-selectivity of doping due to differences in charge and ionic radii of Al^{3+} and AE^{2+} makes it possible to modify the luminescence not only by metal–ligand distances or coordination geometry but also by choice of the emitter (e.g., Cr^{3+} on Al^{3+} sites versus Eu^{2+} on AE^{2+} sites).[52] This makes research on multicationic phosphors, especially aluminum-containing nitrides and nitridophosphates, a promising field worth investigating.

Supporting

Deposition number 2261405 contains the supplementary crystallographic data for this paper. These data are provided free of charge by the joint Cambridge Crystallographic Data Centre and Fachinformationszentrum Karlsruhe Access Structures service.

The data that support the findings of this study are available in the Supporting Information. The authors have cited additional references within the Supporting Information.[53-60]

Acknowledgements

Financial support by the Deutsche Forschungsgemeinschaft DFG (projects SCHN 377/18-1 and OE 513/6-1) is gratefully acknowledged. The authors thank Dr. Peter Mayer and Christian Minke for single-crystal data collection and SEM measurements, respectively (all at LMU Munich) and Dr. P. Strobel and Dr. P. J. Schmidt (Lumileds Phosphor Center Aachen) for luminescence measurements. We are thankful for beamtime at the ESRF for the acquisition of microfocused single-crystal diffraction data (project CH-5663).

3.6. References

[1] H. A. Höppe, *Angew. Chem.* **2009,** *121*, 3626–3636; *Angew. Chem. Int. Ed.* **2009**, *48*, 3572–3582.

[2] A. Marchuk, P. Schultz, C. Hoch, O. Oeckler, W. Schnick, *Inorg. Chem.* **2016,** *55*, 974−982.

[3] S. Horstmann, E. Irran, W. Schnick, *Angew. Chem.* **1997,** *109*, 1938–1940; *Angew. Chem. Int. Ed.* **1997**, *36*, 1873–1875.

[4] E. M. Bertschler, R. Niklaus, W. Schnick, *Chem. Eur. J.* **2017,** *23*, 9592–9599.

[5] J. Liu, P. S. Whitfield, M. R. Saccomanno, S.-H. Bo, E. Hu, X. Yu, J. Bai, C. P. Grey, X.-Q. Yang, P. G. Khalifah, *J. Am. Chem. Soc.* **2017,** *139*, 9192–9202.

[6] V. Schultz-Coulon, W. Schnick, *Z. Anorg. Allg. Chem.* **1997,** *623*, 69–74.

[7] M. Mallmann, S. Wendl, P. Strobel, P. J. Schmidt, W. Schnick, *Chem. Eur. J.* **2020,** *26*, 6257–6263.

[8] E. Mugnaioli, S. J. Sedlmaier, O. Oeckler, U. Kolb, W. Schnick, *Eur. J. Inorg. Chem.* **2012,** *121*, 121–125.

[9] S. J. Sedlmaier, E. Mugnaioli, O. Oeckler, U. Kolb, W. Schnick, *Chem. Eur. J.* **2011,** *17*, 11258–11265.

[10] S. Wendl, L. Eisenburger, P. Strobel, D. Günther, J. P. Wright, P. J. Schmidt, O. Oeckler, W. Schnick, *Chem. Eur. J.* **2020,** *26*, 7292–7298.

[11] S. J. Ambach, M. M. Pointner, S. Falkai, C. Paulmann, O. Oeckler, W. Schnick, *Angew. Chem.* **2023**, e202303580; *Angew. Chem. Int. Ed.* **2023**, e202303580.

[12] S. D. Kloß, L. Neudert, M. Döblinger, M. Nentwig, O. Oeckler, W. Schnick, *J. Am. Chem. Soc.* **2017,** *139*, 12724–12735.

[13] A. Marchuk, S. Wendl, N. Imamovic, F. Tambornino, D. Wiechert, P. J. Schmidt, W. Schnick, *Chem. Mater.* **2015,** *27*, 6432–6441.

[14] A. Marchuk, W. Schnick, *Angew. Chem.* **2015,** *127*, 2413–2417; *Angew. Chem. Int. Ed.* **2015**, *54*, 2383–2387.

[15] R. M. Pritzl, N. Prinz, P. Strobel, P. J. Schmidt, D. Johrendt, W. Schnick, *Chem. Eur. J.* **2023**, e202301218.

[16] A. Marchuk, L. Neudert, O. Oeckler, W. Schnick, *Eur. J. Inorg. Chem.* **2014,** *2014*, 3427–3434.

[17] M. M. Pointner, O. Oeckler, W. Schnick, *Chem. Eur. J.* **2023**, e202301960.

[18] R. Suhrmann, K. Clusius, *Z. Anorg. Allg. Chem.* **1926,** *152*, 52–58.

[19] A. Stock, H. Grüneberg, *Ber. Dtsch. Chem. Ges.* **1907,** *40*, 2573–2578.

[20] D. Rubie, *Phase Transitions* **1999,** *68*, 431–451.

[21] H. Huppertz, *Z. Kristallogr. – Cryst. Mater.* **2004,** *219*, 330–338.

[22] D. Walker, *Am. Mineral.* **1991,** *76*, 1092–1100.

[23] D. Walker, M. Carpenter, C. Hitch, *Am. Mineral.* **1990,** *75*, 1020–1028.

[24] A. Coelho, TOPAS Academic version 6.1, Coelho Software, Brisbane (Australia), **2007**.

[25] H. M. Rietveld, *J. Appl. Crystallogr.* **1969,** *2*, 65–71.

[26] I. Gatan, DigitalMicrograph, version 3.6.5, Pleasanton (California, USA), **1999**.

[27] J. L. Lábár, *Ultramicroscopy* **2005,** *103*, 237–249.

[28] J. P. A. Stadelmann, jEMS software package, version 3.60907U2011, Saas-Fee (Switzerland), **2008**.

[29] Thermo Fisher Scientific, Velox, version 2.14.0.703, Waltham (Massachusetts, USA), **2021**.

[30] Bruker-AXS, APEX3, version 2016.5-0, Karlsruhe (Germany), **2001**.

[31] O. D. Rigaku, CrysAlis^{Pro}, version 171.42.102a, Yarnton, Oxfordshire (England), **2017**.

[32] G. M. Sheldrick, *SADABS, v.2: Multi-Scan Absorption Correction*; Bruker-AXS, Billerica, MA, **2012**.

[33] G. M. Sheldrick, *Acta Crystallogr. Sect. A* **2018**, *71*, 112–122.

[34] K. Brandenburg, Diamond, version 3.2k, Bonn (Germany), **1997–2014**.

[35] A. S. Wills, VaList – A bond valence calculation and analysis program, version 4.0.7, University College London, London (England), **1998–2010**.

[36] N. E. Brese, M. O'Keeffe, *Acta Crystallogr. Sect. B* **1991,** *47*, 192–197.

[37] K. Momma, F. Izumi, *J. Appl. Crystallogr.* **2011,** *44*, 1272–1276.

[38] R. Hoppe, *Angew. Chem.* **1970,** *82*, 7–16; *Angew. Chem. Int. Ed.* **1970**, *9*, 25–34.

[39] R. Hoppe, *Angew. Chem.* **1966,** *78*, 52–63; *Angew. Chem. Int. Ed.* **1966**, *5*, 95–106.

[40] K. Nakamoto, *Infrared and Raman spectra of inorganic and coordination compounds, part B: applications in coordination, organometallic, and bioinorganic chemistry*, John Wiley & Sons, **2009**.

[41] V. A. Blatov, A. P. Shevchenko, D. M. Proserpio, *Cryst. Growth Des.* **2014,** *14*, 3576–3586.

[42] J. Smith, *Acta Crystallogr.* **1953,** *6*, 613−620.

[43] F. Karau, W. Schnick, *Z. Anorg. Allg. Chem.* **2006,** *632*, 231–237.

[44] S. Pennycook, *Annu. Rev. Mater. Sc.* **1992,** *22*, 171–195.

[45] K. Keller, E. Brendler, S. Schermler, C. Röder, G. Heide, J. Kortus, E. Kroke, *J. Phys. Chem. C* **2015**, *119*, 12581–12588.

[46] A. Marchuk, V. R. Celinski, J. Schmedt auf der Günne, W. Schnick, *Chem. Eur. J.* **2015**, *21*, 5836–5842.

[47] L. Neudert, F. Heinke, T. Bräuniger, F. J. Pucher, G. B. Vaughan, O. Oeckler, W. Schnick, *Chem. Commun.* **2017,** *53*, 2709–2712.

[48] R. D. Shannon, *Acta Crystallogr. Sect. A* **1976,** *32*, 751–767.

[49] S. Wendl, L. Eisenburger, M. Zipkat, D. Günther, J. P. Wright, P. J. Schmidt, O. Oeckler, W. Schnick, *Chem. Eur. J.* **2020,** *26*, 5010–5016.

[50] M.-H. Fang, C. O. M. Mariano, P.-Y. Chen, S.-F. Hu, R. S. Liu, *Chem. Mater*. **2020**, *32*, 1748–1759.

[51] R. Shafei, P. Strobel, P. J. Schmidt, D. Maganas, W. Schnick, F. Neese, *Phys. Chem. Chem. Phys.* **2024**, *26*, 6277–6291.

[52] E. O'Brannon III, Q. Williams, *Am. Mineral.* **2019**, *104*, 1656–1662.

[53] K. Landskron, PhD thesis, Ludwig-Maximilians-Universität (Germany), **2001**.

[54] P. Pust, A. S. Wochnik, E. Baumann, P. J. Schmidt, D. Wiechert, C. Scheu, W. Schnick, *Chem. Mater.* **2014,** *26*, 3544–3549.

[55] M. Ludwig, R. Niewa, R. Kniep, *Z. Naturforsch. B* **1999,** *54*, 461–465.

[56] C. Hecht, F. Stadler, P. J. Schmidt, J. r. S. auf der Günne, V. Baumann, W. Schnick, *Chem. Mater.* **2009,** *21*, 1595–1601.

[57] J. A. Kechele, O. Oeckler, F. Stadler, W. Schnick, *Solid State Sci.* **2009,** *11*, 537–543.

[58] K. Horky, W. Schnick, *Eur. J. Inorg. Chem.* **2017,** *2017*, 1100–1106.

[59] T. Schlieper, W. Milius, W. Schnick, *Z. Anorg. Allg. Chem,* **1995,** *621*, 1380–1384.

[60] P. Strobel, R. Niklaus, P. J. Schmidt, W. Schnick, *Chem. Eur. J.* **2018,** *24*, 12678–12685.

Chapter 4

$Cr_{5.7}Si_{2.3}P_8N_{24}$ – A Chromium(+IV) Nitridosilicate Phosphate with Amphibole-Type Structure

Monika M. Pointner, Katherine R. Fisher, Martin Weidemann, Florian Wolf, Jonathan Wright, Eleanor Lawrence Bright, Carlotta Giacobbe, Oliver Oeckler,* and Wolfgang Schnick*

published in: *Angew. Chem.* **2024**, *136*, e202401421, DOI: 10.1002/anie.202401421.

published in: *Angew. Chem. Int. Ed.* **2024**, *63*, e202401421, DOI: 10.1002/anie.202401421.

4.1. Abstract

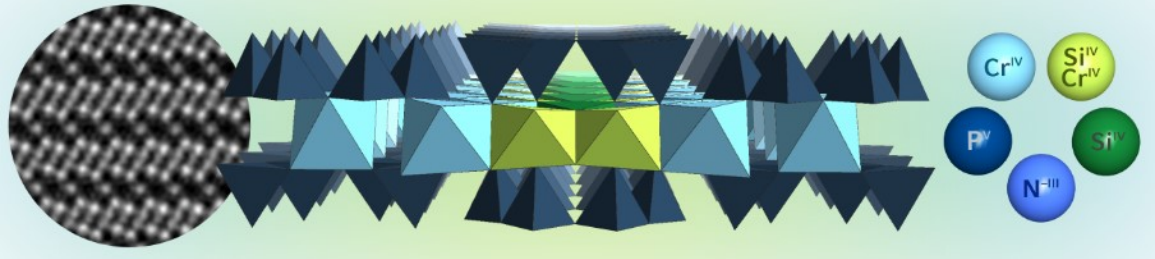

The first nitridic analog of an amphibole mineral, the quaternary nitridosilicate phosphate $Cr_{5.7}Si_{2.3}P_8N_{24}$ was synthesized under high-pressure high-temperature conditions at 1400 °C and 12 GPa from the binary nitrides Cr_2N, Si_3N_4 and P_3N_5, using NH_4N_3 and NH_4F as additional nitrogen source and mineralizing agent, respectively. The crystal structure was elucidated by single-crystal X-ray diffraction with microfocused synchrotron radiation (*C*2/*m,* a = 9.6002(19), b = 17.107(3), c = 4.8530(10) Å, *β* = 109.65(3)°). The elemental composition was analyzed by energy dispersive X-ray spectroscopy. The structure consists of vertex-sharing PN_4 tetrahedra forming zweier double chains and edge-sharing (Si,Cr)-centered octahedra forming separated ribbons. Atomic resolution scanning transmission electron microscopy shows ordered Si and Cr sites next to a disordered Si/Cr site. Optical spectroscopy indicate a band gap of 2.1 eV. Susceptibility measurements show paramagnetic behavior and support the oxidation state Cr^{+IV}, which is confirmed by EPR. The comprehensive analysis expands the field of Cr-N chemistry and provides access to a nitride analog of one of the most prevalent silicate structures.

4.2. Introduction

Silicates are known for their extensive structural diversity that ranges from individual SiO_4 tetrahedra, over chains and sheets to complex network structures. The abundance of Si and O in terms of total mass is the reason why the group of silicates constitutes the majority of the earth's crust but beyond that, the reason why silicates are the mineral group with the most known number of phases is the adaptability of SiO_4 tetrahedra to form various condensation patters.[1] The family of silicates includes amphibole minerals, whose name, first given by René J. Haüy in 1801, aims for their diversity in composition and appearance. Like all silicate minerals, the basic building blocks are silicate tetrahedra, which here are condensed into $[Si_4O_{11}]^{6-}$ double chains. Their microscopic and macroscopic properties originate from the atomic arrangement often resulting in a fiber-like structure. The main characteristic properties of these fibers are chemical inertia and thermal, electrical and sound insulation, leading to several industrial products that include insulation materials for construction, as well as brake linings and pads. Throughout most of the 20th century, amphiboles were commonly used worldwide as a building material and manufactured into approximately 3,000 products by the 1960s and the estimated consumption still stood at roughly $2 \cdot 10^6$ tons in 2010.[2]

Nitridophosphates have attracted significant interest due to the isoelectronic relation of Si/O and P/N. Nitridophosphate structures are often related to those of silicates resulting in similar motifs, primarily based on PN_4 tetrahedra. The close relation between silicates and nitridophosphates becomes most evident in structures that do not only contain the same motifs but feature the same topology. The recently discovered mica and paracelsian counterparts $AESi_3P_4N_{10}(NH)_2$ (*AE* = Mg, Ca, Sr) and $LiNdP_4N_8$, respectively, represent such close analogs.[3-4] Reactions under high-pressure high-temperature (HP/HT) conditions made their discovery possible, however, the synthesis of nitridophosphates has to overcome some challenges. Their formation is unfavorable in the presence of oxygen due to the preferred formation of oxides. A key precursor for most nitridophosphate syntheses is P_3N_5, which has a decomposition temperature of 850 °C. Yet, many easily accessible binary nitrides are inert up to higher temperatures. Further complications include the reduction of P^{+V} to lower oxidation states and the favored formation of stable metal phosphides. This becomes especially prominent in the synthesis of transition metal (*TM*) nitridophosphates with higher oxidation states of the *TM.* A HP/HT approach has successfully addressed these challenges.

Furthermore, the utilization of mineralizers has made compound classes accessible that were previously unattainable even by HP/HT conditions. NH_4F-mediated synthesis may exploit the fluorophily of Si as known from industrial processes of etching with HF. This strategy, performed at pressures in the GPa range and temperatures exceeding 1000 °C provides thermal energy for reactions of P_3N_5 with Si_3N_4 or stable refractory *TM* nitrides. This synthetic pathway not only yielded the above mentioned mica analogs but resulted in the formation of mixed nitridosilicate phosphates and *TM* nitridophosphates.[3, 5-6]

4.3. Experimental Part

4.3.1. Preparation of Starting Materials

For the synthesis of P_3N_5, a fused silica tube and silica boat were dried at 1273 K under dynamic vacuum (<10^{-3} bar). P_4S_{10} (Sigma-Aldrich, 99.99%) was loaded in a constant flow of argon and the setup was saturated with dry ammonia (Air Liquide, 5.0) for 4 h.[7] The reaction was carried out at 1123 K for 4 h in a constant flow of ammonia. The furnace was cooled to room temperature (heating and cooling ramp of 5 K/min), and the product was then washed with diluted HCl and H_2O. The product was obtained as a light orange powder. PXRD and CHNS analysis confirmed its purity: calcd. C 0%, H 0%, N 42.98%, *S 0*%, exp. C 0%, H 0%, N 42.69%, S 0%.

The azide NH_4N_3 was prepared according to the literature.[8] CrN/CrN_2 (Alfa Aesar), amorphous Si_3N_4 (UBE, SNA-00) and NH_4F (Sigma Aldrich, ≥98%) were used as purchased. CrN/Cr_2N was claimed to be a mixture of Cr_2N and CrN by the manufacturer, however, PXRD indicates no CrN but only Cr_2N as the main phase.

4.3.2. Multianvil Synthesis

$Cr_{5.7}Si_{2.3}P_8N_{24}$ was synthesized under high-pressure high-temperature conditions (T = 1400 °C, p = 12 GPa) using a 1000 t hydraulic press (Voggenreiter, Mainleus, Germany) with a modified Walker module. Stoichiometric amounts of the starting materials (Table C.1) were mixed in an agate mortar in an Ar-filled glovebox (Unilab, MBraun, Garching, O_2 < 1 ppm, H_2O < 0.1 ppm) and cautiously pressed into a crucible of h-BN (HeBoSint® S100, Henze, Kempten, Germany), which is sealed with an h-BN lid. The crucible was centered in two graphite tubes (furnace) and a ZrO_2 sleeve (insulator, Cesima Ceramics, Wust-Fischbeck, Germany) using MgO spacers (Cesima Ceramics, Wust-Fischbeck, Germany) at top and bottom. The sample was placed in a pierced octahedron (7% Cr_2O_3 doped MgO, 18 mm edge length, Ceramic Substrates & Components Ltd., Isle of Wright, UK) and contacted by molybdenum discs. The octahedron was surrounded by eight WC (7% Co) cubes with truncated edges (11 mm edge length, Hawedia, Marklkofen, Germany) separated by pyrophyllite gaskets (Ceramic Substrates & Components Ltd, Isle of Wright, UK). Four WC cubes were equipped with PTFE film (Vitaflon Technische Produkte GmbH, Bad Kreuznach, Germany) for insulation. Bristol board (369 gm^{-2}) was used to ensure well-placed gaskets. The assembly was transferred into the multianvil apparatus. More details can be found in the literature.[9-

12] After insertion of the sample, the setup was compressed to 12 GPa and heated to 1400 °C within 15 min. The temperature was held constant for 300 min before it was cooled to room temperature and slowly decompressed.

4.3.3. (High-Temperature) Powder X-Ray Diffraction

The powdered sample was filled in a glass capillary with Ø 0.3 mm, wall thickness 0.01 mm (Hilgenberg GmbH, Malsfeld, Germany). A Stadi P powder diffractometer (Stoe & Cie GmbH, Darmstadt, Germany) was used to collect data (Mo-$K\alpha_1$ radiation, λ = 0.709300 Å, a Ge(111) single crystal monochromator, Si as external standard, para focusing Debye-Scherrer geometry, MYTHEN 1K Si strip detector (Dectris Ltd., Baden, Switzerland)). The powder diffraction pattern was recorded at room temperature with a step width of 0.015° from 2θ = 2–67.3°. TOPAS Academic 6.1 employing a fundamental parameters approach and a Chebyshev polynomial for background treatment was used for Rietveld refinements.[13-14]

For temperature-dependent powder X-ray diffraction, ground samples were filled into silica capillaries with 0.5 mm diameter and 0.01 mm wall thickness (Hilgenberg GmbH, Malsfeld, Germany). A Stadi P diffractometer (STOE & Cie, Darmstadt, Germany) equipped with a STOE resistance graphite furnace for temperature control (Ag-$K\alpha_1$ radiation, λ = 0.5595378 Å, Ge(111)-monochromator, IP-PSD detector) was used. Diffraction patterns were collected in the range 2θ = 2–75° in 50 °C steps from 25 °C up to 900 °C, recording each pattern for 1 h at a constant temperature.

4.3.4. Single-Crystal X-Ray Diffraction

X-ray diffraction data of the crystallites were taken at the ID11 beamline at the ESRF (Grenoble). Crystallites on carbon-film-covered Cu grids (S160 NH finder, Plano GmbH, Lünen, Germany) were centered on a hexapod setup (Symétrie Hexapods Nanopos and PI-MARS P561 piezo stage) in the synchrotron beam with a high magnification telescope.[15] The optical centering was optimized by fluorescence and diffraction scans. Data were collected using a Dectris Eiger2 X 4M CdTe detector. Indexing, integration and semi-empirical absorption correction were performed with the CrysAlis^{Pro} software package.[16] The structure was solved using SHELXT and refined with SHELXL

against $|F|^2$ using the full-matrix least-squares algorithm.[17] Solution and refinement were performed using the SHELXle software package.[18]

4.3.5. Bond Valence Sum Calculations and Partial Values of the Madelung Part of Lattice Energy

VaList was used to perform BVS calculations.[19-20] To verify the assignment of Si, P and N, the program MAPLE (Madelung part of lattice energy) was used.[21-22]

4.3.6. Electron Microscopy and Energy-Dispersive X-Ray Spectroscopy

A FEI Gelios Nanolab G3 Dual Beam UC (Fei, Hillsboro, OR, USA) with a X-Max 80 SDD detector (Oxford Instruments, Abingdon, UK) was used to collect EDX spectra. Single crystals and powder samples were distributed on a conducting carbon foil and coated with carbon.

$Cr_{5.7}Si_{2.3}P_8N_{24}$ was ground thoroughly in absolute ethanol and distributed on a carbon-film-covered Cu grid (S-166-2, Plano GmbH, Lünen, Germany) and mounted in a double-tilt holder (±30°). A FEI Tecnai G20 electron microscope (FEI, USA) with LaB_6 emitter (200 keV) was used for acquiring selected-area electron diffraction (SAED) tilt series. SAED patterns and bright-field images were obtained with a TVIPS camera (TEMCam F216) with a 2048 x 2048 pixel resolution. A Titan Themis 300 (FEI, USA) transmission electron microscope equipped with an X-FEG source, a post-column filter (Enfinium ER-799), a Cs DCOR probe corrector, a US1000XP/FT camera system (Gatan, Germany), and a windowless 4-quadrant Super-X EDX detector was used for EDX measurements and STEM-HAADF images. The system was operated at an acceleration voltage of 300 kV. A 4k × 4k FEI Ceta CMOS camera (FEI, USA) was used to obtain images. An Apollo XLT, EDAX detector with Be window was used for the acquisition of EDX spectra. Digital Micrograph (Fourier filtering of STEM images), ProcessDiffraction7 (calculations of SAEDs), JEMS (SAED simulations) and Velox v3.0 (STEM images, EDX maps) were used for data processing and Fourier filtering.[23-26]

4.3.7. Vibrating Sample Magnetometer

A Quantum Design Inc. Physical Property Measurements System (PPMS) with a vibrating sample magnetometer (VSM) and the PPMS MultiVu software package was used to record isotherms and susceptibility measurements of powdered samples.[27] Data were collected between 2 and 300 K

and field strengths of ±50 kOe. A modified Curie-Weiss equation was used to fit the inverse molar susceptibility data.

$$\frac{1}{\chi_m(T)} = \frac{1}{\chi_0 + \frac{n \cdot (N_A \cdot \frac{\mu_B^2}{3k_B}) \cdot \mu_{eff}}{T - \theta}} = \frac{1}{\chi_0 + \frac{n \cdot 0.12503776 \cdot \mu_{eff}}{T - \theta}}$$

4.3.8. Electron Paramagnetic Resonance

Electron paramagnetic resonance data of $Cr_{5.7}Si_{2.3}P_8N_{24}$ were obtained at 77 K with a Bruker EMXnano in order to give insight into the oxidation state of chromium. Parameters obtained from non linear least square regression model at X-band for Cr(III) and Cr(IV) were further processed with the assistance of the Easy Spin package used in MATLAB.[28]

4.3.9. IR Spectroscopy

An FTIR spectrum was recorded on a Spectrum BX II spectrophotometer (PerkinElmer, Waltham, MA, USA) with a DuraSampler ATR unit using the Fourier transform technique in the range of 650–4400 cm^{-1}.

4.3.10. UV-VIS-NIR

UV-Vis spectra were obtained using a Lambda 1050+ UV/Vis/NIR spectrophotometer (PerkinElmer, Waltham, MA, USA). Diffuse reflectance spectra between 240–2400 cm^{-1} were recorded with a Praying Mantis (Harrick, NY, USA) accessory and were referenced to $BaSO_4$ powder as white standard. Pseudo-absorption spectra were calculated by the Kubelka-Munk function $F(R)=(1-R)^2/2R$ where R is reflectance. Absorption data suggest a direct band gap and $h\nu$ was plotted against $[F(R)h\nu]^{1/n}$ with n = 1/2.[29]

4.4. Results and Discussion

4.4.1. Synthesis

Herein, we report on $Cr_{5.7}Si_{2.3}P_8N_{24}$, the first amphibole-type nitridophosphate. Following the mineralizer-assisted HP/HT approach, the title compound is accessible at 12 GPa and 1400 °C starting from the respective binary nitrides Cr_2N, Si_3N_4, and P_3N_5, with NH_4F added as a mineralizing agent and NH_4N_3 employed as an additional nitrogen source. The synthesis, described by equation (1), involves the oxidation of chromium and the reduction of nitrogen. A modified Walker-type multianvil module was used, and further details on the synthesis are given in the Supporting Information.

$$2.85\ Cr_2N + 2.67\ P_3N_5 + 0.77\ Si_3N_4 + 1.8\ NH_4N_3 \rightarrow Cr_{5.7}Si_{2.3}P_8N_{24} + 2.4\ NH_3 \quad (1)$$

The reaction yields a red-brown microcrystalline powder, which is stable toward air and moisture at ambient conditions. Crystallites exhibit an intergrown fiber-like morphology with a length of up to at least 7 µm and a width of up to 2 µm that makes single-crystal analysis challenging (Figure 4.1, left).

4.4.2. Crystal Structure Determination

Pre-characterization of crystallites by transmission electron microscopy (TEM) made it possible to obtain single-crystal data. Crystals of around 2 to 3 µm in size (Figure 4.1, right) were identified on TEM grids by energy dispersive X-ray (EDX) spectroscopy and selected area electron diffraction (SAED). The precise position was recorded (Figure C.1), and single-crystal X-ray diffraction (SCXRD) data were collected using a microfocused synchrotron beam at beamline ID11 of the ESRF (Grenoble, France). The crystal structure of $Cr_{5.7}Si_{2.3}P_8N_{24}$ was solved and refined in the monoclinic space group *C*2/*m* (no. 12, a = 9.6002(19), b = 17.107(3), c = 4.8530(10) Å, β = 109.65(3)°, Z = 2, R_1 = 0.0255; more details can be found in the Supporting Information). A tilt series of SAED patterns matches simulations and thus confirms the unit cell metrics in space group *C*2/*m* (Figure C.2). Based on the structure model from SCXRD, the product was identified as the main constituent by Rietveld refinement (Figure C.3) on powder data. High-temperature powder XRD data of $Cr_{5.7}Si_{2.3}P_8N_{24}$ demonstrate stability up to at least 900 °C in air and show a minor thermal

expansion up until 900 °C of <8% (Figure C.4). The elemental composition was analyzed by scanning (transmission) electron microscopy (SEM/STEM) EDX; the results fit well with respect to the atomic ratio of Cr:Si:P of 2.85:1:4 (Table C.6). EDX measurements and a FTIR spectrum (Figure C.5) indicate a minor amount of oxygen in the compound and a slight sensitivity to moisture or minor compositional variations cannot be ruled out.

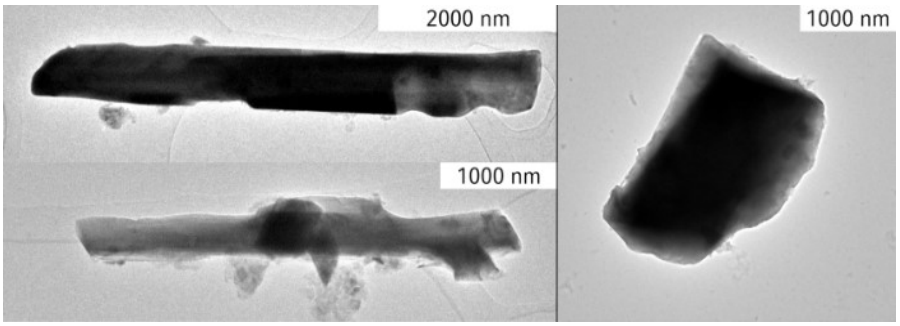

Figure 4.1. Exemplary TEM bright-field images of crystallites of $Cr_{5.7}Si_{2.3}P_8N_{24}$ (left), crystallite used for data collection at beamline ID11 with microfocused synchrotron beam (right).

4.4.3. Structure Description

Crystal structures of amphiboles can adopt monoclinic (clinoamphiboles) or orthorhombic (orthoamphiboles) structures with clinoamphiboles in the space group *C*2/*m* exhibiting the widest range of compositions and cell dimensions. $Cr_{5.7}Si_{2.3}P_8N_{24}$ adopts *C*2/*m* and shows a pronounced structural distortion with the largest β (109.65(3)°) reported for any clinoamphibole. The structure consists of a rigid framework with two principal elements – *zweier* (as defined by Liebau[1]) double chains of vertex-sharing PN_4 tetrahedra and ribbons of edge-sharing octahedra. A unit cell with partially denoted atom sites is displayed in Figure 4.2 a.

The unbranched *zweier* double chains ($[P_4N_{11}]^{13-}$) contain two crystallographically distinct tetrahedra centers, that alternate along the double chain. Both are occupied by P. Interatomic P–N distances range from 1.6026(11) to 1.6574(11) Å and are comparable to those in compounds like TiP_4N_8 (1.5758(15)–1.645(3) Å), $Sc_5P_{12}N_{23}O_3$ (1.5720(10)–1.6434(10) Å) and $AlP_6O_{3x}(NH)_{3-3x}N_9$ with $x \approx 0.33$ (1.602(3)–1.6585(15) Å).[5, 30-31] The structure contains five crystallographically independent octahedrally coordinated sites. Four out of the five form ribbons that extend along *c*. Figure 4.2 b shows the ribbons and their offset to each other by half a unit cell along both *a* and *b*.

Cr5 is isolated from other octahedra and only shares vertices with tetrahedra. This site is commonly vacant or occupied by large, low-in-charge alkali metals and often shows a high degree of positional disorder. All coordination polyhedra are illustrated in Figure C.6. In naturally occurring amphiboles, these octahedral sites are traditionally classified as cation positions A, B, and C with the defined crystallographic sites *M*(1), *M*(2), *M*(3) [C], *M*(4) [B] and *A* [A]. Different atoms with varying sizes and charges occupy these cation positions. However, in $Cr_{5.7}Si_{2.3}P_8N_{24}$, the occupation by Cr^{+IV} and Si^{+IV} (55 and 40 pm ionic radius, CN = 6, respectively) does not follow this concept of separation.[32]

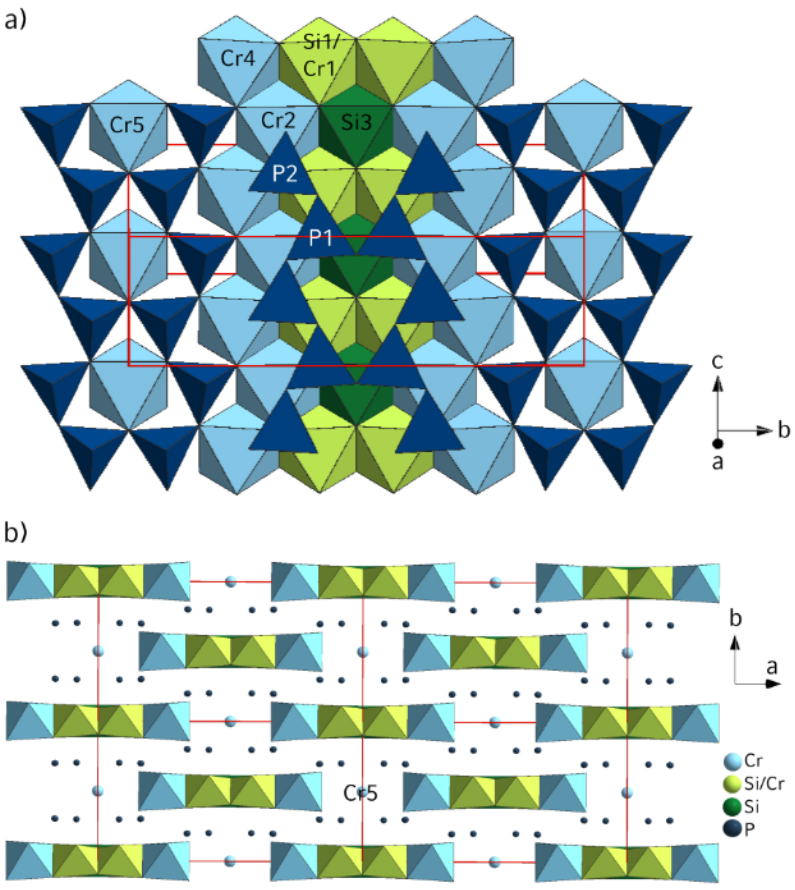

Figure 4.2. a) The crystal structure of $Cr_{5.7}Si_{2.3}P_8N_{24}$ consists of a three-dimensional rigid framework with *zweier* double chains of vertex-sharing PN_4 tetrahedra and ribbons of edge-sharing CrN_6- (light blue), $(Cr_{0.3}Si_{0.7})N_6$- (light green) and SiN_6- (dark green) octahedra. The octahedral Cr5 (light blue) site is isolated from other octahedra. Polyhedra are partially denoted. The unit cell is outlined in red; **b)** Ribbons of edge-sharing octahedra are displayed in four unit cells that shows their offset from each other by half a unit cell along both *a* and *b*. Isolated $Cr5N_6$ octahedra are positioned in between.

Refinement of Si and Cr positional parameters resulted in a structure model with one occupationally disordered site of 0.7:0.3 of Si^{+IV} and Cr^{+IV} (Si1/Cr1). This could be affirmed by comparison of bond lengths and octahedra volumes as the disordered position displays only a slight deviation of 2% from the expected values of a 0.7:0.3 Si:Cr mixed occupancy (Table C.7). STEM high-angle annular dark field (HAADF) images with a *Z*-contrast proportional to Z^2 (Z_{Cr} = 24, Z_{Si} = 14) show different cation-site occupations fitting to fully occupied Cr, fully occupied Si and an occupational disorder on Si1/Cr1 on the expected positions (Figure 4.3 left).[33] The Cr5 site exhibits a lower site symmetry (2/*m*) compared to other Cr sites (2) and therefore a halved absolute intensity compared to the position Cr2.

The tetrahedra double chain in $Cr_{5.7}Si_{2.3}P_8N_{24}$ has a smaller repeat distance (4.85510(11) Å) compared to naturally occurring amphiboles like α-grunerite ($Fe_{5.26}Mg_{1.67}Ca_{0.05}Si_8O_{22}(OH)_2$, 5.3382(9) Å).[34] The presence of P in the tetrahedral position, replacing Si (ionic radius: P = 17 pm, Si = 26 pm), contributes to the reduction in tetrahedra size and the double-chain repeat distance.[32] The reverse effect is observed whenever Al (ionic radius 39 pm) occupies tetrahedral sites.[32, 35] The kinking angle N5–N6–N5 serves as a parameter to quantify the structural distortion. $Cr_{5.7}Si_{2.3}P_8N_{24}$ exhibits a kinking angle of 127.78(7)°, surpassing the high-pressure polymorph of grunerite (137.5(4)°, γ-phase *C*2/*m*, 22 GPa), which had the lowest reported kinking angle so far found in an amphibole, indicating significant structural distortion of the double chain (Figure C.7).[33] Partial values of the Madelung part of lattice energy were compared with literature values to review the electrostatic plausibility of the structure model and provided a sufficient level of agreement (Table C.8). Bond valence sums (BVS) show a notable deviation for the Cr5 site, a phenomenon that can also be observed in other amphiboles for the respective site (Tables C.8–C.9). This is most likely due to the disorder on this position, which leads to pronounced bond length variations. BVS calculations support the assignment of Si und P to octahedral and tetrahedral sites, respectively. Since a definite assignment of Si and P from X-ray data is not possible given the similar X-ray scattering form factors, STEM-EDX mapping was performed. An overlay with an HAADF image (Figure 4.3, right) suggests ordering of Si and P that leads to the conclusion that the title compound consists of PN_4 tetrahedra and SiN_6 octahedra. In nitrides, the high-pressure motif of sixfold N-coordinated Si has so far only been observed in cubic γ-Si_3N_4, and the two nitride imides $SiP_2N_4(NH)$ and $AESi_3P_4N_{10}(NH)_2$ (*AE* = Mg, Ca, Sr).[3, 36-37]

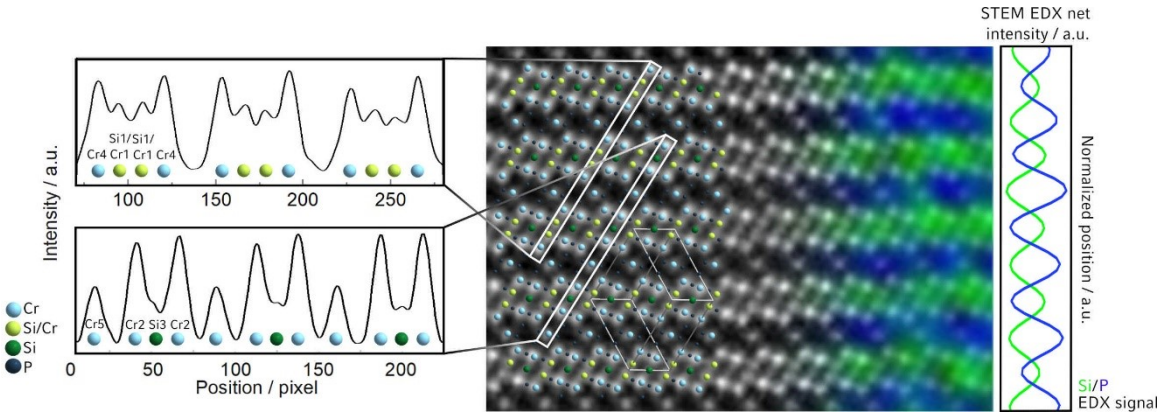

Figure 4.3. STEM-HAADF image (middle) of $Cr_{5.7}Si_{2.3}P_8N_{24}$ along [112] with structure overlay: Cr light blue, Si dark green, Si/Cr disorder light green, P dark blue. Intensity profiles (left) demonstrate the difference in intensity corresponding to different occupancies of atom columns by Cr, Si/Cr and Si atoms. Isolated Cr5 site exhibits a lower site symmetry (2/m) compared to other Cr sites (2) and therefore a lower absolute intensity. STEM-EDX map as overlay (right) shows separated intensity maxima for the EDX signal of P (blue) and Si (green). Unit cell is shown in light gray. An enlarged version of the STEM-HAADF image is given in Figure C.8.

4.4.4. Magnetic Measurements

Magnetic measurements of 3*d* transition metals are sensitive to oxidation states. Especially in compounds with a metallic character, e.g., compounds with an antiperovskite structure type and the general formula Cr_3MN, an assignment of oxidation states is not easily possible.[38-41] Many structures feature Cr^{+III}, such as CrN and (Cr,*M*)N solid solutions, as well as nitridochromates like AE_3CrN_3.[42-46] So far, the number of known nitridic compounds with chromium(+IV) is very limited and examples include the electride $Sr_3CrN_3{:}e^-$ and $LiSr_2[CrN_3]$.[47-48] Oxidation states higher than +IV range up to the maximum of +VI.[49-54] A comprehensive list providing an overview of known binary, ternary and quaternary chromium nitrides and nitridochromates can be found in Table C,10. The magnetic susceptibility was measured between 1.9 and 300 K at a constant field of 3 T (Figure 4.4 a). The open-shell configuration of Cr^{+IV} with two unpaired electrons (d^2, electron configuration $[Ar]3d^24s^0$) is responsible for the magnetic properties of $Cr_{5.7}Si_{2.3}P_8N_{24}$. Results show paramagnetic behavior down to low temperatures with an effective magnetic moment of μ_{eff} = 2.473(2) μ_B per formula unit obtained from a Curie-Weiss fit of the inverse molar susceptibility (inset in Figure 4.4 a). This is in agreement with comparable literature data and the theoretical value of μ_{eff} = 2.83 μ_B for an electronic ground state $^3T_{1g}$ in a d^2 system following the spin-only formula.[55] Magnetization

isotherm and zero-field-cooled/field-cooled magnetization data indicate minor impurities by an unknown ferromagnetic and diamagnetic substance (Figures C.10–C.11), which are highly unlikely to be CrP, as CrP also exhibits Pauli paramagnetism.[56] The electron paramagnetic resonance (EPR) spectrum has a sharp central feature with a turning point at about 35 mT without significant secondary side features (Figure 4.4 b). Simulations for Cr^{+III} and Cr^{+IV} for all four Cr positions are calculated, and Cr^{+IV} shows by far the best-fitting results. The simulation for Cr^{+III} and further information are given in Figure C.12 and Table C.11. The magnetic measurements support the conclusion that exclusively Cr^{+IV} is present in the title compound.

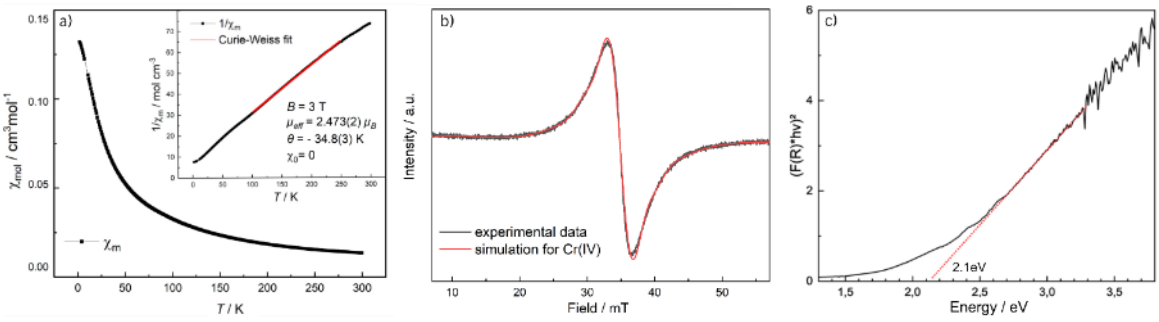

Figure 4.4. a) Magnetic susceptibility of $Cr_{5.7}Si_{2.3}P_8N_{24}$ and inverse magnetic susceptibility (inset) with an extended Curie-Weiss fit (red); **b)** CW X-band EPR spectrum of $Cr_{5.7}Si_{2.3}P_8N_{24}$ measured at 77 K (black) and simulation (red), using the parameters listed in Table C.11; **c)** Tauc plot based on the UV-Vis measurement with an energy axis intercept at 2.1 eV. Absorption data suggest a direct band gap, and linear regression between 2.7 and 3.3 eV was used to determine inflection point yielding the bandgap.

4.4.5. Optical Measurements

The optical bandgap of $Cr_{5.7}Si_{2.3}P_8N_{24}$ can be approximated from the valence to conduction band transition visible in the UV/Vis-spectrum by converting reflectance spectra to the Kubelka– Munk function and calculating a Tauc plot (Figures 4.4 c, C.13). The estimated direct band gap of 2.1 eV indicates that $Cr_{5.7}Si_{2.3}P_8N_{24}$ is a semiconducting material. Nitride semiconductors with layered structures such as delafossite-type $CuNbN_2$ and $CuTaN_2$ feature a strong optical absorption onset at 1.4–1.5 eV.[57-58] Other nitride semiconductors with bandgaps in a similar region are $ZnSnN_2$ (1–2 eV) with a strong dependence on the degree of cation disorder, Ta_3N_5 (1.8–1.9 eV) and InN thin films (1.5–2.5 eV).[59-62]

4.5. Conclusion

Summing up, we present the first nitridic analog of an amphibole mineral. $Cr_{5.7}Si_{2.3}P_8N_{24}$ was obtained by a NH_4F-mediated HP/HT synthesis. Separated Si and P sites, as well as a disordered Si:Cr site could be validated by STEM-HAADF analysis. The oxidation state of Cr is +IV and even though $Cr^{+IV}O_2$ has been a key magnetic storage material dominating data storage in high-performance audio tapes for years, Cr^{+IV} has only been scarcely observed in nitrides prior to this work. The chemical diversity of amphiboles becomes evident by the array of used prefixes, different sized cation positions and frequent anion substitution. We expect that further research on complete and partial substitution of the cation positions by other transition metal and alkali metal ions can provide access to stable nitrides with interesting physical properties like suitable band gaps for semiconductor applications and ion conductivity. This seems close as chromium containing nitrides and transition metal nitrides in general are already being investigated as co-catalyst for photocatalytic hydrogen production or as materials for novel energy harvesting and Fe-rich amphiboles exhibit electric conductivity.[63-67] Further, the influence of mixed anionic frameworks on the electronic structure and properties like electric conductivity and catalytic behavior can be investigated as replacing the hydroxyl group with with F, O, or Cl can already be observed in natural amphiboles.

Supporting Information

Deposition number 2324313 contains the supplementary crystallographic data for this paper. These data are provided free of charge by the joint Cambridge Crystallographic Data Centre and Fachinformationszentrum Karlsruhe Access Structures service.

The data that support the findings of this study are available in the Supporting Information of this article. The authors have cited additional references within the Supporting Information.[68–88]

Acknowledgements

Financial support by the Deutsche Forschungsgemeinschaft DFG (projects SCHN 377/18-1 and OE 530/6-1) is gratefully acknowledged. We thank Amalina Buda (Department of Chemistry at LMU Munich) for SEM investigations and the ESRF for beamtime to acquire microfocused single-crystal diffraction data (project CH-6207).

4.6. References

[1] F. Liebau, *Structural chemistry of silicates: structure, bonding, and classification*, Springer-Verlag, Berlin Heidelberg, **2012**, pp. 59–62.

[2] R. L. Virta, *Asbestos*, *Kirk-Othmer Encyclopedia of Chemical Technology*, Wiley, Weinheim, **2011**, pp 1–40.

[3] L. Eisenburger, P. Strobel, P. J. Schmidt, T. Bräuniger, J. Wright, E. L. Bright, C. Giacobbe, O. Oeckler, W. Schnick, *Angew. Chem. Int. Ed.* **2022**, *61*, e202114902.

[4] S. D. Kloß, W. Schnick, *Angew. Chem. Int. Ed.* **2015**, *54*, 11250–11253.

[5] L. Eisenburger, V. Weippert, C. Paulmann, D. Johrendt, O. Oeckler, W. Schnick, *Angew. Chem. Int. Ed*. **2022**, *61*, e202202014.

[6] L. Eisenburger, O. Oeckler, W. Schnick, *Chem. Eur. J.* **2021**, *27*, 4461–4465.

[7] A. Stock, H. Grüneberg, *Ber. Dtsch. Chem. Ges.* **1907**, *40*, 2573–2578.

[8] W. J. Frierson, W. F. Filbert, *Inorg. Synth.*, Wiley-Blackwell, Hoboken, New Jersey, **2007**, pp. 136–138.

[9] D. Rubie, *Phase Transitions* **1999**, *68*, 431–451.

[10] D. Walker, *Am. Mineral.* **1991**, *76*, 1092–1100.

[11] D. Walker, M. Carpenter, C. Hitch, *Am. Mineral.* **1990**, *75*, 1020–1028.

[12] H. Huppertz, *Z. Kristallogr. – Cryst. Mater.* **2004**, *219*, 330–338.

[13] H. M. Rietveld, *J. Appl. Crystallogr.* **1969**, *2*, 65–71.

[14] A. Coelho, TOPAS Academic, version 6.1, **2007**.

[15] J. Wright, C. Giacobbe, M. Majkut, *Curr. Opin. Solid State Mater. Sci.* **2020**, *24*, 100818.

[16] CrysAlis^{PRO}, Rigaku Oxford Diffraction Ltd, Yarnton, Oxfordshire, **2017**.

[17] G. M. Sheldrick, *Acta Crystallogr., Sect. C* **2015**, *71*, 3–8.

[18] C. B. Hübschle, G. M. Sheldrick, B. Dittrich, *J. Appl. Crystallogr.* **2011**, *44*, 1281–1284.

[19] A. S. Wills, VaList, University College London, London, **1998–2010**.

[20] N. E. Brese, M. O'Keeffe, *Acta Crystallogr., Sect. B* **1991,** *47*, 192–197.

[21] R. Hoppe, *Angew. Chem. Int. Ed. Engl.* **1970**, *9*, 25–34.

[22] R. Hoppe, *Angew. Chem. Int. Ed. Engl.* **1966**, *5*, 95–106.

[23] DigitalMicrograph, Gatan, Pleasanton, California, **1999**.

[24] J. L. Lábár, *Ultramicroscopy* **2005**, *103*, 237–249.

[25] P. A. Stadelmann, *Ultramicroscopy* **1987**, *21*, 131–145.

[26] Velox, version 3, Thermo Fisher Scientific, Waltham, Massachusetts, **2021**.

[27] PPMS MultiVu, version 1.5.11 ed., Quantum Design Inc., San Diego, California, **2013**.

[28] S. Stoll, A. Schweiger, *J. Magn. Reson.* **2006**, 178, 42–55.

[29] J. Tauc, R. Grigorovici, A. Vancu, *Phys. Status Solidi B* **1966**, *15*, 627–637.

[30] L. Eisenburger, V. Weippert, O. Oeckler, W. Schnick, *Chem. Eur. J.* **2021**, *27*, 14184–14188.

[31] L. Neudert, F. Heinke, T. Bräuniger, F. J. Pucher, G. B. Vaughan, O. Oeckler, W. Schnick, *Chem. Commun.* **2017**, *53*, 2709–2712.

[32] R. D. Shannon, *Acta Crystallogr., Sect. A* **1976**, *32*, 751–767.

[33] S. Pennycook, *Annu. Rev. Mater. Sci.* **1992**, *22*, 171–195.

[34] T. Yong, P. Dera, D. Zhang, *Phys. Chem. Miner.* **2019**, *46*, 215–227.

[35] R. Oberti, G. Della Ventura, F. Cámara, *Rev. Mineral. Geochem.* **2007**, *67*, 89–124

[36] M. Schwarz, G. Miehe, A. Zerr, E. Kroke, B. T. Poe, H. Fuess, R. Riedel, *Adv. Mater.* **2000**, *12*, 883–887.

[37] S. Vogel, A. T. Buda, W. Schnick, *Angew. Chem. Int. Ed.* **2019**, *131*, 3436–3439.

[38] M. Nardin, C. Lorthioir, M. M. Barberon, R. Madar, E. Fruchart, R. Fruchart, *C. R. Seances Acad. Sci., Ser. C* **1972**, *274*, 2168–2171.

[39] C. Samson, J.-P. Bouchaud, R. Fruchart, *C. R. Seances Acad. Sci., Ser. C* **1964**, *259*, 392–393.

[40] H. Boller, *Monatsh. Chem.* **1968**, *99*, 2444–2449.

[41] H. Boller, *Monatsh. Chem.* **1969**, *100*, 1471–1476.

[42] R. Blix, *Z. Phys. Chem., Abt. B* **1929,** *3*, 229–239.

[43] M. I. Aivazov, T. V. Rezchikova, V. F. Degtyareva, *Inorg. Mater.* **1975**, *11*, 201–203.

[44] R. Kieffer, P. Ettmayer, F. Petter, *Monatsh. Chem.* **1971,** *102*, 1182–1196.

[45] D. A. Vennos, M. E. Badding, F. J. DiSalvo, *Inorg. Chem.* **1990**, *29*, 4059–4062.

[46] M. G. Barker, M. J. Begley, P. P. Edwards, D. H. Gregory, S. E. Smith, *J. Chem. Soc., Dalton Trans.* **1996**, *1*, 1–5.

[47] P. Chanhom, K. E. Fritz, L. A. Burton, J. Kloppenburg, Y. Filinchuk, A. Senyshyn, M. Wang, Z. Feng, N. Insin, J. Suntivich, G. Hautier, *J. Am. Chem. Soc.* **2019,** *141*, 10595–10598.

[48] N. Gloriozova, Y. Prots, F. Jach, M. Krnel, M. Bobnar, A. Ormeci, Y. Grin, P. Höhn *Inorg. Chem.* **2023**, *62*, 12940–12946.

[49] F. Chevire, C. Ranjan, F. J. DiSalvo, *Solid State Commun.* **2009,** *149*, 273–276.

[50] A. Tennstedt, R. Kniep, M. Hueber, W. Haase, *Z. Anorg. Allg. Chem,* **1995**, *621*, 511–515.

[51] O. Hochrein, M. Kohout, W. Schnelle, R. Kniep, *Z. Anorg. Allg. Chem.* **2002**, *628*, 2738–2743.

[52] R. Juza, J. Haug, *Z. Anorg. Allg. Chem.* **1961**, *309*, 276–282.

[53] A. Gudat, S. Haag, R. Kniep, A. Rabenau, *Z. Naturforsch., B: J. Chem. Sci.* **1990**, *45*, 111–120.

[54] R. Niewa, D. A. Zherebtsov, P. Hoehn, *Z. Kristallogr. – New Cryst. Struct.* **2003**, *218*, 163.

[55] J. R. Akridge, J. H. Kennedy, *J. Solid State Chem.* **1978**, *26*, 147–152.

[56] K. Motizuki, H. Ido, T. Itoh, and M. Morifuji, *Electronic Structure and Magnetism of 3d-Transition Metal Pnictides*, Springer Series in Materials Science, Springer-Verlag, Berlin, **2010**, pp. 17–71.

[57] M. Yang, A. Zakutayev, J. Vidal, X. Zhang, D. S. Ginley, F. J. DiSalvo, *Energy Environ. Sci.* **2013**, *6*, 2994–2999.

[58] A. Zakutayev, A. J. Allen, X. Zhang, J. Vidal, Z. Cui, S. Lany, M. Yang, F. J. DiSalvo, D. S. Ginley, *Chem. Mater.* **2014**, *26*, 4970–4977.

[59] N. Feldberg, J. Aldous, W. Linhart, L. Phillips, K. Durose, P. Stampe, R. Kennedy, D. Scanlon, G. Vardar, R. Field, *Appl. Phys. Lett.* **2013**, *103*, 042109.

[60] T. Veal, N. Feldberg, N. F. Quackenbush, W. M. Linhart, D. O. Scanlon, L. F. Piper, S. M. Durbin, *Adv. Energy Mater.* **2015**, *5*, 1501462.

[61] J. M. Morbec, I. Narkeviciute, T. F. Jaramillo, G. Galli, *Phys. Rev. B* **2014**, *90*, 155204.

[62] T. Tansley, C. Foley, *J. Appl. Phys.* **1986**, *59*, 3241–3244.

[63] R. S. Ningthoujam, N. S. Gajbhiye, *Prog. Mater. Sci.* **2015**, *70*, 50–154.

[64] X. Meng, W. Qi, W. Kuang, S. Adimi, H. Guo, T. Thomas, S. Liu, Z. Wang, M. Yang, *J. Mater. Chem. A* **2020**, *8*, 15774–15781.

[65] P. Eklund, S. Kerdsongpanya, B. Alling, *J. Mater. Chem. C* **2016**, *4*, 3905–3914.

[66] E. Schmidbauer, T. Kunzmann, T. Fehr, R. Hochleitner, *Phys. Chem. Minerals* **1996**, *23*, 99–106.

[67] D. Wang, Y. Gui, Y. Yu, S. Karato, *Contrib. Mineral. Petrol.* **2012**, *164*, 17–25.

[68] K. Landskron, PhD thesis, Ludwig-Maximilians-Universität (DE), **2001**.

[69] K. Köllisch, PhD thesis, Ludwig-Maximilians-Universität (DE), **2001**.

[70] H. D. Grundy, F. C. Hawthorne, *Can. Mineral.* **1976**, *14*, 334–345.

[71] R. Oberti, F. Camara, J. M. Caballero, *Am. Mineral.* **2004**, *89*, 888–893.

[72] R. Oberti, F. C. Hawthorne, F. Camara, M. Raudsepp, *Am. Mineral.* **1999**, *84*, 102–111.

[73] M. D. Welch, J. J. Reece, S. A. T. Redfern, *Mineral. Mag.* **2008**, *72*, 877–886.

[74] G. D. Ventura, J. L. Robert, M. Raudsepp, F. C. Hawthorne, M. D. Welch, *Am. Mineral.* **1997**, *82*, 291–301.

[75] R. Oberti, M. Boiocchi, F. C. Hawthorne, R. Kristiansen, *Mineral. Mag.* **2014**, *78*, 861–869.

[76] A. Reitz, H. Pazniak, C. Shen, H. K. Singh, K. Jayanthi, N. Kubitza, A. Navrotsky, H. Zhang, U. Wiedwald, C. S. Birkel, *Chem. Mater.* **2022**, *34*, 10304–10310.

[77] L. Zu, B. Hong, S. Lin, M. Yang, Z. Wang, Y. Zhang, W. Zhao, *J. Alloys Compd.* **2023**, *939*, 168681.

[78] P. Ettmayer, A. Vendl, G. Banik, R. Kieffer, *Monatsh. Chem.* **1978**, *109*, 1005–1008.

[79] S.-J. Kim, T. Marquart, H. F. Franzen, *J. Less-Common Met.* **1990**, *158*, 9–10.

[80] R. Marchand, V. Lemarchand, *J. Less-Common Met.* **1981**, *80*, 157–163.

[81] S. Broll, W. Jeitschko, *Z. Naturforsch., B: J. Chem. Sci.* **1995**, *50*, 905–912.

[82] K. S. Weil, P. N. Kumt, *J. Solid State Chem.* **1997**, *128*, 185–190.

[83] T. Steiner, S. R. Meka, B. Rheingans, E. Bischof, T. Waldenmaier, G. Yeli, T. L. Martina, P. A. J. Bagot, M. P. Moody, E. J. Mittemeijer, *Philos. Mag.* **2016**, *96*, 1509–1537.

[84] R. Benz, W. H. Zachariasen, *J. Nucl. Mater.* **1970**, *37*, 109–113.

[85] M. S. Bailey, M. N. Obrovac, E. Baillet, T. K. Reynolds, D. B. Zax, F. J. DiSalvo, *Inorg. Chem.* **2003,** *42*, 5572–5578.

[86] M. S. Bailey, F. J. DiSalvo, *Dalton Trans.* **2003**, 2621–2625.

[87] N. W. Falb, J. N. Neu, T. Besara, J. B. Whalen, D. J. Singh, T. Siegrist, *Inorg. Chem.* **2019**, *58*, 3302–3307.

[88] Y. Cao, M. A. Kirsanova, M. Ochi, W. Al Maksoud, T. Zhu, R. Rai, S. Gao, T. Tsumori, S. Kobayashi, S. Kawaguchi, E. Abou-Hamad, K. Kuroki, C. Tassel, A. M. Abakumov, Y. Kobayashi, H. Kageyama, *Angew. Chem. Int. Ed.* **2022,** *61*, e202209187.

Chapter 5

$P_{1-x}Ta_{8+x}N_{13}$ (x = 0.1–0.15): A Phosphorus Tantalum Nitride With High Specific Resistivity Featuring Mixed-Valent Tantalum and P/Ta Disorder

Monika M. Pointner, Claude Ceniza, Martin Weidemann, Lukas Nusser, Florian Wolf, Lucien Eisenburger, Alexander Moewes, Oliver Oeckler,* and Wolfgang Schnick*

published in: *Angew. Chem.* **2024**, e202411441, DOI: 10.1002/ange.202411441.

published in: *Angew. Chem. Int. Ed.* **2024**, e202411441, DOI: 10.1002/ange.202411441.

5.1. Abstract

We report on the synthesis, crystal, and electronic structure, as well as the magnetic, and electric properties of the phosphorus-containing tantalum nitride $P_{1-x}Ta_{8+x}N_{13}$ (x = 0.1–0.15). A high-pressure high-temperature reaction (8 GPa, 1400 °C) of Ta_3N_5 and P_3N_5 with NH_4F as a mineralizing agent yields the compound in the form of black, rod-shaped crystals. Single-crystal X-ray structure elucidation (space group $C2/m$ (no. 12), a = 16.202(3), b = 2.9155(4), c = 11.089(2) Å, β = 126.698(7)°, Z = 2) shows a network of face- and edge-sharing Ta-centered polyhedra that contains small vacant channels and PN_6 octahedra strands. Atomic resolution transmission electron microscopy reveals an unusual P/Ta disorder. Mixed-valent tantalum atoms exhibit interatomic distances similar to those in metallic tantalum, however, the electrical resistivity is quite high in the order of 10^{-1} Ω cm. The density of states and the electron localization function indicate localized electrons in both covalent and ionic bonds between P/Ta and N atoms, combined with less localized electrons that do not contribute to interatomic bonds.

5.2. Introduction

Transition metal (*TM*) nitrides and ternary metal nitrides have become an integral part of today's electrochemical energy applications and fundamental research projects because they offer a versatile range of desirable properties for sustainable energy conversion, including photovoltaics, thermoelectric materials, and solid-state lighting.[1-2] Tantalum nitrides exhibit properties like tunable electrical conductivity ideal for applications in, e.g., microelectronics, solar energy harvesting, and catalysis.[3-5] The Ta-N system spans a spectrum from tantalum-rich solid solutions to nitrogen-rich compounds with varying oxidation states from 0 to +V. Known phases include the solid solution of nitrogen in tantalum,[6] α-Ta(N) and β-Ta_2N,[6-9] three modifications of TaN (ε, δ, θ),[9-15] as well as nitrogen-rich compounds like Ta_5N_6,[7] Ta_4N_5, [7] Ta_2N_3,[16-17] and Ta_3N_5.[18] The binary system Ta-N is so intriguing that calculations are being made to explore the less accessible high-pressure/high-temperature Ta-N phase diagram.[19]

Ternary compounds with Ta and N often form nitridotantalates with discrete or edge-sharing $Ta^{+V}N_4$ tetrahedra if alkaline and alkaline earth metals are included.[20-24] Nitridotantalates like $LiTa_3N_4$, $MgTa_2N_3$, $Na_2Ta_3N_5$ and $Na_xTa_3N_5$ ($0 \leq x \leq 1.4$) show mixed-valency of the Ta species.[25-26] The systems Ta/*TM*/N were studied in detail in the mid 20th century and it was shown that compounds with *TM* = Ti–Ni, Zr–Nb typically form disordered rocksalt-type structures.[9, 12, 27] With copper as a second *TM*, the layered delafossite-type structure with $Ta^{+V}N_6$ octahedra is obtained.[28] Recently discovered $MnTa_2N_4$ and $ScTaN_2$, feature pronounced magnetic frustration and metal–metal bonds, respectively.[29-30] A handful of ternary Ta-N compounds involve rare-earth metals. $RE_3[Ta_2N_6]$ (*RE* = La, Ce, Pr) are isotypic to the high T_C cuprate semiconductor $La_{2-x}Sr_xCaCu_2O_6$ (x = 0.2–0.55) and contain layers of vertex-sharing square TaN_5 pyramids.[31] $TaThN_3$ was the first nitride perovskite in literature.[32] For the main group elements from groups 13 to 15, Ta_5Ga_3N forms an intermetallic alloy, and tantalum carbonitrides have been reported due to the solubility of TaN in C.[12, 33-34] However, *TM* nitrides containing main group elements have not yet been described.

The introduction of phosphorus into *TM* nitrides led to anionic nitridophosphate network systems dominated by PN_4 tetrahedra[35-36] and *TM* nitrides containing phosphorus are mostly unexplored. Therefore, we search for possible synthesis routes and relationships between structures and properties.

5.3. Experimental Part

5.3.1. Preparation of Starting Materials

A fused silica tube and a silica boat were dried at 1273 K under dynamic vacuum (<10^{-3} bar). P_4S_{10} (Sigma-Aldrich, 99.99%) served as a precursor and was loaded in a constant flow of argon. The setup was saturated with ammonia (Air Liquide, 5.0) for 4 h and the reaction was carried out at 1123 K for 4 h (5 K/min heating/cooling ramp).[37] The obtained product was washed with diluted HCl and H_2O and dried. P_3N_5 was yielded as a light orange powder. PXRD and CHNS analysis were carried out to confirm its purity. CHNS: calc. C0%, H 0%, N 42.98%, S 0%, exp. C 0%, H 0%, N 42.69%, S 0%. A fused silica tube and a silica boat were dried at 1273 K under dynamic vacuum (<10^{-3} bar). Ta_2O_5 powder (Sigma-Aldrich, 99%) was evenly distributed over the entire length of the silica boat. Kroll-titanium was placed upstream serving both as purification and activator to NH_3. The whole setup was saturated with ammonia (Air Liquide, 5.0) for 1 h. The reaction was carried out for 48 h at 900 °C (heating ramp: 5 °C/min, cooling ramp: 10 °C/min) with a constant flow of NH_3.[38] The product was yielded as a dark red powder. PXRD analysis confirmed its purity. NH_4F (Sigma Aldrich, ≥98%) was used as purchased.

5.3.2. Multianvil Synthesis

$P_{1-x}Ta_{8+x}N_{13}$ (x = 0.1–0.15) was synthesized under high-pressure high-temperature conditions (T = 1400 °C, p = 8 GPa) using a 1000 t hydraulic press (Voggenreiter, Mainleus, Germany) with a modified Walker module. The starting materials (Table D.1) were mortared in an agate mortar in an Ar-filled glovebox (Unilab, MBraun, Garching, O_2<1 ppm, H_2O<0.1 ppm) and cautiously pressed into a crucible of h-BN (HeBoSint® S100, Henze, Kempten, Germany). The crucible was sealed with an h-BN lid and centered in two graphite tubes (furnace) and a ZrO_2 sleeve (insulator, Cesima Ceramis, Wurst-Fischbeck, Germany) using MgO spacers (Cesima Ceramics, Wust-Fischbeck, Germany) at top and bottom. The sample was placed in a pierced octahedron (7% Cr_2O_3 doped MgO, 18 mm edge length, Ceramic Substrates & Components Ltd., Isle of Wright, UK). Two molybdenum discs function as contacts. The octahedron was surrounded by eight WC cubes with truncated edges (7% Co, 11 mm edge length, Hawedia, Marklkofen, Germany) separated by pyrophyllite gaskets (Ceramic Substrates & Components Ltd, Isle of Wright, UK). WC cubes were

equipped with PTFE film (Vitaflon Technische Produkte GmbH, Bad Kreuznach, Germany) and Bristol board (369 gm^{-2}) for insulation and placement of the gaskets, respectively. More details can be found in the literature.[39-42] After insertion of the sample, the setup was compressed to 8 GPa and heated to 1400 °C within 60 min. The temperature was held constant for 300 min before it was cooled to room temperature (60 min) and slowly decompressed.

5.3.3. (High-Temperature) Powder X-Ray Diffraction and Rietvled Refinement

Ground samples were transferred in glass capillaries with Ø 0.3 mm, wall thickness 0.01 mm (Hilgenberg GmbH, Malsfeld, Germany). Data were collected at room temperature with a Stadi P powder diffractometer (Stoe & Cie GmbH, Darmstadt, Germany) and Mo-$K\alpha_1$ radiation (λ = 0.709300 Å), a Ge(111) single crystal monochromator, Si as external standard, para focused Debye-Scherrer geometry and a MYTHEN 1K Si strip detector (Dectris Ltd., Baden, Switzerland). The powder diffraction pattern was recorded with a step width of 0.015 °/step from 2θ = 2–37.16°. TOPAS Academic 6.1, the Rietveld method, the fundamental parameter approach and a Chebyshev polynomial were used for refinement of structure models.[43-44]

Temperature-dependent powder X-ray diffraction patterns were recorded on a Stadi P diffractometer (STOE & Cie, Darmstadt, Germany) equipped with a STOE resistance graphite furnace for temperature control and Ag-$K\alpha_1$ radiation (λ = 0.5595378 Å, Ge(111)-monochromator, IP-PSD detector). Samples were filled into silica capillaries with 0.5 mm diameter and 0.01 mm wall thickness (Hilgenberg GmbH, Malsfeld, Germany). Diffraction patterns were collected in the range 2θ = 3.11–77.38° in 50 °C steps from 50 °C up to 900 °C within 1 h at a constant temperature. Lattice parameters were extracted from Rietveld-Fits.

5.3.4. Single-Crystal X-Ray Diffraction

Single-crystal X-ray diffraction data was collected on a Bruker D8 Venture TXS diffractometer (rotating anode, Mo-Kα radiation, λ = 0.71073 Å, multilayer monochromator) with combined φ- and ω-scans. The program package APEX3 was used for indexing, integration, and semiempirical absorption correction.[45] The structure was solved by direct methods using the SHELXT algorithm and refined with SHELXL against $|F|^2$ on all data using the full-matrix least-squares algorithm.[46] Solution and refinement were performed using the shelxtl software package.[47]

5.3.5. Energy-Dispersive X-Ray Spectroscopy

EDX spectra were collected with a FEI Gelios NanoLab G3 Dual Beam UC (Fei, Hillsboro, OR, USA) equipped with a X-Max 80 SDD detector (Oxford Instruments, Abingdon, UK). Single crystals and powder was carefully distributed on a conducting carbon foil and spin-coated with carbon.

5.3.6. (Scanning) Transmission Electron Microscopy

The sample was grounded thoroughly and mixed with absolute EtOH. The sample was distributed on a carbon film-covered Cu grid (S-166-2, Plano GmbH, Lünen, Germany). Experiments were realized using a double-tilt holder (±30 °). A FEI Tecnai G20 electron microscope (FEI, USA, LaB_6 emitter, 200 keV) was used for acquiring the tilt series. SAED diagrams and bright field images were obtained with a TVIPS camera (TEMCam F216, Tietz Company, 2048 x 2048 pixel resolution). STEM-HAADF images were obtained on a Fei Titan (Titan Themis 300, FEI, USA, 300 keV) transmission electron microscope, which is equipped with an X-FEG source, a post-column filter (Enfinium ER-799), a Cs DCOR probe corrector, a US1000XP camera system (Gatan, Germany), and a windowless 4-quadrant Super-X energy-dispersive X-ray spectroscopy detector. A 4k × 4k FEI Ceta CMOS camera (FEI, USA) was used to obtain bright-field images. An Apollo XLT, EDAX detector with Be window was used for the acquisition of EDX spectra. Digital Micrograph (Fourier filtering of STEM images), ProcessDiffraction7 (calculations of SAEDs), JEMS (SAED simulations) and Velox (STEM images, EDX maps) were used for data processing and Fourier filtering.[48-51]

5.3.7. Physical Property Measurement System

5.3.7.1. Temperature-Dependent Resistivity Measurements

Temperature-dependent measurements of specific resistivity were conducted over a range of 2 K to 296 K. These measurements were carried out using the alternating-current resistivity option at a typical frequency of 19 Hz on a Physical Property Measurement System (PPMS, Quantum Design Inc., San Diego, CA). Currents ranging from 1 mA to 100 mA were applied to a pellet sample. The van der Pauw technique was employed for these measurements. Thin gold wires were affixed to the sample using silver paint. The sample was mounted and the PPMS cryostat was evacuated to high vacuum conditions (≤10^{-5} mbar) while cooling down to the temperature of liquid helium. The resistance of the sample was measured as the temperature was gradually increased.

5.3.7.2. Vibrating Sample Magnetometer

A vibrating sample magnetometer (VSM) and the PPMS MultiVu software package were used to conduct isotherm and susceptibility measurements on the ground sample (in gelatin capsules, 9 mg).[52] The data collection spanned a temperature range of 2 K to 300 K, and magnetic field strengths of ±50 kOe were applied. To analyze the inverse molar susceptibility data, we employed a modified Curie-Weiss equation for fitting. The magnetic susceptibility was measured between 1.9 and 300 K at a constant field of 3 T.

$$\frac{1}{\chi_m(T)} = \frac{1}{\chi_0 + \frac{n \cdot (N_A \cdot \frac{\mu_B^2}{3k_B}) \cdot \mu_{eff}}{T - \theta}} = \frac{1}{\chi_0 + \frac{n \cdot 0.12503776 \cdot \mu_{eff}}{T - \theta}}$$

5.3.8. Electron Paramagnetic Resonance

Electron paramagnetic resonance studies were obtained at room temperature with a Bruker EMXnano.

5.3.9. Density Functional Theory Calculations

We used Density Functional Theory (DFT) calculations (mixed occupation not taken into account) using the commercial WIEN2k software package.[53-56] This software employs the Full-Potential Linearized Augmented Plane Wave (FP-LAPW) method for electronic structure calculations.[57-61] In this method, atomic-like orbitals are used inside the atomic spheres (also known as muffin-tin spheres), while plane waves are utilized in the interstitial region between these atomic spheres. We set the energy cutoff at –6.0 Rydberg to distinguish core electrons from valence electrons. Additionally, we chose an RK_{max} value of 7.0, which dictates the expansion of plane waves in the interstitial region. We set the muffin-tin radii (RMT) to 1.72 for N, 2.10 for Ta, and 1.66 for P. This configuration ensures that the muffin-tin spheres are just touching. This is done to maximize the accuracy in modelling the electronic potential around atoms and maintaining computational efficiency. For the Brillouin zone sampling, we used a grid of 19x6x19 *k*-points. This grid was generated using a special *k*-point generation scheme to ensure symmetrical distribution of *k*-points. For the self-consistent field (SCF) calculations, we used the PBE-GGA type exchange-correlation and on-site hybrid functionals. [62-63] The convergence criteria were set at 10^{-6} for energy and 10^{-3}

for charge. This precision ensures that the energy difference in each SCF cycle is accurate up to 10^{-3} mRy/cell, balancing accuracy with computational practicality. Calculations using semilocal functionals of the Generalized Gradient Approximation (GGA) types - including PBE-GGA, PBEsol-GGA, and WC-GGA (Wu-Cohen 06) - as well as hybrid functionals, yielded similar results for the calculated phosphorus DOS.[62, 64]

5.3.10. Electron Localization Function and Bader Analysis

We performed first-principle electronic structure calculations based on periodic DFT. For that the Vienna Ab initio Simulation Package (VASP) was used.[65-68] Core and valence electrons were separated using projector augmented waves (PAW) and the exchange and correlation energy was calculated via generalized gradient approximation (GGA), as described by Perdew, Burke and Ernzerhof (PBE).[69-70] The Brillouin zone was sampled on a 1x5x2 Gamma centered *k*-point grid with a plane wave energy cutoff of 520 eV.[62, 71] Structure parameters were optimized via conjugate gradient algorithm until the convergence criteria of 10^{-3} eV/Å for interatomic forces was reached.[72] A bonding analysis was performed by calculating the electron localization function (ELF) with an electronic convergence criteria of 10^{-7} eV.[73] To further analyze the bonding situation, Bader analysis was performed on the title compound as well as selected Ta-N/Ta-O compounds, using the VASP package.[65-68] For all compounds, including the title compound, the charge density grids used for Bader analysis were derived from experimentally determined and unoptimized structures. Again, core and valence electrons were separated using PAW potentials, the exchange and correlation energy was treated via PBE-GGA functionals.[69-70] The Brillouin zones were sampled using Gamma centered *k*-point grids with a *k*-space resolution of ~0.2 $Å^{-1}$ for all compounds.[71] The exact *k*-point grid sizes for all compounds can be found in Table 5.1. Charge density grids were derived from self consistent calculations with convergence criteria of 10^{-6} eV for the total energies. The Bader charges were obtained by summing the core and valence charge densities and applying the Bader Charge Analysis Code.[74-76]

Table 5.1. *k*-point grid sizes for all Bader analysis calculations.

compound	*spacegroup*	*k-point grid*
PTa_8N_{13}	*C*2*m*	11x11x4
HP-Ta_3N_5	*Pnma*	3x12x2
Ta_3N_5	*Cmcm*	9x9x3
TaON	$P2_1/c$	6x6x6
Ta_2N_3	*Pnma*	4x11x4
ϑ-TaN	$P\bar{6}m2$	12x12x11
ε-TaN	*P*6/*mmm*	7x7x11
δ-TaN	$Fm\bar{3}m$	12x12x12

5.3.11. UV-Vis-NIR Spectroscopy

UV-Vis spectra were obtained using a Lambda 1050+ UV/Vis/NIR spectrophotometer (PerkinElmer, Waltham, MA, USA). Diffuse reflectance spectra between 370–1800 nm were recorded with a Praying Mantis (Harrick, NY, USA) accessory and were referenced to $BaSO_4$ powder as white standard. Pseudo-absorption spectra were calculated by the Kubelka-Munk function $F(R)=(1-R)^2/2R$ where R is reflectance.

5.4. Results and Discussion

5.4.1. Synthesis

In this contribution, we present $P_{1-x}Ta_{8+x}N_{13}$ (x = 0.1–0.15) – the ternary transition metal nitride containing phosphorus. The compound combines an occupational disorder of Ta and P, mixed-valent tantalum with a formal oxidation state of +4.25 and PN_6 octahedra, a structure motif typically found in high-pressure chemistry within diamond anvil cells.[77-79] The title compound was obtained by applying high-pressure high-temperature conditions (T = 1400 °C, p = 8 GPa). The respective binary nitrides Ta_3N_5 and P_3N_5, whereas a surplus of P_3N_5 and 1 eq. NH_4F, later serving as a mineralizing agent, are employed. The synthesis is assumed to follow the reaction equation (1), in which the surplus and mixed occupation are not accounted for and further details of the multi-anvil setup are given in the Experimental Section in the Supporting Information.

$$8\ Ta_3N_5 + P_3N_5 + NH_4F \rightarrow 3\ Ta_8PN_{13} + 3\ N_2 + HF \qquad (1)$$

The reaction yields a black microcrystalline powder, which is stable towards air and moisture. Single crystals are rod-shaped and around 2 µm in width and 10 µm in length (Figure 5.1, Figure D.1).

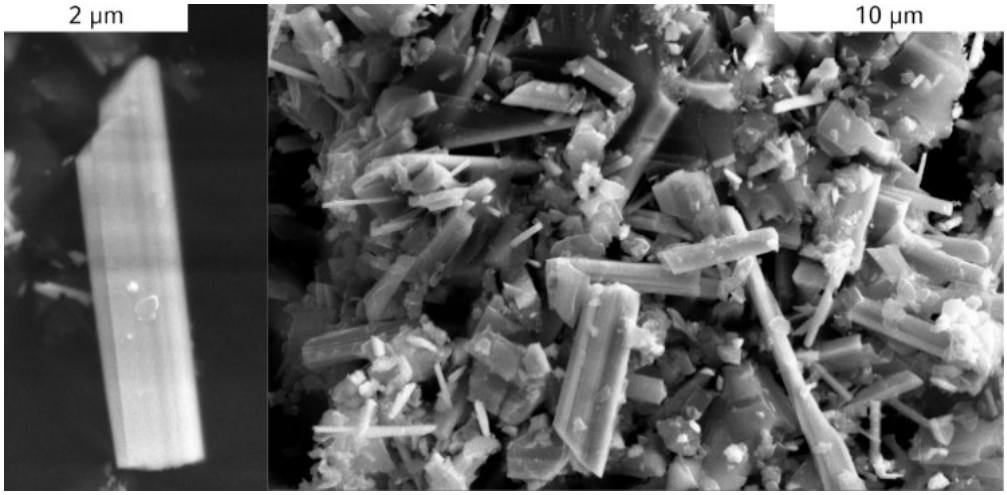

Figure 5.1. Secondary electron image of single crystals of $P_{1-x}Ta_{8+x}N_{13}$ (x = 0.1–0.15). Crystals are around 2 µm in width and up to 10 µm in length.

5.4.2. Crystal Structure Determination

The crystal structure of $P_{1-x}Ta_{8+x}N_{13}$ (x = 0.1–0.15) was solved and refined from single-crystal X-ray diffraction (SCXRD) data in the monoclinic space group $C2/m$ (no. 12), a = 16.202(3) Å, b = 2.9155(4) Å, c = 11.0893(18) Å, β = 126.698(7)°, Z = 2, R_1 = 0.0586; more details can be found in the Supporting Information. A tilt series of selected area electron diffraction (SAED) patterns matches simulations and confirms unit cell metrics (Figure D.2). Rietveld refinements on powder X-ray diffraction (PXRD) data were used to analyze the phase compositions (Figure D.4). No traces of crystalline side phases are present even while working in surplus of phosphorus. Electron microscopy gives no indication for amorphous side phases. High-temperature PXRD demonstrates stability up to at least 900 °C in air and reveals a minor thermal expansion of less than 15% in cell volume up to 900 °C (Figure D.5). The elemental composition was analyzed by energy dispersive X-ray spectroscopy (EDX) and SEM-EDX measurements indicate a minor amount of oxygen in the compound (Table D.6), which is congruent with reports that tantalum nitrides are very susceptive to incorporating oxygen impurities.[80-81] Slight compositional variations cannot be ruled out so a phase width according to $P_{1-x}Ta_{8+x}N_{13-y}O_y$ (x = 0.1–0.15, $y \leq 1$) could be considered.

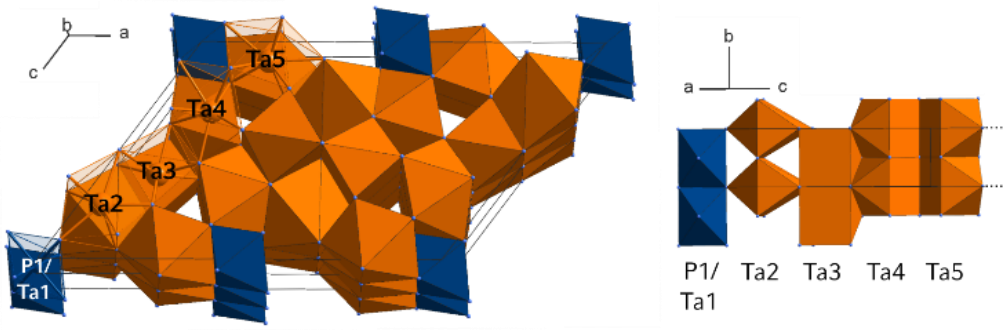

Figure 5.2. The crystal structure consists of a three-dimensional network of TaN_7- and TaN_8-polyhedra (orange) and $(P/Ta)N_6$ octahedra (blue). Left: Two unit cells stacked along the b axis. Right: Section of unit cell displaying the edge-(Ta2) and face-sharing (Ta3–Ta5) of Ta-centered polyhedra along b. Atom sites are partially denoted.

5.4.3. Structure Description

The structure of $P_{1-x}Ta_{8+x}N_{13}$ (x = 0.1–0.15) can be described as a network of face- and edge-sharing Ta-centered polyhedra. Small vacant three-membered rings form condensed channels along *b* and P atoms occupy edge-sharing octahedra (Figure 5.2). The structure shows a striking similarity with the high-pressure polymorph Ta_3N_5 (*Pnma*, U_3Te_5 type structure, Figure D.6). Both structures exhibit a similar condensed network with small vacant channels and a short *b* axis that spans one Ta-centered polyhedron ($P_{1-x}Ta_{8+x}N_{13}$: 2.9155(4) Å, HP-Ta_3N_5; 2.691(5) Å).

Four crystallographic distinct Ta sites are seven or eightfold coordinated by nitrogen, respectively. Ta2 and Ta3 form capped trigonal prisms (CN = 7) and Ta4, as well as Ta5 form dicapped trigonal prisms (CN = 8). Polyhedra predominantly share faces along *b* while edge-sharing prevails along the [010] plane. $d_{Ta–N}$ (Ta2–Ta5) range from 2.10(5) to 2.49(4) Å and are in agreement with other tantalum nitrides.[7, 9, 18] Trigonal prisms are a well-known coordination motif in binary and ternary tantalum nitrides and capped versions are observed in the high-pressure phases, e.g. Ta_3N_5 (*Pnma*) and *η*-Ta_2N_3 (*Pnma*).[17] All coordination polyhedra are illustrated in Figure D.7.

PN_6 octahedra share edges along the *b* axis. The phosphorus site exhibits a mixed occupation of P_{1-x} and Ta_x with x = 0.1–0.15, which is derived from single-crystal data. $d_{P–N}$ range from 1.78(4) Å to 1.94(3) Å, and mean interatomic $d_{P–N}$ distances are longer compared to other phases with PN_6 octahedra, e.g., β-BP_3N_6 (1.81(4) Å, atmospheric pressure).[79] The mixed occupation of P and Ta is most likely the reason for this increase, as the atomic radius for Ta^{+V} (64 pm) is almost double in size compared to P^{+V} (38 pm), which significantly expands the volumes of the octahedra. The structural motif of PN_6-octahedron is characteristic of high-pressure phases obtained in diamond anvil cells (~40–140 GPa).[77-79] $P_{1-x}T_{8+x}N_{13}$ (x = 0.1–0.15) demonstrates that a suitable network makes it possible to stabilize this characteristic high-pressure motif already at significantly lower pressures (<20 GPa).

The structure model has been validated by scanning transmission electron microscopy high-angle annular dark-field (STEM-HAADF) images with a Z-contrast according to Z^2 (Z_P = 15, Z_{Ta} = 73).[82] STEM-HAADF images along [010] show consistent intensity for all Ta positions and positions with almost no intensity. Latter can be assigned to the P1 site by an atomic resolution EDX map (Figure 5.3 a). The occupational disorder of Ta and P is clearly visible as high intensity occupies

the P1 site. A dedicated intensity profile of the EDX map shows that P1 positions occupied by Ta experience a clear loss of P-EDX signal and an increase in Ta-EDX signal (Figure 5.3 b). Three different magnifications indicate that the disorder occurs throughout the whole crystal (Figure 5.3 c).

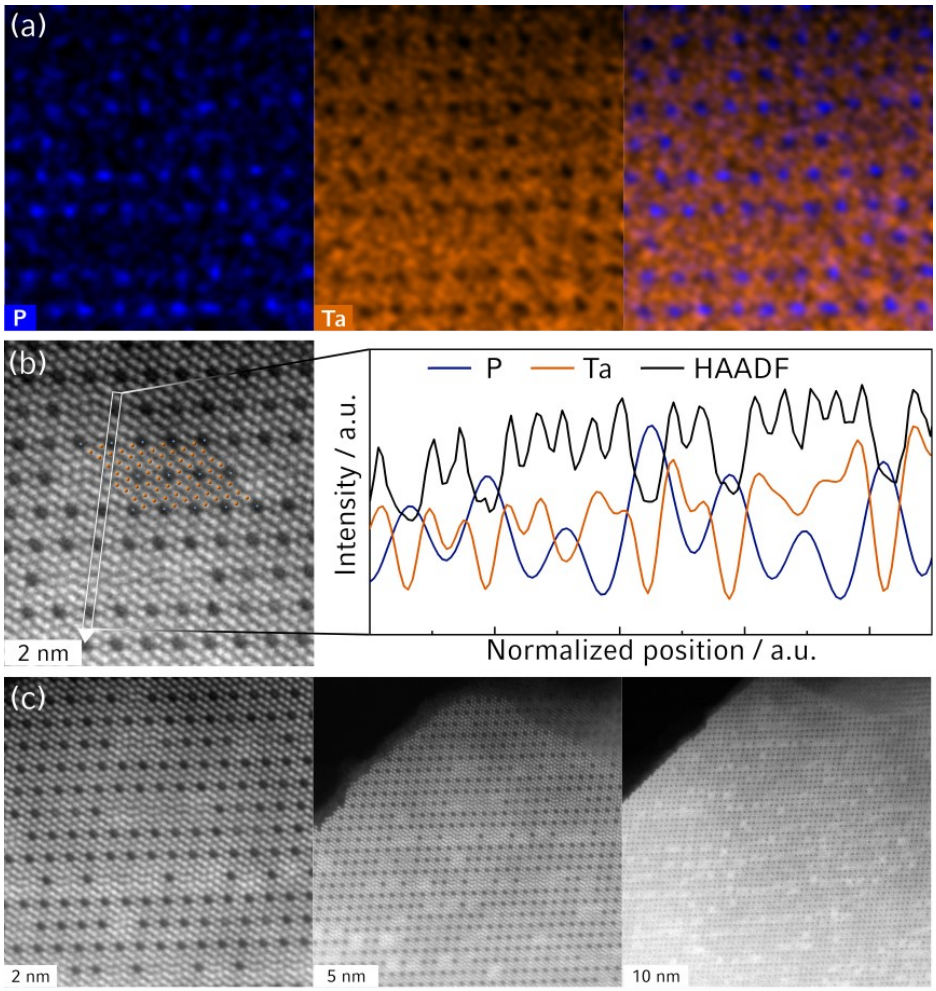

Figure 5.3. STEM-HAADF analysis of $P_{1-x}Ta_{8+x}N_{13}$ (x = 0.1–0.15) along [010]; **(a)** atomic resolution EDX map of P (blue), Ta (orange), and combined map; **(b)** STEM-HAADF image with structure overlay (left) and a combined line scan of the STEM-HAADF signal with EDX signal. Different intensities correspond to two different occupancies of atom columns by Ta and P atoms. Areas with high intensity exhibit Ta signal in the map and areas with low intensity exhibit P signal; **(c)** different magnifications. More details and enlarged versions are given in Figures D.8–D.11.

5.4.4. Magnetic Measurements

We observe poor metallic conduction with a large specific resistivity ρ(T) in the order of 10^{-1} Ω cm (Figure 5.4 a). The increase is linear with increasing temperature, and $P_{1-x}Ta_{8+x}N_{13}$ (x = 0.1–0.15) shows a metallic behavior even though the resistivity is way higher compared to conventional metals (≈ 10^{-8} Ω cm). The order of the specific resistivity is similar to some bivalent transition metal oxides, e.g., Magnéli type oxides.[83] $d_{Ta–Ta}$ distances (2.9155(5)–3.099(5) Å) are short and in the range of Ta–Ta bonds known from metallic tantalum and ϑ-,ε-TaN (2.86–2.91 Å). The conductivity is believed to originate from the limited 5*d* electrons of Ta that do not contribute to covalent Ta–N bonds. A diffuse reflectance spectrum shows strong optical absorption already in the near IR regime, due to excitable states around the Fermi-level E_F, further emphasizing the metallic character of the material (Figure D.12). Further information follows in the paragraph about the Density Functional Theory calculations.

Magnetic susceptibility measurements show a paramagnetic behavior down to low temperatures with an effective magnetic moment of μ_{eff} = 2.41(2) μ_B per formula unit obtained from a Curie Weiss fit of the inverse molar susceptibility (Figure D.13). The magnetization isotherm shows no sign of superconducting or ferromagnetic impurities (Figure D.14). The EPR spectrum lacks distinct features, suggesting the absence of unpaired electrons from tantalum atoms (Figure D.15).

5.4.5. Bader Charge Population Analysis

We conducted a Bader charge population analysis, to quantify the transferred electronic charge and to determine the electronic state of the Ta atoms.[74-76] Based on the obtained structure model of PTa_8N_{13} (mixed occupation not taken into account) the cation sites exhibit values from +2.07e to +2.30e (Ta) and +2.83e (P), and values for all N atoms range from –1.49e to –1.65e. This demonstrates the occurring charge transfer from Ta/P to N atoms. These values can be compared to a group of tantalum nitrides known from the literature (Figure 5.4 b [7, 14, 16-18, 84-85]). Bader charges for tantalum nitrides with an assignable oxidation state of Ta^{+V} and Ta^{+III} range from 2.27e to 2.67e (HP-Ta_3N_5, Ta_3N_5, δ-TaON) and from 1.57e to 1.94e (θ-, δ-TaN), respectively. Ta_2N_3 is described with Ta in the formal oxidation states of +4.56(5) and +4.47(5), and Bader charges range from 2.20e

to 2.31e. ε-TaN exhibits a wider range of Bader charges with metallic (0.80e) to ionic (2.23e) bonds. We conclude that the Ta atoms in $P_{1-x}Ta_{8+x}N_{13}$ (x = 0.1–0.15) experience almost the same electronic environment. Bader charges are close to values for +4.5 and +5 for the electronic states but an assignment is not straightforward possible. All Bader charges and valence electron values are given in Tables D.7–D.8.

5.4.6. Density Functional Theory and Electron Localization Function Calculations

Density Functional Theory (DFT) calculations (mixed occupation not considered) were carried out (Figure 5.4 c) and partial DOS calculations for all atom types and some pairs of atoms are given in Figures D.17–D.19. The composition of the valence band ranges from –12 to 0 eV (Figure 5.4 c) and mainly consists of nitrogen sites with *p* character and tantalum sites with *d* character. The fraction of phosphorus states in the total Density of States (DOS) is low and *s*, *p*, and *d* states of phosphorus are hybridized within the valence band. PTa_8N_{13} predominantly shows ionic bonding between phosphorus and nitrogen atoms. The *p* and *d* states of the P1 site are degenerated and *p* valence bands of nitrogen atoms (N1, N7) contain significantly more electronic states, leading to an electron localization near the N atoms. Bonds between tantalum and the nitrogen atoms (N2/N4–N6) exhibit a combination of ionic and covalent characteristics. *p* valence bands of N2/N4–N6 have more electronic states than the *d* band of tantalum atoms, and these, too, are degenerated across the valence band. Interactions between Ta2/3 and N3 predominantly form covalent bonds without significant ionic components, because *d* valence bands of tantalum have comparable electronic states to the *p* valence band of nitrogen N3. The powder sample has a dark optical appearance which aligns with the *d* states of tantalum at the Fermi energy E_F. Additionally, there are states from an interstitial region that cannot be decomposed into orbital-like bands. Calculations using the Electron Localization Function (ELF) support the findings of the DOS calculations. They reveal that valence electrons of tantalum are not incorporated into Ta–N bonds. Instead, electron density is concentrated between clusters of three tantalum atoms. This can be observed in two spatial orientations: Firstly, electrons localize in small channels, as seen in Figure 5.4 d on the left, and secondly, they appear in small vacant areas within the structure, as illustrated on the right side of Figure 5.4 d.

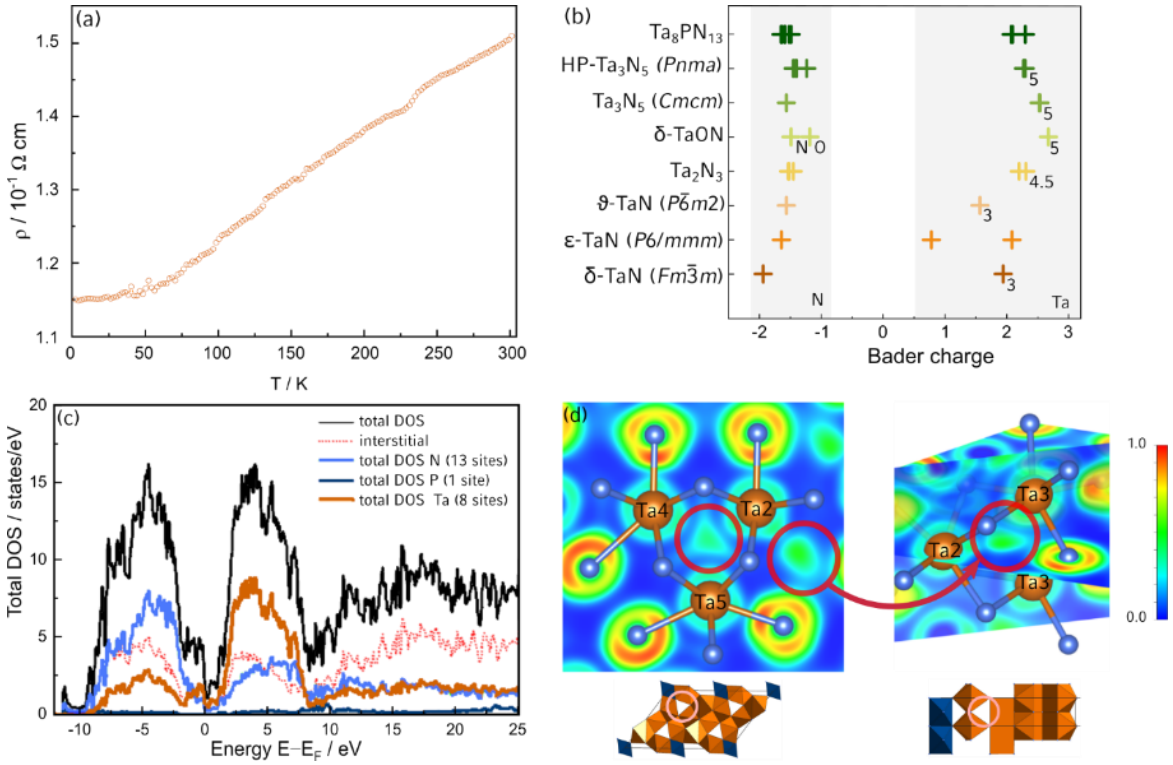

Figure 5.4. (a) Temperature dependence of the electric resistivity for $P_{1-x}Ta_{8+x}N_{13}$ (x = 0.1–0.15) follows a typical conductor; **(b)** Bader charge analysis results for PTa_8N_{13} compared to tantalum (oxo)nitride compounds known from literature; **(c)** Total Density of States calculation of PTa_8N_{13}. The valence band consists mainly of the *p* character of N sites and *d* character of Ta sites, *d* states of Ta cross E_F; total DOS from –40 to 25 eV is given in Figure D.16; **(d)** ELF isosurfaces display electron density located in between groups of three Ta atoms inside small three-membered channels (left) and vacant spots inside the structure (right), Ta: orange, N: light blue.

5.5. Conclusion

In summary, $P_{1-x}Ta_{8+x}N_{13}$ (x = 0.1–0.15) stands out as a ternary transition metal nitride containing phosphorus. Our study encompasses bulk synthesis through a high-pressure high-temperature approach, structural elucidation, as well as investigations into magnetic and electric properties. The condensed $TaN_{7/8}$-polyhedra network incorporates edge-sharing PN_6 octahedra. Electron microscopy directly illustrates the P/Ta disorder. Measurements and calculations suggest positive polarized Ta atoms with a marginal distinct electronic environment for different coordination states. $P_{1-x}Ta_{8+x}N_{13}$ serves as a model structure, with a bonding situation experiencing both covalent and metallic character. As a consequence, this allows for the exploration of unconventional physical properties, like a high resistivity with metallic character. We expect that further research on the variation of the *TM*/P ratio and on the incorporation of phosphorus into other promising transition metal systems can provide valuable insight into chemical and physical properties and result in favorable properties like catalytic performance, strong light absorption in the visible range, and electron conductivity. This seems close as transition metal nitrides already offer desirable bandgaps with relevance for solar energy applications and photo(electro)catalytic energy conversion. Further, transition metal-phosphorus-based materials gain more and more attention due to their potential in sustainable energy, including water electrolysis, and metal-air batteries.[86-87]

Supporting Information

Deposition number 2345638 contains the supplementary crystallographic data for this paper. These data are provided free of charge by the joint Cambridge Crystallographic Data Centre and Fachinformationszentrum Karlsruhe Access Structures service.

Acknowledgements

We thank Kristian Witthaut, Amalina Buda and Dominik Werhahn (Department of Chemistry at LMU Munich) for ELF calculations, SEM investigations and preliminary susceptibility measurements. We thank Katherine R. Fisher for helping measuring and analyzing the Electron Paramagnetic Resonance data. Financial support by the Deutsche Forschungsgemeinschaft DFG. The authors acknowledge funding support from the Deutsche Forschungsgemeinschaft (DFG, German Research Foundation) under Germany's Excellence Strategy-EXC 2089/1-390776260 (e-Con-version) as well as the projects projects SCHN 377/18-1 and OE 530/6-1. Furthermore, we thank the Natural Sciences and Engineering Research Council of Canada (NSERC) and the Canada Research Chair program for their financial support. We also thank the Graham HPC cluster and the Digital Research Alliance of Canada for providing computing resources.

5.6. References

[1] Y. Zhong, X. Xia, F. Shi, J. Zhan, J. Tu, H. J. Fan, *Adv. Sci.* **2016**, *3*, 1500286.

[2] A. L. Greenaway, C. L. Melamed, M. B. Tellekamp, R. Woods-Robinson, E. S. Toberer, J. R. Neilson, A. C. Tamboli, *Annu. Rev. Mater. Res.* **2021**, *51*, 591–618.

[3] Y. Xiao, C. Feng, J. Fu, F. Wang, C. Li, V. F. Kunzelmann, C.-M. Jiang, M. Nakabayashi, N. Shibata, I. D. Sharp, *Nat. Catal.* **2020**, *3*, 932–940.

[4] C.-M. Jiang, L. I. Wagner, M. K. Horton, J. Eichhorn, T. Rieth, V. F. Kunzelmann, M. Kraut, Y. Li, K. A. Persson, I. D. Sharp, *Mater. Horiz.* **2021**, *8*, 1744–1755.

[5] F. S. Hegner, A. Cohen, S. S. Rudel, S. Kronawitter, M. Grumet, X. Zhu, R. Korobko, L. Houben, C.-M. Jiang, W. Schnick, G. Kieslich, O. Yaffe, I. D. Sharp, D. A. Egger, *Adv. Energy Mater.* **2024**, *14*, 2470077.

[6] G. Brauer, W. Kiliani, *Z. Anorg. Allg. Chem.* **1979**, *452*, 17–26.

[7] N. Terao, *Jpn. J. Appl. Phys.* **1971**, *10*, 248.

[8] L. Conroy, A. N. Christensen, *J. Solid State Chem.* **1977**, *20*, 205–207.

[9] N. Schönberg, W. Overend, A. Munthe-Kaas, N. A. Sörensen, *Acta Chem. Scand.* **1954**, *8*, 1217–1221.

[10] G. Brauer, K. H. Zapp, *Z. Anorg. Allg. Chem.* **1954**, *277*, 129–139.

[11] A. N. Christensen, B. Lebech, *Acta Crystallogr., Sect. B: Struct. Crystallogr. Cryst. Chem.* **1978**, *34*, 261–263.

[12] J. Gatterer, G. Dufek, P. Ettmayer, R. Kieffer, *Monatsh. Chem.* **1975**, *106*, 1137–1147.

[13] T. Mashimo, S. Tashiro, T. Toya, M. Nishida, H. Yamazaki, S. Yamaya, K. Oh-Ishi, Y. Syono, *J. Mater. Sci.* **1993**, *28*, 3439–3443.

[14] G. Brauer, E. Mohr, A. Neuhaus, A. Skokan, *Monatsh. Chem.* **1972**, *103*, 794–798.

[15] T. Mashimo, S. Tashiro, *J. Mater. Sci. Lett.* **1994**, *13*, 174–176.

[16] A. Y. Ganin, L. Kienle, G. V. Vajenine, *Eur. J. Inorg. Chem.* **2004**, *2004*, 3233–3239.

[17] A. Zerr, G. Miehe, J. Li, D. A. Dzivenko, V. K. Bulatov, H. Höfer, N. Bolfan-Casanova, M. Fialin, G. Brey, T. Watanabe, *Adv. Funct. Mater.* **2009**, *19*, 2282–2288.

[18] N. E. Brese, M. O'Keeffe, P. Rauch, F. J. DiSalvo, *Acta Crystallogr., Sect. C: Cryst. Struct. Commun.* **1991**, *47*, 2291–2294.

[19] H. Alkhaldi, P. Kroll, *J. Phys. Chem. C* **2020**, *124*, 22221–22227.

[20] R. Niewa, D. A. Zherebtsov, H. Borrmann, R. Kniep, *Z. Anorg. Allg. Chem.* **2002**, *628*, 2505–2508.

[21] C. Wachsmann, H. Jacobs, *J. Alloys Compd.* **1992**, *190*, 113–116.

[22] P. Höhn, R. Kniep, J. Maier, *Angew. Chem. Int. Ed.* **1993**, *9*, 1350–1352.

[23] F. K.-J. Helmlinger, P. Höhn, R. Kniep, *Z. Naturforsch., B: J. Chem. Sci.* **1993**, *48*, 1015–1018.

[24] H. Jacobs, E. Von Pinkowski, *J. Less-Common Met.* **1989**, *146*, 147–160.

[25] T. Brokamp, H. Jacobs, *J. Alloys Compd.* **1992**, *183*, 325–344.

[26] S. Clarke, F. DiSalvo, *J. Solid State Chem.* **1997**, *132*, 394–398.

[27] H. Holleck, F. Thümmler, *Monatsh. Chem.* **1967**, *98*, 133–134.

[28] U. Zachwieja, H. Jacobs, *Eur. J. Solid State Inorg. Chem.* **1991**, *28*, 1055–1062.

[29] R. Trócoli, C. Frontera, J. Oró-Solé, C. Ritter, P. Alemany, E. Canadell, M. R. Palacín, J. Fontcuberta, A. Fuertes, *Chem. Mater.* **2022**, *34*, 6098–6107.

[30] R. Niewa, D. A. Zherebtsov, W. Schnelle, F. R. Wagner, *Inorg. Chem.* **2004**, *43*, 6188–6194.

[31] L. Cario, Z. A. Gál, T. P. Braun, F. J. DiSalvo, B. Blaschkowski, H. J. Meyer, *J. Solid State Chem.* **2001**, *162*, 90–95.

[32] N. E. Brese, F. J. DiSalvo, *J. Solid State Chem.* **1995**, *120*, 378–380.

[33] W. Jeitschko, H. Nowotny, F. Benesovsky, *Monatsh. Chem.* **1964**, *95*, 1242–1246.

[34] G. Brauer, R. Lesser, *Int. J. Mater. Res.* **1959**, *50*, 512–515.

[35] L. Eisenburger, V. Weippert, C. Paulmann, D. Johrendt, O. Oeckler, W. Schnick, *Angew. Chem. Int. Ed*. **2022**, *61*, e202202014.

[36] S. D. Kloß, O. Janka, T. Block, R. Pöttgen, R. Glaum, W. Schnick, *Angew. Chem. Int. Ed.* **2019**, 58, 4685–4689.

[37] A. Stock, H. Grüneberg, *Ber. Dtsch. Chem. Ges.* **1907**, *40*, 2573–2578.

[38] G. Brauer, J. Weidlein, J. Strähle, *Z. Anorg. Allg. Chem.* **1966**, *348*, 298–308.

[39] D. Rubie, *Phase Transitions* **1999**, *68*, 431–451.

[40] H. Huppertz, *Z. Kristallogr.* **2004**, *219*, 330–338.

[41] D. Walker, *Am. Mineral.* **1991**, *76*, 1092–1100.

[42] D. Walker, M. Carpenter, C. Hitch, *Am. Mineral.* **1990**, *75*, 1020–1028.

[43] H. M. Rietveld, *J. Appl. Crystallogr.* **1969**, *2*, 65–71.

[44] A. Coelho, TOPAS Academic version 6.1, **2007**.

[45] Bruker-AXS, APEX3, version 2016.5-0, Karlsruhe, **2001**.

[46] G. M. Sheldrick, *Acta Crystallogr., Sect. C: Cryst. Struct. Commun.* **2015**, *71*, 3–8.

[47] C. B. Hübschle, G. M. Sheldrick, B. Dittrich, *J. Appl. Crystallogr.* **2011**, *44*, 1281–1284.

[48] DigitalMicrograph, Gatan, Pleasanton, California, **1999**.

[49] J. L. Lábár, *Ultramicroscopy* **2005,** *103*, 237–249.

[50] P. A. Stadelmann, jEMS software package, Saas-Fee, **2008**.

[51] Thermo Fisher Scientific, Velox, version 3, Waltham, Massachusetts, **2021**.

[52] Quantum Design Inc., version 1.5.11 ed., San Diego, **2013**.

[53] K. Schwarz, P. Blaha, G. K. H. Madsen, *Comput. Phys. Commun.* **2002,** *147*, 71–76.

[54] K. Schwarz, *J. Solid State Chem.* **2003,** *176*, 319–328.

[55] P. Blaha, K. Schwarz, F. Tran, R. Laskowski, G. K. H. Madsen, L. D. Marks, *J. Chem. Phys.* **2020**, 074101.

[56] K. Schwarz, P. Blaha, S. B. Trickey, *Mol. Phys.* **2010,** *108*, 3147–3166.

[57] J. O. Dimmock in *Solid State Phys.*, Vol. 26 (Eds.: H. Ehrenreich, F. Seitz, D. Turnbull), Elsevier, **1971**, pp 103–274.

[58] O. K. Andersen, *Phys. Rev. B* **1975**, 3060.

[59] D. D. Koelling, G. O. Arbman, *J. Phys. F: Met. Phys.* **1975,** *5*, 2041.

[60] E. Sjöstedt, L. Nordström, D. J. Singh, *Solid State Commun.* **2000,** *114*, 15–20.

[61] G. K. H. Madsen, P. Blaha, K. Schwarz, E. Sjöstedt, L. Nordström, *Phys. Rev. B* **2001,** *64*, 195134.

[62] J. P. Perdew, K. Burke, M. Ernzerhof, *Phys. Rev. Lett.* **1996,** 77, 3865–3868.

[63] F. Tran, P. Blaha, K. Schwarz, P. Novák, *Phys. Rev. B* **2006,** *74*, 155108.

[64] F. Tran, P. Blaha, *Phys. Rev. B* **2011,** *83*, 235118.

[65] G. Kresse, J. Hafner, *Phys. Rev. B* **1993,** *47*, 558.

[66] G. Kresse, J. Hafner, *Phys. Rev. B* **1994,** *49*, 14251.

[67] G. Kresse, J. Furthmüller, *Comput. Mat. Sci.* **1996,** *6*, 15–50.

[68] G. Kresse, *Phys. Rev. B* **1996,** *54*, 169.

[69] G. Kresse, D. Joubert, *Phys. Rev. B* **1999,** *59*, 1758.

[70] P. E. Blöchl, *Phys. Rev. B* **1994,** *50*, 17953–17979.

[71] H. J. Monkhorst, J. D. Pack, *Phys. Rev. B* **1976,** *13*, 5188.

[72] W. H. Press, B. P. Flannery, S. A. Teukolsky, W. T. Vetterling, *Numerical Recipes*, Cambridge Univ. Press, New York, **1986**.

[73] B. Silvi, A. Savin, *Nature* **1994,** *371*, 683–686.

[74] R. F. Bader, *Acc. Chem. Res* **1985,** *18*, 9–15.

[75] R. Bader, W. H. Henneker, P. E. Cade, *J. Chem. Phys.* **1967**, *46*, 3341–3363.

[76] G. Henkelman, A. Arnaldsson, H. Jónsson, *Comput. Mater. Sci.* **2006,** *36*, 354–360.

[77] S. Vogel, M. Bykov, E. Bykova, S. Wendl, S. D. Kloß, A. Pakhomova, N. Dubrovinskaia, L. Dubrovinsky, W. Schnick, *Angew. Chem.* **2020**, *59*, 2752–2756.

[78] D. Laniel, F. Trybel, A. Néri, Y. Yin, A. Aslandukov, T. Fedotenko, S. Khandarkhaeva, F. Tasnádi, S. Chariton, C. Giacobbe, *Chem. Eur. J.* **2022**, *28*, e202201998.

[79] S. Vogel, M. Bykov, E. Bykova, S. Wendl, S. D. Kloß, A. Pakhomova, S. Chariton, E. Koemets, N. Dubrovinskaia, L. Dubrovinsky, *Angew. Chem. Int. Ed*. **2019**, *58*, 9060–9063.

[80] J. Wang, J. Jiang, J. Chen, Y. Li, A. Ma, *Comput. Mater. Sci.* **2018**, *143*, 368–373.

[81] S. J. Henderson, A. L. Hector, *J. Solid State Chem.* **2006**, *179*, 3518–3524.

[82] S. Pennycook, *Annu. Rev. Mater. Sci.* **1992**, *22*, 171–195.

[83] P. Hagenmuller, *Prog. Solid State Chem.* **1971**, *5*, 71–144.

[84] A. Salamat, K. Woodhead, S. I. U. Shah, A. L. Hector, P. F. McMillan, *Chem. Comm.* **2014**, *50*, 10041–10044.

[85] T. Lüdtke, A. Schmidt, C. Göbel, A. Fischer, N. Becker, C. Reimann, T. Bredow, R. Dronskowski, M. Lerch, *Inorg. Chem.* **2014**, *53*, 11691–11698.

[86] Z. Cheng, W. Qi, C. H. Pang, T. Thomas, T. Wu, S. Liu, M. Yang, *Adv. Funct. Mater.* **2021**, *31*, 2100553.

[87] H. Zhao, Z.-Y. Yuan, *Catal. Sci. Technol.* **2017**, *7*, 330–347.

Chapter 6

Conclusion and Outlook

6.1. Prospects on the Synthesis of Nitrides and Nitridophosphates

In this work, the group of nitridophosphate-based structures was expanded by $SrAl_5P_4N_{10}O_2F_3$ (Chapter 2), the isostructural series $AE_2AlP_8N_{15}NH$ (*AE* = Ca, Sr, Ba, Chapter 3), and $Cr_{5.7}Si_{2.3}P_8N_{24}$ (Chapter 4). Additionally, the ternary transition metal phosphorus nitride $P_{1-x}Ta_{8+x}N_{13}$ (x = 0.1–0.15, Chapter 5) could be obtained. The structural characterization of the six novel compounds was carried out by single-crystal X-ray diffraction and STEM-HAADF analysis. A routine SCXRD-STEM workflow combining X-ray data acquisition with electron microscopy atomic resolution *Z*-contrast imaging and elemental mapping was established.

All compounds were synthesized by the NH_4F-mediated high-pressure high-temperature route, an established systematic approach to overcome the challenges associated with nitridophosphate syntheses (Chapter 1.2). This approach involves applying pressures ranging from 5 to 12 GPa and temperatures up to 1400 °C. Stable and readily available nitrides such as Cr_2N, Si_3N_4, and AlN, as well as reactive azides like $Sr(N_3)_2$ and $Ba(N_3)_2$, serve as suitable starting materials. These synthesis conditions facilitate the partial reduction of transition metals, such as tantalum from Ta(V) (Ta_3N_5) to a formal oxidation state of +4.25 in $P_{1-x}Ta_{8+x}P_{13}$, and the oxidation of Cr_2N with a formal oxidation state of +1.5 to Cr(IV) in $Cr_{5.7}Si_{2.3}P_8N_{24}$. This suggests that synthesis conditions can vary between reducing and oxidizing atmospheres depending on the starting materials, pressure, and temperature conditions applied. The versatility of high-pressure chemistry has yielded a great number of nitridophosphate network compounds. Moreover, beyond these anionic networks, the transition metal phosphorus nitride $P_{1-x}Ta_{8+x}P_{13}$ demonstrates that motifs like 6-fold coordinated phosphorus, characteristic for syntheses in diamond-anvil cells, can be synthetically accessible within the pressure and temperature range achievable using large volume presses.

Future variation of synthesis conditions by the selection of starting materials, cation ratio (*M*:P) and reaction conditions undoubtedly allow for the exploration of numerous phases. The pressure range provided by the large volume press technique has not been fully explored in this work. Higher pressures typically result in higher coordination numbers and denser networks. The successful stabilization of characteristic high-pressure motifs, such as PN_6 octahedra in $P_{1-x}Ta_{8+x}N_{13}$, by multianvil technique conditions is a promising outlook and further exploration expected to yield novel ternary or multinary phosphorus nitrides. Lower pressures can yield lower coordination numbers and less compact structures. This potentially provides access to mixed nitridic networks like nitridoalumophosphates, where aluminum is not octahedrally but tetrahedrally coordinated.

6.2. Prospects on Analytical Methods

Parallel to the synthetic progress, STEM-HAADF imaging and atomic resolution mapping was further applied to this class of materials. This led to the establishment of a routine SCXRD-STEM workflow. Single-crystal X-ray diffraction was utilized as the primary method for structural elucidation. Synchrotron data proved particularly beneficial when crystal sizes are too small for a laboratory single-crystal X-ray diffractometer. Laboratory X-ray data were evaluated for $SrAl_5P_4N_{10}O_2F_3$, $(Ca,Ba)_2AlP_8N_{15}NH$, and $P_{1-x}Ta_{8+x}N_{13}$, while synchrotron data were used for the structural elucidation of $Sr_2AlP_8N_{15}NH$ and $Cr_{5.7}Si_{2.3}P_8N_{24}$. Structures obtained from X-ray data were further verified by electron microscopy. Bright-field imaging provided information on crystal sizes and topology, diffraction methods verified cell metrics and EDX techniques identified elements and their respective atomic ratios. STEM-HAADF imaging confirmed the cationic structure and mixed occupancies of the atom combinations Cr/Si and Ta/P were revealed. Atomic resolution STEM EDX-mapping comprehensively analyzed the intricate disorder involving atoms with similar atomic form factors such as aluminum, silicon, and phosphorus.

These methods were complemented by additional analytical techniques and computational methods, providing valuable insights for a thorough structural analysis. Bond valence sum, charge distribution calculations and partial Madelung part of the lattice energy values were utilized to support cationic and anionic assignments. Infrared spectroscopy and nuclear magnetic resonance provided information on imide groups. Electron paramagnetic resonance spectroscopy aided in the determination of the rather unusual oxidation state of chromium(IV) in nitrides. Magnetic susceptibility measurements revealed Pauli paramagnetism in $Cr_{5.7}Si_{2.3}P_8N_{24}$ and $P_{1-x}Ta_{8+x}N_{13}$. Conductivity measurements quantified the metallic behavior and the high specific resistivity of $P_{1-x}Ta_{8+x}N_{13}$. Optical measurements including UV-Vis spectroscopy were used to determine the band gap of $Cr_{5.7}Si_{2.3}P_8N_{24}$ and further characterize the metallic behavior of $P_{1-x}Ta_{8+x}N_{13}$. Bader charge analysis, density functional theory calculations, and electron localization function analysis on $P_{1-x}Ta_{8+x}N_{13}$ revealed less localized 5d electrons of tantalum next to covalent and ionic bonding character between P/Ta and N atoms, that provided an explanation for the physiochemical behavior. Luminescence measurements of $SrAl_5P_4N_{10}O_2F_3$:Eu^{2+} and $AE_2AlP_8N_{15}(NH)$:Eu^{2+} (*AE* = Ca, Sr, Ba) showed emission in the green to blue region of the visible spectrum upon radiation with UV light and provided insights into the doping behavior of Eu^{2+} in nitridic alkaline-earth compounds.

Combining different analytical methods in a thoughtful manner and understanding the strengths of each method is crucial. The SCXRD-STEM combination optimally utilizes the strengths of both techniques. Synchrotron radiation and a nanofocused beam setup offer a structural elucidation with almost no limits set by crystallite sizes. A combination with temperature-dependent and low-temperature single-crystal measurements could further provide valuable insights into magnetically ordered phases, providing information on temperature-dependent structure-property relationships. Electron microscopy is often constrained by the beam stability of samples. Integrating the high-resolution low-dose method can render the analysis of beam-sensitive crystalline materials accessible.[1] In addition to STEM-HAADF analysis, a next logical step would be to incorporate electron energy loss spectroscopy (EELS) in the SCXRD-STEM process. This step allows gathering information regarding oxidation states and local environments directly through electron microscopy.

6.3. Prospects on the Structural Composition of Nitrides and Nitridophosphates

The structural overview of nitridophosphates in Chapter 1.2.2. and Figure 1.2 emphasizes the significance of the metal ion *M* to phosphorus P ratio, i. e. the cation ratio CR = N(*M*)/N(P), and the influence of the metal ion's nature on resulting structures. Coordination polyhedra around the metal and phosphorus cations serve as a basis for comparing structures and identifying patterns. The figure can now be updated to include two new structures – $Cr_{5.7}Si_{2.3}P_8N_{24}$ and $P_{1-x}Ta_{8+x}N_{13}$ – that align well with the presented trends. With a CR of 1, $Cr_{5.7}Si_{2.3}P_8N_{24}$ is expected to exhibit PN_4 tetrahedra connected in a chain-like manner, with a metal substructure characterized by coordination polyhedra around Cr and Si ions sharing common edges and vertices. This can be observed and the structure includes double chains of vertex-sharing PN_4 tetrahedra and ribbons of edge-sharing (Cr,Si)-centered octahedra. In contrast, $P_{1-x}Ta_{8+x}N_{13}$ is tantalum-rich (CR = 8), and the anticipated condensed Ta-centered polyhedra network is observed that stabilizes phosphorus with a six-fold coordination.

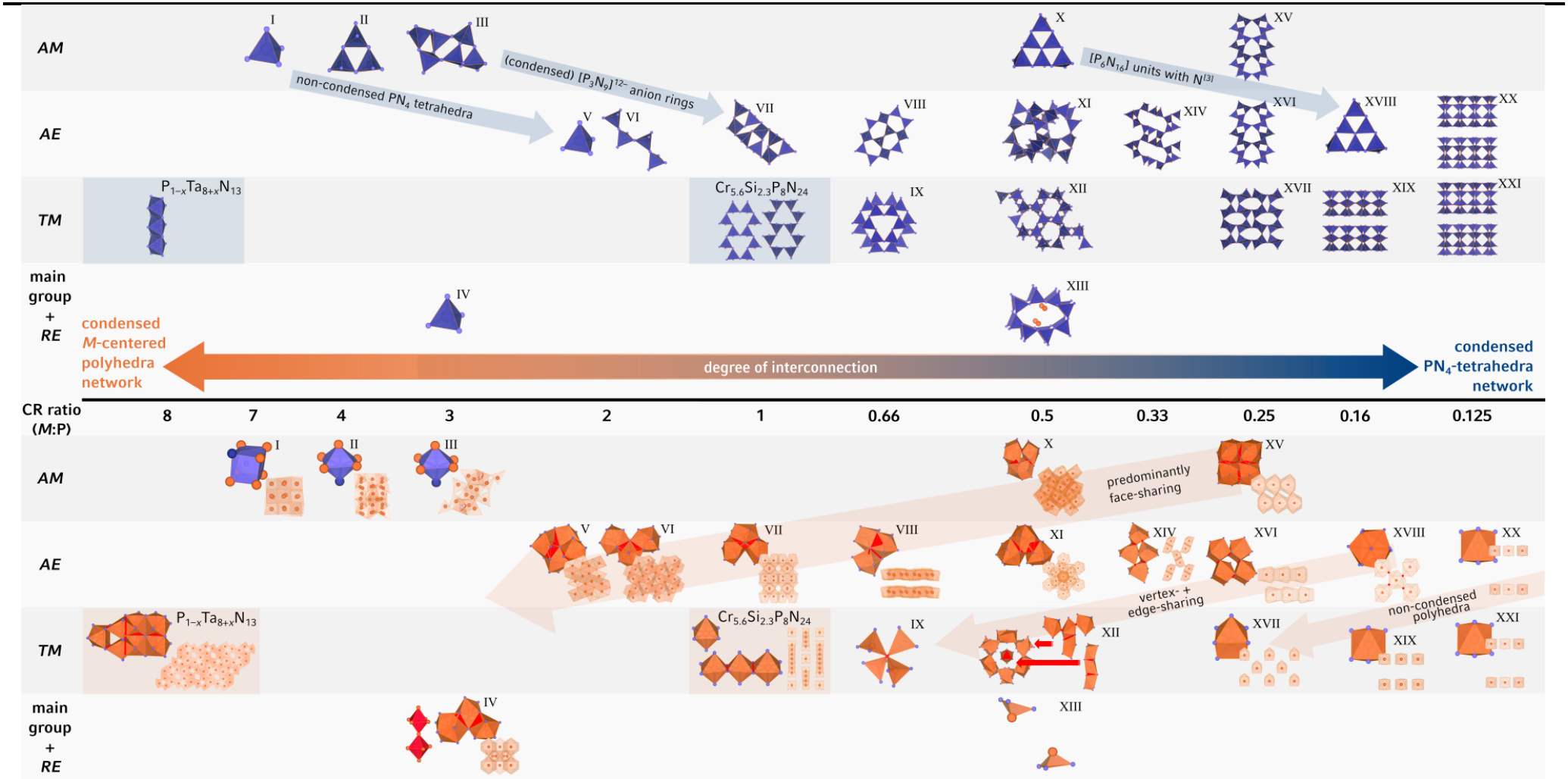

Figure 6.1. Updated Figure 1.2. showing the transition of structures with a dominating *M*-centered polyhedra structure to structures with a dominating PN_4 tetrahedra network depenting on the CR.; $P_{1-x}Ta_{8+x}N_{13}$ ($x \approx 0.1–0.15$) and $Cr_{5.7}Si_{2.3}P_8N_{24}$ are now included; the structures are sorted by CR (from 8 to 0.125) and by metal cation (*AM* = alkali metal, *AE* = alkaline-earth metal, *TM* = transition metal, *RE* = rare earth metal); structures are numbered by roman numerals with the respective sum formula given in Chapter 1.1.2.; *M*-centered coordination polyhedra (orange), PN_4 network (blue); *M* (orange), P (dark blue), N/O/F (bright blue), OHo_6 octahedra (red), $N(Li,P)_{6/8}$ polyhedra (bright blue); red highlights mark common faces, edges, and vertices of *M*-centered polyhedra for better visibilty.

As discussed in Chapter 1.1.3., magnesium and silicon were previously the only additional cations known in multicationic alkaline-earth (Ca, Sr, Ba) nitridophosphates. Alkaline-earth nitridophosphates are widely studied for their luminescent properties through activator ions like Eu^{2+} and multicationic alkaline-earth nitridophosphates contain Mg^{2+}, Al^{3+} and Si^{4+} as additional metal cations. The additional ions are large enough that they are not necessarily incorporated into the tetrahedra network, but too small to serve as a potential Eu^{2+} position. Concerning the cation ratio CR = N(*M*)/N(P), now the additional metal as well as the alkaline-earth ions contribute as counter cations to N(*M*). The available compositional range could be expanded to include aluminum (Figure 6.2). $SrAl_5P_4N_{10}O_2F_3$ features a high CR of 1.5, displaying a compact AlN_6 octahedra substructure of 10 edge-sharing octahedra, previously unknown in network compounds. The densely packed structure is apparent by the pronounced face- and edge-sharing of *M*-centered coordination polyhedra. In contrast, $AE_2AlP_8N_{15}(NH)$ (*AE* = Ca, Sr, Ba) exhibits a low CR of 0.375, leading to a significantly lower condensation of the *M*-centered polyhedra with sharing common vertices and edges and a less dense overall structure. Chapter 2 and 3 cover the structural analysis of the modified anionic tetrahedra networks in the two multicationic nitridophosphates. Emission in the visible range upon doping with Eu^{2+} is characterized and demonstrates the suitability of alkaline-earth aluminum nitridophosphates as a host lattices for rare-earth activator ions. Further studies on possible site-selectivity of doping due to differences in charge and ionic radii of Al^{3+} and AE^{2+} can result in modifying the luminescence not only by metal–ligand distances or coordination geometry, but also by choice of the emitter, such as Cr^{3+} on Al^{3+} sites and Eu^{2+} on AE^{2+} sites.[2-3]

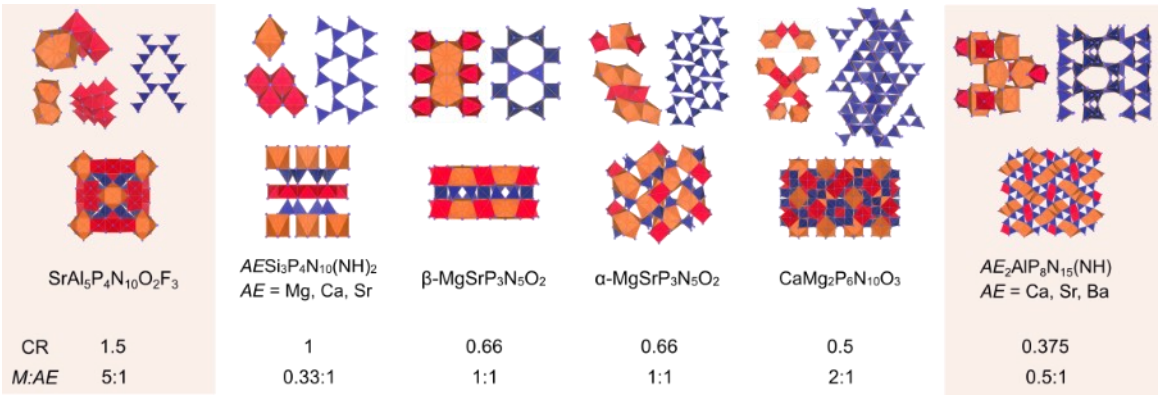

Figure 6.2. Updated version of known multinary alkaline-earth nitridophosphates; $SrAl_5P_4N_{10}O_2F_3$ and $AE_2AlP_8N_{15}(NH)$ (*AE* = Ca, Sr, Ba) are now included; Alkaline-earth-centered polyhedra (orange), $(Al/Si/Mg)(O,N)_6$ octahedra (red) and PN_4 tetrahedra (blue), for reasons of clarity, no distinction was made between N, O and F.

Figure 6.1 illustrates the unexplored compositional ranges within the groups of ternary nitridophosphates and phosphorus nitrides. Main group and rare-earth nitridophosphates remain limited, and the metal-rich side of nitridophosphates, irrespective of the metal cation, remains largely unexplored. Additionally, multinary nitridophosphates offer possibilities for discovering new structures with intriguing properties. By carefully selecting starting materials and synthesis conditions, compositional gaps can be filled. While some of these new structures may incorporate known and anticipated structural motifs, predicting solid-state structures remains challenging. However, the potential for discovering unforeseen structures with unexpected physiochemical properties emphasizes the importance of thorough structural analysis.

[1] J. P. Buban, Q. Ramasse, B. Gipson, N. D. Browning, H. Stahlberg, *J. Electron Microsc.* **2010,** *59*, 103–112.
[2] H. Zhou, H. Cai, J. Zhao, Z. Song, Q. Liu, *Inorg. Chem. Front.* **2022,** *9*, 1912–1919.
[3] E. O'Brannon III, Q. Williams, *Am. Mineral.* **2019,** *104*, 1656–1662.

Chapter 7

Summary

Tetra-Face-Capped Octahedra in a Tetrahedra Network – Structure Determination and Scanning Transmission Electron Microscopy of $SrAl_5P_4N_{10}O_2F_3$

Monika M. Pointner, Oliver Oeckler, and Wolfgang Schnick

published in: *Chem. Eur. J.* **2023**, *29*, e202301960, DOI: 10.1002/chem.202301960.

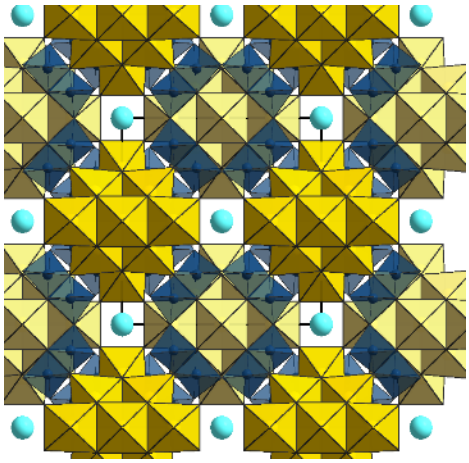

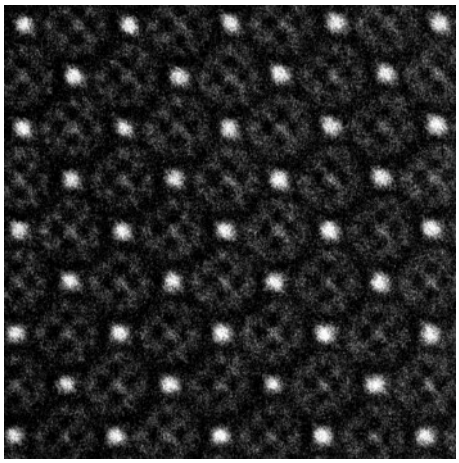

$SrAl_5P_4N_{10}O_2F_3$ was synthesized under high-temperature and high-pressure conditions at 1400 °C, and 5 GPa. $Sr(N_3)_2$, c-PON, P_3N_5, and AlN were used as starting materials, and NH_4F was utilized as a mineralizing agent. The crystal structure was elucidated by single-crystal X-ray diffraction. A three-dimensional vertex-sharing PN_4 tetrahedra network incorporates chains of face-sharing Sr^{2+}-centered cuboctahedra. Ten Al^{3+}-centered octahedra form a novel structure motif that can be described as a highly condensed tetra-face-capped octahedra-based unit. Atomic-resolution EDX mapping in combination with STEM *Z*-contrast images support the atom assignments. STEM-EDX mapping could confirm that Al and P occupy different sites in the crystal structure, which was further corroborated by bond valence sum calculations. Eu^{2+}-doped $SrAl_5P_4N_{10}O_2F_3$ shows blue emission when irradiated with UV light.

Tetrahedra Networks with Additional Cations – Isolated AlN_6 Octahedra in the Imidonitridophosphates $AE_2AlP_8N_{15}(NH)$ (*AE* = Ca, Sr, Ba)

Monika M. Pointner, Reinhard M. Pritzl, Jonas M. Albrecht, Leopold Blahusch, Jonathan P. Wright, Eleanor Lawrence Bright, Carlotta Giacobbe, Oliver Oeckler, and Wolfgang Schnick

published in: *Chem. Eur. J.* **2024**, e202400766, DOI: 10.1002/chem.202400766.

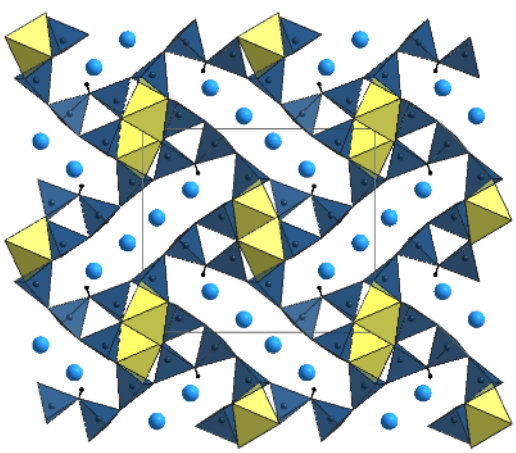

The isostructural imidonitridophosphates $AE_2AlP_8N_{15}(NH)$ (*AE* = Ca, Sr, Ba) were synthesized at high-pressure high-temperature conditions at 1400 °C and 5–9 GPa. Alkaline-earth metal nitrides or azides Ca_3N_2/$Sr(N_3)_2$/$Ba(N_3)_2$ and the binary nitrides AlN and P_3N_5 were used as starting materials and NH_4F served as a hydrogen source and mineralizing agent. The crystal structures were determined by in-house single-crystal X-ray diffraction and synchrotron radiation. A vertex-sharing PN_4 tetrahedra network forms diverse-sized rings that are occupied by non-condensed AlN_6 octahedra and alkaline-earth-centered polyhedra. Latter share common edges with the AlN_6 octahedra and edges, as well as vertices with each other. Atomic resolution STEM-HAADF imaging and EDX mapping could verify the assignment of phosphorus and aluminium to different crystallographic sites. Solid-state NMR and FTIR measurements further support the structure model. Eu^{2+}-doped samples show strong luminescence with narrow emissions in the range of green to blue under UV excitation.

$Cr_{5.7}Si_{2.3}P_8N_{24}$ – A Chromium(+IV) Nitridosilicate Phosphate with Amphibole-Type Structure

Monika M. Pointner, Katherine R. Fisher, Martin Weidemann, Florian Wolf, Jonathan Wright, Eleanor Lawrence Bright, Carlotta Giacobbe, Oliver Oeckler,* and Wolfgang Schnick*

published in: *Angew. Chem.* **2024**, *136*, e202401421, DOI: 10.1002/anie.202401421.
published in: *Angew. Chem. Int. Ed*. **2024**, *63*, e202401421, DOI: 10.1002/anie.202401421.

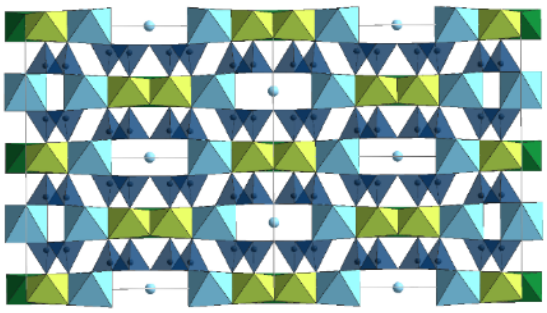

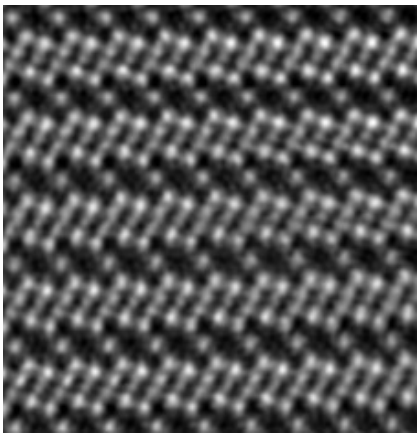

$Cr_{5.7}Si_{2.3}P_8N_{24}$ was synthesized under high-pressure high-temperature conditions at 1400 °C and 12 GPa. The binary nitrides Cr_2N, Si_3N_4 and P_3N_5, were used as starting materials and NH_4N_3 and NH_4F functioned as additional nitrogen source and mineralizing agent. The crystal structure was elucidated by single-crystal X-ray diffraction with microfocused synchrotron radiation. The elemental composition was analyzed by energy dispersive X-ray spectroscopy. The amphibole mineral-type structure consists of vertex-sharing PN_4 tetrahedra forming zweier double chains and edge-sharing (Si,Cr)-centered octahedra forming separated ribbons. STEM HAADF analysis showed ordered Si and Cr sites next to a disordered Si/Cr site. STEM-EDX mapping further indicates that phosphorus and silicon occupy different sites in the structure. Susceptibility and electron paramamagnetic resonance measurements support the oxidation state Cr^{+IV}.

$P_{1-x}Ta_{8+x}N_{13}$ (x = 0.1–0.15): A Phosphorus Tantalum Nitride With High Specific Resistivity Featuring Mixed-Valent Tantalum and P/Ta Disorder

Monika M. Pointner, Claude Ceniza, Martin Weidemann, Lukas Nusser, Florian Wolf, Lucien Eisenburger, Alexander Moewes, Oliver Oeckler,* and Wolfgang Schnick*

published in: *Angew. Chem.* **2024**, e202411441, DOI: 10.1002/ange.202411441.

published in: *Angew. Chem. Int. Ed.* **2024**, e202411441, DOI: 10.1002/ange.202411441.

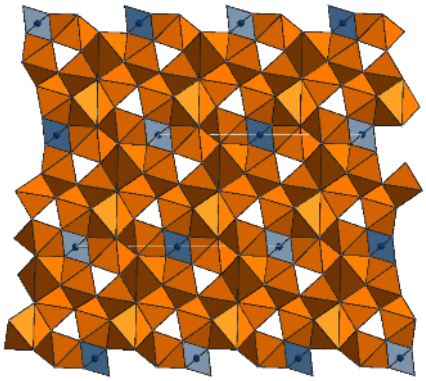

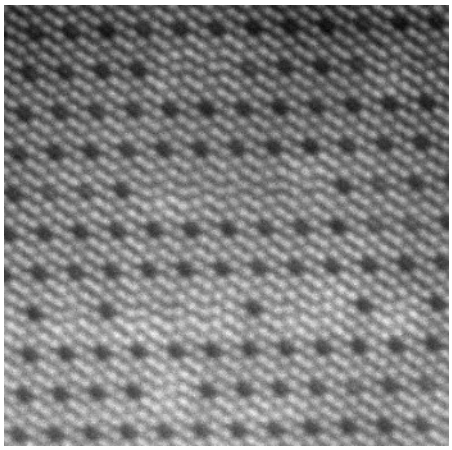

The phosphorus tantalum nitride $P_{1-x}Ta_{8+x}N_{13}$ (x = 0.1–0.15) was synthesized under high-pressure high-temperature conditions at 8 GPa, 1400 °C. The binary nitrides Ta_3N_5 and P_3N_5 were used as starting materials and NH_4F functions as a mineralizing agent. The single-crystal X-ray analysis of the black rod-shaped crystals was elucidated by single-crystal X-ray diffraction. The structure consists of a network of face- and edge-sharing Ta-centered polyhedra with small vacant channels and columns of edge-sharing PN_6 octahedra. Atomic scale STEM HAADF imaging and EDX-mapping reveals an unexpected P/Ta disorder. Electronic resistivity measurements show a high specific resistivity in the order of 10^{-1} Ω cm. Density of States, and Electron Localization Function calculations suggest localized electrons in covalent and ionic bonds, combined with less localized 5*d* electrons of tantalum.

Chapter 8

Appendix

A. Supporting Information for Chapter 2

A.1. Synthesis

Table A.1. Weighed portions of starting materials for the syntheses of $SrAl_5P_4N_{10}O_2F_3$.

	starting material				
	$Sr(N_3)_2$	PON	P_3N_5	AlN	NH_4F
in mg	14.9	10.6	9.4	17.8	9.82
in mmol	0.087	0.174	0.058	0.434	0.265

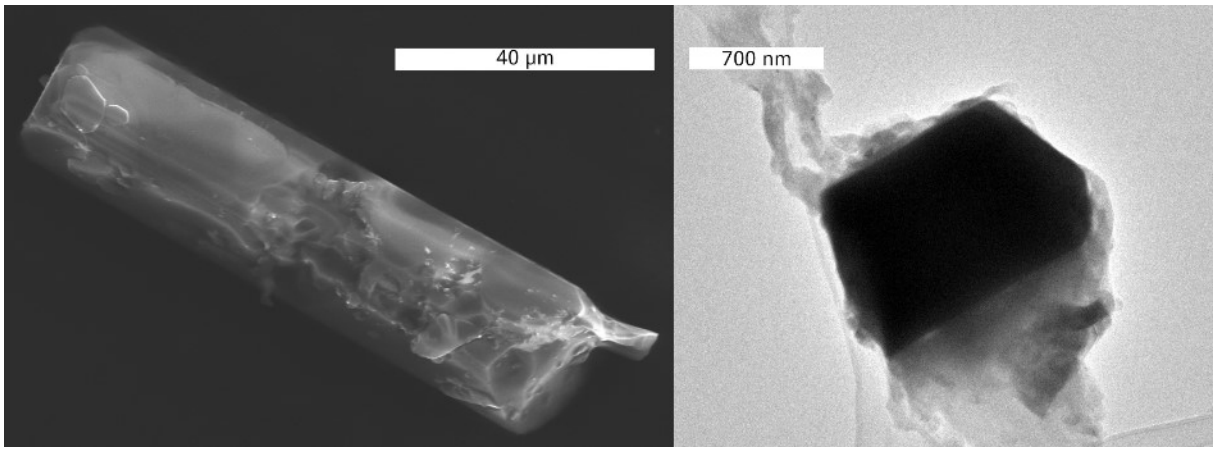

Figure A.1. Left: Back scattered electron image of $SrAl_5P_4N_{10}O_2F_3$; the crystal morphology is rod-shaped; right: bright field image of a typical crystallite used for TEM EDX.

A.2. Rietveld Refinement

Table A.2. Crystallographic data from the Rietveld refinements, standard deviations are given in parentheses.

formula	$SrAl_5P_4N_{10}O_2F_3$
molar mass / g·mol^{-1}	1151.00
crystal system	tetragonal
space group	$I\bar{4}m2$ (no. 119)
lattice parameters / Å	a = 11.17931(5)
	c = 7.85305(5)
cell volume / Å^3	981.45(1)
formula units / unit cell	2
X-ray density / g·cm^{-3}	3.895
radiation	Cu-Kα_1 (λ = 1.54056 Å)
monochromator	Ge(111)
detector	Mythen 1K
2θ range / °	$3.0 \leq 2\theta \leq 93.4$
data points	6030
observed reflections	153
refined parameters	34
no. of background parameters	18
GooF	2.231
R_p, R_{wp}	0.043, 0.061
R_{Bragg}	0.045

A.3. FTIR Spectrum

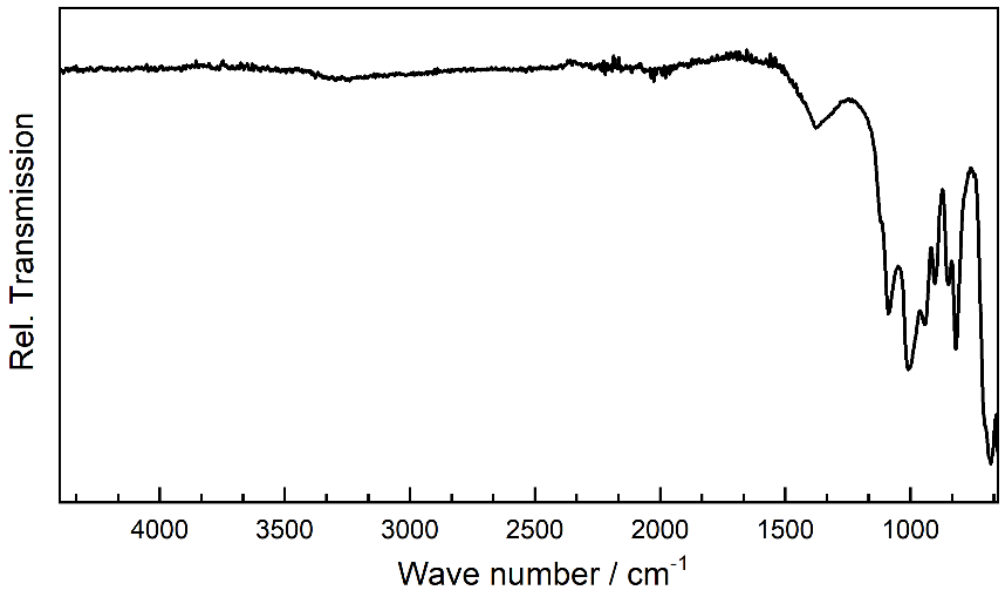

Figure A.2. FTIR spectrum of $SrAl_5P_4N_{10}O_2F_3$.

A.4. Crystallographic Data

Table A.3. Atomic coordinates, equivalent isotropic displacement parameters (Å^2), and site occupancies as determined by single-crystal structure refinement. Standard deviations are given in parentheses.

atom	*Wyckoff*	*x*	*y*	*z*	U_{eq}	*s.o.f.*
Sr1	4*e*	0	0	0.72169(6)	0.02146(13)	1
P1	16*j*	0.62600(5)	0.75862(5)	0.88620(7)	0.00282(9)	1
Al1	4*f*	0	½	0.48340(18)	0.0040(2)	1
Al2	8*i*	0.75439(9)	0	0.98360(13)	0.00677(16)	1
Al3	8*h*	0.86212(6)	0.36212(6)	¾	0.00879(17)	1
F1	2*c*	0	½	¾	0.0181(9)	1
F2	2*d*	0	½	¼	0.0068(6)	1
F3	8*g*	0.88965(13)	0.88965(13)	0	0.0107(3)	1
O1	8*i*	0.74083(19)	0	0.2225(3)	0.0056(3)	1
N1	16*j*	0.87877(15)	0.62677(15)	0.9995(2)	0.0038(2)	1
N2	8*g*	0.63863(14)	0.63863(14)	0	0.0042(3)	1
N3	8*i*	0.7593(2)	0	0.7257(3)	0.0041(3)	1
N4	8*h*	0.26248(15)	0.76248(15)	¾	0.0040(4)	1

Table A.4. Anisotropic displacement parameters with standard deviations in parentheses.

atom	U_{11}	U_{22}	U_{33}	U_{12}	U_{13}	U_{23}
Sr1	0.00411(16)	0.0498(4)	0.01047(19)	0	0	0
P1	0.00254(17)	0.00289(19)	0.00304(18)	0.00010(14)	0.00005(16)	0.00005(16)
Al1	0.0036(5)	0.0034(5)	0.0051(5)	0	0	0
Al2	0.0065(4)	0.0079(4)	0.0059(4)	0	-0.0001(3)	0
Al3	0.0116(3)	0.0116(3)	0.0031(3)	-0.0057(3)	0.0000(2)	0.0000(2)
F1	0.0224(14)	0.0224(14)	0.009(2)	0	0	0
F2	0.0082(9)	0.0082(9)	0.0040(15)	0	0	0
F3	0.0104(5)	0.0104(5)	0.0114(7)	0.0003(6)	-0.0001(5)	0.0001(5)
O1	0.0081(8)	0.0055(8)	0.0031(7)	0	-0.0006(7)	0
N1	0.0034(5)	0.0046(6)	0.0036(5)	-0.0003(4)	0.0005(5)	-0.0002(5)
N2	0.0042(5)	0.0042(5)	0.0041(8)	-0.0002(7)	-0.0010(5)	0.0010(5)
N3	0.0062(9)	0.0021(8)	0.0041(8)	0	-0.0010(8)	0
N4	0.0042(5)	0.0042(5)	0.0036(9)	-0.0014(7)	-0.0007(5)	0.0007(5)

A.5. Transmission Electron Microscopy

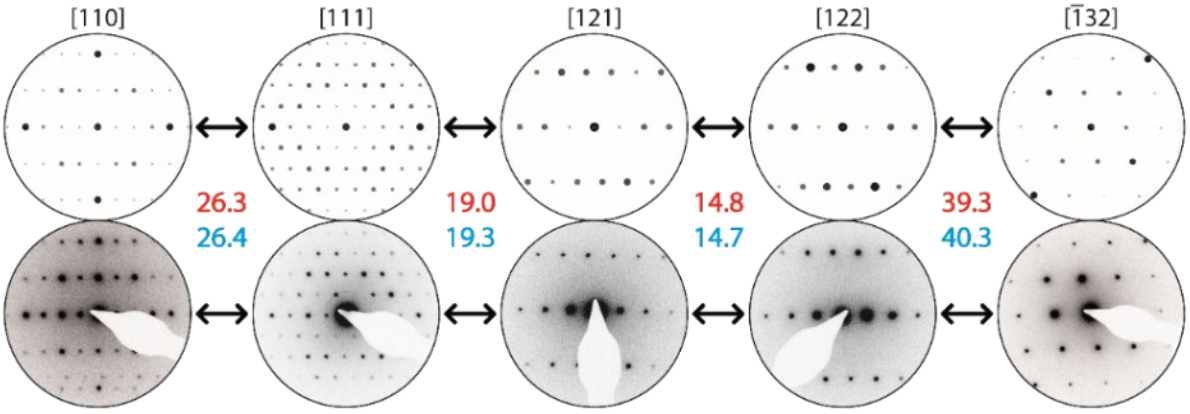

Figure A.3. Experimental selected area electron diffraction (SAED) patterns (bottom) and simulated ones (top) based on the structure model in I$\bar{4}$m2 as derived from single-crystal data. Due to imperfect orientation, the [110] pattern shows some HOLZ reflections in the lower part.

Table A.5. TEM-EDX results compared to values derived from sum formula.

atom %	*Sr*	*Al*	*P*	*N*	*O*	*F*
measuring point 1	3.9	20.2	15.3	38.3	10.6	11.8
measuring point 2	3.9	20.2	15.3	38.2	10.6	11.8
measuring point 3	3.1	20.4	15.4	38.5	10.7	11.9
measuring point 4	2.7	20.5	15.5	38.7	10.7	11.9
measuring point 5	3.1	20.3	15.6	38.9	10.6	11.6
measuring point 6	3.5	21.6	16.3	36.1	10.5	12.0
average	3.3(4)	20.5(5)	15.5(3)	38.1(9)	10.6(1)	11.8(1)
$SrAl_5P_4N_{10}O_2F_3$	4	20	16	40	8	12

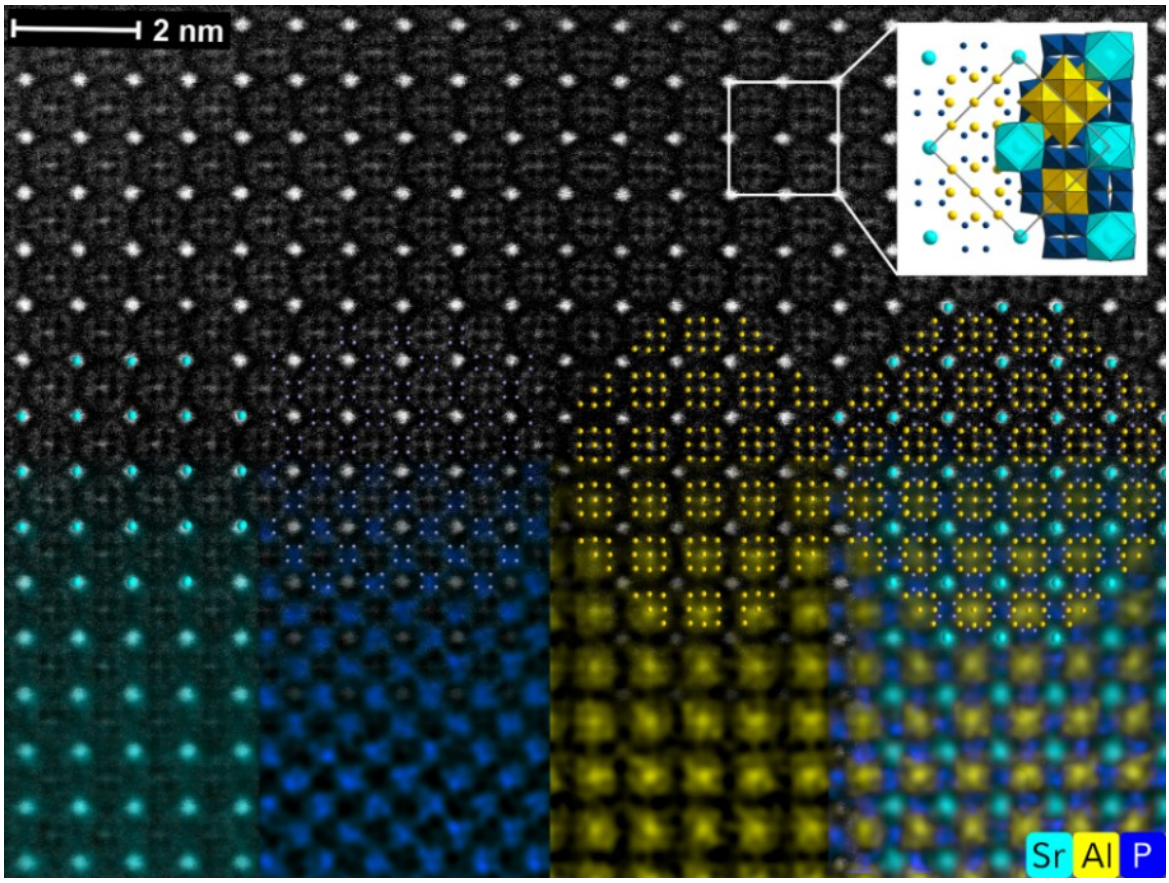

Figure A.4. STEM and EDX mapping along [001] (enlarged version of Fig. 2 in the manuscript). STEM-HAADF image (top) with structure overlay (middle, Sr cyan, P blue, Al yellow). The corresponding EDX maps are shown on the bottom: Sr cyan, P blue, Al yellow; and the resulting combined map. The unit cell is shown in the inset and marked with a white box.

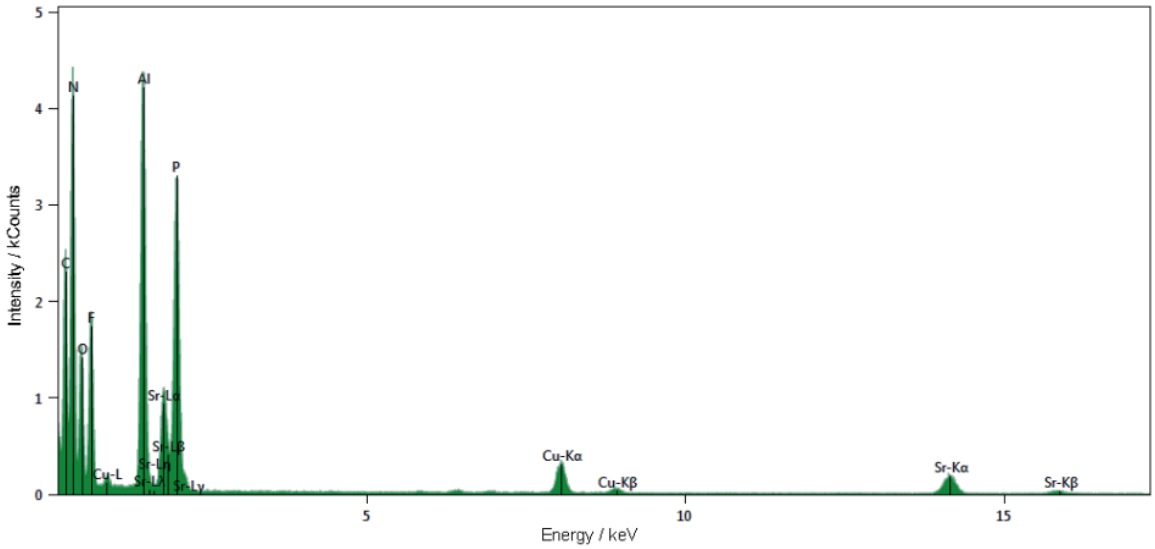

Figure A.5. Raw EDX spectrum of the EDX mapping shown in Figure A.4. Cu and C signals originate in the TEM grid.

A.6. Structure Description

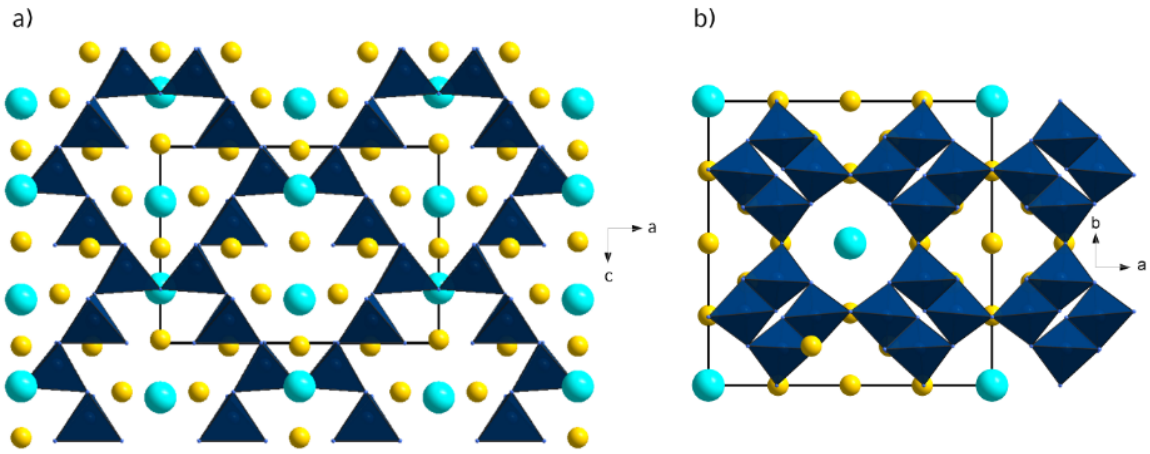

Figure A.6. Three-dimensional network of vertex-sharing PN_4 tetrahedra. Display of a) zehner rings and b) achter rings, PN_4 tetrahedra blue, Sr cyan, Al yellow.

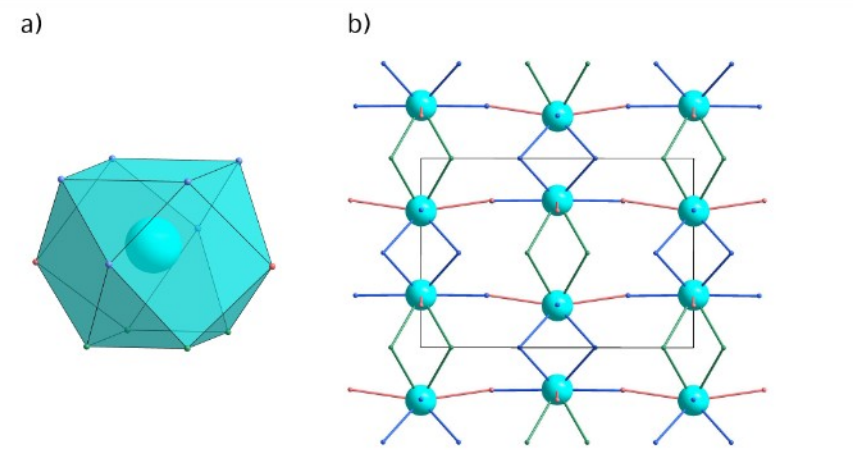

Figure A.7. a) Coordination sphere of Sr (cyan) with N atoms (light blue), O atoms (light red) and F atoms (light green); b) Sr-centered cuboctahedra showing the more acute Sr-N-Sr angles as well as the more obtuse Sr-F-Sr angles; viewing direction [100], Sr–N bonds light blue, Sr–O bonds light red, Sr–F bonds light green.

Table A.6. Interatomic distances (Å) and angles (°) of the Al_{10} unit, standard deviations are given in parentheses.

atom 1	*atom 2*	*count*	*distance*	*atom 1*	*atom 2*	*atom 3*	*angle*
Al1	Al2	4x	2.8412(10)	Al1	-Al2-	Al3	63.41(3)
Al2	Al3	8x	2.9045(9)	Al3	-Al2-	Al3	64.04(4)
Al1	Al3	8x	3.0201(11)	Al2	-Al3-	Al2	173.34(5)
Al3	Al3	4x	3.0798(14)	Al2	-Al1-	Al2	179.94(7)

Table A.7. Interatomic distances (Å) and bond angles (°), standard deviations are given in parentheses. Values and their errors were derived from the statistics. Any systematic errors are not included.

atom 1	*atom 2*	*count*	*distance*	*atom 1*	*atom 2*	*atom 3*	*angle*
Sr1	N3	2x	2.688(2)	N2	-P1-	N3	105.33(12)
	F3	4x	2.7944(13)	N4		N3	107.45(9)
	N2	4x	2.7967(18)	N2		N4	108.37(8)
	O1	2x	2.927(2)	N1		N4	109.63(8)
P1	N1		1.6141(18)	N1		N2	112.44(8)
	N2		1.6167(13)	N1		N3	113.35(10)
	N4		1.6419(13)	N1	-Al1-	F1	86.08(6)
	N3		1.6708(15)	N1		N1	87.18(10)
Al1	F2		1.8319(14)	N1		N1	92.28(10)
	N1	4x	1.9636(16)	F2		N1	93.92(6)
	F1		2.0924(14)	N1		N1	172.17(13)
Al2	O1		1.881(2)	F2		F1	180.0(0)
	F3	2x	1.9539(8)	F3	-Al2-	F3	78.21(12)
	N1	2x	1.9703(19)	O1		N1	82.80(7)
	N3		2.025(3)	N1		N1	86.81(10)
Al3	O1	2x	1.9340(13)	O1		F3	89.80(6)
	N4		1.968(3)	F3		N3	92.57(6)
	N1	2x	1.9710(18)	N1		N3	94.99(8)
	F1		2.1778(10)	F3		N1	96.97(8)
				F3		N1	171.23(8)
				O1		N3	176.95(11)
				O1	-Al3-	N1	81.45(9)
				O1		F1	81.80(6)
				N1		F1	83.61(6)
				N4		N1	96.39(6)
				O1		N1	96.72(9)
				O1		N4	98.20(6)
				O1		O1	163.60(12)
				N1		N1	167.22(11)
				N4		F1	180.00(7)

A.7. Luminescence Spectrum

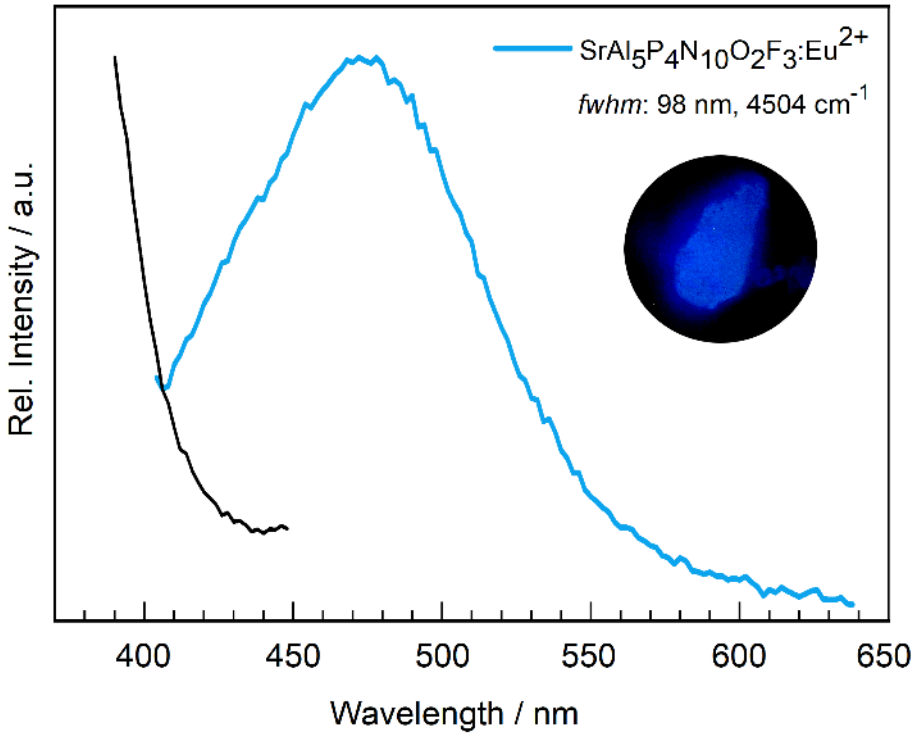

Figure A.8. Normalized single-particle photoluminescence spectrum (blue); excitation spectrum λ_{exc}= 390 nm (black); emission maximum λ_{em}= 469 nm; insert: photograph of a luminescent particle with λ_{exc}= 420 nm.

B. Supporting Information for Chapter 3

B.1. Synthesis

Table B.1. Weighed portions of starting materials for the syntheses of $AE_2AlP_8N_{15}(NH)$.

title compounds	*starting material*			
$Ca_2AlP_8N_{15}(NH)$	Ca_3N_2	AlN	P_3N_5	NH_4F
in mg	6.5	2.7	28.5	0.8
in mmol	0.044	0.066	0.175	0.022
$Sr_2AlP_8N_{15}(NH)$	$Sr(N_3)_2$	AlN	P_3N_5	NH_4F
in mg	19.3	2.3	24.5	0.7
in mmol	0.113	0.056	0.150	0.019
$Ba_2AlP_8N_{15}(NH)$	$Ba(N_3)_2$	AlN	P_3N_5	NH_4F
in mg	21.7	2.0	21.3	0.6
in mmol	0.098	0.049	0.0131	0.016

B.2. Crystallographic Data

Table B.2. Atomic coordinates, isotropic displacement parameters (Å^2), and occupancy of $Ca_{1.88}Eu_{0.12}AlP_8N_{15}(NH)$.

atom	*Wyckoff*	*x*	*y*	*z*	*U*	*s.o.f.*
Ca1	4c	0.06553(4)	¼	0.43226(4)	0.01119(16)	0.9766(15)
Eu1	4c	0.06553(4)	¼	0.43226(4)	0.01119(16)	0.0234(14)
Ca2	4c	0.28262(4)	¼	0.81208(5)	0.01911(16)	0.9087(16)
Eu2	4c	0.28262(4)	¼	0.81208(5)	0.01911(16)	0.0913(15)
Al1	4c	0.51364(6)	¼	0.57718(6)	0.00474(13)	1
P1	8d	0.11649(3)	0.07513(6)	0.13715(4)	0.00476(9)	1
P2	8d	0.34244(3)	0.07275(6)	0.42365(4)	0.00455(8)	1
P3	8d	0.03258(3)	0.06885(5)	0.72656(3)	0.00371(8)	1
P4	8d	0.32135(3)	0.06542(6)	0.06620(4)	0.00506(8)	1
N1	8d	0.23696(11)	0.0630(2)	0.17200(12)	0.0066(2)	1
N2	8d	0.09146(11)	0.57737(18)	0.04694(12)	0.0054(2)	1
N3	8d	0.39166(11)	0.57617(19)	0.34159(12)	0.0054(2)	1
N4	8d	0.05599(11)	0.06624(19)	0.25790(12)	0.0061(2)	1
N5	8d	0.08429(11)	0.05239(19)	0.60127(12)	0.0066(2)	1
N6	8d	0.22633(11)	0.07513(6)	0.44816(13)	0.0081(3)	1
N7	4c	0.35004(17)	¼	0.36122(18)	0.0074(4)	1
N8	4c	0.09264(16)	¼	0.06611(18)	0.0055(3)	1
N9	4c	0.36579(18)	¼	0.0383(2)	0.0101(4)	1
N10	4c	0.47563(15)	¼	0.75909(18)	0.0040(3)	1
H1	8d	0.26(2)	0.13(3)	0.231(16)	0.4(2)	0.5

Table B.3. Anisotropic displacement parameters for $Ca_{1.88}Eu_{0.12}AlP_8N_{15}(NH)$ with standard deviations in parentheses.

atom	U_{11}	U_{22}	U_{33}	U_{12}	U_{13}	U_{23}
Ca1	0.0177(3)	0.0098(2)	0.0061(2)	0	-0.00100(16)	0
Eu1	0.0177(3)	0.0098(2)	0.0061(2)	0	-0.00100(16)	0
Ca2	0.0094(2)	0.0299(3)	0.0180(2)	0	0.00167(16)	0
Eu2	0.0094(2)	0.0299(3)	0.0180(2)	0	0.00167(16)	0
Al1	0.0049(3)	0.0052(3)	0.0042(3)	0	0.0000(2)	0
P1	0.00521(16)	0.00527(17)	0.00381(16)	-0.00015(14)	0.00061(13)	-0.00167(13)
P2	0.00396(16)	0.00588(17)	0.00382(16)	-0.00025(14)	0.00028(13)	0.00006(13)
P3	0.00394(16)	0.00409(16)	0.00311(16)	-0.00007(13)	0.00030(12)	0.00019(13)
P4	0.00467(16)	0.00551(17)	0.00499(16)	-0.00075(14)	-0.00121(13)	0.00142(14)
N1	0.0042(5)	0.0104(6)	0.0053(5)	-0.0004(5)	-0.0002(4)	0.0001(5)
N2	0.0063(5)	0.0054(5)	0.0047(5)	-0.0002(5)	0.0011(4)	0.0005(5)
N3	0.0058(5)	0.0059(5)	0.0046(5)	-0.0002(5)	0.0013(4)	-0.0013(5)
N4	0.0064(5)	0.0068(6)	0.0052(5)	-0.0010(5)	0.0012(4)	-0.0016(5)
N5	0.0069(6)	0.0082(6)	0.0048(5)	0.0008(5)	0.0015(4)	0.0032(5)
N6	0.0048(5)	0.0139(7)	0.0054(6)	0.0014(5)	0.0005(4)	-0.0023(5)
N7	0.0092(9)	0.0076(9)	0.0053(8)	0	-0.0013(7)	0
N8	0.0066(8)	0.0050(8)	0.0051(8)	0	-0.0009(6)	0
N9	0.0098(9)	0.0056(8)	0.0148(10)	0	0.0057(8)	0
N10	0.0041(7)	0.0023(7)	0.0057(8)	0	-0.0010(6)	0

Table B.4. Atomic coordinates, isotropic displacement parameters ($Å^2$), and occupancy of $Sr_2AlP_8N_{15}(NH)$.

atom	*Wyckoff*	*x*	*y*	*z*	*U*	*s.o.f.*
Sr1	4c	0.06544(2)	¼	0.43354(3)	0.01142(8)	1
Sr2	4c	0.28707(2)	¼	0.80949(3)	0.01550(8)	1
Al1	4c	0.51502(7)	¼	0.57596(9)	0.00677(17)	1
P1	8d	0.11448(4)	0.07477(6)	0.13607(5)	0.00669(11)	1
P2	8d	0.34203(4)	0.07440(6)	0.42725(5)	0.00640(11)	1
P3	8d	0.03721(4)	0.06719(6)	0.73173(5)	0.00578(11)	1
P4	8d	0.31701(4)	0.06627(7)	0.07007(5)	0.00739(11)	1
N1	8d	0.23296(13)	0.0641(2)	0.17274(17)	0.0086(3)	1
N2	8d	0.09043(13)	0.5779(2)	0.04696(17)	0.0070(3)	1
N3	8d	0.38972(13)	0.5737(2)	0.34577(17)	0.0077(3)	1
N4	8d	0.05364(13)	0.0619(2)	0.25365(17)	0.0086(3)	1
N5	8d	0.08744(13)	0.0440(2)	0.60829(18)	0.0095(3)	1
N6	8d	0.22692(13)	0.0203(2)	0.45430(18)	0.0094(3)	1
N7	4c	0.35065(19)	¼	0.3640(2)	0.0088(5)	1
N8	4c	0.09053(19)	¼	0.0664(2)	0.0080(5)	1
N9	4c	0.3573(2)	¼	0.0368(3)	0.0121(5)	1
N10	4c	0.48360(18)	¼	0.7560(2)	0.0069(4)	1
H1	8d	0.246(9)	0.146(13)	0.222(10)	0.12(5)	0.5

Table B.5. Anisotropic displacement parameters for $Sr_2AlP_8N_{15}(NH)$ with standard deviations in parentheses.

atom	U_{11}	U_{22}	U_{33}	U_{12}	U_{13}	U_{23}
Sr1	0.01785(14)	0.00810(12)	0.00832(14)	0	-0.00136(10)	0
Sr2	0.00873(13)	0.01879(14)	0.01897(17)	0	0.00094(10)	0
Al1	0.0065(4)	0.0065(4)	0.0073(4)	0	0.0003(3)	0
P1	0.0075(2)	0.0055(2)	0.0071(3)	-0.00002(18)	0.00094(18)	-0.00091(16)
P2	0.0060(2)	0.0061(2)	0.0071(3)	-0.00051(17)	0.00047(17)	0.00009(16)
P3	0.0056(2)	0.0049(2)	0.0068(3)	-0.00003(17)	0.00034(17)	0.00013(16)
P4	0.0072(2)	0.0066(2)	0.0084(3)	-0.00064(18)	-0.00134(18)	0.00099(17)
N1	0.0052(7)	0.0112(8)	0.0093(9)	-0.0011(6)	-0.0010(6)	0.0001(6)
N2	0.0074(7)	0.0062(7)	0.0075(8)	0.0013(6)	0.0012(6)	0.0009(6)
N3	0.0081(7)	0.0068(7)	0.0083(9)	0.0005(6)	0.0013(6)	-0.0008(6)
N4	0.0091(7)	0.0077(7)	0.0090(9)	-0.0014(6)	0.0012(6)	-0.0017(6)
N5	0.0084(7)	0.0113(8)	0.0087(9)	0.0000(7)	0.0017(6)	0.0041(6)
N6	0.0070(7)	0.0131(8)	0.0079(9)	0.0010(7)	0.0010(6)	-0.0004(6)
N7	0.0113(11)	0.0068(10)	0.0084(13)	0	0.0011(9)	0
N8	0.0080(10)	0.0062(10)	0.0098(13)	0	-0.0005(9)	0
N9	0.0142(12)	0.0064(10)	0.0156(15)	0	0.0051(10)	0
N10	0.0057(9)	0.0057(10)	0.0095(13)	0	-0.0018(8)	0

Table B.6. Atomic coordinates, isotropic displacement parameters ($Å^2$), and occupancy of $Ba_{1.85}Eu_{0.15}AlP_8N_{15}(NH)$.

atom	*Wyckoff*	*x*	*y*	*z*	*U*	*s.o.f.*
Ba1	4c	0.06294(2)	¼	0.43777(2)	0.00859(3)	0.886(5)
Eu1	4c	0.06294(2)	¼	0.43777(2)	0.00859(3)	0.114(5)
Ba2	4c	0.29221(2)	¼	0.80058(2)	0.00944(3)	1
Eu2	4c	0.51626(4)	¼	0.57475(5)	0.00561(10)	1
Al1	4c	0.10984(2)	¼	0.13645(3)	0.00413(5)	1
P1	8d	0.34180(2)	0.07557(4)	0.43263(3)	0.00402(5)	1
P2	8d	0.04333(2)	0.07493(4)	0.73671(3)	0.00337(5)	1
P3	8d	0.31189(2)	0.06581(4)	0.07425(3)	0.00499(6)	1
P4	8d	0.22701(8)	0.06884(4)	0.17395(9)	0.00578(17)	1
N1	8d	0.09041(8)	0.07047(14)	0.04943(9)	0.00541(16)	1
N2	8d	0.38783(8)	0.57683(13)	0.35073(9)	0.00588(17)	1
N3	8d	0.05016(8)	0.56919(13)	0.25159(9)	0.00599(17)	1
N4	8d	0.09464(9)	0.05556(14)	0.61731(9)	0.00808(19)	1
N5	8d	0.22918(8)	0.03615(15)	0.46254(9)	0.00668(17)	1
N6	8d	0.34857(13)	0.02358(15)	0.37064(14)	0.0069(2)	1
N7	4c	0.08575(12)	¼	0.06992(13)	0.0056(2)	1
N8	4c	0.34930(14)	¼	0.03899(16)	0.0101(3)	1
N9	4c	0.49480(11)	¼	0.75580(14)	0.0055(2)	1
N10	4c	0.241(5)	¼	0.231(4)	0.050(19)	1
H1	8d	0.06294(2)	0.133(7)	0.43777(2)	0.00859(3)	0.5

Table B.7. Anisotropic displacement parameters for $Ba_{1.85}Eu_{0.15}AlP_8N_{15}(NH)$ with standard deviations in parentheses.

atom	U_{11}	U_{22}	U_{33}	U_{12}	U_{13}	U_{23}
Ba1	0.01333(5)	0.00656(5)	0.00588(5)	0	-0.00133(3)	0
Eu1	0.01333(5)	0.00656(5)	0.00588(5)	0	-0.00133(3)	0
Ba2	0.00658(5)	0.01093(5)	0.01081(5)	0	0.00088(4)	0
Al1	0.0062(2)	0.0057(2)	0.0049(2)	0	0.00029(18)	0
P1	0.00495(12)	0.00369(12)	0.00376(12)	-0.00010(9)	0.00074(10)	-0.00084(9)
P2	0.00384(12)	0.00450(12)	0.00371(12)	-0.00030(9)	0.00035(9)	0.00017(9)
P3	0.00343(11)	0.00324(12)	0.00344(12)	-0.00002(9)	0.00037(9)	0.00020(9)
P4	0.00499(12)	0.00498(13)	0.00501(12)	-0.00042(10)	-0.00165(10)	0.00111(10)
N1	0.0041(4)	0.0089(4)	0.0044(4)	-0.0008(3)	0.0001(3)	-0.0004(3)
N2	0.0069(4)	0.0046(4)	0.0047(4)	0.0005(3)	0.0011(3)	0.0002(3)
N3	0.0068(4)	0.0045(4)	0.0063(4)	0.0014(3)	0.0023(3)	0.0002(3)
N4	0.0068(4)	0.0063(4)	0.0049(4)	-0.0007(3)	0.0017(3)	-0.0029(3)
N5	0.0072(4)	0.0119(5)	0.0051(4)	0.0011(4)	0.0023(3)	0.0042(4)
N6	0.0048(4)	0.0103(4)	0.0049(4)	0.0011(3)	0.0009(3)	-0.0006(3)
N7	0.0112(7)	0.0036(5)	0.0059(6)	0	-0.0008(5)	0
N8	0.0080(6)	0.0038(6)	0.0050(6)	0	0.0004(5)	0
N9	0.0131(7)	0.0043(6)	0.0129(7)	0	0.0055(6)	0
N10	0.0046(6)	0.0027(5)	0.0093(6)	0	-0.0006(5)	0
Ba1	0.01333(5)	0.00656(5)	0.00588(5)	0	-0.00133(3)	0

B.3. Transmission Electron Microscopy

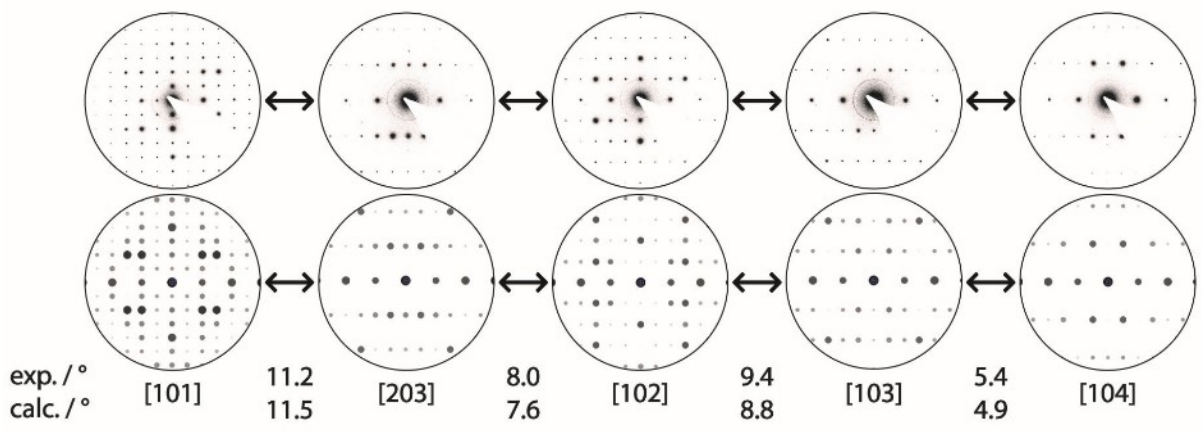

Figure B.1. Tilt series of experimental selected area electron diffraction (SAED) patterns of $Sr_2AlP_8N_{15}(NH)$ (top) and simulated ones (bottom) based on the structure model *Pnma* as derived from single-crystal data. Experimental and expected goniometer settings are given in degree.

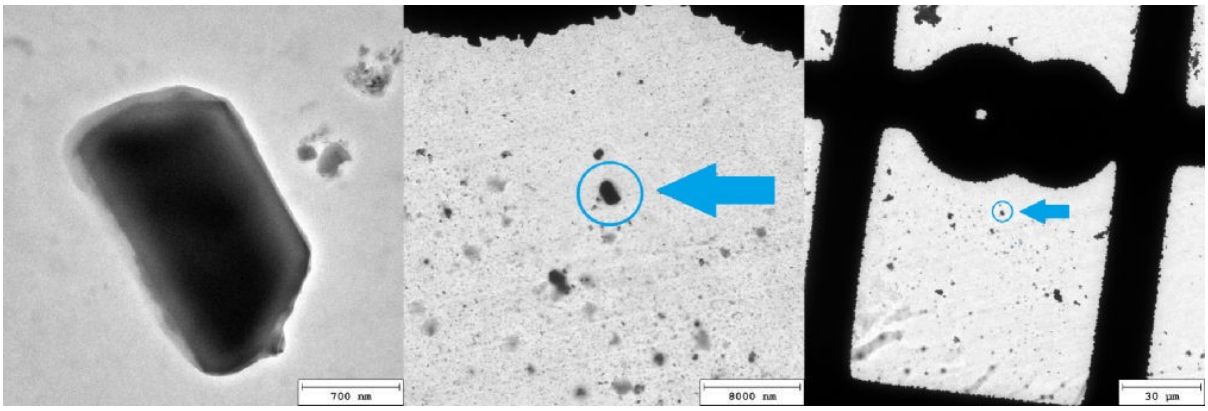

Figure B.2. TEM bright-field images of the crystallite used for data collection with micro-focused synchrotron radiation at beamline ID11, ESRF, Grenoble, France.

B.4. Rietveld Refinements

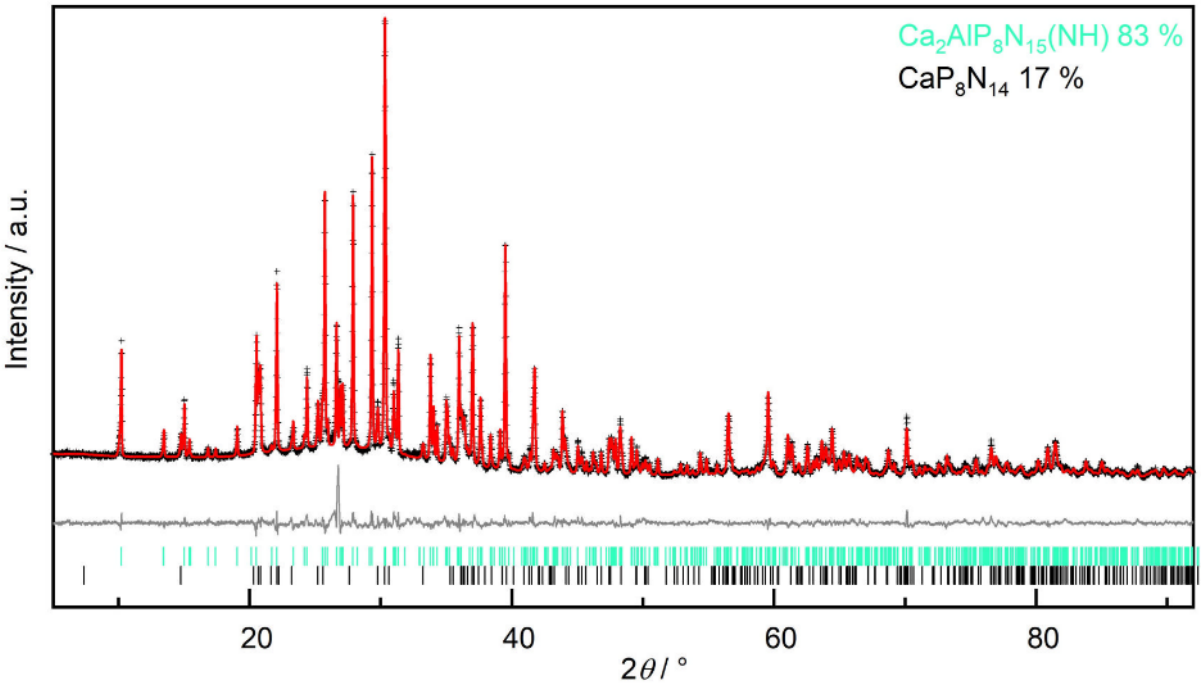

Figure B.3. Rietveld refinement for $Ca_2AlP_8N_{15}(NH)$; observed (black data points) and calculated (red line) X-ray powder diffraction patterns, positions of Bragg reflections of $Ca_2AlP_8N_{15}(NH)$ (vertical green bars), CaP_8N_{14} (vertical black bars), and difference profile (gray line).

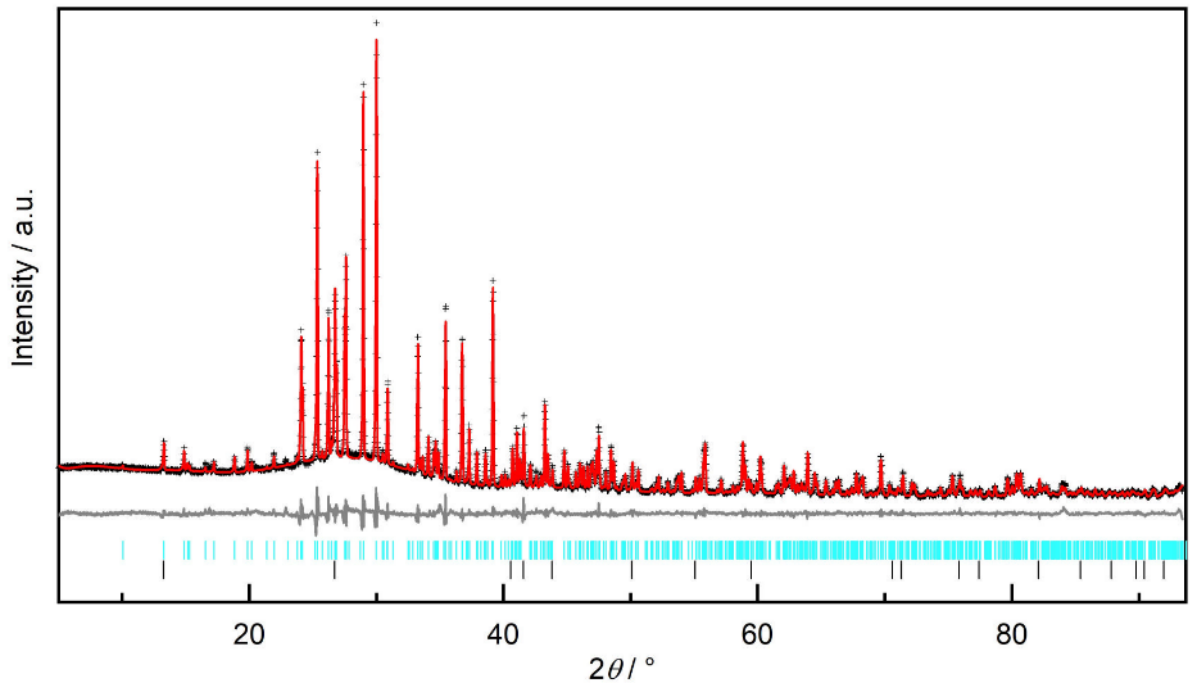

Figure B.4. Rietveld refinement for $Sr_2AlP_8N_{15}(NH)$; observed (black data points) and calculated (red line) X-ray powder diffraction patterns, positions of Bragg reflections of $Sr_2AlP_8N_{15}(NH)$ (vertical cyan bars), h-BN (vertical black bars, crucible material), and difference profile (gray line).

B.5. High-Temperature PXRD

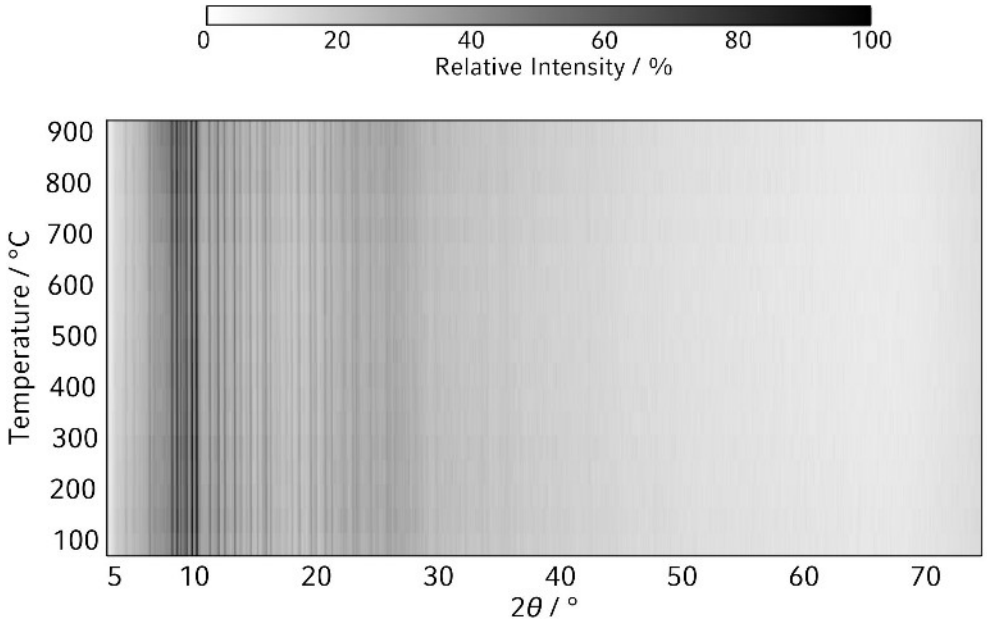

Figure B.5. Temperature-dependent powder X-ray diffraction patterns (Ag-$K\alpha_1$ radiation, λ = 0.5595378 Å) of $Ba_2AlP_8N_{15}(NH)$ showing no expansion of lattice parameters with increasing temperature, and decomposition above 900 °C.

B.6. Partial MAPLE Values

Table B.8. Partial MAPLE values in kJmol^{-1} for the atom sites in the crystal structure of $AE_2AlP_8N_{15}(NH)$ (*AE* = Ca, Sr, Ba). The numbers in brackets indicate the number of P tetrahedra or Al octahedra centers directly bound to N, respectively. Only N3, N8 and N10 have one neighboring Al center.

	partial MAPLE value				*partial MAPLE value*		
AE =	Ca	Sr	Ba	*AE* =	Ca	Sr	Ba
*AE*1	2549	2450	2309	N1H1[2]	4598	4657	4559
*AE*2	1994	1926	1820	N2[2]	6768	6766	6781
Al1	5048	5043	4851	N3[3]	6363	6395	6416
P1	14170	14183	14148	N4[2]	6058	6077	6056
P2	14839	14865	14835	N5[2]	5880	5895	5913
P3	15299	15378	15356	N6[2]	6086	6088	6060
P4	14999	15007	15048	N7[2]	6054	6055	5999
				N8[3]	6859	6861	6878
				N9[2]	5930	5986	5993
				N10[3]	6103	6109	6104

Ca^{+II}	1715–2929 (in CaP_2N_4)[53]
	1841 (in $CaLiAl_3N_4$)[54]
Sr^{+II}	1790–1832 (in $Sr_3Al_2N_4$)[55]
	1782–2075 (in SrP_2N_4)[53]
	1752–1766 (in $SrAlSi_4N_7$)[56]
Ba^{+II}	1843–1855 (in $BaSi_2O_2N_2$)[57]
	1550–2200 (in $Ba_{32}[Li_{15}Si_9W_{16}N_{67}O_5]$)[58]
Al^{+III}	5137–5335 (in $SrAl_5P_4N_{10}O_2F_3$); [17] (CN = 6)
P^{+V}	14200–16221(in CaP_2N_4)[53]
	15506–16033 (in SrP_2N_4)[53]
N^{-III}	5569–7176 (in CaP_2N_4)[53]
	5745–6577 (in SrP_2N_4)[53]
	5236−6150 (in $Sr_2Si_5N_8$)[59]
	5053–6226 (in $SrAlSi_4N_7$)[56]
O^{-II}	2132–2454 (in α/β-$SrBeO_2$)[60]

B.7. Bond Valence Sum Calculations

Table B.9. Bond length and partial bond valence sums for the alkaline-earth atom sites in the crystal structure of $AE_2AlP_8N_{15}(NH)$ (*AE* = Ca, Sr, Ba). Gray shading for bonding partners associated with forming a bond.

bonding partner	*bond length*	*partial BVS*	*bond length*	*partial BVS*	*bond length*	*partial BVS*
*AE*1	Ca		Sr		Ba	
N4	2.494	0.384	2.59	0.378	2.724	0.503
N4	2.494	0.384	2.59	0.378	2.724	0.503
N5	2.522	0.356	2.642	0.328	2.786	0.426
N5	2.522	0.356	2.642	0.328	2.786	0.426
N9	2.647	0.254	2.782	0.225	2.909	0.305
N6	2.856	0.144	2.841	0.192	2.929	0.289
N6	2.856	0.144	2.841	0.192	2.929	0.289
N5	3.154	0.065	3.156	0.082	3.232	0.128
N5	3.154	0.065	3.156	0.082	3.232	0.128
N10	3.740	0.013	3.772	0.015	3.748	0.032
*AE*2						
N10	2.609	0.282	2.679	0.297	2.797	0.413
N6	2.629	0.267	2.761	0.238	2.913	0.302
N6	2.629	0.267	2.761	0.238	2.913	0.302
N3	2.705	0.217	2.774	0.23	2.93	0.288
N3	2.705	0.217	2.774	0.23	2.959	0.267
N9	2.820	0.159	2.804	0.212	2.959	0.267
N1	3.000	0.098	3.002	0.124	3.027	0.222
N1	3.000	0.098	3.002	0.124	3.027	0.222
N4	3.371	0.036	3.347	0.049	3.335	0.097
N4	3.371	0.036	3.347	0.049	3.335	0.097
N2	3.736	0.013	3.728	0.017	3.660	0.04
N2	3.736	0.013	3.728	0.017	3.660	0.04

Table B.10. Bond valence sums and expected charges for the atom sites in the crystal structure of $AE_2AlP_8N_{15}(NH)$ (*AE* = Ca, Sr, Ba). Value without hydrogen in the crystal structure/value with hydrogen in the crystal structure.

atom site	*charge$_{exp.}$*	*bond valence sums*		
AE =		Ca	Sr	Ba
*AE*1	2	2.18/2.17	2.20/2.20	3.03/3.02
*AE*2	2	1.75/1.70	1.83/1.83	2.56/2.56
Al1		3.17/3.17	3.15/3.15	2.84/2.84
P1	3	5.22/4.96	5.00/5.00	4.92/4.92
P2	5	4.93/4.91	4.97/4.97	4.90/4.90
P3	5	5.04/5.03	5.10/5.10	5.03/5.03
P4	5	5.19/5.00	5.04/5.01	4.99/4.99
N1	−3	−2.54/−4.80	−2.62/−4.79	−2.60/−4.86
N2	−3	−3.00/−3.01	−3.01/−3.01	−2.95/−2.95
N3	−3	−2.99/−3.00	−3.04/−3.05	−3.06/−3.07
N4	−3	−3.10/−3.12	−3.14/−3.16	−3.25/−3.27
N5	−3	−3.04/−3.05	−3.05/−3.06	−3.18/−3.19
N6	−3	−2.93/−2.95	−2.96/−2.97	−3.08/−3.09
N7	−3	−2.71/−2.77	−2.71/−2.77	−2.62/−2.66
N8	−3	−3.00/−3.03	−3.00/−3.03	−2.95/−2.97
N9	−3	−2.88/−2.92	−2.96/−2.99	−3.13/−3.15
N10	−3	−3.04/−3.04	−3.10/−3.10	−3.18/−3.18

B.8. Charge Distribution Calculations

Table B.11. Charge distribution values and expected charges for the atom sites in the crystal structure of $AE_2AlP_8N_{15}(NH)$ (*AE* = Ca, Sr, Ba). Value without hydrogen in the crystal structure/value with hydrogen in the crystal structure.

atom site	$charge_{exp.}$	*charge distribution*		
AE =		Ca	Sr	Ba
*AE*1	2	1.96/1.96	1.96/1.96	1.96/1.96
*AE*2	2	2.05/2.00	2.05/2.00	2.07/1.99
Al1	3	3.05/3.05	3.07/3.07	3.03/3.03
P1	5	5.23/4.99	5.20/4.97	5.21/4.97
P2	5	5.10/5.10	5.15/5.15	5.16/5.18
P3	5	4.93/4.93	4.94/4.94	4.93/4.93
P4	5	5.20/4.97	5.17/4.95	5.18/4.96
N1	–3	–2.51/–3.02	–2.60/–3.08	–2.52/–3.02
N2	−3	−2.93/−2.93	−2.91/−2.91	−2.93/−2.93
N3	–3	–3.04/–2.97	–2.97/–2.97	–2.99–2.99
N4	−3	−3.14/−3.12	−3.15/−3.15	−3.12/−3.13
N5	–3	−3.05/−3.07	−3.04/−3.04	−3.06/−3.06
N6	−3	−3.04/−3.03	−3.01/−3.01	−3.01/−3.01
N7	–3	−2.84/−2.84	−2.79/−2.79	−2.74/−2.74
N8	−3	−2.94/−2.94	−2.91/−2.91	−2.98/−2.98
N9	–3	−2.96/−2.95	−2.98/−3.04	−3.02/−3.02
N10	−3	−2.99/−2.99	−2.98/−2.98	−3.00/−3.00

B.9. EDX Measurements

Table B.12. TEM-EDX measurements for $AE_2AlP_8N_{15}(NH)$ (*AE* = Ca, Sr, Ba) compared to values derived from sum formula.

	Ca	*Al*	*P*	*N*	*O*
crystal 1	6.0	3.3	24.7	62.9	3.2
crystal 2	6.8	3.6	27.7	60.8	1.1
crystal 3	6.6	3.5	26.7	61.8	1.5
crystal 4	6.4	3.5	26.3	62.8	1.0
crystal 5	6.5	3.6	26.7	60.4	2.8
average	6.5(3)	3.5(1)	26(1)	62(1)	1.9(9)
$Ca_2AlP_8N_{15}(NH)$ exp.	7.4	3.7	29.6	59.3	-
	Sr	**Al**	**P**	**N**	**O**
crystal 1	9.8	5.3	39.8	41.1	3.5
crystal 2	10.7	5.2	37.7	43.8	2.7
crystal 3	7.9	3.8	31.8	50.8	5.7
crystal 4	8.6	4.0	33.3	50.8	3.3
average	9(1)	4.6(7)	36(3)	47(4)	4(1)
$Sr_2AlP_8N_{15}(NH)$ exp.	7.4	3.7	29.6	59.3	-
	Ba	**Al**	**P**	**N**	**O**
crystal 1	7.6	4.0	29.5	55.8	3.1
crystal 2	5.5	3.7	32.5	56.5	1.8
crystal 3	7.5	4.0	29.4	57.3	1.9
crystal 4	7.7	4.0	30.1	56.6	1.9
crystal 5	6.3	3.7	26.1	62.3	1.6
average	6.9(9)	3.9(1)	30(2)	58(2)	2.1(5)
$Ba_2AlP_8N_{15}(NH)$ exp.	7.4	3.7	29.6	59.3	-

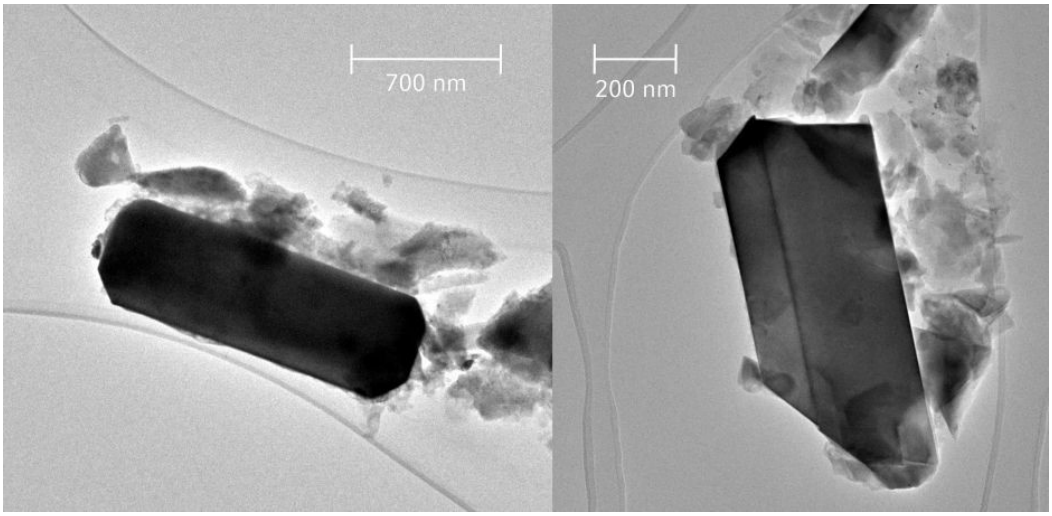

Figure B.6. Bright-field images of $AE_2AlP_8N_{15}(NH)$ crystallites (left: $Sr_2AlP_8N_{15}(NH):Eu^{2+}$, right: $Ba_2AlP_8N_{15}(NH):Eu^{2+}$ used for electron diffraction analysis, EDX measurements and STEM.

B.10. FTIR Spectrum

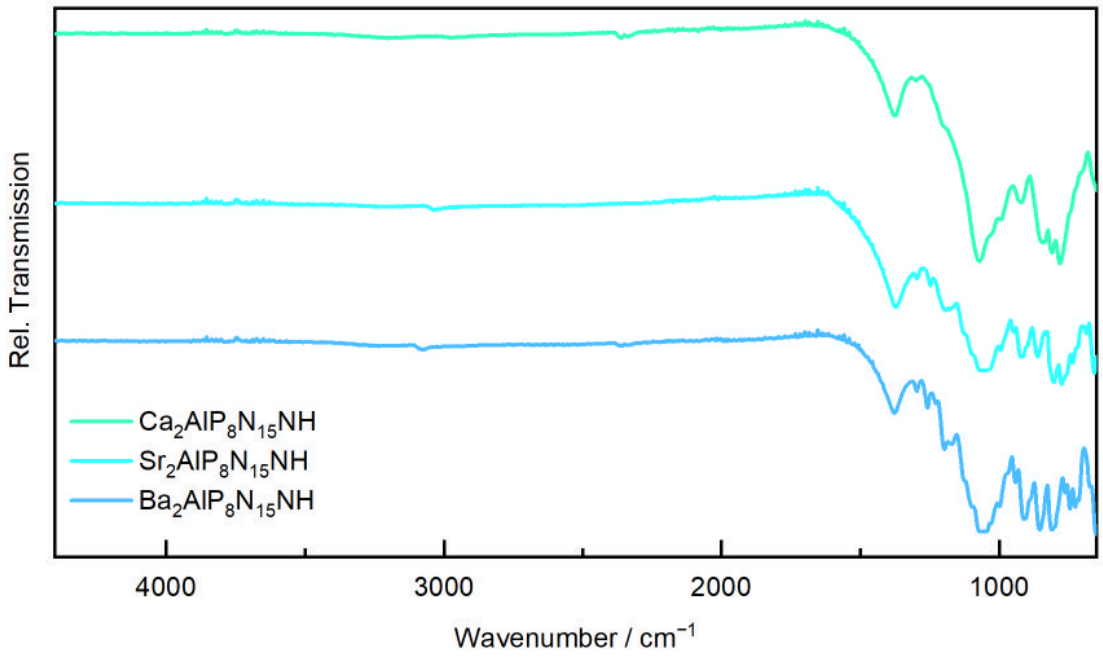

Figure B.7. FTIR spectrum of $Ca_2AlP_8N_{15}(NH)$ (green), $Sr_2AlP_8N_{15}(NH)$ (cyan) and $Ba_2AlP_8N_{15}(NH)$ (blue).

B.11. Structure Description

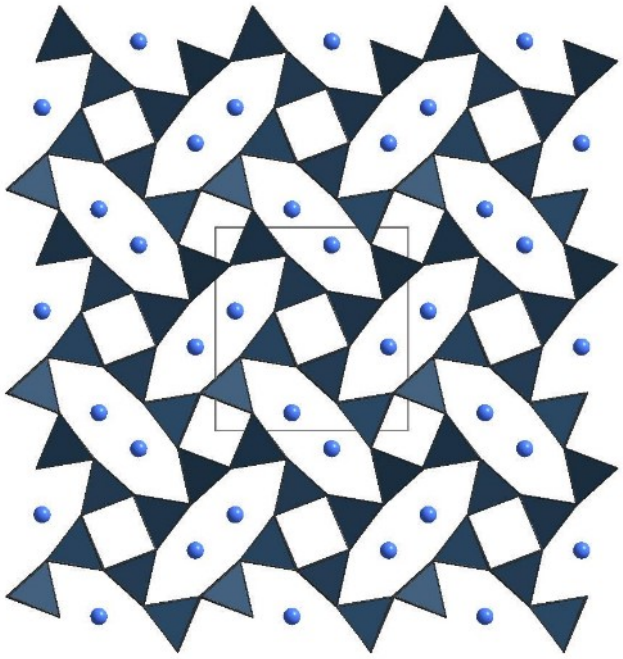

Figure B.8. Crystal structure of the mineral paracelsian $BaAl_2Si_2O_8$ along [001]. It shows similar structural motifs with smaller ring sizes of four- and eight-membered rings built up by $(Al/Si)O_4$ tetrahedra.

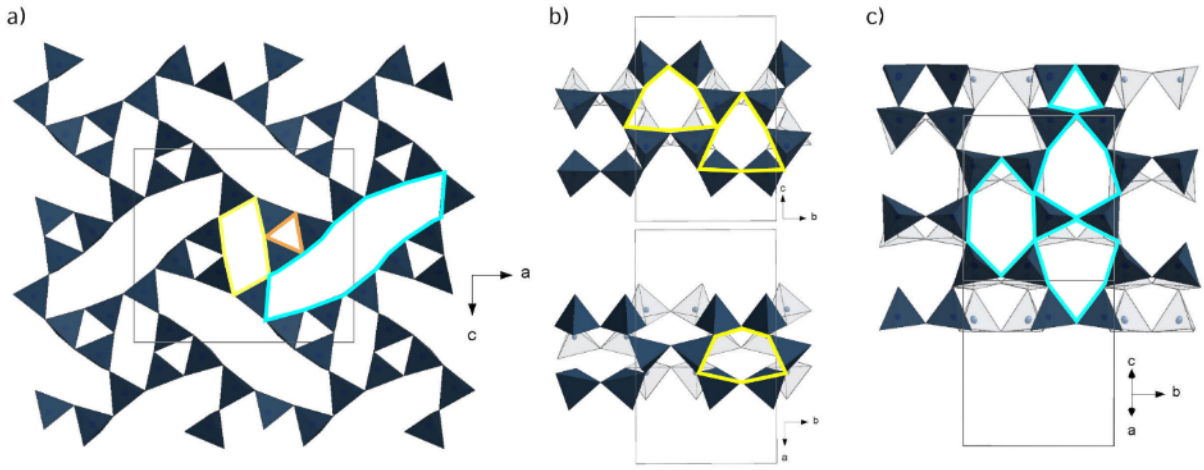

Figure B.9. Illustration of different ring types; **a)** Illustration of the ring sizes along [010]. Three-membered rings are marked in orange, six-membered rings in yellow, and twelve-membered rings in cyan; **b)** Two illustrations of three different six-membered rings along [100] and [001], connecting the six-membered rings along b; **c)** Illustration of three different six-membered rings and one four-membered ring, connecting the twelve-membered rings along b.

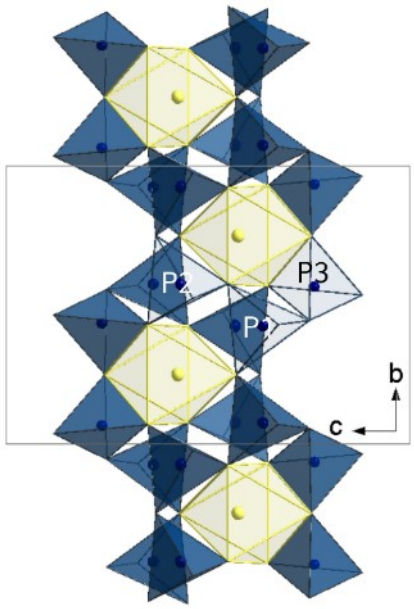

Figure B.10. Six-membered rings of PN_4 tetrahedra in [100]. AlN_6 octahedra occupy the channels and share vertices and edges with tetrahedra but are isolated from each other. PN_4 tetrahedra in dark blue, AlN_6 octahedra with octahedra edges in yellow. Unit cell displayed in gray, P1+P2+P3 are partially labeled. H is not included.

B.12. Interatomic Distances

Table B.13. Interatomic distances (Å) and bond angles (°) in $Ca_2AlP_8N_{15}(NH)$.

atom 1	*atom 2*	*count*	*distance*	*atom 1*	*atom 2*	*atom 3*	*angle*
Ca1	N4	2x	2.4933(16)	N3	-Al1-	N10	72.82(6)
Ca1	N5	2x	2.5222(16)	N3		N3	83.87(9)
Ca1	N9		2.646(3)	N2		N2	88.54(10)
Ca1	N6	2x	2.8558(18)	N2		N10	90.47(7)
Ca1	N5	2x	3.1545(17)	N2		N3	91.42(6)
Ca2	N10		2.608(2)	N8		N3	93.41(7)
Ca2	N6	2x	2.6294(18)	N8		N2	102.88(7)
Ca2	N3	2x	2.7047(16)	N8		N10	161.20(10)
Ca2	N9		2.821(3)	N2		N3	163.29(7)
Ca2	N1	2x	3.0001(17)	N4	-P1-	N1	105.44(8)
Al1	N8		1.947(2)	N2		N8	106.62(9)
Al1	N2	2x	1.9895(17)	N1		N2	107.71(8)
Al1	N3	2x	2.0921(17)	N1		N8	110.73(10)
Al1	N10		2.150(2)	N4		N8	111.79(10)
P1	N4		1.6011(16)	N4		N2	114.53(8)
P1	N1		1.6367(16)	N6	-P2-	N3	104.41(9)
P1	N2		1.6394(16)	N3		N2	107.31(8)
P1	N8		1.6565(13)	N7		N2	109.25(10)
P2	N7		1.5997(12)	N6		N2	110.44(8)
P2	N6		1.6265(16)	N7		N3	111.41(10)
P2	N3		1.6562(16)	N7		N6	113.77(11)
P2	N2		1.6627(16)	N10	-P3-	N3	99.33(10)
P3	N5		1.5971(16)	N4		N10	104.97(9)
P3	N4		1.6030(16)	N5		N4	110.72(9)
P3	N10		1.6472(11)	N5		N10	110.92(10)
P3	N3		1.6563(16)	N4		N3	111.83(8)
P4	N5		1.6127(16)	N5		N3	117.79(8)
P4	N6		1.6199(17)	N5	-P4-	N6	106.25(9)
P4	N9		1.6279(11)	N5		N9	108.02(11)
P4	N1		1.6453(16)	N5		N1	109.04(8)
				N6		N9	109.05(12)
				N6		N1	110.71(8)
				N9		N1	113.49(10)

Table B.14. Interatomic distances (Å) and bond angles (°) in $Sr_2AlP_8N_{15}(NH)$.

atom 1	*atom 2*	*count*	*distance*	*atom 1*	*atom 2*	*atom 3*	*angle*
Sr1	N4	2x	2.5894(19)	N3	-Al1-	N10	72.13(8)
	N5	2x	2.641(2)	N3		N3	84.75(10)
	N9		2.782(3)	N2		N2	87.93(11)
	N6	2x	2.8414(19)	N2		N3	91.39(7)
	N5	2x	3.157(2)	N2		N10	91.67(8)
Sr2	N10		2.679(3)	N8		N3	93.42(8)
	N6	2x	2.760(2)	N8		N2	102.56(9)
	N3		2.7737(18)	N8		N10	160.10(11)
	N9	2x	2.804(3)	N2		N3	163.76(9)
	N1	2x	3.002(2)	N4	-P1-	N1	105.08(10)
	N4	2x	3.3476(19)	N2		N1	107.01(11)
Al1	N8		1.936(3)	N2		N8	108.23(10)
	N2	2x	1.9986(19)	N1		N8	110.94(11)
	N3	2x	2.108(2)	N4		N2	112.23(12)
	N10		2.136(3)	N4		N8	113.32(9)
P1	N4		1.592(2)	N3	-P2-	N2	106.14(10)
	N1		1.6301(19)	N6		N3	106.74(9)
	N2		1.6404(19)	N7		N2	109.47(12)
	N8		1.6591(16)	N6		N2	110.40(12)
P2	N7		1.5994(15)	N7		N3	110.55(10)
	N6		1.6186(19)	N7		N6	113.30(12)
	N3		1.6507(19)	N10	-P3-	N3	98.99(11)
	N2		1.656(2)	N4		N10	104.37(10)
P3	N5		1.594(2)	N5		N4	109.52(10)
	N4		1.6012(18)	N5		N10	111.36(12)
	N10		1.6424(12)	N4		N3	112.25(10)
	N3		1.644(2)	N5		N3	118.99(10)
P4	N5		1.6105(19)	N5	-P4-	N6	105.90(10)
	N6		1.6213(13)	N5		N9	108.12(12)
	N9		1.625(2)	N9		N6	108.21(14)
	N1		1.635(2)	N5		N1	109.20(11)
				N6		N1	110.89(10)
				N9		N1	114.17(12)

Table B.15. Interatomic distances (Å) and bond angles (°) in $Ba_2AlP_8N_{15}(NH)$.

atom 1	*atom 2*	*count*	*distance*	*atom 1*	*atom 2*	*atom 3*	*angle*
Ba1	N4	2x	2.7240(11)	N3	-Al1-	N10	71.03(4)
	N5	2x	2.7861(11)	N3		N3	86.40(6)
	N9		2.9087(19)	N2		N2	87.50(7)
	N6	2x	2.9292(11)	N2		N3	90.76(4)
	N5	2x	3.2320(13)	N2		N10	92.90(5)
Ba2	N10		2.7968(16)	N8		N3	93.95(5)
	N3	2x	2.9132(11)	N8		N2	102.22(5)
	N9		2.9300(19)	N8		N10	158.95(7)
	N6	2x	2.9593(12)	N2		N3	163.74(5)
	N1	2x	3.0273(12)	N4	-P1-	N1	104.79(6)
	N4		3.3354(12)	N2		N1	107.76(6)
Al1	N8		1.9565(17)	N2		N8	108.71(6)
	N2	2x	2.0443(12)	N1		N8	109.83(7)
	N3	2x	2.1564(12)	N4		N2	112.32(6)
	N10		2.1658(17)	N4		N8	113.24(7)
P1	N4		1.5949(11)	N3	-P2-	N2	106.75(6)
	N2		1.6375(11)	N6		N3	107.48(6)
	N1		1.6495(11)	N7		N2	109.90(7)
	N8		1.6602(9)	N6		N2	109.92(6)
P2	N7		1.6096(8)	N7		N3	110.08(7)
	N6		1.6223(11)	N7		N6	112.51(8)
	N3		1.6481(11)	N3	-P3-	N10	99.65(7)
	N2		1.6618(11)	N4		N10	104.05(7)
P3	N5		1.5955(12)	N5		N4	108.98(6)
	N4		1.6145(11)	N5		N10	111.18(7)
	N3		1.6427(11)	N4		N3	112.67(6)
	N10		1.6436(7)	N5		N3	118.99(6)
P4	N5		1.6127(12)	N5	-P4-	N6	106.30(6)
	N9		1.6184(8)	N5		N9	108.73(8)
	N6		1.6226(12)	N9		N6	108.76(8)
	N1		1.6492(12)	N5		N1	109.00(6)
				N6		N1	110.42(6)
				N9		N1	113.37(7)

B.13. Scanning Transmission Electron Microscopy

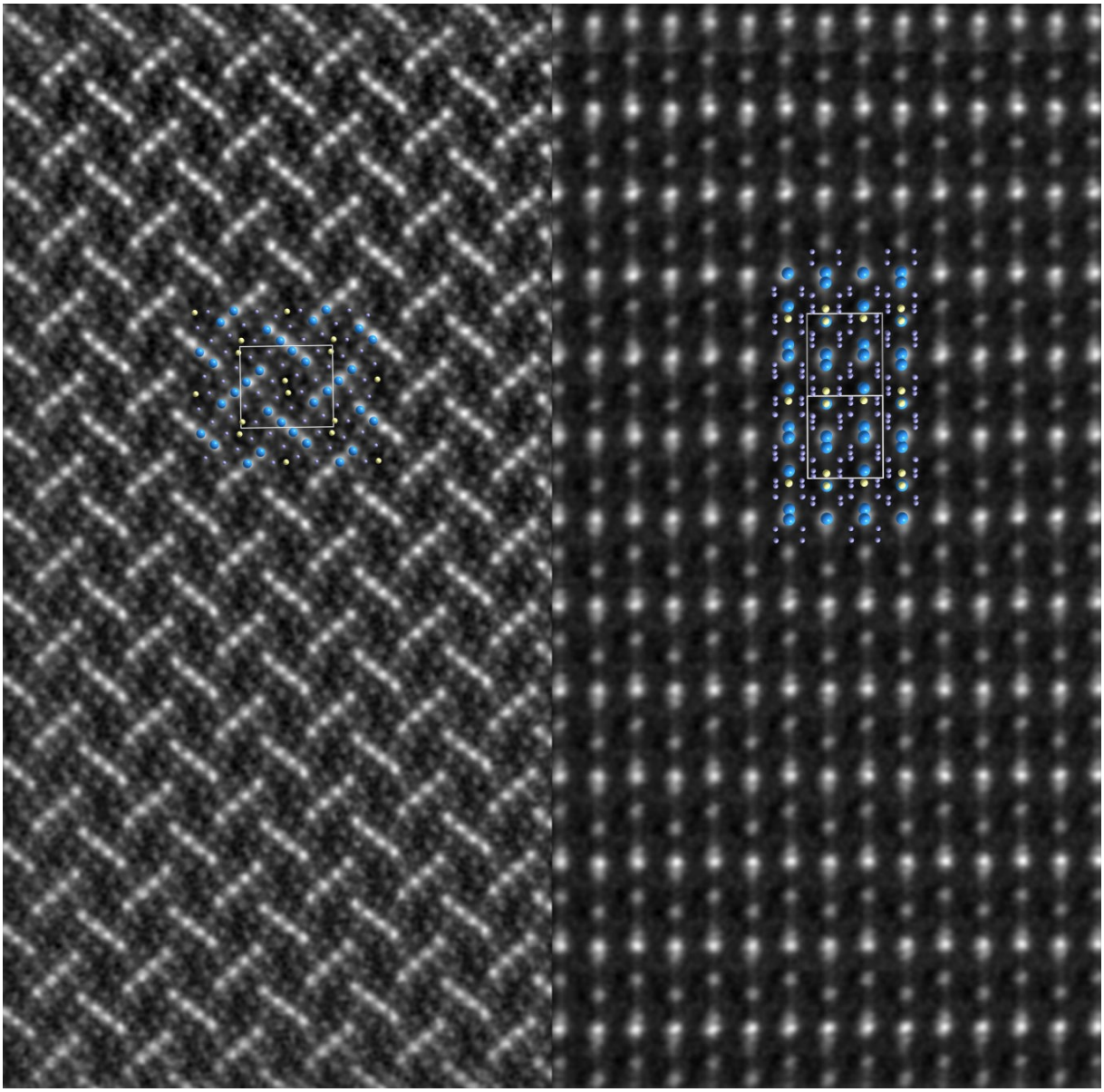

Figure B.11. STEM HAADF image of $Ba_2AlP_8N_{15}(NH):Eu^{2+}$ in (a) [010] and (b) [101] direction with structural overlays (Ba orange, P pale blue, Al yellow) and a resolution of [010]: 0.92 Å and [101]: 1.06 Å. For better visibility, the dark blue P atoms are less saturated, unit cell is marked with white lines.

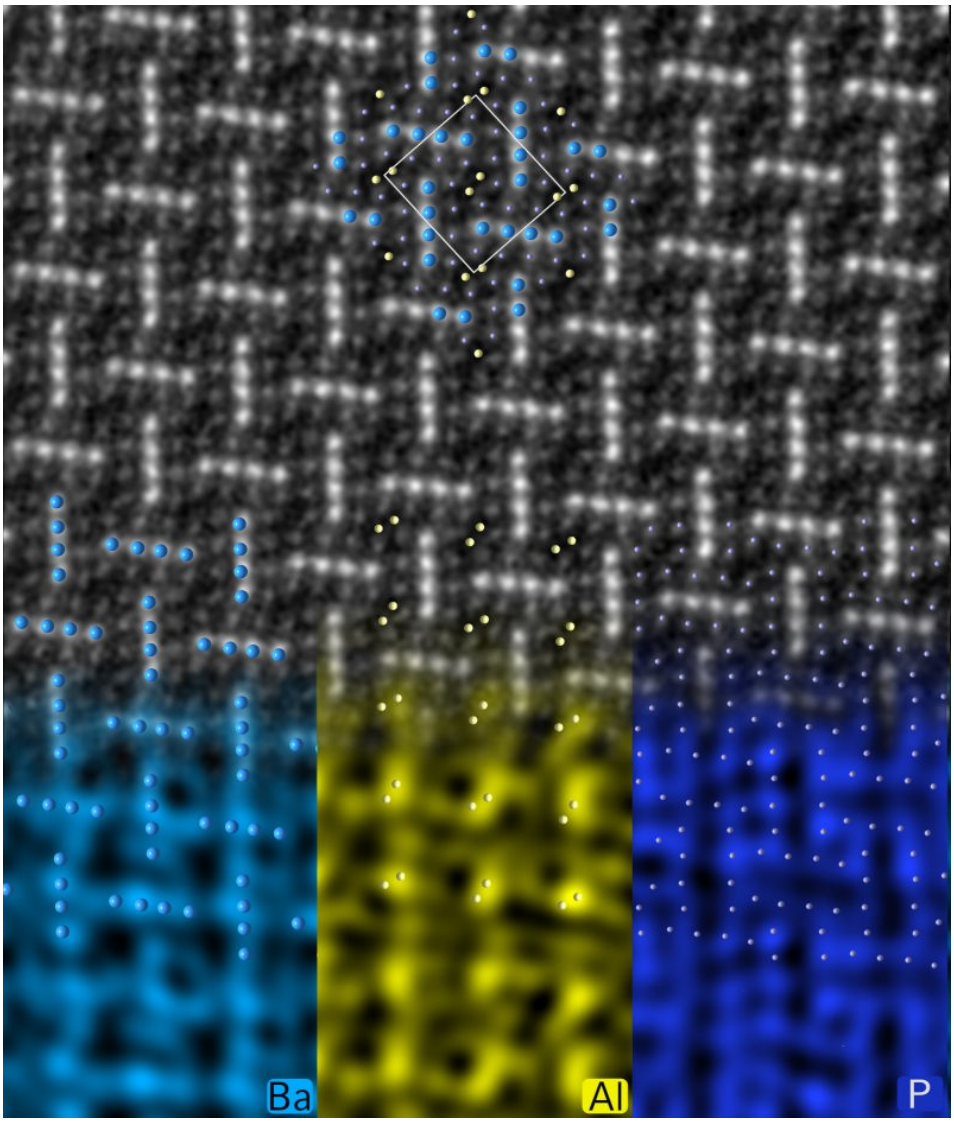

Figure B.12. STEM and EDX mapping of $Ba_2AlP_8N_{15}(NH):Eu^{2+}$ along [010]. STEM HAADF image (top) with structure overlay (Ba light blue, Al yellow, P pale blue) and unit cell insert in white. The corresponding EDX maps are shown on the bottom: Ba light blue, Al yellow, P dark blue.

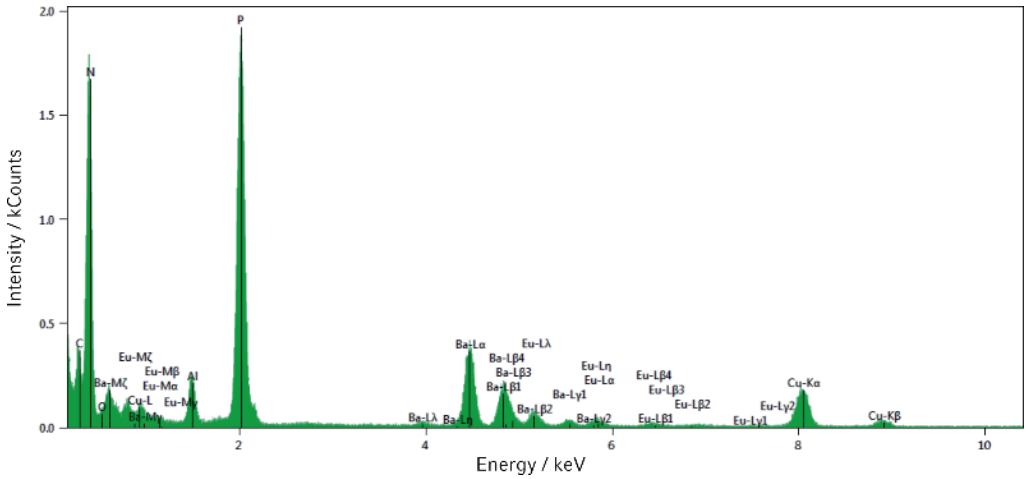

Figure B.13. Raw EDX spectrum of the obtained STEM-EDX map; Cu and C originate from the TEM grid.

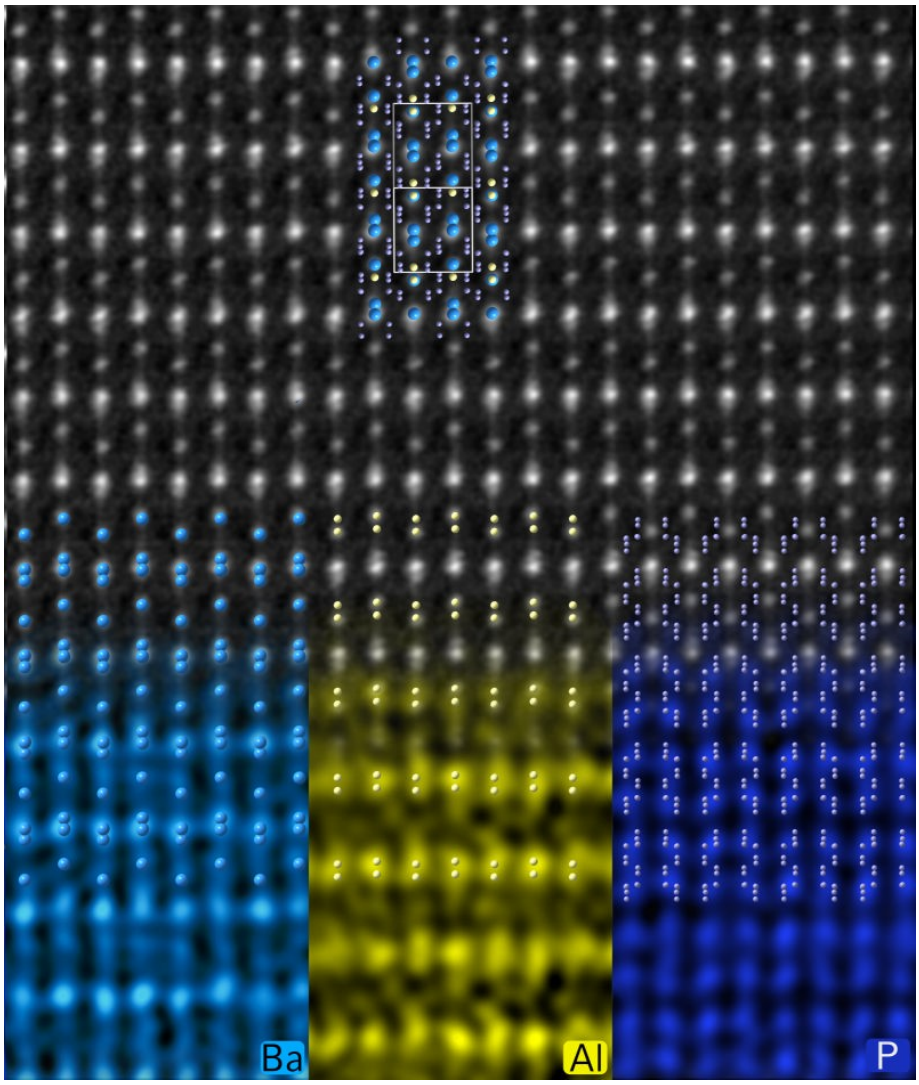

Figure B.14. STEM and EDX mapping of $Ba_2AlP_8N_{15}(NH):Eu^{2+}$ along [101]. STEM HAADF image (top) with unit cell insert in white; structure overlay (middle, Sr orange, P blue, Al yellow). The corresponding EDX maps are shown on the bottom: Ba orange, P pale blue, Al yellow; and the resulting combined map.

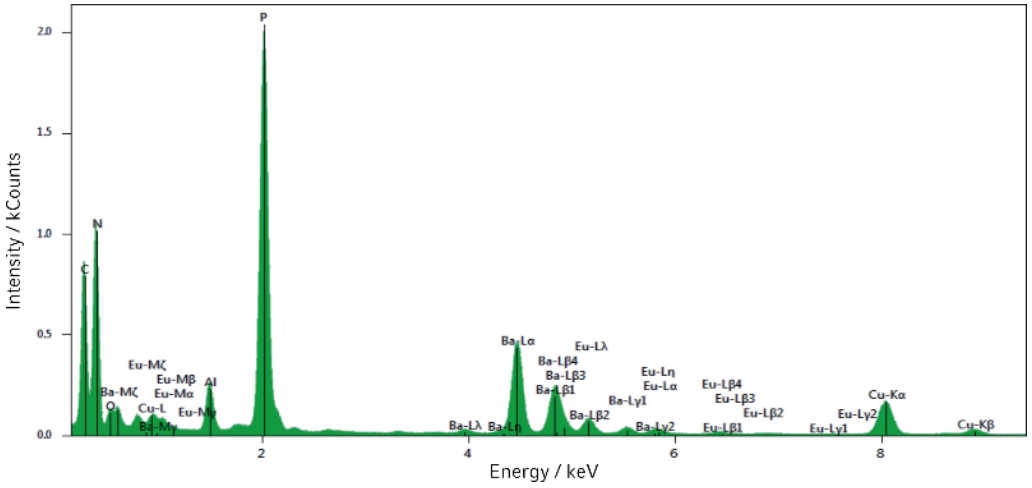

Figure B.15. Raw EDX spectrum of the obtained STEM-EDX map; Cu and C originate from the TEM grid.

B.14. Luminescence

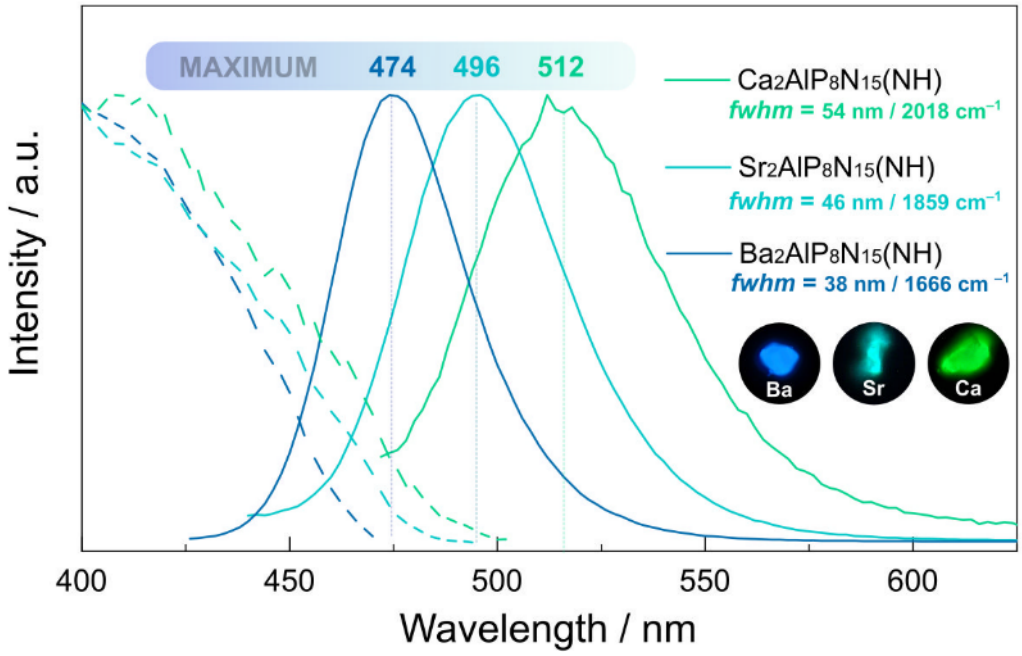

Figure B.16. Unsmoothed luminescence spectra of single particles of $AE_2AlP_8N_{15}(NH)$ (*AE* = Ca, Sr, Ba). $Ba_2AlP_8N_{15}(NH)$ and $Sr_2AlP_8N_{15}(NH)$ were excited with 400 nm, $Ca_2AlP_8N_{15}(NH)$ was excited with 450 nm. Normalized excitation spectra (left) and emission spectra (middle) for Ca (green), Sr (cyan), Ba (blue); insert: photograph of luminescent particles (λ_{exc}= 420 nm).

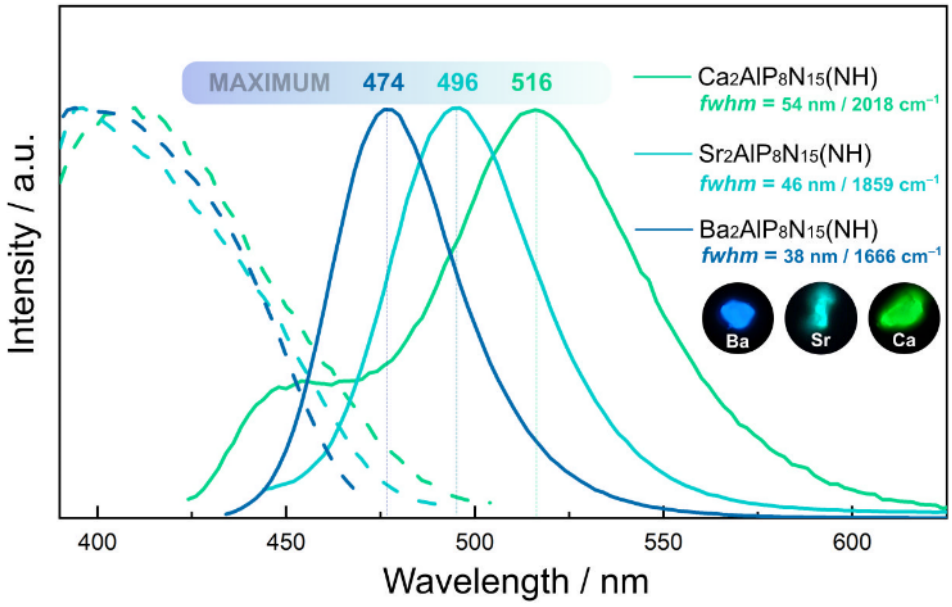

Figure B.17. Luminescence spectra of single particles of $AE_2AlP_8N_{15}(NH)$ (*AE* = Ca, Sr, Ba). All compounds were excited with 400 nm. Normalized excitation spectra (left) and emission spectra (middle) for Ca (green), Sr (cyan), Ba (blue); insert: photograph of luminescent particles (λ_{exc}= 420 nm).

C. Supporting Information for Chapter 4

C.1. Synthesis

Table C.1. Weighed portions of starting materials for the syntheses of $Cr_{5.7}Si_{2.3}P_8N_{24}$.

	starting material			
	Cr_2N	Si_3N_4	P_3N_5	NH_4F
mg	10.08	4.00	13.93	3.17
mmol	0.85	0.85	0.03	0.85

C.2. Structure Determination

Due to fiber-like crystals with single crystals around 2-3 µm in size, the sample was pre-characterized on TEM grids and datasets of suitable single crystals were obtained at the ID11 line at the ESRF.

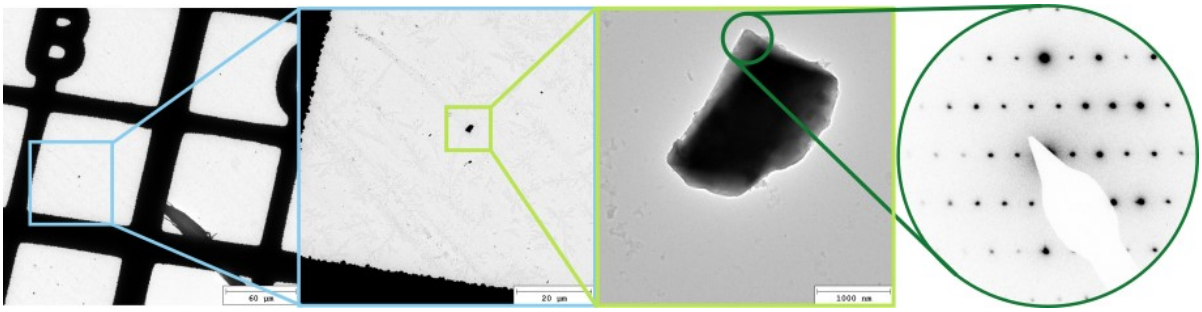

Figure C.1. Crystal pre-characterized with TEM and measured at the beamline ID11 at the ESRF.

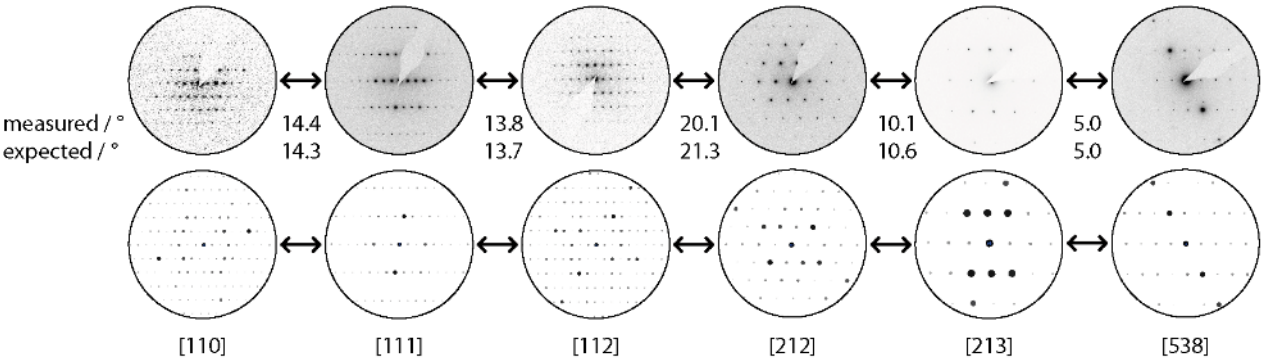

Figure C.2. Experimental selected area electron diffraction (SAED) patterns of $Cr_{5.7}Si_{2.3}P_8N_{24}$ (top) and simulated ones (bottom) based on the structure model in *C*2/*m* as derived from single-crystal data.

Table C.2. Crystallographic data of the single-crystal structure refinement of $Cr_{5.7}Si_{2.3}P_8N_{24}$. Standard deviations are given in parentheses.

formula	$Cr_{5.68}Si_{2.32}P_8N_{24}$
molar mass / g·mol^{-1}	954.005
crystal system	monoclinic
space group	*C*2/*m* (no. 12)
lattice parameters / Å, °	*a* = 9.6042(5)
	b = 17.1132(2)
	c = 4.85510(10)
	β = 109.645(5)
cell volume / Å^3	751.53(5)
formula units / unit cell	2
density / g·cm^{-3}	4.174
μ / mm^{-1}	0.4147
temperature / K	293(2)
absorption correction	sphere
radiation	Synchrotron, ESRF ID11, (λ = 0.28469 Å)
F(000)	913.6
θ range / °	1.773–18.319
total no. of reflections	3789
independent reflections [I≥2σ(I) / all]	1664 / 1433
R_σ, R_{int}	0.0200, 0.0243
refined parameters	100
restraints	0
GooF	1.082
R values [I≥2σ(I)]	*R*1 = 0.0268, *wR*2 = 0.0771
R values (all data)	*R*1 = 0.0306, *wR*2 = 0.0790
$\Delta\rho_{max}$, $\Delta\rho_{min}$ / e·Å^{-3}	0.220, −0.657

Table C.3. Atomic coordinates, isotropic displacement parameters (Å^2), and site occupancies.

atom	*Wyckoff*	*x*	*y*	*z*	U^2	*s.o.f.*
Si1	4*g*	0	0.08524(2)	0	0.00608(13)	0.659(4)
Cr1	4*g*	0	0.08524(2)	0	0.00608(13)	0.341(4)
Cr2	4*h*	0	0.17477(2)	½	0.00646(9)	1
Si3	2*c*	0	0	½	0.00431(13)	1
Cr4	4*g*	0	0.26379(2)	0	0.00591(8)	1
Cr5	2*d*	0	½	½	0.00572(10)	1
P1	8*j*	0.20245(4)	0.41948(2)	0.13896(8)	0.00507(9)	1
P2	8*j*	0.30138(4)	0.16216(2)	0.36107(8)	0.00551(9)	1
N1	8j	0.38549(15)	0.41888(7)	0.2623(3)	0.0082(2)	1
N2	8j	0.11953(15)	0.16909(7)	0.2265(3)	0.0085(2)	1
N3	4i	0.09531(19)	0	0.2427(4)	0.0075(3)	1
N4	8j	0.37437(13)	0.23711(6)	0.2658(2)	0.00553(19)	1
N5	8j	0.14019(14)	0.34579(7)	0.2804(2)	0.00644(19)	1
N6	8j	0.35718(14)	0.08479(6)	0.2212(3)	0.00593(19)	1
N7	4i	0.64052(19)	0	0.2400(3)	0.0065(3)	1

Table C.4. Anisotropic displacement parameters (Å^2) with standard deviations in parentheses. The anisotropic displacement factor is expressed as $\exp[-2\pi^2 (U_{11}h^2a^{*2} + U_{22}k^2b^{*2} + U_{33}l^2c^{*2} + U_{12}hka^*b^* + U_{13}hla^*c^* + U_{23}klb^*c^*)$.

atom	U_{11}	U_{22}	U_{33}	U_{12}	U_{13}	U_{23}
Si1	0.0051(2)	0.0069(2)	0.0062(2)	0	0.00184(16)	0
Cr1	0.0051(2)	0.0069(2)	0.0062(2)	0	0.00184(16)	0
Cr2	0.00580(16)	0.00641(14)	0.00721(14)	0	0.00224(12)	0
Si3	0.0037(3)	0.0052(3)	0.0039(3)	0	0.0010(2)	0
Cr4	0.00533(15)	0.00608(13)	0.00574(14)	0	0.00108(11)	0
Cr5	0.0058(2)	0.00574(17)	0.00551(17)	0	0.00181(15)	0
P1	0.00458(17)	0.00507(14)	0.00519(15)	0.00011(9)	0.00116(12)	0.00010(10)
P2	0.00489(18)	0.00620(14)	0.00507(15)	-0.00017(9)	0.00118(13)	0.00030(10)
N1	0.0060(5)	0.0080(4)	0.0094(5)	0.0012(3)	0.0009(4)	0.0000(4)
N2	0.0053(5)	0.0126(5)	0.0073(5)	0.0013(3)	0.0016(4)	0.0021(4)
N3	0.0035(7)	0.0123(7)	0.0061(6)	0	0.0009(5)	0
N4	0.0061(5)	0.0055(4)	0.0054(4)	-0.0005(3)	0.0026(4)	-0.0012(3)
N5	0.0066(5)	0.0071(4)	0.0053(4)	0.0003(3)	0.0014(4)	-0.0006(3)
N6	0.0061(5)	0.0060(4)	0.0051(4)	-0.0002(3)	0.0012(4)	0.0005(3)
N7	0.0069(7)	0.0060(6)	0.0068(6)	0	0.0025(5)	0

Table C.5. Interatomic distances (Å) and bond angles (°) with standard deviations given in parentheses.

atom 1	*atom 2*	*count*	*distance*	*atom 1*	*atom 2*	*atom 3*	*angle*
Cr1	N3	2x	1.9049(11)	N3	–Cr1–	N1	80.04(6)
Cr1	N2	2x	1.9333(14)	N3		N3	80.05(8)
Cr1	N1	2x	1.9439(13)	N2		N2	84.15(8)
Cr2	N4	2x	2.0250(11)	N2		N1	90.73(5)
Cr2	N2	2x	2.0287(13)	N2		N1	92.35(5)
Cr2	N2	1x	2.0287(13)	N3		N1	96.74(6)
Cr2	N1	2x	2.0630(12)	N3		N2	98.43(6)
Si3	N3	2x	1.7799(16)	N3		N2	171.97(6)
Si3	N1	4x	1.9013(13)	N1		N1	175.84(7)
Cr4	N4	2x	2.0416(11)	N1	–Cr2–	N1	78.06(7)
Cr4	N2	2x	2.0748(13)	N4		N4	83.72(7)
Cr4	N5	2x	2.0984(12)	N2		N1	84.79(5)
Cr5	N7	2x	2.1353(16)	N2		N1	84.80(5)
Cr5	N6	4x	2.1379(12)	N2		N1	90.94(5)
P1	N7	1x	1.6400(9)	N4		N2	91.70(5)
P1	N5	1x	1.6419(12)	N4		N2	92.39(5)
P1	N6	1x	1.6484(12)	N4		N1	99.18(5)
P1	N1	1x	1.6557(14)	N2		N2	174.51(7)
P2	N4	1x	1.6026(11)	N4		N1	176.00(5)
P2	N5	1x	1.6451(12)	N3	–Si3–	N1	84.44(5)
P2	N2	1x	1.6505(14)	N1		N1	86.20(8)
P2	N6	1x	1.6574(11)	N1		N1	93.80(8)
				N3		N1	95.56(5)
				N1		N1	180.00(5)
				N3		N3	180
				N2	–Cr4–	N2	77.28(7)
				N4		N5	88.94(5)
				N4		N2	89.42(5)
				N4		N2	89.91(5)
				N4		N5	91.63(4)
				N2		N5	93.35(5)
				N5		N5	96.06(7)
				N2		N5	170.49(5)
				N4		N4	179.14(6)
				N6	–Cr5–	N6	85.48(6)
				N7		N6	88.62(5)
				N7		N6	91.38(5)
				N6		N6	94.52(6)
				N6		N6	180.00(4)
				N7		N7	180
				N6		N6	180
				N7	–P1–	N5	107.48(6)

N7		N6	108.84(7)
N6		N1	109.36(6)
N5		N1	109.61(6)
N7		N1	110.17(7)
N5		N6	111.35(6)
N4	–P2–	N6	106.74(6)
N5		N6	108.98(6)
N2		N6	109.88(6)
N4		N5	110.18(6)
N5		N2	111.34(6)

C.3. Rietveld Refinement

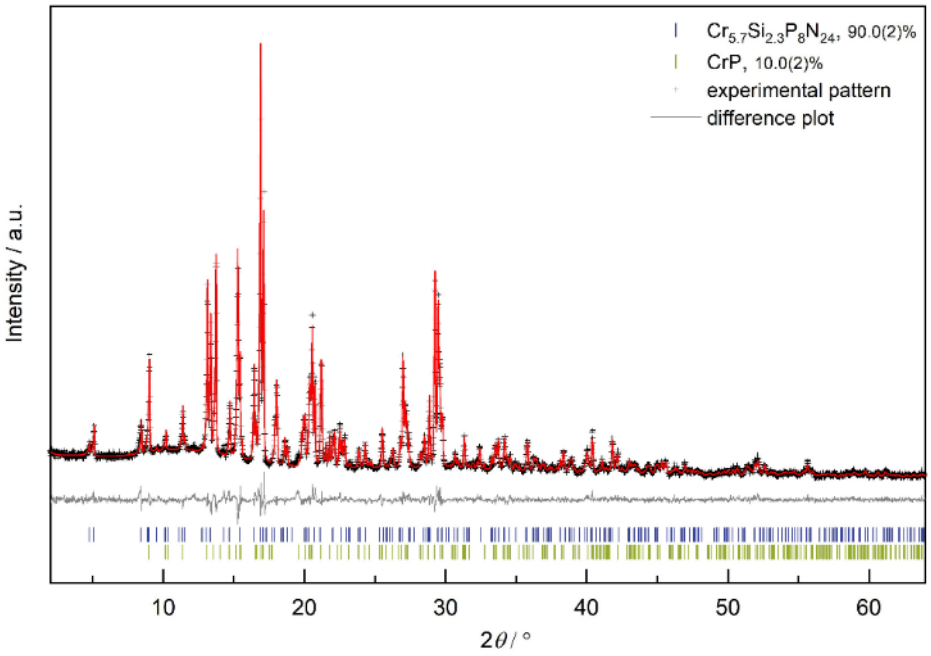

Figure C.3. Rietveld refinement for $Cr_{5.7}Si_{2.3}P_8N_{24}$. Observed (black crosses) and calculated (red line) X-ray powder diffraction patterns, positions of Bragg reflections of $Cr_{5.7}Si_{2.3}P_8N_{24}$ (vertical blue bars), CrP (vertical green bars), and difference profile (gray line); R_p = 0.052, R_{wp} = 0.069, R_{exp} = 0.045, R_{Bragg} = 0.024.

C.4. High-Temperature PXRD

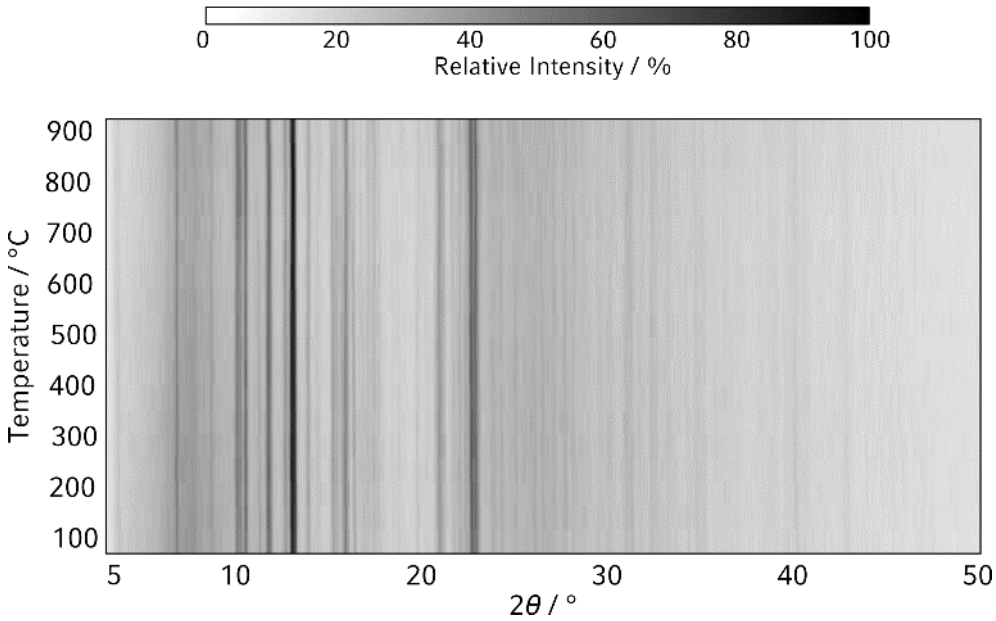

Figure C.4. Temperature-dependent powder X-ray diffraction patterns (Ag-Kα_1 radiation, λ = 0.5595378 Å) showing no decomposition up to 900 °C.

C.5. Elemental Analysis

Table C.6. (S)TEM-EDX measurements (several point analyses) compared to values derived from sum formula.

	EDX measuring point / at%	*Cr*	*Si*	*P*	*N*
STEM	1	13	6	22	59
	2	13	6	22	60
	3	16	6	23	56
	4	13	6	22	59
	5	15	8	20	57
	6	13	5	20	62
	7	15	6	23	57
	average	14(1)	6(1)	22(1)	58(2)
SEM	1	17	4	24	54
	2	17	5	24	54
	average	16(0)	5(1)	24(1)	54(1)
	$Cr_{5.7}Si_{2.3}P_8N_{24}$	14.25	5.75	20	60

C.6. FTIR spectrum

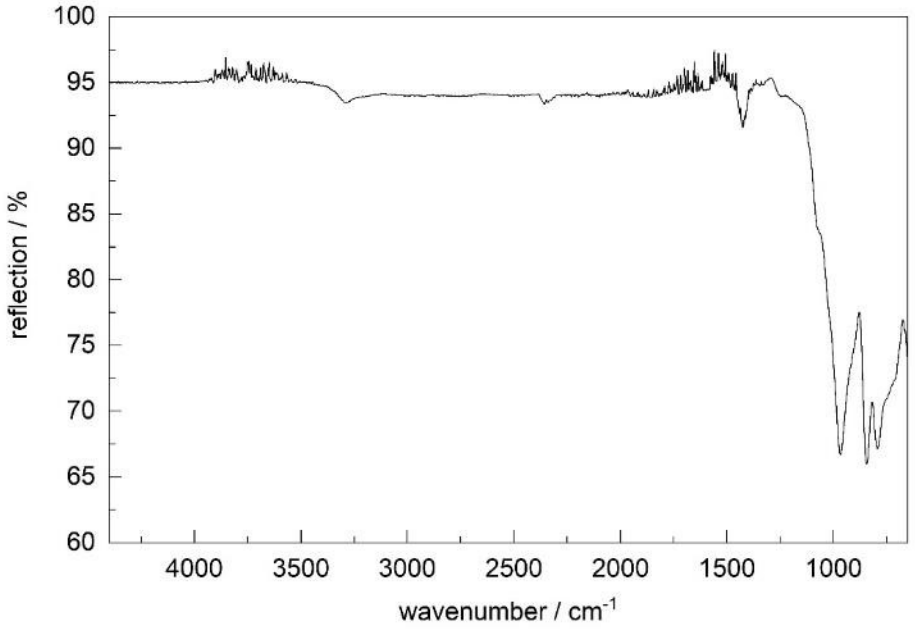

Figure C.5. FTIR spectra of Cr5.7Si2.3P8N24. The small signal around 3350 cm-1 could correspond to O–H or N–H oscillations, most likely due to a small extent of surface hydrolysis.

C.7. Coordination Environments

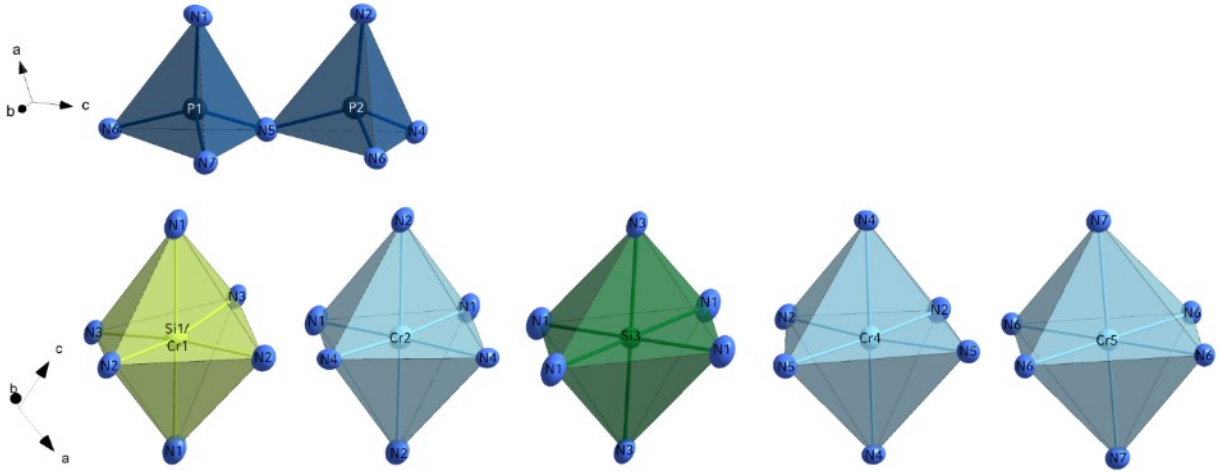

Figure C.6. Coordination polyhedra of P1, P2, Si1/Cr1, Cr2, Si3, Cr4 and Cr5. The thermal ellipsoids are shown with 90% probability.

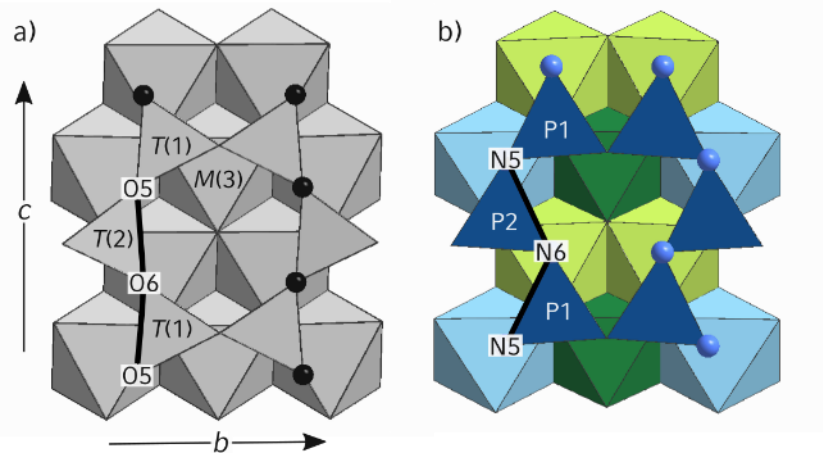

Figure C.7. Cutout of the structure of showing the structural similarities and differences between (b) and an idealized amphibole (a) in the space group C2/m, projection along [100]. In black, the characterized kinking angle N5–N6–N5 is marked. The kinking angle is decreased until the symmetry of the ring, which consists of six corner-sharing PN4 tetrahedra is almost a threefold rotation symmetry. P dark blue, Si green, Cr light blue, Si/Cr disorder light green.

C.8. Polyhedra Volumina

Table C.7. Average bond lengths (Å) and polyhedra volumes (Å^3). The octahedral site occupied by Si shows smaller values compared to the three octahedral sites occupied by Cr. The mixed position lies in between with a deviation from the expected values of a 0.7:0.3 Si:Cr mixed occupancy of around 2%.

position	*polyhedra volumina*	*average bond length*	*occ.*	*deviation from expected value / %*
Cr2	11.1179	2.00387	Cr	
Cr4	11.7294	2.0703	Cr	
Cr5	12.9429	2.1359	Cr	
Si1/Cr1	9.3386	1.9280	~ Si 70% : Cr 30%	2%
Si3	8.4806	1.8611	Si	
P1	2.2846	1.6454	P	
P2	2.2541	1.6383	P	

C.9. BVS Calculations and Partial MAPLE Values

Table C.8. Bond valence sum (BVS) and partial MAPLE values in kJmol^{-1} for the atom sites.

atom site	*bond valence sum*	*occ.*	*deviation / %*	*atom site*	*partial MAPLE value*
Si1|Cr1	3.95	1.00	1.35	Cr1|Si1	9892
Cr2	3.60	1.00	9.95	Cr2	8733
Si3	4.20	1.00	5.00	Si3	10658
Cr4	3.30	1.00	17.45	Cr4	8775
Cr5	2.76	1.00	30.95	Cr5	8772
P1	5.01	1.00	0.20	P1	14960
P2	5.12	1.00	2.48	P2	15235
				N1	5934
				N2	6069
				N3	4568
				N4	5602
				N5	6358
				N6	6172
				N7	6214

typical MAPLE values (in kJ/mol):[68-69]: Si^{+IV}: 9000–10200; P^{+V}: 14100–15500; N^{3-}: 5500–7200

Table C.9. Charge distribution and partial MAPLE values in kJmol^{-1} for the atom sites.

refined formula	*element*	*site*	*BVS*	*occ.*	*deviation / %*	*reference*
	Cr	Cr5|A	2.76	1.00	30.95	
$(Na_{0.38}K_{0.12}Ca_{1.80})Mg_5(Al_{0.24}Si_{7.76})O_{22}(O_{1.33}H_{1.34}F_{0.66}Cl_{0.01})$	K, Na	A	0.11	0.15	23.96	[70]
$(Na_{1.17}Li_{1.70})(Mg_{1.36}Fe_{2.77}Mn_{0.13}Zn_{0.32})Si_8O_{22}(OH)_2F_{0.48}$	Na	A	0.36	0.50	27.80	[71]
$Na_{1.88}Mg_{6.12}V_{0.03}Si_8O_{22}F_2$	Na	A	0.21	0.27	22.40	[72]
$K(NaCa)(Mg_{2.5}Ni_{2.5})Si_8O_{22}(OD)_2$	K	A	0.38	0.50	24.60	[73]
$Na(Na_{0.96}Ca_{1.02})Ni_{4.96}Si_8O_{22}O_2$	Na	A	0.32	0.49	34.40	[74]
$K_{0.32}Na_{2.67}Li_{0.78}Mg_{1.67}Zn_{0.29}Fe_{1.74}Al_{0.23}Mn_{0.26}Ti_{0.02}Si_8O_{22}[OH]_{0.41}F_{1.59}$	K, Na	A	0.50	0.30	65.44	[75]

C.10. Scanning Transmisison Electron Microscopy

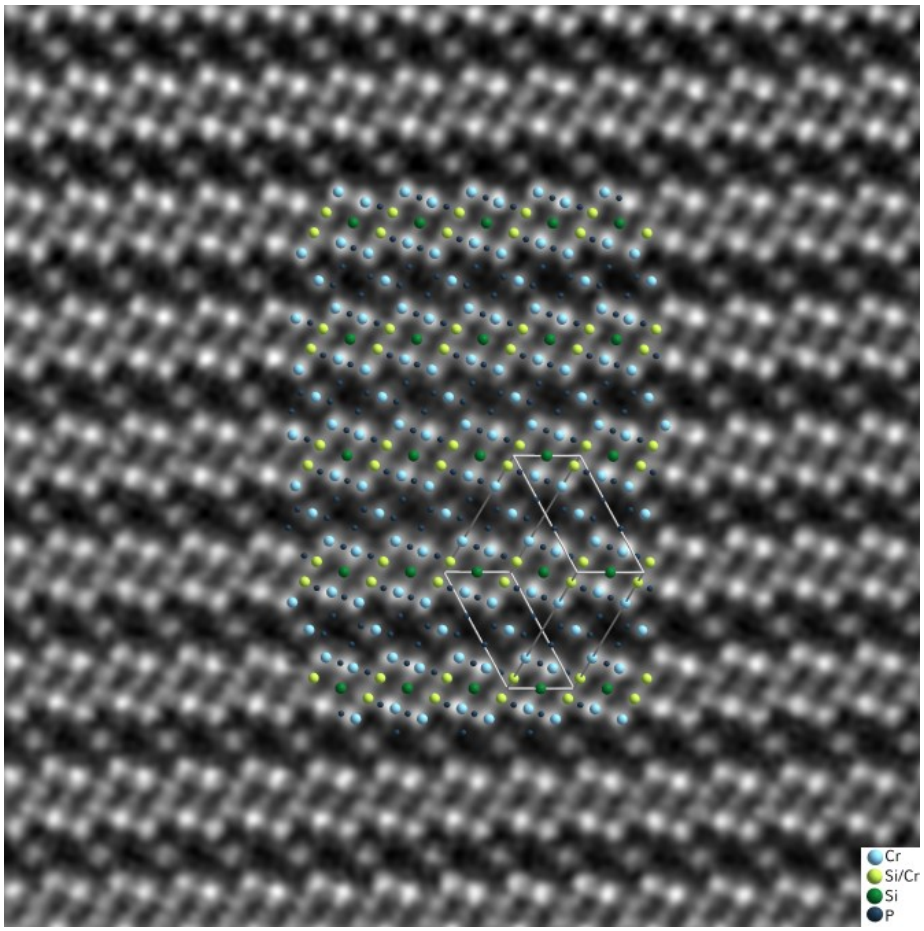

Figure C.8. STEM-HAADF image along [112] of with structure overlay. Intensity differences identify different elemental occupancies of chromium, silicon-chromium and silicon positions

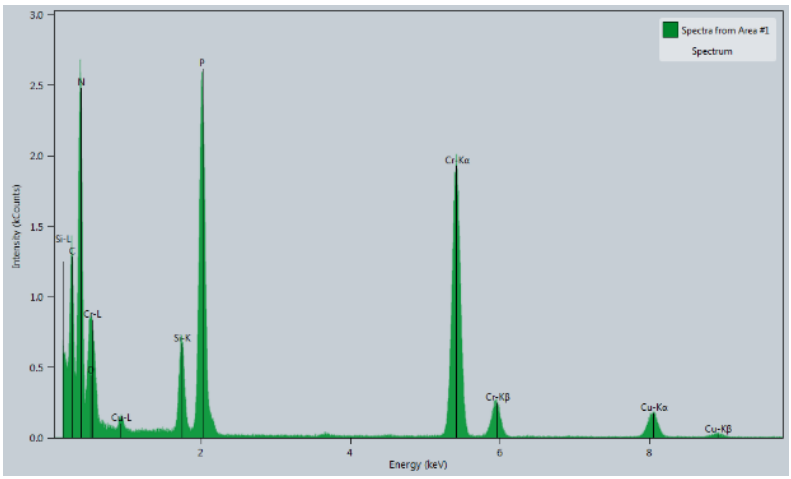

Figure C.9. Raw EDX spectrum of the obtained STEM-EDX map; Cu and C originate from the TEM grid.

C.11. References to Known Nitridochromates and Chromium Nitrides

Table C.10. List of binary, ternary and quaternary nitridochromates and chromium nitrides. The corresponding structure types are specified if known. The table is loosely sorted from chromium-rich to nitrogen-rich compounds. Oxidation states are given if a clear assignment is possible.

Cr/N ratio	*compound*	*space group*	*structure type*		*reference*
3	Cr_3GeN	$P\bar{4}2_1m$			[18]
	Cr_3GeN	*Cmcm*	antiperovskite	Cr_3C_2	[76]
	Cr_3AsN	*I*4/*mcm*		$SrZrO_3$	[17]
	Cr_3GaN	$Pm\bar{3}m$		$CaTiO_3$	[16]
	Cr_3MN *M* = Ir, Pd, Pt, Rh, Sn	$Pm\bar{3}m$		$CaTiO_3$	[15]
2.8–3	$(Cr_{3-x}Mn_x)GeN$ with *x* = 0.2–0.4	*I*4/*mcm*	$SrZrO_3$		[77]
2.6–2.8	$(Cr_{3-x}Mn_x)GeN$ with *x* = 0–0.2	$P\bar{4}2_1m$			[77]
2	Cr_2N	$P\bar{3}1m$	V_2N		[78-79]
1	$Cr^{III}N$	$Fm\bar{3}m$	NaCl		[19]
	$(Cr^{III},M)N$ *M* = Ti, V, Zr, Hf				[20-21]
0.9	$La_6Cr_{21}N_{23}$ / $La_3Cr^{II,III}_{10-x}N_{11}$	$Fm\bar{3}m$	$Cr_{21}La_6N_{23}$		[80, 81]
0.5	$Cr^{III}WN_2$	*R*3*m*H	$AgCrS_2$		[82]
	$Cr^{III}MoN_2$				[83]
0.33	$Ca_3Cr^{III}N_3$	*Cmcm*	Ca_3CrN_3		[22]
	$AE_3Cr^{III}N_3$ *AE* = Sr, Ba	*P*6$_3$/*m*	Ba_3FeN_3		[23]
	$Sr_2Cr^{IV}N_3{:}e^-$	*P*6$_3$/*m*			[24]
	$U_2Cr^{III}N_3$	*Immm*	Sr_2CuO_3		[84]
	$Th_2Cr^{III}N_3$				[84]
	$Ce^{IV}_2[Cr^{I}N_3]^{-VIII}$				[81]
	$Ca_6[Cr^{III,IV}_2N_6]H$	$R\bar{3}$H	Mo_6PbS_8		[85]
	$LiSr_2[Cr^{IV}N_3]$	*P*2$_1$			[25]
	$La_3Cr_2N_6$	*I*4/*mmm*			[26]
	$Li_4Sr_2[Cr^{V}_2N_6]$	*Pbca*			[28]
	$AE_4[Cr^{V}_2N_6]$ *AE* = Ca, Sr	$P\bar{1}$			[86]
	$Ba_3[Cr^{IV}N_3]H$	*P*6$_3$/*m*			[87]
	$Ca_3[Cr^{IV}N_3]H$	*P*6$_3$/*m*			[88]
0.25	$Li_6Cr^{VI}N_4$	*P*4$_2$/*nmc*			[30]
	$Sr_3Cr^{VI}N_4$	*Pbca*	$(Ba,Sr)_3MoN_4$		[31]
0.22	$Li_{15}Cr^{VI}_2N_9$	*P*4/*nccZ*			[30]
0.2	$Ba_5[Cr^{V}N_4]N$	*C*2/*m*			[27]
0.2	$Li_{7.2}Cr^{VI}_{0.8}N_4$	$Fm\bar{3}m$	CaF_2		[29]

C.12. Magnetization Isotherm

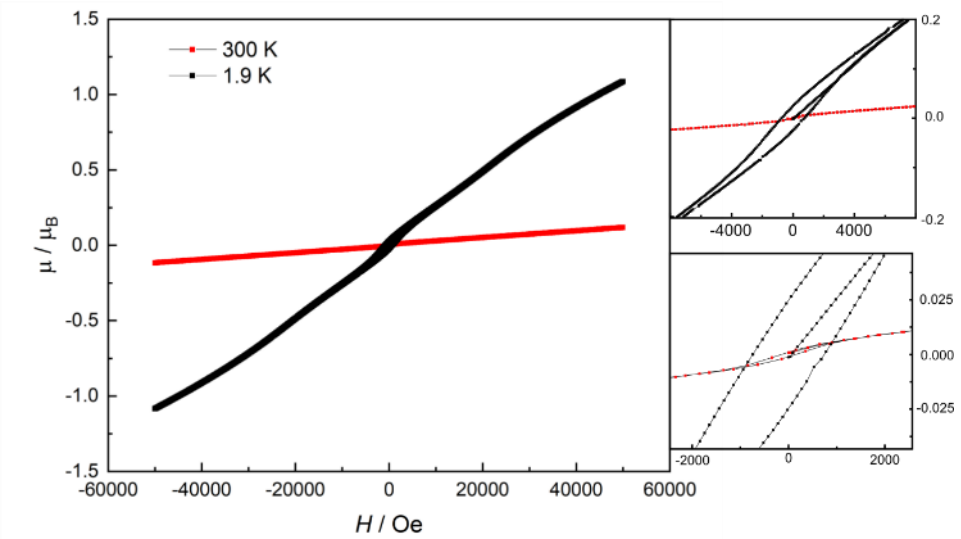

Figure C.10. Magnetization isotherm at 300 K (red) and at 1.9 K (black). A hysteresis behavior at low field strengths indicates a minor amount of a ferromagnetic impurity which can still be seen at 300 K (shown in the two magnifications).

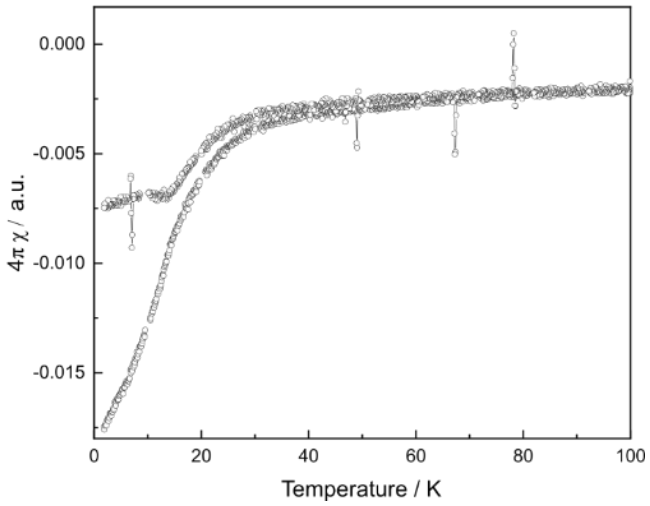

Figure C.11. Zero-field-cooled/field-cooled magnetization studies measured at 15 Oe show a superconducting transition indicating a very small amount of diamagnetic impurity with superconducting behavior. A slight hysteresis of the data indicates the minor ferromagnetic impurity.

C.13. Electron Paramagnetic Resonance

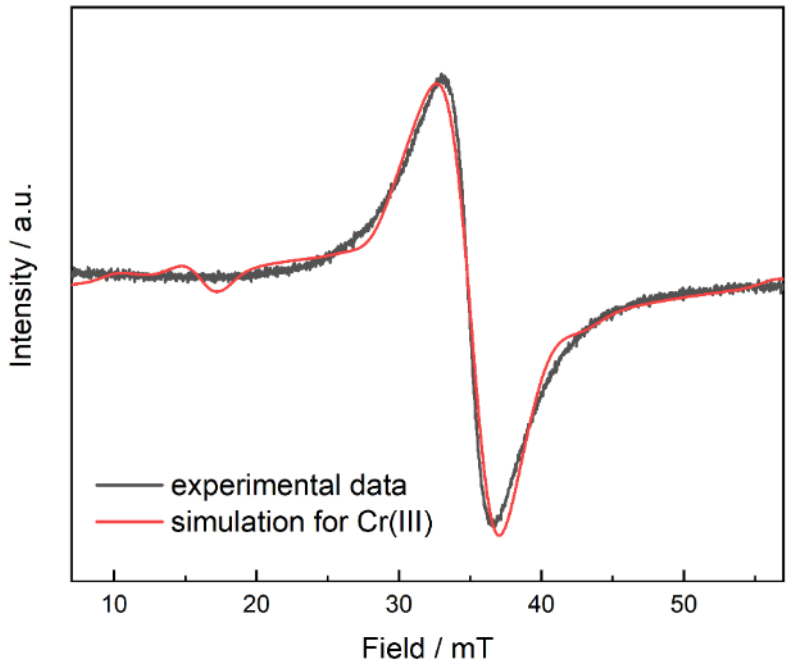

Figure C.12. CW X-band / EPR spectrum of $Cr_{5.7}Si_{2.3}P_8N_{24}$ measured at 77 K (black) and simulation (red), using the parameters in table C.11.

Table C.11. Parameters obtained from non-linear least square regression model at X-band for Cr(III) and Cr(IV). D is the axial parameter and corresponds to the ligand field splitting parameter b_0^2, E is the rhombohedral parameter and corresponds to 1/3 b_2^2, lwwp describes the line-width peak to peak and therefore the broadening of the peak. The site Si1/C1 can be precisely assigned based on the Si:Cr ratio. CrA–C correspond to the centers Cr2, Cr4, and Cr5 due to an uncertainty in precise identity determination.

Cr center	*CrC*	*CrB*	*CrA*	*Si1/Cr1*	*CrC*	*CrB*	*CrA*	*Si1/Cr1*
ox. state		III				IV		
ratio	1	1	1	0.3	1	1	1	0.3
$g_{average}$	2.067	1.846	1.986	2.123	1.798	2.197	2.091	1.989
D (cm^{-1})	0.022	0.26	0.015	0	0.081	0.251	0.011	0.014
E (cm^{-1})	0.005	0.04	0.001	0	0.002	0.042	0.001	0.006
lwpp:	200	23.17744	28.2932	155.8246	67.51317	73.10666	100.6019	29.29519
residuals of best fit:		13.0832				2.79887		

C.14. UV-Vis Spectrum

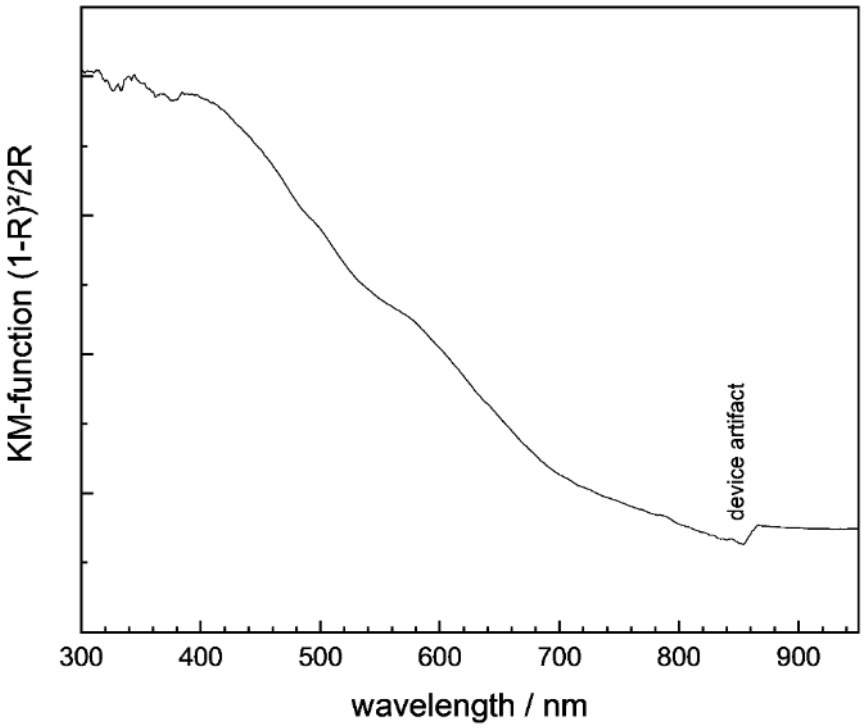

Figure C.13. Kubelka-Munk function applied to the UV-Vis spectrum.

D. Supporting Information for Chapter 5

D.1. Synthesis

Table D.1. Weighed portions of starting materials for the synthesis in a multi-anvil press.

	starting material		
	Ta_3N_5	P_3N_5	NH_4F
in mg	34.25	22.76	3.17
in mmol	0.55	1.39	0.83

D.2. Structure Elucidation

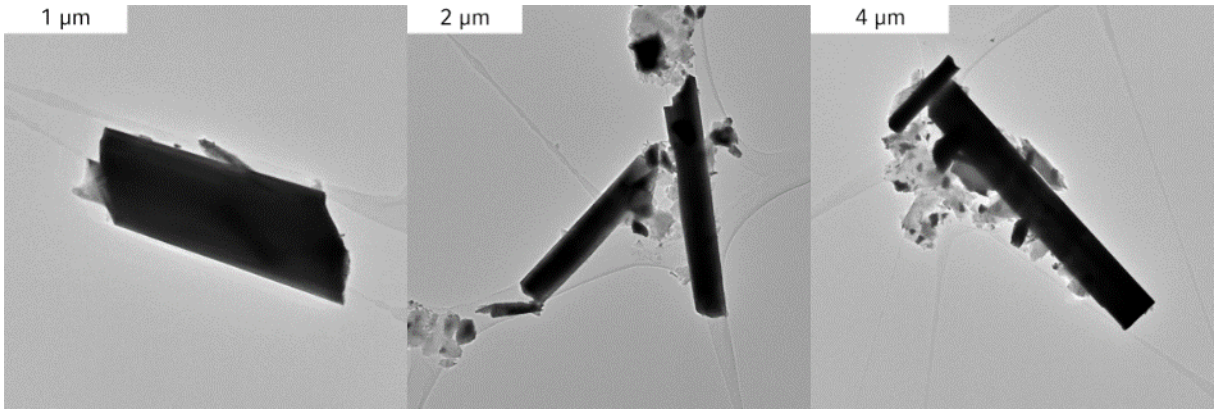

Figure D.1. Exemplary TEM bright-field images of crystals.

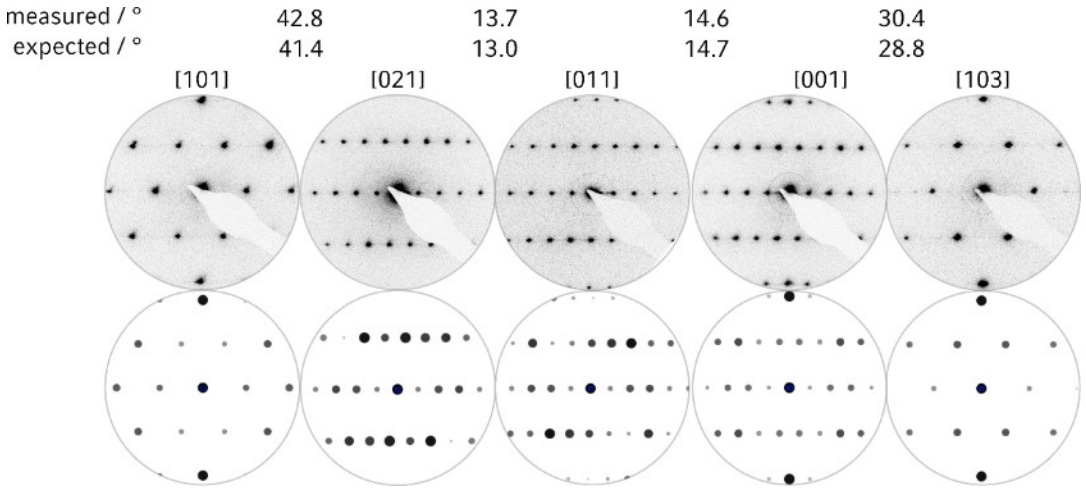

Figure D.2. Experimental selected area electron diffraction (SAED) patterns (top) and simulated ones (bottom) based on the structure model in *C*2/*m* as derived from single-crystal data.

Table D.2. Crystallographic data of the single-crystal structure refinement. Standard deviations are given in parentheses.

formula	$P_{0.9}Ta_{8.1}N_{13}$
molar mass / g·mol^{-1}	1675.79
crystal system	monoclinic
space group	*C*2/*m* (no. 12)
lattice parameters / Å, °	*a* = 16.202(3)
	b = 2.9155(4)
	c = 11.0893(18)
	β = 126.698(7)
cell volume / Å^3	420.00(11)
formula units / unit cell	2
density / g·cm^{-3}	13.251
μ / mm^{-1}	105.218
temperature / K	299(2)
absorption correction	semi-empirical
radiation	Mo-K*α* (*λ* = 0.71073 Å)
F(000)	1392
θ range / °	3.136–24.706
total no. of reflections	905
independent reflections [I≥2σ(I) / all]	718 / 905
R_σ	0.0730
refined parameters	44
restraints	0
GooF	1.094
R values [I≥2σ(I)]	*R*1 = 0.0586, *wR*2 = 0.1418
R values (all data)	*R*1 = 0.0815, *wR*2 = 0.1576
$\Delta\rho_{max}$, $\Delta\rho_{min}$ / e·Å^{-3}	3.795, –3.763

Table D.3. Atomic coordinates, isotropic displacement parameters (in Å^2), and site occupancies.

atom	*Wyckoff*	*x*	*y*	*z*	*U*	*s.o.f.*
P1	4*d*	½	0	½	0.025(7)	0.90(2)
Ta1	4*d*	½	0	½	0.025(7)	0.10(2)
Ta2	2*d*	0.12723(17)	½	0.0797(3)	0.0076(7)	1
Ta3	2*d*	0.44318(18)	½	0.7494(3)	0.0070(7)	1
Ta4	2*d*	0.34360(17)	½	0.1772(3)	0.0065(7)	1
Ta5	2*d*	0.29664(18)	½	0.4096(3)	0.0061(7)	1
N1	4*d*	0	0	0	0.007(4)	1
N2	2*d*	0.335(3)	0	0.574(5)	0.007(4)	1
N3	2*d*	0.367(4)	0	0.345(5)	0.007(4)	1
N4	2*d*	0.566(3)	0	0.839(5)	0.007(4)	1
N5	2*d*	0.312(4)	½	0.747(5)	0.007(4)	1
N6	2*d*	0.217(3)	0	0.063(5)	0.007(4)	1
N7	2*d*	0.524(3)	½	0.409(5)	0.007(4)	1

Table D.4. Anisotropic displacement parameters (Å^2) with standard deviations in parentheses. The anisotropic displacement factor is expressed as $\exp[-2\pi^2 (U_{11}h^2a^{*2} + U_{22}k^2b^{*2} + U_{33}l^2c^{*2} + U_{12}hka^*b^* + U_{13}hla^*c^* + U_{23}klb^*c^*)$.

atom	U_{11}	U_{22}	U_{33}	U_{12}	U_{13}	U_{23}
P1	0.006(9)	0.010(8)	0.025(11)	0	-0.009(7)	0
Ta1	0.006(9)	0.010(8)	0.025(11)	0	-0.009(7)	0
Ta2	0.0071(13)	0.0057(12)	0.0123(14)	0	0.0070(11)	0
Ta3	0.0062(12)	0.0043(11)	0.0124(13)	0	0.0065(11)	0
Ta4	0.0066(13)	0.0036(11)	0.0108(13)	0	0.0061(11)	0
Ta5	0.0035(12)	0.0046(11)	0.0104(13)	0	0.0043(10)	0

Table D.5. Interatomic distances (Å) and bond angles (°) with standard deviations given in parentheses.

atom 1	*atom 2*	*count*	*distance / Å*	*atom 1*	*atom 2*	*atom 3*	*angle / °*
P1	N3	2x	1.78(5)	N7	–P1–	N7	83(2)
P1	N7	4x	1.94(3)	N3		N7	90.0(16)
Ta2	N5	2x	2.13(3)	N7		N7	97(2)
Ta2	N6	2x	2.15(3)	N3		N3	180
Ta2	N4	1x	2.22(4)	N7		N7	180
Ta2	N1	2x	2.2311(17)	N5	–Ta2–	N6	69.2(15)
Ta3	N5	1x	2.10(5)	N5		N1	74.2(11)
Ta3	N7	1x	2.12(4)	N6		N4	74.5(14)
Ta3	N4	2x	2.17(3)	N1		N1	81.59(8)
Ta3	N2	2x	2.21(3)	N4		N1	83.2(9)
Ta3	N1	1x	2.348(2)	N6		N6	85.4(16)
Ta4	N4	2x	2.15(3)	N5		N5	86.4(17)
Ta4	N6	2x	2.19(3)	N6		N1	92.2(9)
Ta4	N3	2x	2.21(3)	N5		N6	124.9(17)
Ta4	N6	1x	2.22(4)	N5		N1	128.5(12)
Ta4	N7	1x	2.49(4)	N5		N4	135.9(9)
Ta5	N2	2x	2.12(3)	N6		N1	157.5(12)
Ta5	N5	2x	2.14(3)	N5	–Ta3–	N1	72.3(13)
Ta5	N3	2x	2.22(3)	N7		N2	74.2(14)
Ta5	N2	1x	2.25(4)	N5		N2	74.2(15)
Ta5	N7	1x	2.34(4)	N7		N4	76.4(14)
				N4		N1	81.6(12)
				N2		N2	82.5(15)
				N4		N4	84.3(16)
				N4		N2	89.3(13)
				N2		N1	125.8(10)
				N5		N4	130.4(11)
				N5		N7	137.6(18)
				N7		N1	150.1(12)
				N4		N2	150.6(16)
				N3	–Ta4–	N7	67.8(14)
				N4		N7	69.4(14)
				N6		N3	71.4(14)
				N6		N6	73.4(16)
				N4		N6	74.7(14)
				N4		N3	80.7(14)
				N3		N3	82.6(15)
				N6		N6	83.3(15)
				N4		N4	85.6(16)
				N4		N6	86.9(13)
				N6		N3	124.0(15)
				N6		N7	130.3(16)

N6		N7	135.4(9)
N4		N3	137.3(17)
N3		N6	137.7(8)
N4		N6	148.0(17)
N5	–Ta5–	N3	68.1(15)
N3		N7	70.3(14)
N2		N7	71.5(14)
N5		N2	72.7(15)
N2		N2	74.8(16)
N3		N3	82.0(15)
N2		N3	83.2(13)
N2		N5	84.6(13)
N5		N5	85.8(17)
N2		N2	87.1(16)
N5		N3	121.3(16)
N2		N7	133.0(16)
N5		N7	133.9(10)
N3		N2	136.4(9)
N2		N3	141.7(17)
N2		N5	147.5(18)

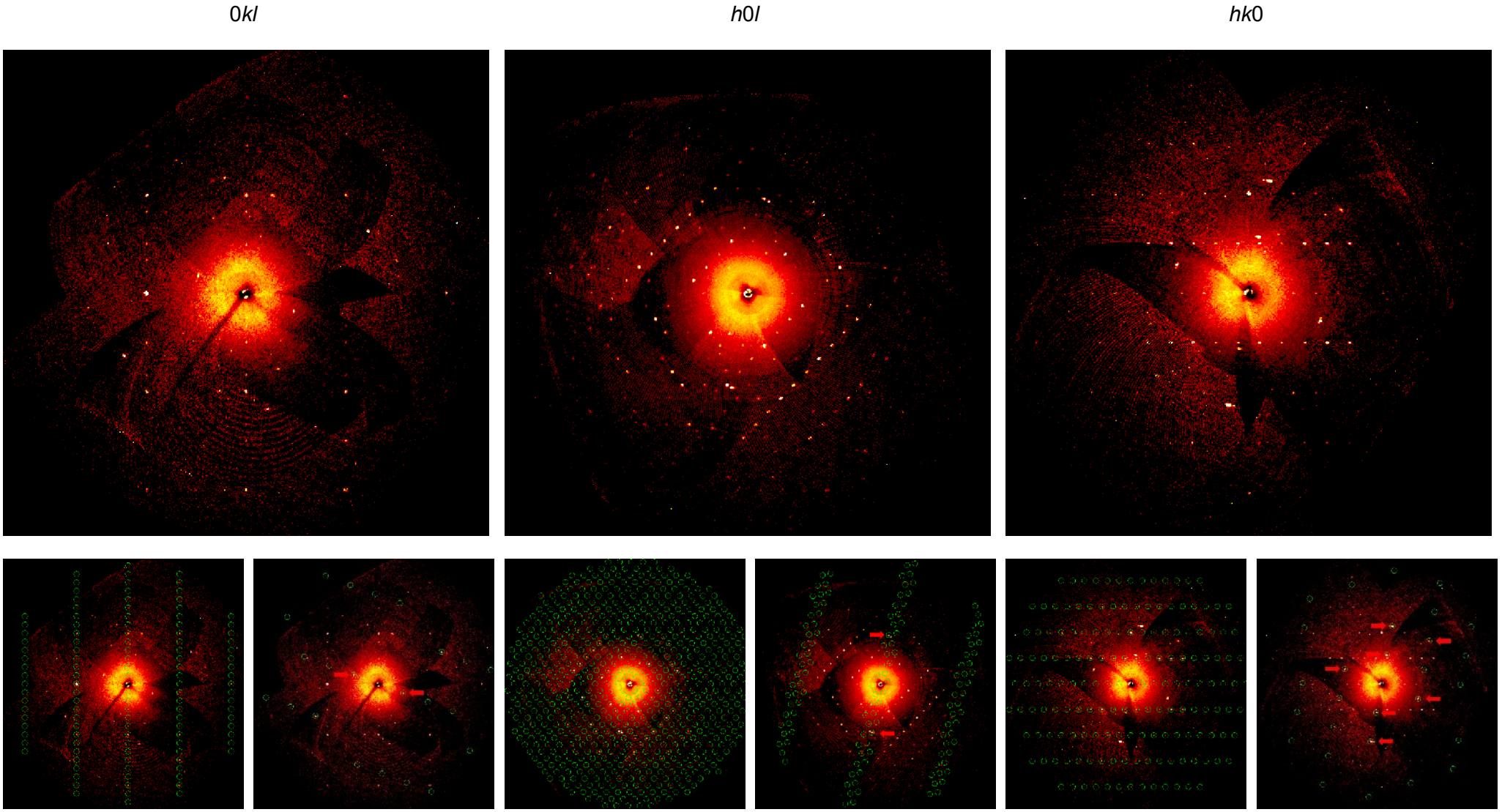

Figure D.3. Reciprocal lattice sections shows multicrystallic character; calculated with resolution limit 0.6 Å.

D.3. Rietveld Refinement

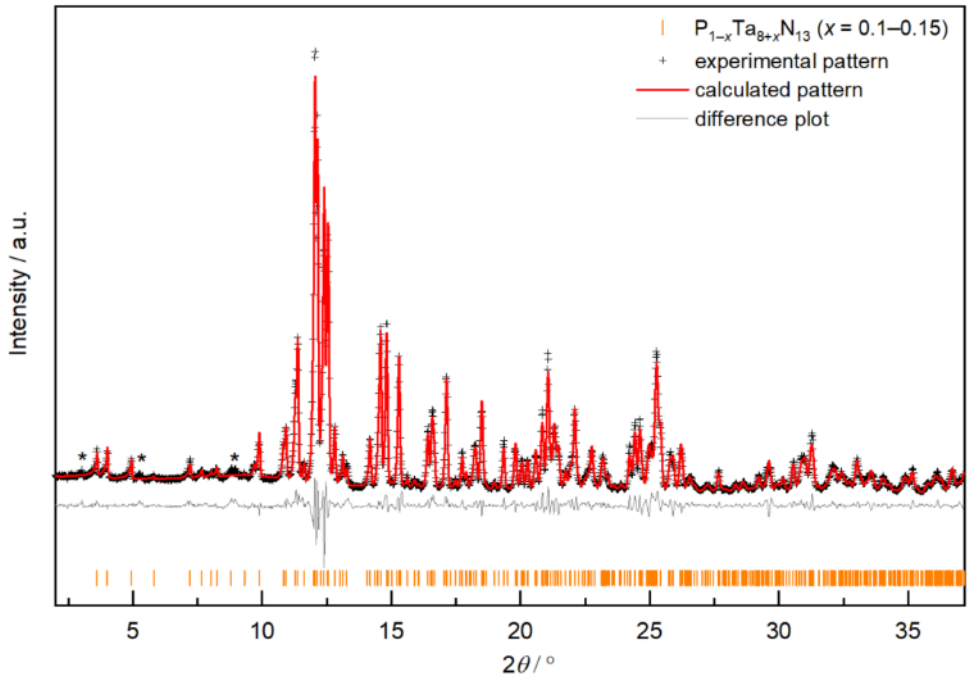

Figure D.4. Rietveld refinement with observed (black cross) and calculated (red line) X-ray powder diffraction patterns, positions of Bragg reflections of $P_{1-x}Ta_{8+x}N_{13}$ ($x \approx 0.1–0.15$) (vertical orange bars), and difference profile (gray line), asterisks mark unassigned signals.

D.4. High-Temperature PXRD

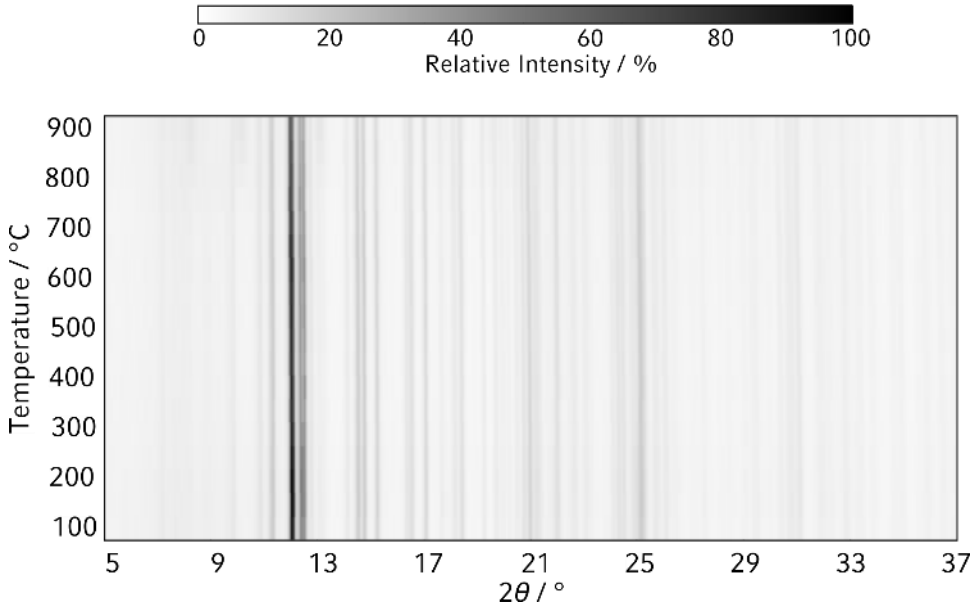

Figure D.5. Temperature-dependent powder X-ray diffraction patterns (Ag-Kα_1 radiation, λ = 0.5595378 Å) show a subtle shift due to an increase in lattice parameters with increasing temperature up to 900 °C.

D.5. Elemental Analysis

Table D.6. SEM-EDX measurements (several point analyses) compared to values derived from sum formula.

element	*Ta*	*P*	*N*	*O*
measuring spot 1	33	5	62	0
measuring spot 2	31	5	59	4
measuring spot 3	36	5	54	5
measuring spot 4	36	5	54	5
measuring spot 5	32	7	56	6
measuring spot 6	36	5	51	8
measuring spot 7	37	5	50	8
measuring spot 8	37	5	50	8
average	35(2)	5.2(6)	55(4)	5(2)
$P_{0.85}Ta_{8.15}N_{13}$ exp.	37	5	59	-

D.6. Comparison with Ta_3N_5

(x = 0.1–0.15). The structural elucidation of HP-Ta_3N_5 was carried out at 22 GPa and the pressure difference is likely the cause for the compression.

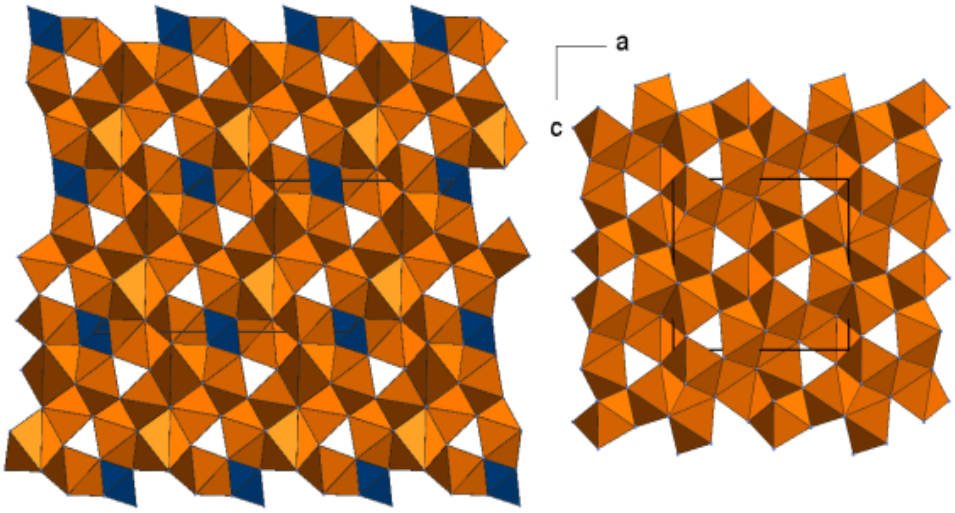

Figure D.6. Structural familiarity between the title compound $P_{1-x}Ta_{8+x}N_{13}$ ($x \approx 0.1$–0.15) (left, C2/m, a = 16.202(3) Å, b = 2.9155(4) Å, c = 11.0893(18) Å, β = 126.698(7)°) and the high-pressure polymorph of Ta_3N_5 (right, *Pnma*, a = 9.944(2) Å, b = 2.691(5) Å, c = 9.015(6) Å) [40] along [010].

D.7. Coordination Environment

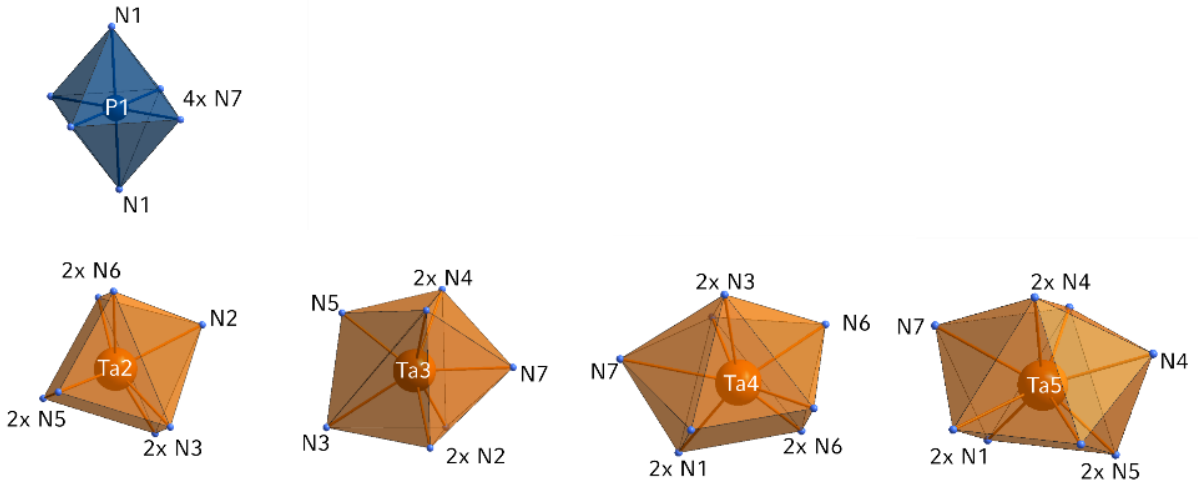

Figure D.7. Coordination polyhedra of P1, Ta2–Ta5 (isotropic calculated).

D.8. Scanning Transmission Electron Microscopy

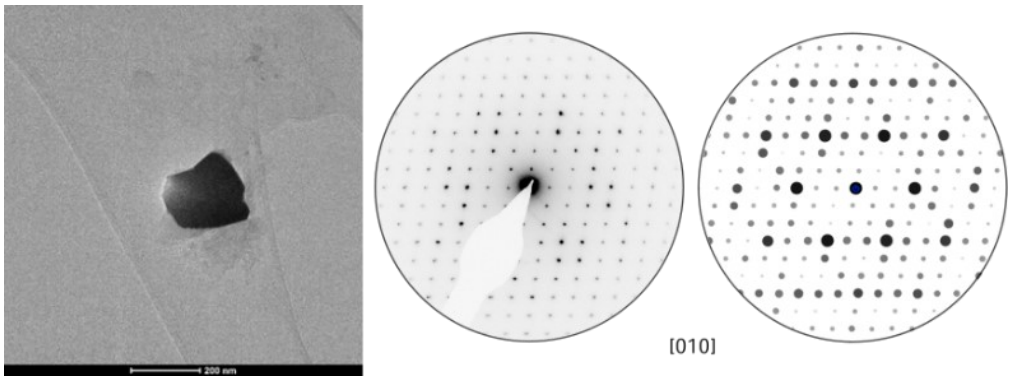

Figure D.8. Crystal used for STEM-HAADF analysis with respective SAED pattern (experimental left, simulated right) aligned along zone axis [010].

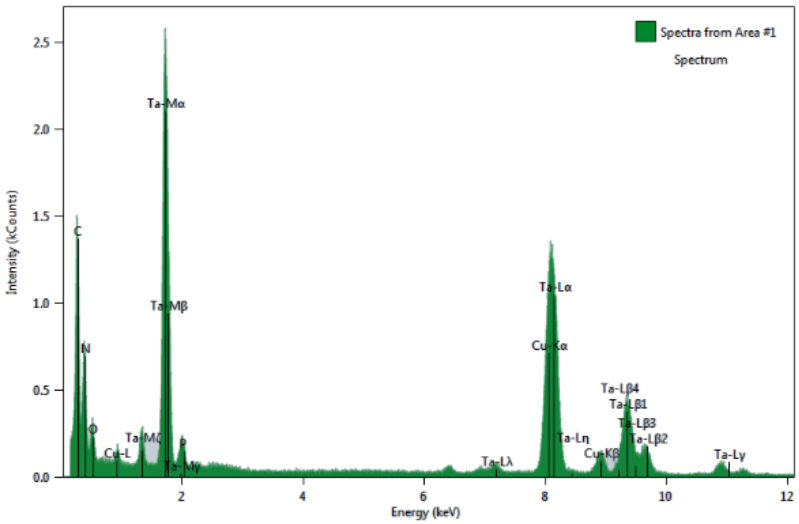

Figure D.9. Raw EDX spectrum of the obtained STEM EDX map; Cu and C originate from the used TEM grid.

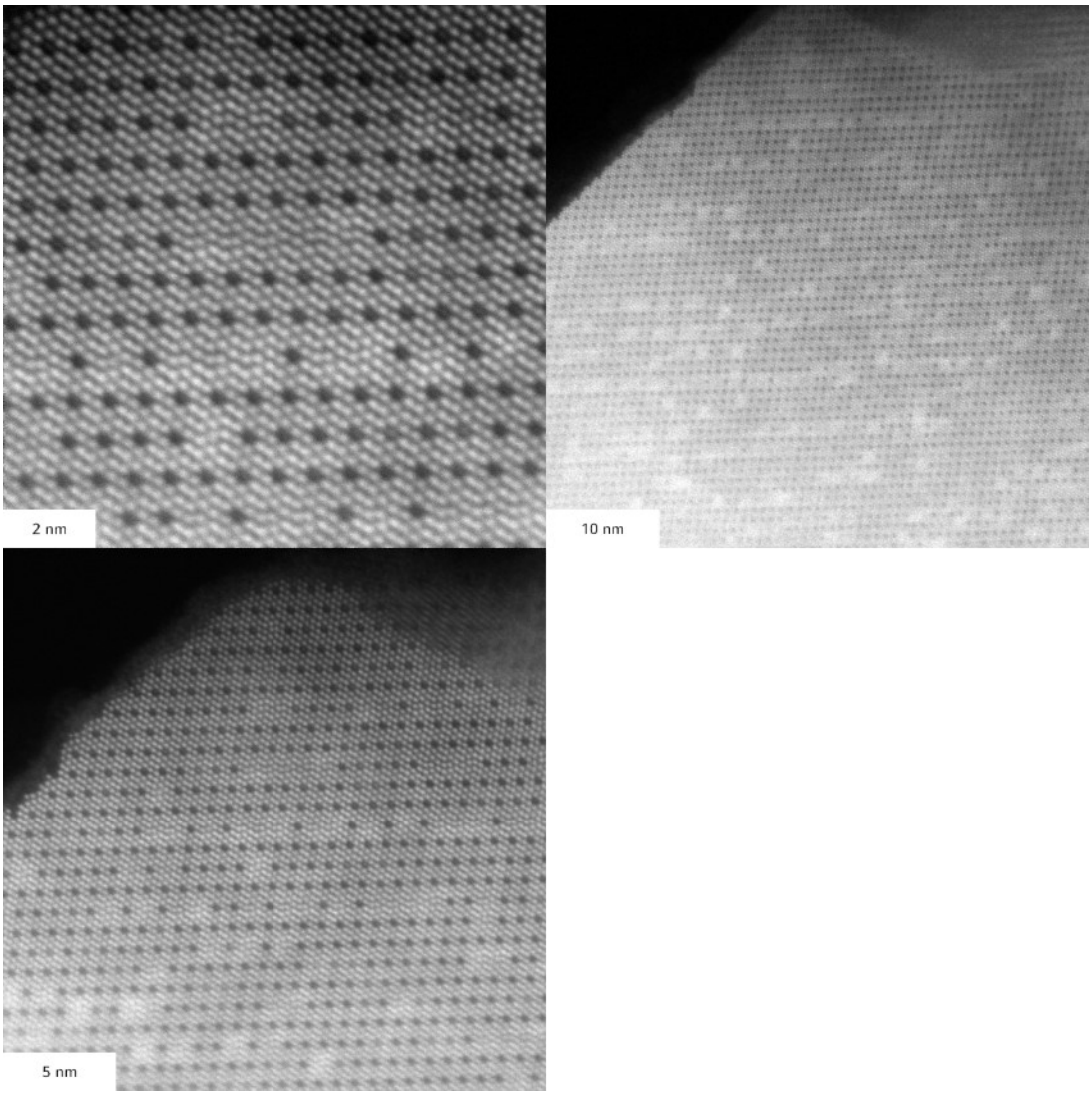

Figure D.10. Three different magnifications show that the occupational disorder of P and Ta appears throughout the entire crystal.

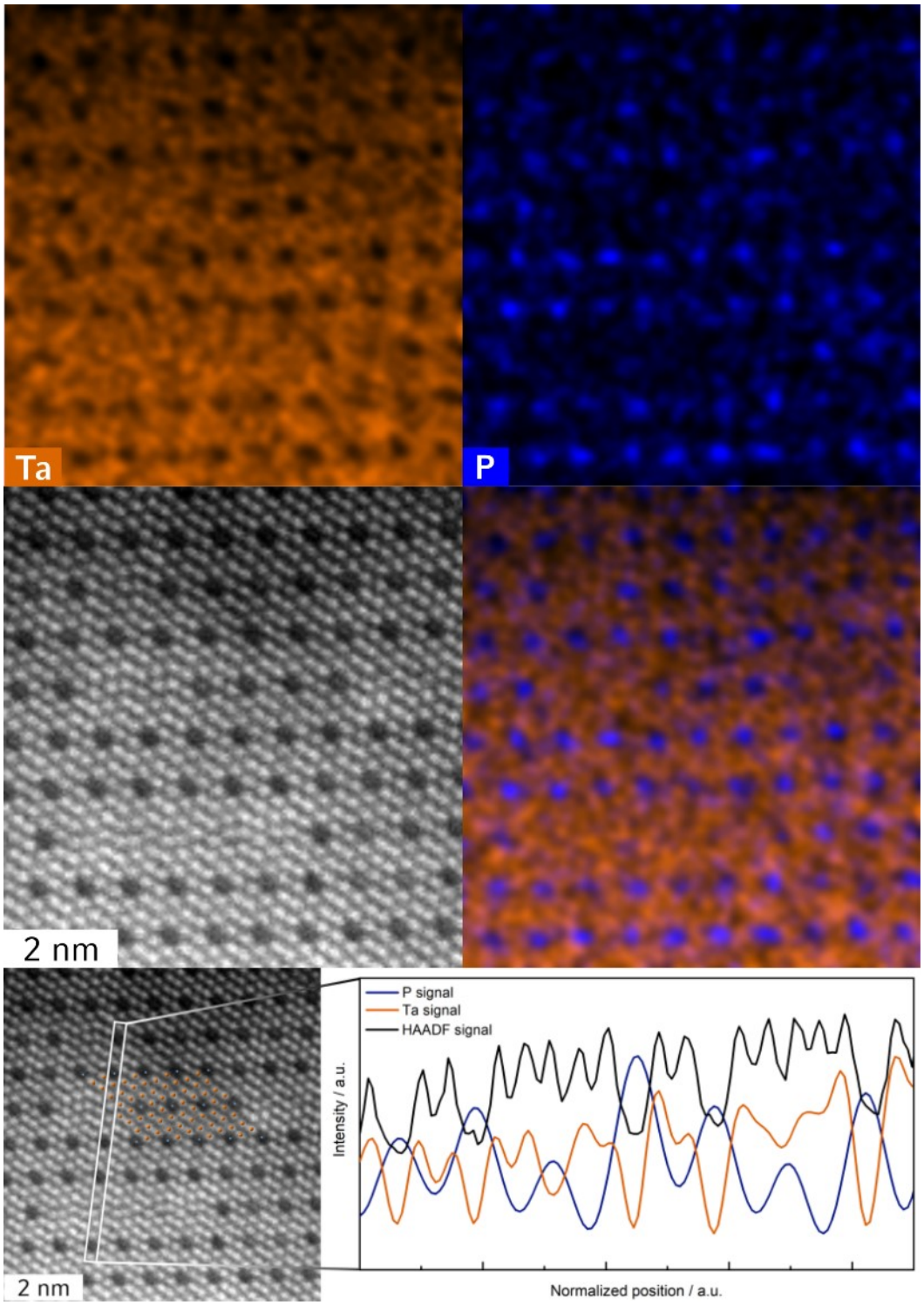

Figure D.11. Magnification of Figure x. STEM-HAADF analysis along [010]. Top: Atomic resolution EDX map Ta (orange) and P (blue); middle: STEM-HAADF image and combined EDX map. Bottom: STEM-HAADF image with structure overlay (left). Line scan of STEM-HAADF image and EDX maps demonstrates the difference in intensity corresponding to two different occupancies of atom columns by Ta and P atoms. Areas with high intensity exhibit Ta signal in the EDX map and areas with low intensity exhibit P signal. Disorder of P and Ta is clearly visible.

D.9. UV-Vis-NIR Spectroscopy

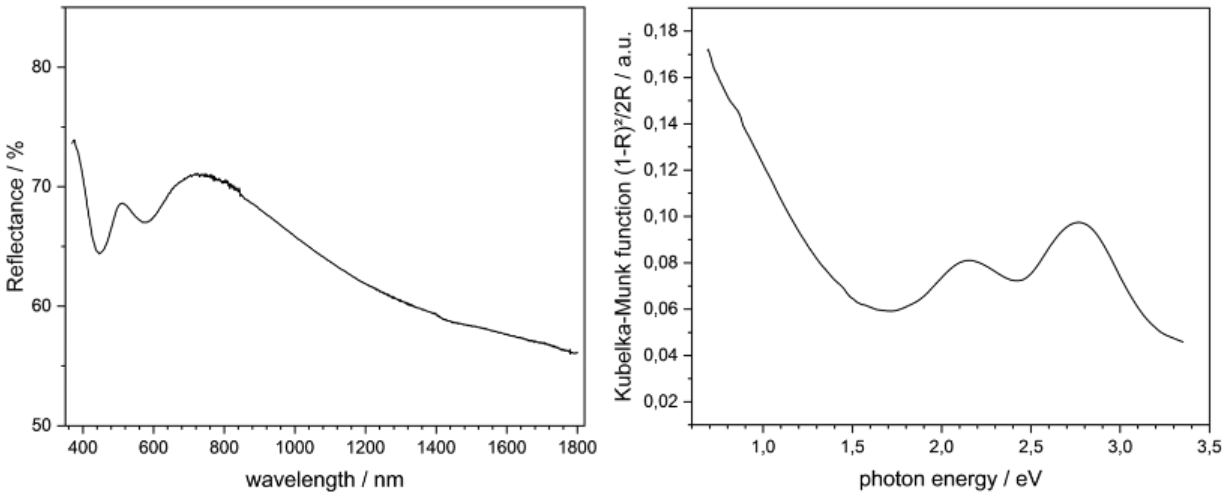

Figure D.12. Diffuse reflectance spectrum, diluted with $BaSO_4$ and calculated photon energy-dependent pseudo-absorption spectrum using Kubelka-Munk´s function.

D.10. Magnetic Measurements

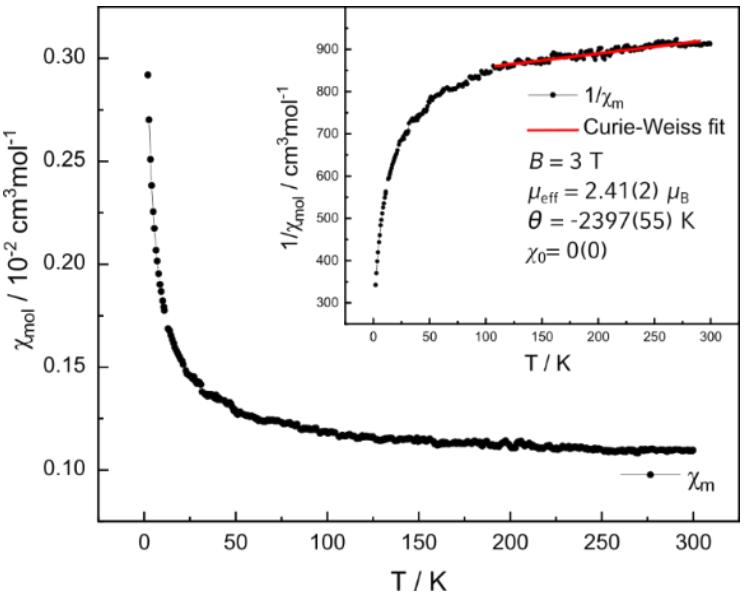

Figure D.13. Magnetic susceptibility and inverse magnetic susceptibility (inset) with an extended Curie-Weiss fit (red).

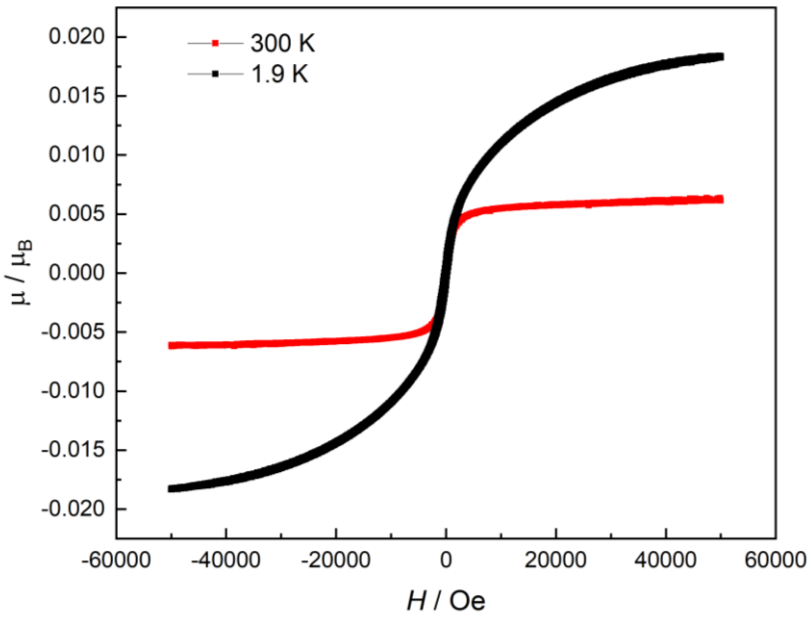

Figure D.14. Magnetization isotherm at 2 K (black) and 300 K (red).

D.11. Electron Paramagnetic Resonance Measurements

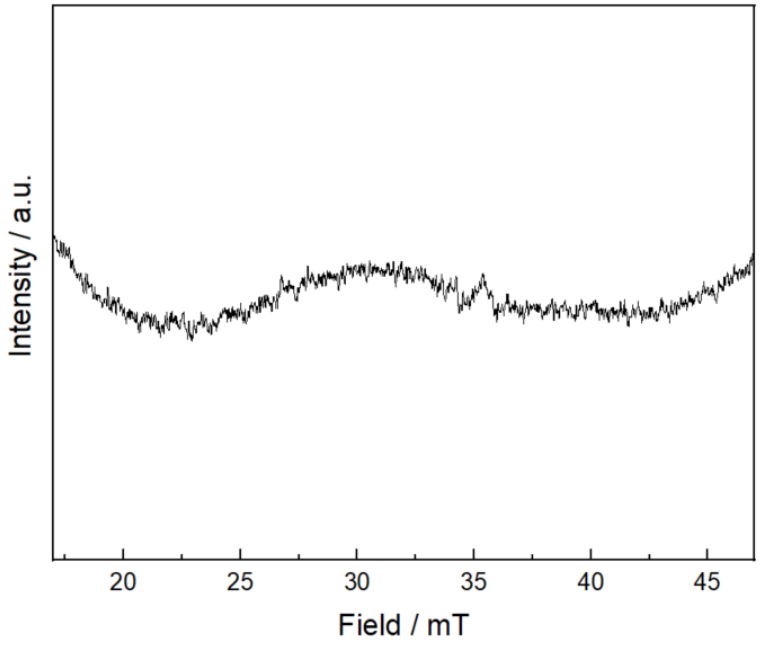

Figure D.15. CW X-band / EPR spectrum measured at room temperature shows no signal that could be evaluated indicating.

D.12. Bader Charge Population Analysis

Table D.7. Bader charge values values for all calculated compounds.

	PTa_8N_{13} *C2/m*	Ta_3N_5 *Pnma*	Ta_3N_5 *Cmcm*	TaON $P2_1c$	Ta_2N_3 *Pnma*	TaN $P\bar{6}m2$	ε-TaN *P6mmm*	δ-TaN $Fm\bar{3}m$	π-TaN $P\bar{6}2m$
Ta	2.07	2.27	2.54	2.67	2.20	1.57	0.80	1.81	1.33
	2.07	2.29	2.52		2.31		2.23		1.96
	2.09	2.30							
	2.09								
	2.30								
	2.30								
	2.30								
	2.30								
P	2.83								
N/O	–1.49	–1.42	–1.57	–1.49	–1.52	–1.57	–1.75	–1.81	–1.75
	–1.49	–1.24	–1.45	–1.49	–1.45				
	–1.52	–1.40	–1.56		–1.53				
	–1.52	–1.45		–1.18					
	–1.52			–1.18					
	–1.52								
	–1.58								
	–1.58								
	–1.59								
	–1.59								
	–1.64								
	–1.65								
	–1.65								

Table D.8. Valence electron values values for all calculated compounds.

	PTa_8N_{13}	Ta_3N_5	Ta_3N_5	TaON	Ta_2N_3	TaN	ε-TaN	δ-TaN	π-TaN
	C2/m	*Pnma*	*Cmcm*	$P2_1c$	*Pnma*	$P\bar{6}m2$	*P6mmm*	$Fm\bar{3}m$	$P\bar{6}2m$
Ta	8.93	8.73	8.46	8.33	8.80	9.43	10.20	9.19	9.67
	8.93	8.71	8.48		8.69		8.77		9.04
	8.91	8.70							
	8.91								
	8.70								
	8.70								
	8.70								
	8.70								
P	2.17								
N/O	6.49	6.42	6.57	6.49	6.52	6.57	6.75	6.81	6.75
	6.49	6.24	6.45	6.49	6.45				
	6.52	6.40	6.56		6.53				
	6.52	6.45		7.18					
	6.52			7.18					
	6.52								
	6.58								
	6.58								
	6.59								
	6.59								
	6.64								
	6.65								
	6.65								

D.13. Density Functional Theory Calculations

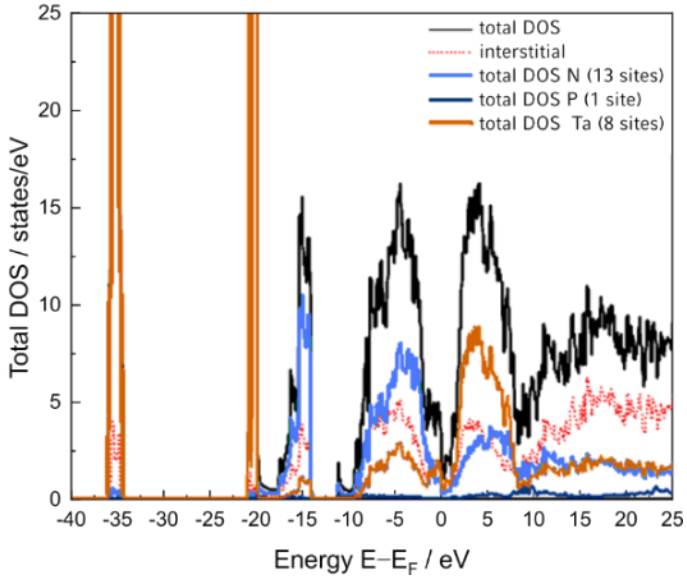

Figure D.16. Total Density of States calculation of PTa_8N_{13}. The calculated total DOS shows core states at around –35 eV and –21 eV (top), relative to E_F. The valence band consists mainly of the p character of the nitrogen sites and d character of tantalum sites. All Ta sites exhibit a significant d character in the valence band. States at E_F are dominated by Ta d states. P states overall contribute only little to the total DOS.

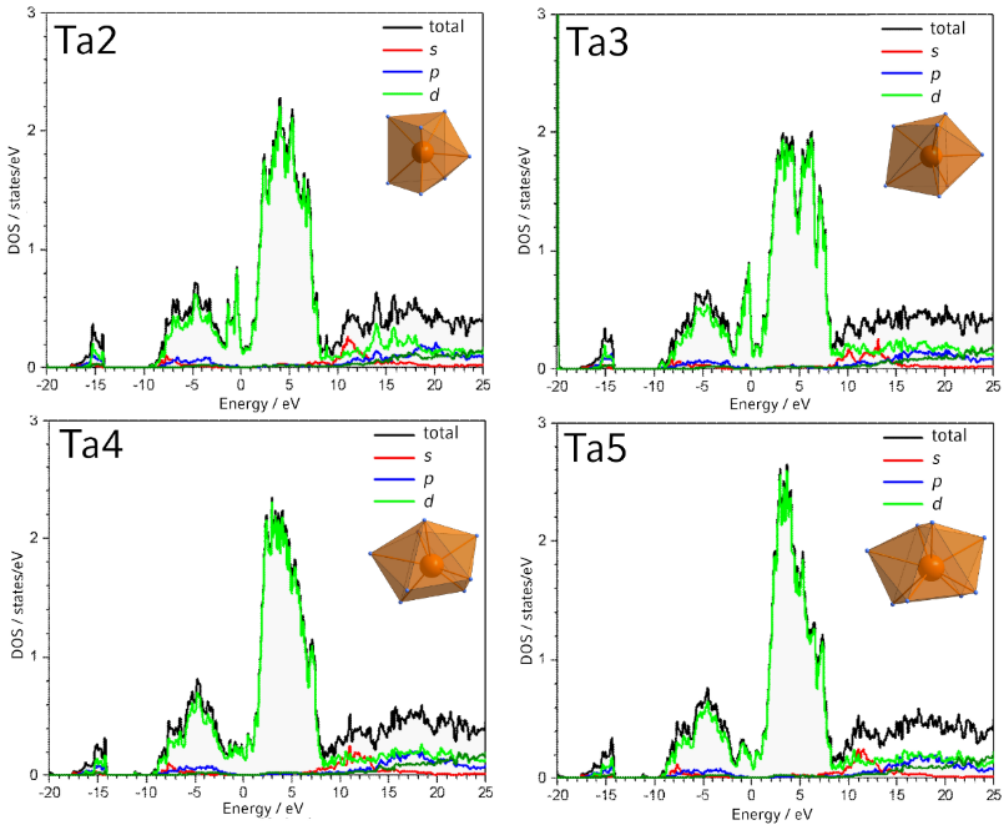

Figure D.17. Partial Density of States calculations Ta atoms. All tantalum sites exhibit a significant d character for the valence band and d states at E_F.

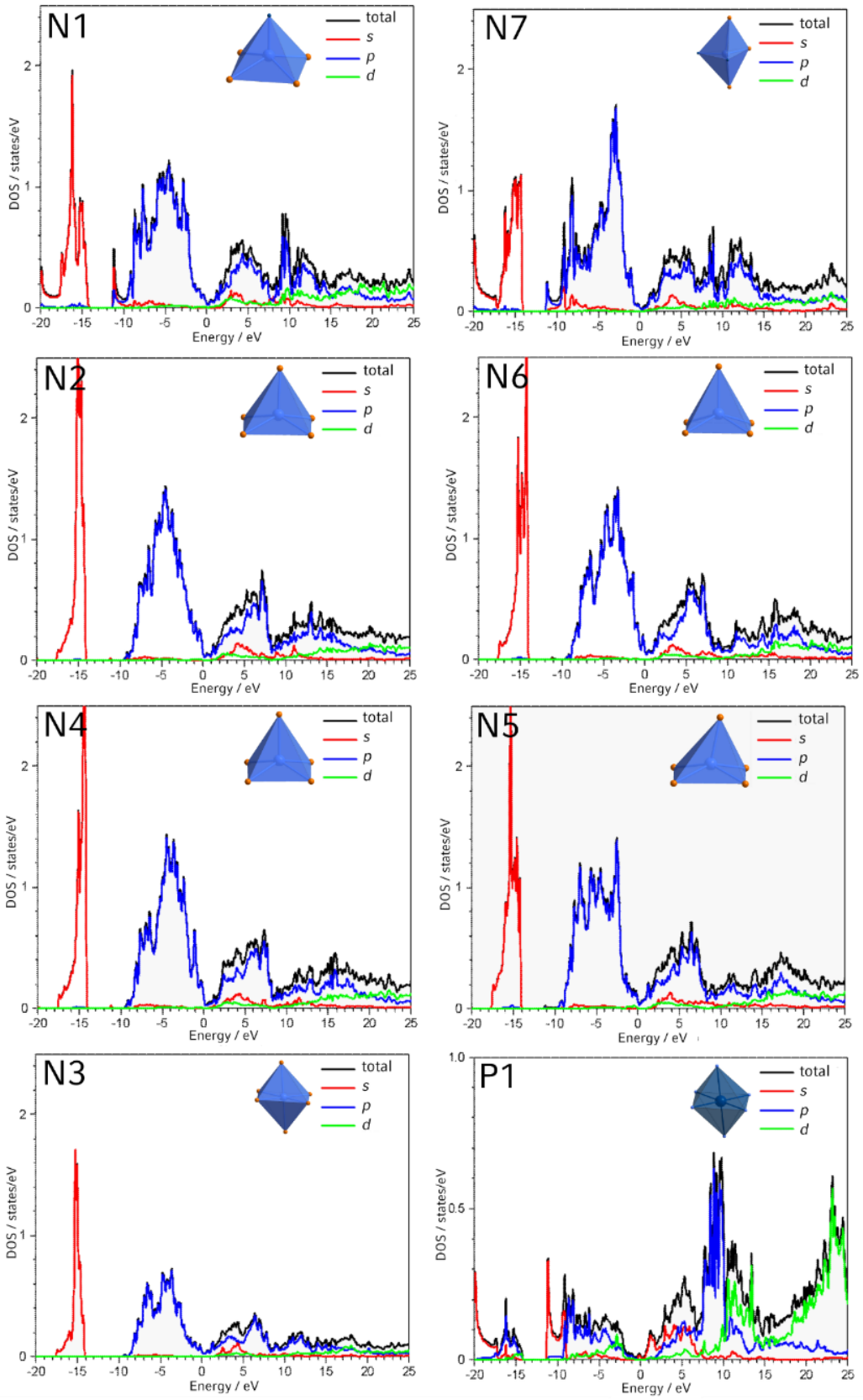

Figure D.18. Partial Density of States calculations for N and P atoms. The N1 and N7 sites exhibit hybridization of p and s states in the valence band. N2, N3, N4, N5, and N6 mainly have a valence band with a strong presence of p character. The s, p, and d states of phosphorus are hybridized in the valence band. P exhibits a slight metallic character due to a small amount of s states at E_F. Below the Fermi energy, the valence band of P is dominated by a strong p and d character.

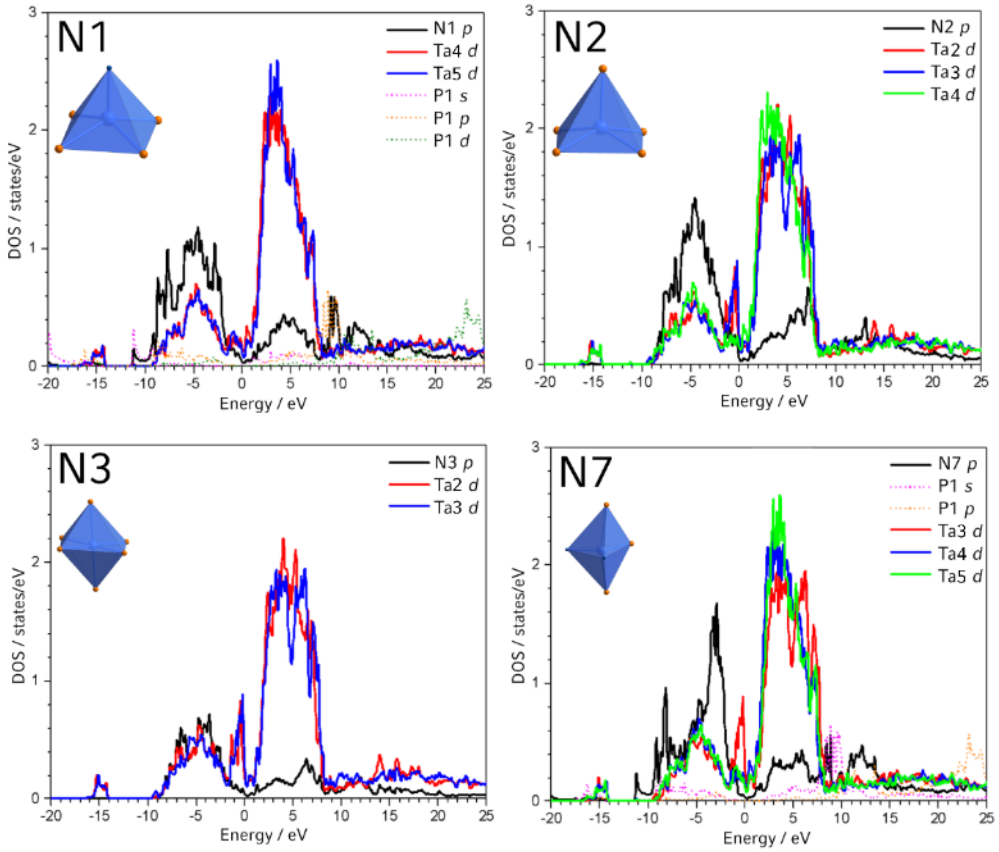

Figure D.19. Partial Density of States calculations for pairs of atoms that are closes to each other. Displayed are interactions between N1 and Ta4/Ta5/P1; N2 and Ta2/Ta3/Ta4; N3 and Ta2/Ta3; N7 and Ta3/Ta4/Ta5/P1.

Chapter 9

Miscellaneous

A. List of Publications Within this Thesis

The following list contains all publications of this dissertation, including authors, and author contributions.

- Tetra-Face-Capped Octahedra in a Tetrahedra Network – Structure Determination and Scanning Transmission Electron Microscopy of $SrAl_5P_4N_{10}O_2F_3$

  Monika M. Pointner, Oliver Oecker, and Wolfgang Schnick

  published in: *Chem. Eur. J.* **2023**, *29*, e202301960, DOI: 10.1002/chem.202301960.

  Monika M. Pointner conducted the synthesis, analysis, and manuscript writing. Supervision of the work was provided by Oliver Oeckler and Wolfgang Schnick. All authors participated in the manuscript revision.

- Multicationic Tetrahedra Networks: Alkaline-Earth-Centered Polyhedra and Non-Condensed AlN_6 octahedra in the Imidonitridophosphates $AE_2AlP_8N_{15}(NH)$ (*AE* = Ca, Sr, Ba)

  Monika M. Pointner, Reinhard M. Pritzl, Jonas M. Albrecht, Leopold Blahusch, Jonathan P. Wright, Eleanor Lawrence Bright, Carlotta Giacobbe, Oliver Oeckler, and Wolfgang Schnick

  published in: *Chem. Eur. J.* **2024**, e202400766, DOI: 10.1002/chem.202400766.

  Monika M. Pointner conducted the synthesis, data acquisition at the ESRF, analysis, and manuscript writing. Supervision of the work was provided by Oliver Oeckler and Wolfgang Schnick. All authors participated in the manuscript revision.

- $Cr_{5.7}Si_{2.3}P_8N_{24}$ – A Chromium(+IV) Nitridosilicate Phosphate with Amphibole-Type Structure

  Monika M. Pointner, Katherine R. Fisher, Martin Weidemann, Florian Wolf, Jonathan Wright, Eleanor Lawrence Bright, Carlotta Giacobbe, Oliver Oeckler,* and Wolfgang Schnick*

  published in: *Angew. Chem.* **2024**, *136,* e202401421; *Angew. Chem. Int. Ed.* **2024**, *63,* e202401421, DOI: 10.1002/anie.202401421.

  Monika M. Pointner conducted the synthesis, analysis, and manuscript writing. Supervision of the work was provided by Oliver Oeckler and Wolfgang Schnick. All authors participated in the manuscript revision.

- $P_{1-x}Ta_{8+x}N_{13}$ (x = 0.1–0.15): A Phosphorus Tantalum Nitride With High Specific Resistivity Featuring Mixed-Valent Tantalum and P/Ta Disorder

  Monika M. Pointner, Martin Weidemann, Lukas Nusser, Florian Wolf, Lucien Eisenburger, Oliver Oecker, and Wolfgang Schnick

  published in: *Angew. Chem.* **2024**, e202411441, *Angew. Chem. Int. Ed.* **2024**, e202411441, DOI: 10.1002/ange.202411441.

  Monika M. Pointner conducted the synthesis, analysis, and manuscript writing. Supervision of the work was provided by Oliver Oeckler and Wolfgang Schnick. All authors participated in the manuscript revision.

B. List of Publications Beyond this Thesis

The following list contains all publications of this dissertation, including authors, citation, and author contributions.

- Investigating the electronic properties of novel Titanium Oxonitridophosphate, $Ti_5P_{12}N_{24}O_2$, through structural distortions at the Titanium sites

  P. Ufondu, T. D. Boyko, **M. M. Pointner**, L. Eisenburger, W. Schnick, A. Moewes

  published in: *J. Mater. Chem. C* **2024**, *12*, 4392–4398, DOI: 10.1039/d4tc00248b.

  Conceptualization of the project and synthesis was done by Peter Ufondu. The manuscript was written by Peter Ufondu in a leading role with the support of Monika Pointner. A. Moewes supervised the project.

- Tunable Narrow-Band Cyan-Emission of Eu^{2+}-doped Nitridomagnesophosphates $Ba_{3-x}Sr_x[Mg_2P_{10}N_{20}]:Eu^{2+}$ (x = 0–3)

  Reinhard M. Pritzl, **Monika M. Pointner**, Kristian Witthaut, Philipp Strobel, Peter J. Schmidt, and Wolfgang Schnick

  published in: *Angew. Chem.* **2024**, e202403648; *Angew. Chem. Int. Ed.* **2024**, e202403648, DOI: 10.1002/ange.202403648.

  Conceptualization of the project and synthesis was done by Reinhard Pritzl. Electron microscopic analysis was carried out by Monika Pointner. Peter Schmidt and Philipp Strobel

carried out luminescence measurements. The manuscript was written by Reinhard Pritzl in a leading role with the support of all coauthors. W. Schnick supervised the project.

- (Dis)Order and Luminescence in Silicon-Rich (Si,P)–N Network $Sr_5Si_7P_2N_{16}:Eu^{2+}$

  Marwin Dialer, **Monika M. Pointner**, Philipp Strobel, Peter J. Schmidt, and Wolfgang Schnick

  published in: *Inorg. Chem.* **2024**, *63*, 2, 1480–1487, DOI: 10.1021/acs.inorgchem.3c04109.

  Conceptualization of the project and synthesis was done by Marwin Dialer. Electron microscopic analysis was carried out by Monika Pointner. Peter Schmidt and Philipp Strobel carried out luminescence measurements. The manuscript was written by Marwin Dialer in a leading role with the support of all coauthors. W. Schnick supervised the project.

- Order and Disorder in Mixed (Si,P)–N Networks $Sr_2SiP_2N_6:Eu^{2+}$ and $Sr_5Si_2P_6N_{16}:Eu^{2+}$

  Marwin Dialer, **Monika M. Pointner**, Sophia L. Wandelt, Philipp Strobel, Peter J. Schmidt, Lkhamsuren Bayarjargal, Bjoern Winkler and Wolfgang Schnick

  published in: *Adv. Optival Mater.* **2023**, 2302668, DOI: 10.1002/adom.202302668.

  Conceptualization of the project and synthesis was done by Marwin Dialer. Electron microscopic analysis was carried out by Monika Pointner. Peter Schmidt and Philipp Strobel carried out luminescence measurements. The manuscript was written by Marwin Dialer in a leading role with the support of all coauthors. W. Schnick supervised the project.

- Combining MN_6 Octahedra and PN_5 Trigonal Bipyramids in the Mica-like Nitridophosphates MP_6N_{11} (M = Al, In)

  Sebastian J. Ambach, **Monika M. Pointner**, Sophie Falkai, Carsten Paulmann, Oliver Oeckler, and Wolfgang Schnick

  published in: *Angew. Chem.* **2023**, *135*, e202303580; *Angew. Chem. Int. Ed.* **2023**, *62*, e202303580, DOI: 10.1002/chem.202301960.

  Conceptualization of the project was done by Sebastian Ambach. Synthesis was carried out by Sophie Falkai under the supervision of Sebastian Ambach. Synchrotron diffraction data collection and data reduction were performed by Monika Pointner and Oliver Oeckler as a supporting role. Carsten Paulmann assisted with measurements at DESY. The manuscript was written by Sebastian Ambach. W. Schnick supervised the project.

- High Thermoelectric Properties in the Sodalite Compounds $BaGe_8As_{14}$ and AGe_7As_{15} (A = Rb, Cs)

  Valentin Weippert, Kristian Witthaut, **Monika M. Pointner**, Malte Sachs, Lucien Eisenburger, Florian Kraus, and Dirk Johrendt

  published in: *Chem. Mater.* **2021**, *33*, 8248–8258, DOI: 10.1021/acs.chemmater.1c02349.

  The conceptualization, synthesis and organization of the project was done by Valentin Weippert. Monika Pointner performed electron microscopy analysis. The manuscript was written by Valentin Weippert in a leading role with the support of Kristian Witthaut, Monika Pointner. D. Johrendt supervised the project.

- Electronic properties of semiconducting $Zn(Si,Ge,Sn)N_2$ alloys

  Masako Ogura, Dan Han, **Monika M. Pointner**, Laura S. Junkers, Stefan S. Rudel, Wolfgang Schnick, and Hubert Ebert

  published in: *Phys. Rev. Materials* **2021**, *5*, 024601, DOI: 10.1103/PhysRevMaterials.5.024601.

  The theoretical calculations and data analysis were performed by Masako Ogura, Dan Han, Monika Pointner, and Laura Junkers. Masako Ogura wrote the manuscript with the assistance of Monika Pointner and Laura Junkers. Hubert Ebert supervised the project.

C. Contributions to Conferences and Seminars

1. Studies on the Distribution of Eu atoms in $Ca_2Si_5N_8:Eu^{2+}$ by Scanning Transmission Electron Microscopy

   Monika M. Pointner, Lucien A. Eisenburger, Oliver Oeckler, Wolfgang Schnick

   Poster presentation, Undergraduate Research Conference on Molecular Sciences, 2019, Irsee, Germany.

2. Synthesis and Analysis of Nitrido(phospho)silicates and an Alumooxonitridophosphate using Mineralizer-Assisted HP/HT-Technology and TEM

   Monika M. Pointner, Wolfgang Schnick

   Seminar Schnick Group, 2020, Munich, Germany.

3. Luminescent “Nitridoalumooxophosphates” by High-Pressure/High-Temperature Synthesis

   Monika M. Pointner, Oliver Oeckler, Wolfgang Schnick

   Oral presentation, Deutsche Gesellschaft für Kristallographie, 2021, online.

4. Das kleine 1x1 der Elektronenmikroskopie für Festkörperchemiker

   Monika M. Pointner, Wolfgang Schnick

   Seminar Schnick Group, 2021, Munich, Germany.

5. Ein kleiner Überblick zu ID11 und ein größerer zu Kettensilicaten

   Monika M. Pointner, Wolfgang Schnick

   Seminar Schnick Group, 2022, Munich, Germany.

6. Supertetrahedra and Cation Distribution in the Strontium Aluminium Oxonitridophosphate $SrAl_5P_4N_{10}O_2F_3$ by SCXRD and STEM

   Monika M. Pointner, Oliver Oeckler, Wolfgang Schnick

   Poster presentation, 33. European Crystallographic Meeting, 2022, Versailles, France.

7. Raufasertapeten

   Monika M. Pointner, Wolfgang Schnick

   Seminar Schnick Group, 2022, Munich, Germany.

8. Ambivalent Amphibole

   Monika M. Pointner, Wolfgang Schnick

   Oral presentation, 6th Obergurgl-Seminar Solid-State Chemistry, 2023, Obergurgl, Austria.

9. A Nitridosilicatephosphate with Amphibole Structure

   Monika M. Pointner, Martin Weidemann, Katherine Fisher, Florian Wolf, Eleanor Lawrence Bright, Carlotta Giacobbe, Jonathan Wright, Oliver Oeckler, Wolfgang Schnick

   Poster presentation, Deutsche Gesellschaft für Kristallographie, 2023, Frankfurt, Germany.

10. Amphibole Analog and Uncommon Oxidation State of Chromium(IV) – The Nitridophosphate $Cr_{5.7}Si_{2.3}P_8N_{24}$

    Monika M. Pointner, Martin Weidemann, Katherine Fisher, Florian Wolf, Eleanor Lawrence Bright, Carlotta Giacobbe, Jonathan Wright, Oliver Oeckler, Wolfgang Schnick

    Poster presentation, Undergraduate Research Conference on Molecular Sciences, 2023, Irsee, Germany.

11. To be, or not to be: Bad metal edition

    Monika M. Pointner, Wolfgang Schnick

    Oral presentation, 7th Obergurgl-Seminar Solid-State Chemistry, 2024, Obergurgl, Austria.

12. Power-Pointner-Präsentation: Elektronen – gerührt, nicht geschüttelt

    Monika M. Pointner, Wolfgang Schnick

    Seminar Schnick Group, 2024, Munich, Germany.

D. Deposited Crystallographic Data

Crystallographic data of compounds featured in this dissertation can be obtained through the Fachinformationszentrum (FIZ) Karlsruhe, Germany or the Cambridge Crystallographic Data Centre upon quoting the corresponding depository number.

Table 9.1. All compounds featured in this dissertation with depository numbers.

compound	*deposition number*
$SrAl_5P_4N_{10}O_2F_3$	2261405
$Sr_2AlP_8N_{15}(NH)$	2301149
$Ca_2AlP_8N_{15}(NH):Eu^{2+}$	2301150
$Ba_2AlP_8N_{15}(NH):Eu^{2+}$	2301151
$Cr_{5.7}Si_{2.3}P_8N_{24}$	2324313
$P_{0.85}Ta_{8.15}N_{13}$	2345638

E. Curriculum Vitae

Education

Since 09/2020	**Research assistant** in the group of Prof. Dr. Wolfgang Schnick (Department of Chemistry, Ludwig-Maximilians-Universität München) **Doctoral thesis**: "Synergy of Single-Crystal X-Ray Diffraction and Atomic Scale Electron Microscopy – Structure Elucidation of Novel Nitridophosphates and Nitrides"
12/2019–07/2020	**Master thesis** (Inorganic Chemistry) Ludwig-Maximilians-Universität München, Prof. Dr. Wolfgang Schnick Title: „Synthesis and Analysis of Nitrido(phospho)silicates and an Alumoxonitridophosphate using Mineralizer-Assisted HP/HT Technology and TEM"
10/2018–07/2020	**Master of Science** (Chemistry) Ludwig-Maximilians-Universität München, Germany Focus in Inorganic Chemistry and Physical Chemistry
05/2018–08/2018	**Bachelor thesis** (Inorganic Chemistry) Ludwig-Maximilians-Universität München, Prof. Dr. Wolfgang Schnick Title: „Studies on the Distribution of Eu atoms in $Ca_2Si_5N_8:Eu^{2+}$ by Scanning Transmission Electron Microscopy"
10/2015–08/2018	**Bachelor of Science** (Chemistry and Biochemistry) Ludwig-Maximilians-Universität Munich, Germany
06/2015	**Allgemeine Hochschulreife**
10/2012–06/2015	**Secondary School** Korbinian Aigner Gymnasium, Erding, Germany
06/2012	**Realschulreife**